

Leading twist nuclear shadowing phenomena in hard processes with nuclei

L. Frankfurt

*Nuclear Physics Department, School of Physics and Astronomy, Tel Aviv
University, 69978 Tel Aviv, Israel*

V. Guzey

*Theory Center, Thomas Jefferson National Accelerator Facility, Newport News,
VA 23606, USA*

M. Strikman

*Department of Physics, the Pennsylvania State University, State College,
PA 16802, USA*

Abstract

We present and discuss the theory and phenomenology of the leading twist theory of nuclear shadowing which is based on the combination of the generalization of the Gribov-Glauber theory, QCD factorization theorems, and the HERA QCD analysis of diffraction in lepton-proton deep inelastic scattering (DIS). We apply this technique for the analysis of a wide range of hard processes with nuclei—inclusive DIS on deuterons, medium-range and heavy nuclei, coherent and incoherent diffractive DIS with nuclei, and hard diffraction in proton-nucleus scattering—and make predictions for the effect of nuclear shadowing in the corresponding sea quark and gluon parton distributions. We also analyze the role of the leading twist nuclear shadowing in generalized parton distributions in nuclei and in certain characteristics of final states in nuclear DIS. We discuss the limits of applicability of the leading twist approximation for small x scattering off nuclei and the onset of the black disk regime and methods of detecting it. It will be possible to check many of our predictions in the near future in the studies of the ultraperipheral collisions at the Large Hadron Collider (LHC). Further checks will be possible in pA collisions at the LHC and forward hadron production at the Relativistic Heavy Ion Collider (RHIC). Detailed

tests will be possible at an Electron-Ion Collider (EIC) in the USA and at the Large Hadron-Electron Collider (LHeC) at CERN.

Contents

1	Introduction	4
2	Gribov results for nuclear shadowing	10
2.1	Gribov picture of space-time evolution of high-energy processes	10
2.2	Nuclear shadowing in pion-deuteron scattering	12
2.3	Comparison of Gribov and Glauber results for nuclear shadowing	18
2.4	The AGK cutting rules and nuclear shadowing	21
3	Leading twist theory of nuclear shadowing for quark and gluon nuclear parton distribution functions	23
3.1	Derivation of the master equation for nuclear parton distribution functions	23
3.2	Space-time picture of leading twist shadowing in the nucleus infinite momentum frame and the transverse structure of the nuclear wave function	43
3.3	On nuclear shadowing of valence quark parton distributions	47
3.4	The upper limit on nuclear shadowing in nuclear PDFs	49
3.5	Diffraction in DIS and the QCD factorization theorem	52
3.6	Summary of QCD analysis of the data on hard diffraction at HERA	56
4	Nuclear shadowing in DIS on deuterium	65
4.1	Nuclear shadowing for unpolarized deuteron structure functions	65
4.2	Nuclear shadowing in tagged DIS processes on deuterium	70
5	Phenomenology of nuclear shadowing for nuclear structure functions and parton distributions for medium and heavy nuclei	75
5.1	Predictions for nuclear parton distributions	75

Email addresses: frankfur@tauphy.tau.ac.il (L. Frankfurt), vguzey@jlab.org (V. Guzey), strikman@phys.psu.edu (M. Strikman).

5.2	Nuclear shadowing in longitudinal structure function $F_L^A(x, Q^2)$	90
5.3	Energy and Q^2 dependence of nuclear shadowing	92
5.4	The A dependence of nuclear shadowing	97
5.5	Impact parameter dependent nuclear PDFs	98
5.6	The transverse size of parton distributions in nuclei	103
5.7	The role of the finite coherence length	105
5.8	Comparison of the color fluctuation and quasi-eikonal approximations	106
5.9	Uncertainties of predictions of the leading twist theory of nuclear shadowing	107
5.10	Predictions for leading twist nuclear shadowing at the leading-order accuracy	111
5.11	The double scattering contribution to nuclear shadowing vs. the full result	112
5.12	Comparison with the nPDFs obtained from the DGLAP fits to the data	113
5.13	Comparison to the soft QCD model of [97–99]	116
5.14	The leading twist theory of nuclear shadowing vs. dipole model eikonal approximation	116
5.15	QCD evolution trajectories	128
5.16	Comparison of predictions of the leading twist theory of nuclear shadowing with fixed-target data	131
5.17	The EMC effect for heavy nuclei and the Lorentz dilation of the nuclear Coulomb field	134
6	Final states in DIS with nuclei at small x	138
6.1	Nuclear diffractive structure functions and diffractive parton distribution functions	138
6.2	Exclusive diffraction at small x	159
6.3	Nuclear effects in inclusive leading hadron spectra in eA collisions	178
6.4	Hadron production at central rapidities	180
7	Leading twist nuclear shadowing and suppression of hard coherent diffraction in proton-nucleus scattering	183

7.1	Soft coherent diffraction off nuclei	184
7.2	Hard coherent diffraction in pA scattering	186
7.3	Suppression factor for hard proton-nucleus coherent diffraction	187
7.4	Hard diffraction and ultraperipheral proton-nucleus collisions	192
8	The black disk regime	199
8.1	Introduction	199
8.2	BDR <i>vs.</i> weak density limit	202
8.3	Formal definition of BDR	202
8.4	Observations of an onset of the BDR	204
8.5	The onset of BDR in the dipole model: inclusive scattering	206
8.6	Diffractive final states	221
8.7	Post-selection mimicking fractional parton energy losses in inclusive spectra in the vicinity of BDR	223
8.8	Post-selection phenomenon as a precursor of the BDR	227
8.9	Evidence for post-selection effect in the forward pion production in the deuteron-Gold collisions at RHIC	230
8.10	Implications of energy-momentum conservation for the onset of BDR	234
8.11	BDR as new phase transition with the change of continuous symmetry	235
8.12	BDR <i>vs.</i> DGLAP approximation regime	236
8.13	BDR <i>vs.</i> parton saturation hypothesis	237
9	Conclusions	239
	References	241

1 Introduction

The most straightforward way to analyze the microscopic structure of atomic nuclei is to study distributions of quarks and gluons in nuclei using high-energy hard processes with

nuclear targets. The term "hard" means that such processes contain a large momentum transfer (scale), which allows one to resolve the parton content of the target. The presence of the large scale allows one to use collinear factorization theorems which introduce various universal distributions of partons in the hadronic target and determine their QCD evolution when the hard scale is varied (DGLAP evolution). In another limit, when the hard scale Q^2 is fixed and the energy tends to infinity, the DGLAP evolution breaks down and ultimately the black disk regime sets in.

In this review, we discuss nuclear parton distribution functions (nPDFs), nuclear diffractive parton distribution functions (nDPDFs), and nuclear generalized parton distributions (nGPDs) at small values of Bjorken x .

Nuclear PDFs is one of the key elements in the evaluation of numerous high energy hard phenomena involving nuclei. Their understanding is also important for the searches of the new phases of the QCD matter. Hence, the aim of this paper is to review legitimate calculations of the nuclear shadowing phenomena, analyze the range of the applicability of the theory, and provide numerical results. These results are topical and increasingly important because the phenomenon of nuclear shadowing is involved in the interpretation of Relativistic Heavy Ion Collider (RHIC) data, the evaluation of hard phenomena in proton-nucleus and nucleus-nucleus collisions at the Large Hadron Collider (LHC), the estimation of the onset of the black disk limit in ultra high-energy proton-nucleus and real photon-nucleus interactions at the LHC and also in DIS of leptons off nuclei at a future Electron-Ion Collider (EIC).

So far most of the information on nPDFs has been obtained from the measurements of the ratio of the nuclear to nucleon structure functions, $F_{2A}(x, Q^2)/[AF_{2N}(x, Q^2)]$, in inclusive deep inelastic scattering (DIS) of leptons on nuclear targets [1–22]. Complementary information on nPDFs has also been obtained in J/ψ production in DIS [23] and in proton-nucleus high-mass dimuon production (nuclear Drell-Yan) [24,25]. Also, nPDFs can be constrained by dijet production in DIS and photoproduction and by W and Z production in proton-nucleus and nucleus-nucleus scattering.

Nuclear DPDFs can be studied in diffractive DIS of leptons on nuclear targets [26,27] and, to some extent, in hard proton-nucleus diffraction.

Nuclear GPDs enter the theoretical description of hard exclusive processes with nuclei such as deeply virtual Compton scattering (DVCS) [28–32], coherent exclusive production of vector mesons in lepton-nucleus DIS, coherent photoproduction of heavy vector mesons (J/ψ and Υ) in ultraperipheral nucleus-nucleus collisions [33–35]. All three types of nuclear distributions—nPDFs, nDPDFs and nGPDs—can be studied at a future Electron-Ion Collider [36,37].

The experimental data on lepton-nucleus scattering obtained in a series of fixed target experiments have established that the cross section of scattering off nuclei is significantly

smaller than the sum of free nucleon cross sections for $x \leq 0.03$, see the review in [38]. This phenomenon is called nuclear shadowing; it is expected to be present for all parton flavors (sea and valence quarks and gluons), i.e., the ratio of the nuclear PDF of flavor j , $f_{j/A}(x, Q^2)$, to the corresponding PDF of a free nucleon, $f_{j/N}(x, Q^2)$, is suppressed for $x \leq 0.03$, $f_{j/A}(x, Q^2)/[Af_{j/N}(x, Q^2)] < 1$ (A is the number of nucleons). As one increases x , the suppression is followed by an enhancement, $f_{j/A}(x, Q^2)/[Af_{j/N}(x, Q^2)] > 1$ for $0.05 \leq x \leq 0.2$, which is called antishadowing. The analyses of the data indicate that antishadowing takes place for valence quarks and gluons and is absent for sea quarks.

Practically all presently available information on nPDFs in the shadowing region comes from DIS experiments. The major obstacle that prevents the reliable determination of nPDFs at small x from these experiments is the fact that these are fixed (stationary) target experiments. In the fixed target kinematics, the values of x and Q^2 are strongly correlated, and, hence, one measures nPDFs essentially in a narrow band in the $x - Q^2$ plane rather than on the entire plane. Moreover, requiring that Q^2 is sufficiently large for the application of perturbative QCD (factorization theorem), e.g., $Q^2 > 1 \text{ GeV}^2$, the data cover the region $x > 5 \times 10^{-3}$ (for the NMC energies), where the effect of nuclear shadowing is rather small.

This makes the extraction of nuclear quark PDFs problematic for $x \leq 0.01$ and impossible for $x \leq 0.005$, where the maximal value of Q^2 is of the order of 1 GeV^2 . The situation is even worse for the gluon nPDF since it is extracted indirectly using the scaling violations of $F_{2A}(x, Q^2)$. As a result, the fits to the current data do not have predictive power for nPDFs for $x < 0.01$. Indeed, the global fits to the available data performed by various groups by modeling nPDFs at some initial scale Q_0^2 , produce very different results because nPDFs at small x are not constrained by the available data [39–52]. Moreover, the uncertainties of the resulting predictions for nPDFs are very large, especially in the gluon channel [44,45,51]. It would take a lepton-nucleus collider—a future EIC—to open up the kinematics and probe deep in the shadowing region while keeping sufficiently large Q^2 to reliably determine nPDFs at small x .

Significant nuclear shadowing is also theoretically predicted for nuclear diffractive PDFs [26] and nuclear GPDs [29–32]. In addition, large shadowing is predicted for various cross sections in the formalisms which do not separate leading twist (LT) and non-LT contributions (see below).

Note that besides DIS off nuclear targets, the data on proton-nucleus high-mass dimuon production (nuclear Drell-Yan) is also used in the global QCD fits. These data mostly provide additional constraints on the sea quark nPDFs for $x \geq 0.03$ and $Q^2 \geq 16 \text{ GeV}^2$. In the gluon channel, additional constraints on the nuclear gluon distribution can be inferred from inclusive prompt photon [53] and J/ψ [54] production in proton-nucleus scattering. A recent analysis of nPDFs also included in the fits the RHIC data on inclusive high- p_T hadron production in deuteron-gold scattering at RHIC [50,51]. However, it is not clear how to separate various effects in nPDF in this case since the LT approximation is strongly

violated in the considered RHIC kinematics (see the discussion in Sec. 8).

The situation with the low- x uncertainty in the extraction of nPDFs will soon change with the start of the studies of ultra-peripheral nucleus-nucleus collisions at the LHC, which will allow one to probe nPDFs and nGPDs (especially in the gluon channel) down to $x = 10^{-5}$ and for large virtualities. Also, single hadron production in proton-nucleus (^{208}Pb) scattering at the LHC will provide stringent tests on nPDFs [55] provided one would find the kinematics where the factorization assumption underlying global nPDF fits holds and the nuclear shadowing effect is still significant.

Hence, at present, the only realistic way to determine nuclear PDFs at small x is to build the theory of nuclear shadowing based on the well understood properties of QCD; this is the aim of the present paper. We use the approach based on the leading twist approximation to the theory of nuclear shadowing in which nuclear shadowing is expressed in terms of elementary diffraction, i.e., nuclear shadowing in eA scattering is expressed in terms of ep diffraction. Our formalism—which we call the leading twist theory of nuclear shadowing—is based on the combination of the following ingredients:

- (i) The generalization of the technique developed by Gribov for the case of nuclear shadowing in soft processes (pion-deuteron scattering) [56] to hard processes, notably, to DIS with arbitrary nuclei [57],
- (ii) QCD factorization theorems (the leading twist approximation) for inclusive cross section of DIS [58] and diffraction in DIS [59],
- (iii) QCD analyses of the Hadron-Electron Ring Accelerator (HERA) data on diffraction in DIS [60–73] which confirmed the validity of QCD factorization for diffraction and determined diffractive PDFs of the nucleon.

Some of the ingredients listed above are formulated in the nucleus rest frame, others—in the nucleus fast frame. It is the QCD factorization theorems which allow one to connect them in an unambiguous way.

Several theoretical phenomena complicate calculations of nuclear shadowing.

- (i) The dominance of particle production in high energy processes invalidates the eikonal approximation, which is legitimate within the framework of non-relativistic quantum mechanics. A famous example is the Glauber correction for hadron-deuteron cross section which disappears at high energies since the space-time evolution of high energy processes is different in a quantum field theory and quantum mechanics, see the discussion in Sec. 2.3. V. Gribov has demonstrated how to account for the rapid increase of the longitudinal distances with an increase of energy (Lorentz time dilation) and calculated the shadowing correction [56] that matches well the Glauber correction valid at lower energies.
- (ii) The eikonal approximation strongly violates energy-momentum conservation at the energies where inelastic processes dominate, see Sec. 3.1.4. An account of the diffractive processes within the method of color fluctuations allows one to overcome this problem by taking into account the splitting of the virtual photon energy between the interacting par-

tons long before the collision. The resulting series in terms of the number of collisions with the target nucleons has the same combinatoric structure as the Glauber series, where the factors $(\sigma_{\text{tot}})^n$ are replaced by the interaction averaged over the color fluctuations, $\langle \sigma^n \rangle$. (iii) It is necessary to account properly for the Q^2 evolution of the nuclear PDFs which mixes contributions of small and large x . This problem is naturally solved by using the QCD factorization theorems.

The leading twist theory of nuclear shadowing was proposed in [57] and later developed and elaborated on in [74–76]. The theory is consistent with the leading twist evolution equations to all orders in the strong coupling constant α_s and predicts next-to-leading order (NLO) nPDFs and nDPDFs of different parton flavors (quarks and gluons) as a function of Bjorken x and the impact parameter b at some initial scale Q_0^2 . The Q^2 dependence of nPDFs and nDPDFs is given by the Dokshitzer-Gribov-Lipatov-Altarelli-Parisi (DGLAP) evolution equations [77]. The approach also allows us to predict nGPDs in a special limit.

We point out that the crucial part of the leading twist theory of nuclear shadowing is the use of the QCD factorization theorem for hard diffraction in DIS [59]. Only this does allow us to make predictions for nPDFs of different parton flavors, i.e., separately for quarks and gluons. This key feature distinguishes the leading twist theory of nuclear shadowing from all other theoretical approaches to nuclear shadowing (see the discussion below).

Before the first HERA data on diffraction in DIS on hydrogen was obtained and analyzed in the middle of the 1990s, a large number of model calculations of nuclear shadowing in lepton-nucleus scattering based on the Gribov work on nuclear shadowing [56] were performed. Initially, nuclear shadowing was estimated for the interaction of real and quasi-real (small Q^2) photons with nuclei, where the generalized vector dominance model gives a good description of diffraction, see e.g., [78–80]. Later nuclear shadowing in deep inelastic lepton-nucleus scattering was evaluated using models of diffraction in the virtual photon-nucleon scattering, some of which in part were based on the first HERA data on hard diffraction in DIS. These models include the QCD-improved aligned jet model [81,82], the two-gluon exchange model which neglected the Sudakov suppression of the $q\bar{q}$ aligned jet contribution [83,84], the two-component model based on the sum of the vector meson (for low-mass diffraction) and continuum (for high-mass diffraction) contributions [85–93], the generalized vector dominance model with off-diagonal transitions [94,95], the model based on the Pomeron and Reggeon contributions to the γ^*p diffraction [96].

Among recent approaches to nuclear shadowing, one should mention the one [97–99] based on the combination of the Regge-motivated model for the diffractive structure function $F_2^{D(3)}$ measured by HERA in hard diffractive DIS with the Gribov connection between shadowing and diffraction. The approach gives a good description of the data on nuclear shadowing at intermediate values of Q^2 .

Nuclear shadowing in quasi-real photon-nucleus scattering is successfully described us-

ing the Gribov theory of nuclear shadowing combined with the phenomenological fit to inclusive diffraction in photon-nucleon scattering [100–102].

In general, most of the models mentioned above use the connection between nuclear shadowing and diffraction, but lack the consistency with the QCD evolution equations at large Q^2 and do not account for the difference between the gluon-induced and quark-induced diffraction.

A number of reviews on nuclear shadowing exists in the literature. The 1988 review of Frankfurt and Strikman [81] discusses a wide range of hard processes with nuclei and corresponding phenomena, including nuclear shadowing. The review of Arneodo [38] discusses the phenomenology of modifications of nuclear structure functions known by 1994, with an emphasis on the EMC effect. The review of Piller and Weise [101] is a thorough account of experimental and theoretical understanding of nuclear structure functions achieved by 1999. The recent work of Armesto [103] reviews several approaches to nuclear shadowing, including the kinematics where the decomposition over twists is not valid.

The present review focuses on two limits which are comparatively well understood now. These are the limit of sufficiently large Q^2 and small but fixed x , where the leading twist (LT) approximation is justified, and the opposite regime— $x \rightarrow 0$ and Q^2 is large but fixed—where the interaction reaches the maximally possible strength allowed by the probability conservation and the black disk regime (BDR) sets in. In the LT approximation, the QCD factorization theorems allow us to separate the hard interaction of partons with a given probe from the soft interactions with the target nucleus, which have the same structure as in soft dynamics. Hence, the expected accuracy of the treatment of nuclear shadowing in DIS is as good as in the soft hadron-nucleus interactions, i.e., a few percent; a comparable uncertainty comes from the uncertainty in the ep diffractive data. In the BDR limit, predictions for the total cross section are rather straightforward and do not depend on the details of the BDR dynamics. At the same time, the suppression of the leading particle production in the current fragmentation region provides an early signal for the onset of the BDR and is sensitive to the details of the BDR dynamics, in particular, to the expectation of the emergence of the three x -layers of different symmetries in the hadron wave function.

The gluon nuclear shadowing affects numerous observables in heavy ion collisions for all rapidities in the LHC kinematics and forward rapidities at RHIC. In the near future, the best tool to study the nuclear shadowing related phenomena will be ultraperipheral heavy ion collisions at the LHC, including forward jet production, hard diffraction and exclusive production of J/ψ and Υ . Feasibility of these studies, in which x down to 10^{-4} could be covered, was demonstrated recently in the review [35], so there is no need to repeat it here. Studies of pA collisions at the LHC will also be promising; a challenge in this case would be to disentangle the effects due to onset of the black disk regime and the leading twist effects. In a longer run, an Electron-Ion Collider in USA, which can reach down $x \sim 10^{-3}$, would provide a perfect tool to study the kinematics of the onset of nuclear

shadowing and to test a number of model-independent predictions made in this review. A plan of a Large Hadron-Electron Collider (LHeC) discussed now at CERN would be perfect for checking our predictions for smaller x , where one explores both the kinematics, where leading twist effects dominate, and the kinematics, where an onset of the black disk regime is expected for rather large virtualities.

This review is structured as follows. In Sec. 2, we present the Gribov picture of high-energy hadron-nucleus scattering and the results for nuclear shadowing in hadron-deuteron scattering. The generalization of the Gribov work to DIS off arbitrary nuclei and the derivation of master equations for nuclear PDFs are presented in Sec. 3. The section also contains a mini-review of hard inclusive diffraction in DIS at HERA. Nuclear shadowing in DIS off the deuteron is presented in Sec. 4. Section 5 concerns with numerous applications of the theory of the leading twist nuclear shadowing. In this section, among several results, we give our predictions for nPDFs and nuclear structure functions, including their dependence on the impact parameter, discuss the accuracy of our predictions, compare our results to the eikonal approximation and to the selected available fixed-target data. In Sec. 6, we present our predictions for nuclear shadowing in nuclear diffractive PDFs and structure functions, nuclear GPDs and exclusive diffraction at small x as well as for nuclear effects in inclusive spectra in eA collisions and in hadron production at central rapidities. Leading twist nuclear shadowing and suppression of hard coherent diffraction in proton-nucleus scattering is discussed in Sec. 7. Finally, we present and discuss our results on the high-energy black disk regime in Sec. 8, which include the results for the total γ^*A cross section and the post-selection effect of the suppression of the leading hadron production in eA and pA collisions. We conclude our review with a short summary in Sec. 9.

2 Gribov results for nuclear shadowing

In this section, we describe the Gribov results for nuclear shadowing in hadron-nucleus scattering which are based on the space-time picture of the strong interactions at high energies. Since this approach was formulated before the development of QCD as the theory of the strong interactions, it does not distinguish between soft and hard QCD processes.

2.1 Gribov picture of space-time evolution of high-energy processes

The space-time picture of the strong interactions developed by Gribov is based on the observation that the distances important in the strong interactions at high energies rapidly increase with energy [104–106].

The following discussion is based on [107,108]. Let us consider, for example, pion-nucleus

scattering in the laboratory reference frame. Since we would like to consider creation of particles, we should take into account that the pion has a partonic structure (in the sense of the Feynman parton model [109]). When the momentum of the incoming pion is large, the pion fluctuates into its partons and these fluctuations exist for a long time. The fluctuation time is called the coherence length, l_c .

Let us consider for certainty the case when the incoming pion with the large momentum \vec{p} (it is convenient to take \vec{p} along the z -direction) and mass μ fluctuates into two partons with momenta \vec{p}_1 and $\vec{p} - \vec{p}_1$ and mass μ_1 . We also assume that the transverse component \vec{p}_{1t} is energy-independent (as is the case of soft QCD) and introduce $\alpha \equiv p_{1z}/|\vec{p}_1|$, $0 < \alpha < 1$. The corresponding non-conservation of energy, ΔE , is

$$\begin{aligned} \Delta E &= \sqrt{\mu_1^2 + \vec{p}_1^2} + \sqrt{\mu_1^2 + (\vec{p} - \vec{p}_1)^2} - \sqrt{\mu^2 + \vec{p}^2} \approx \frac{\mu_1^2 + \vec{p}_{1t}^2}{2|p_{1z}|} + \frac{\mu_1^2 + \vec{p}_{1t}^2}{2|p_z - p_{1z}|} - \frac{\mu^2}{2|p_z|} \\ &= \frac{\mu_1^2 + \vec{p}_{1t}^2}{2|p_z|} \frac{1}{\alpha(1-\alpha)} - \frac{\mu^2}{2|p_z|}. \end{aligned} \quad (1)$$

Because of the uncertainty principle, the lifetime of the considered fluctuation is inversely proportional to ΔE . Correspondingly, the length over which the considered partonic configuration remains coherent is $l_c = 1/\Delta E$. It follows from Eq. (1) that

$$l_c \equiv \frac{1}{\Delta E} = \frac{2|\vec{p}|}{\frac{\mu_1^2 + \vec{p}_{1t}^2}{\alpha(1-\alpha)} - \mu^2} \propto |\vec{p}|, \quad (2)$$

and, therefore, l_c grows with energy and, at sufficiently large energies (large $|\vec{p}|$), l_c exceeds by far the diameter of the target. As a result, the pion interacts with all nucleons located at the same impact parameter in the same partonic configuration.

The process of the parton branching described above continues and leads to the following physical picture. At high energies, the incoming pion with a large momentum can be described as a coherent ensemble of long-lived non-interacting partons and some small-momenta partons. The pion-nucleus interaction is described by the diagram presented in Fig. 1. At a time t_1 , the pion fluctuates into its partonic configurations. The configurations strongly interact with the nuclear target denoted by A and live for the time $l_c = t_2 - t_1$. At a time t_2 , the final pion (or some other final state) is formed.

In order to numerically estimate the applicability of the space-time picture presented in Fig. 1, let us assume that the target nucleus is deuteron and the intermediate parton configuration has the mass comparable to that of the ρ meson [56]. Then from the requirement that $l_c = R_d$, where $R_d \approx 4$ fm is the radius of the deuteron (the average

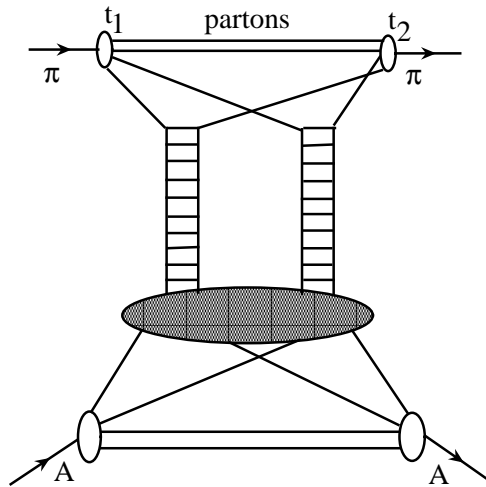


Fig. 1. The space-time picture of the interaction of a fast pion with two nucleons of a nuclear target.

distance between the proton and neutron), we obtain from Eq. (1):

$$|\vec{p}| \geq \frac{R_d}{2} (m_\rho^2 - \mu^2) = 5.8 \text{ GeV}/c. \quad (3)$$

Therefore, in pion-deuteron scattering, the Gribov space-time picture starts to be applicable when the incoming momentum is larger than 6 GeV/c.

2.2 Nuclear shadowing in pion-deuteron scattering

In this subsection, we present key steps in the derivation of the connection between the nuclear shadowing correction to the total hadron-deuteron cross section and the hadron-nucleon diffractive cross section; this connection was first derived by Gribov in 1968 [56]. Note that the Gribov derivation is justified by the small binding energy of the deuteron; it has been realized long time ago that many characteristics of the deuteron can be understood within this approximation [110]. This example of soft QCD dynamics will be of use for us in the consideration of hard nuclear processes in Sec. 3.

For certainty, let us consider scattering of a pion with high momentum p on a deuteron at rest. The corresponding scattering amplitude is given by the sum of the diagrams in Fig. 2. The left graph corresponds to the interaction with one nucleon of the target; this contribution is called the impulse approximation. The right graph corresponds to the simultaneous interaction with both nucleons of the target and leads to a small negative contribution to the total pion-deuteron cross section, which is called the nuclear shadowing correction.

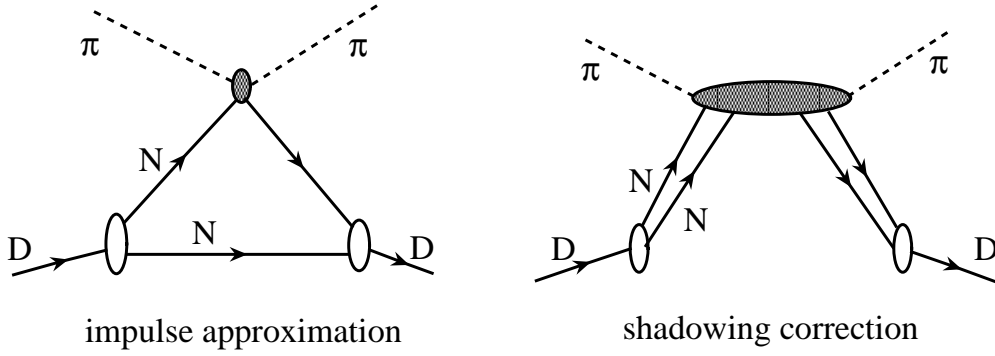


Fig. 2. Graphs for pion-deuteron scattering.

Below we consider each graph in detail, assuming for simplicity that all involved particles and the deuteron are spinless and the proton and the neutron are indistinguishable.

The contribution of the impulse approximation to the pion-deuteron scattering amplitude, $F_D^{\text{imp}}(s, q)$, is

$$\begin{aligned}
 F_D^{\text{imp}}(s, q) = & i \int \frac{d^4 k}{(2\pi)^4} \frac{1}{[(\frac{p_1}{2} + k)^2 - m^2 + i\epsilon][(\frac{p_1}{2} - k)^2 - m^2 + i\epsilon][(\frac{p_1}{2} + q + k)^2 - m^2 + i\epsilon]} \\
 & \times \Gamma \left(\left(\frac{p_1}{2} - k \right)^2, \left(\frac{p_1}{2} + k \right)^2 \right) \Gamma \left(\left(\frac{p_1}{2} - k \right)^2, \left(\frac{p_1}{2} + q + k \right)^2 \right) \\
 & \times f_N \left(\left(p + \frac{p_1}{2} + k \right)^2, q^2, \left(\frac{p_1}{2} + k \right)^2, \left(\frac{p_1}{2} + q + k \right)^2 \right), \quad (4)
 \end{aligned}$$

where Γ is the $D \rightarrow NN$ vertex; f_N is the pion-nucleon scattering amplitude; m is the nucleon mass; q is the momentum transfer; p_1 is the momentum of the initial deuteron. The momentum flow used in Eq. (4) is depicted in Fig. 3.

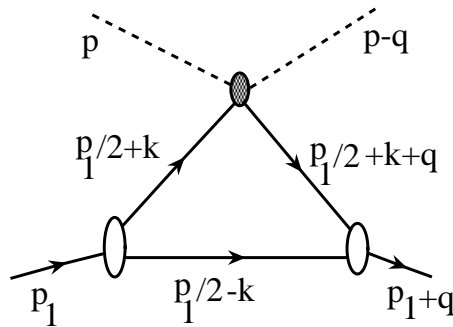


Fig. 3. The momentum flow in the left graph in Fig. 2 and in Eq. (4).

In the deuteron rest frame, the inverse nucleon propagators in Eq. (4) are

$$\begin{aligned}
\left(\frac{p_1}{2} + k\right)^2 - m^2 + i\epsilon &= -\Delta^2 + Mk^0 + (k^0)^2 - \vec{k}^2 + i\epsilon, \\
\left(\frac{p_1}{2} - k\right)^2 - m^2 + i\epsilon &= -\Delta^2 - Mk^0 + (k^0)^2 - \vec{k}^2 + i\epsilon, \\
\left(\frac{p_1}{2} + q + k\right)^2 - m^2 + i\epsilon &= -\Delta^2 + M(q^0 + k^0) - (\vec{q} + \vec{k})^2 + i\epsilon,
\end{aligned} \tag{5}$$

where $\Delta^2 = m^2 - M^2/4$ and M is the deuteron mass. The nucleon motion within the deuteron is effectively non-relativistic since $k^0 \approx \Delta^2/(2m)$. Hence, the contribution of k^0 to Eq. (5) can be neglected. The small value of the deuteron binding energy, $\epsilon_D = 2.2$ MeV, leads to the dominance of large internucleon distances in the impulse approximation [Eq. (4)] of the order of $1/\sqrt{\epsilon_D m}$, which are significantly larger than the radius of the strong interaction for small momentum transfers, $\vec{q}^2 \sim \Delta^2$. In this case, all nucleons in the loop in Fig. 3 are near the mass-shell,

$$\begin{aligned}
\left(\frac{p_1}{2} \pm k\right)^2 &= m^2 + \mathcal{O}(\Delta^2), \\
\left(\frac{p_1}{2} + q + k\right)^2 &= m^2 + \mathcal{O}(\Delta^2).
\end{aligned} \tag{6}$$

Therefore, the pion-nucleon scattering amplitude f_N in Eq. (4) can be replaced by the on-shell scattering amplitude evaluated at the invariant mass squared s_1 and the momentum transfer q , where

$$s_1 = \left(p + \frac{p_1}{2} + k\right)^2 = \mu^2 + p^0 M + m^2 + \mathcal{O}(\Delta^2) \approx p^0 M \approx \frac{s}{2}, \tag{7}$$

and $s = (k + p_1)^2$ is the pion-deuteron invariant mass squared. Since now f_N does not depend on the integration variables, it can be taken out the integral. The remaining integral is proportional to the deuteron form factor of the baryon density current (evaluated in the theory where the nucleon fields are scalar), $\rho(q^2)$,

$$\begin{aligned}
\rho(q^2) &= \frac{i}{2} \int \frac{d^4 k}{(2\pi)^4} \frac{1}{[(\frac{p_1}{2} + k)^2 - m^2 + i\epsilon][(\frac{p_1}{2} - k)^2 - m^2 + i\epsilon][(\frac{p_1}{2} + q + k)^2 - m^2 + i\epsilon]} \\
&\quad \times \Gamma\left(\left(\frac{p_1}{2} - k\right)^2, \left(\frac{p_1}{2} + k\right)^2\right) \Gamma\left(\left(\frac{p_1}{2} - k\right)^2, \left(\frac{p_1}{2} + q + k\right)^2\right).
\end{aligned} \tag{8}$$

With this definition, $\rho(0) = 1$. Therefore, the contribution of the left graph in Fig. 2 is equal to

$$F_D^{\text{imp}}(s, q) = 2f_N \left(\frac{s}{2}, q^2\right) \rho(q^2). \tag{9}$$

Note that in the derivation, we neglected for simplicity the difference between the pion-proton and pion-neutron scattering amplitudes.

Turning to the evaluation of the right graph in Fig. 2, we find that its contribution reads:

$$\begin{aligned}
F_D^{\text{shad}}(s, q) = & - \int \frac{d^4 k}{(2\pi)^4} \frac{d^4 k'}{(2\pi)^4} \frac{1}{[(\frac{p_1}{2} + k')^2 - m^2 + i\epsilon][(\frac{p_1}{2} - k')^2 - m^2 + i\epsilon]} \\
& \times \frac{1}{[(\frac{p_1}{2} + k + k')^2 - m^2 + i\epsilon][(\frac{p_1}{2} + q - k - k')^2 - m^2 + i\epsilon]} \\
& \times \Gamma \left(\left(\frac{p_1}{2} + k' \right)^2, \left(\frac{p_1}{2} - k' \right)^2 \right) \Gamma \left(\left(\frac{p_1}{2} + k + k' \right)^2, \left(\frac{p_1}{2} + q - k - k' \right)^2 \right) \\
& \times f \left(s_1, \vec{k}^2, (\vec{q} - \vec{k})^2, \vec{q}^2, s' \right), \tag{10}
\end{aligned}$$

where $s' = (p - k)^2 = \mu^2 - 2p^0 k^0 + 2|\vec{p}\vec{k}_z - k^2$. The momentum flow used in Eq. (10) is depicted in Fig. 4.

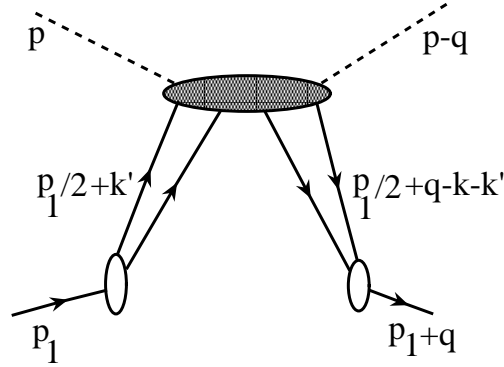


Fig. 4. The momentum flow in the right graph in Fig. 2 and in Eq. (10).

An analysis similar to the one presented above for $F_D^{\text{imp}}(s, q)$ leads to the conclusion that the dominant contribution to the loop integrals in Eq. (10) is given by the values of $k^0, k'^0 \sim k^2/M$ and $\vec{k}^2, \vec{k}'^2 \gg \Delta^2$. The integration over \vec{k}^2 is cut off by the wave function of the deuteron. As a result, the shadowing contribution is controlled by the small internucleon distances $\ll r_D = 1/\sqrt{\epsilon_D m}$ [cf. Eq. (20)]. Consequently, in the numerical calculations of nuclear shadowing, the nucleon momenta up to ~ 400 MeV/c are important. In particular, the D-wave gives a large fraction of the shadowing correction in spite of the small probability of the D-wave in the deuteron, cf. the discussion in Sec. 4.

In the non-relativistic approximation, the vertex functions Γ depend only on the absolute value of the relative three-momentum of the nucleons,

$$\begin{aligned} \Gamma\left(\left(\frac{p_1}{2} + k'\right)^2, \left(\frac{p_1}{2} - k'\right)^2\right) &= \Gamma(\vec{k}^2), \\ \Gamma\left(\left(\frac{p_1}{2} + k + k'\right)^2, \left(\frac{p_1}{2} + q - k - k'\right)^2\right) &= \Gamma\left(\left(\vec{k} + \vec{k}' + \frac{\vec{q}}{2}\right)^2\right). \end{aligned} \quad (11)$$

Another quantity in Eq. (10), the scattering amplitude f , depends only on the five indicated variables, which is a consequence of the assumption that f depends only on the momentum transfer to the nucleons. This approximation means that we neglected the effects of the motion of the nucleons (Fermi motion), see e.g., [111]. In addition, in the non-relativistic approximation, the term proportional to k^0 in the expression for s' can be neglected.

Integration over k^0 and k'^0 in Eq. (10) gives

$$\begin{aligned} F_D^{\text{shad}}(s, q) &= \frac{1}{(2M)^2} \int \frac{d^3\vec{k}}{(2\pi)^3} \frac{d^3\vec{k}'}{(2\pi)^3} \frac{1}{[\Delta^2 + (\vec{k}')^2][\Delta^2 + (\vec{k} + \vec{k}' - \frac{\vec{q}}{2})^2]} \\ &\quad \times \Gamma(\vec{k}^2) \Gamma\left(\left(\vec{k} + \vec{k}' + \frac{\vec{q}}{2}\right)^2\right) f(s_1, \vec{k}^2, (\vec{q} - \vec{k})^2, \vec{q}^2, s'). \end{aligned} \quad (12)$$

Equation (12) can be written in a compact form by introducing the deuteron form factor $\rho(q^2)$:

$$F_D^{\text{shad}}(s, q) = \frac{2}{M} \int \frac{d^3\vec{k}}{(2\pi)^3} \rho((2\vec{k} + q)^2) f(s_1, \vec{k}^2, (\vec{q} - \vec{k})^2, \vec{q}^2, s'). \quad (13)$$

Indeed, integrating over k^0 in Eq. (8), one obtains

$$\rho(q^2) = \frac{1}{8M} \int \frac{d^3\vec{k}'}{(2\pi)^3} \frac{1}{[\Delta^2 + (\vec{k}')^2][\Delta^2 + (\vec{k}' + \frac{\vec{q}}{2})^2]} \Gamma((\vec{k}')^2) \Gamma\left(\left(\vec{k}' + \frac{\vec{q}}{2}\right)^2\right). \quad (14)$$

A comparison of Eqs. (14) and (12) leads to Eq. (13).

Let us now consider the $q = 0$ forward scattering case. The shadowing correction becomes:

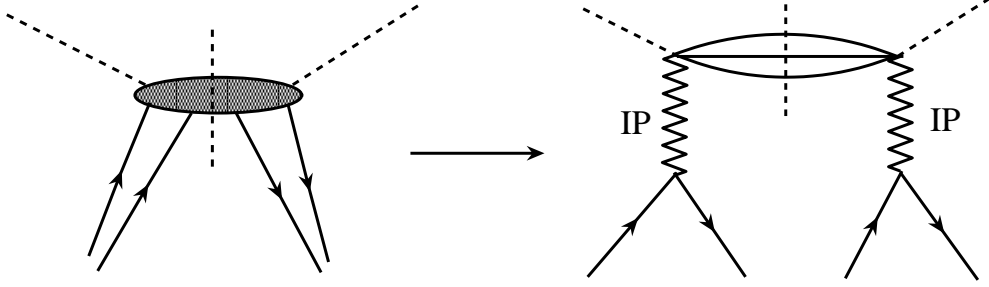


Fig. 5. Graphical representation of the imaginary part of the scattering amplitude f in terms of Pomeron exchanges in the t -channel.

$$\begin{aligned}
F_D^{\text{shad}}(s) \equiv F_D^{\text{shad}}(s, 0) &= \frac{2}{M} \int \frac{d^3 \vec{k}}{(2\pi)^3} \rho(4\vec{k}^2) f(s_1, \vec{k}^2, s') \\
&= \frac{1}{M} \int \frac{d\vec{k}^2}{4\pi^2} \rho(4\vec{k}^2) \int_{-2|\vec{p}||\vec{k}|+\mu^2}^{2|\vec{p}||\vec{k}|+\mu^2} \frac{ds'}{2|\vec{p}|} f(s_1, \vec{k}^2, s') \\
&= \frac{2}{M} \int \frac{d\vec{k}^2}{4\pi^2} \rho(4\vec{k}^2) \int_0^{2|\vec{p}||\vec{k}|+\mu^2} \frac{ds'}{2|\vec{p}|} f(s_1, \vec{k}^2, s'). \tag{15}
\end{aligned}$$

The optical theorem relates the imaginary part of the scattering amplitude f to the $\pi N \rightarrow XN$ cross section. Since at high energies inelastic processes are determined by the Pomeron exchange in the t -channel, $\Im m f$ is determined by the diagram presented in Fig. 5. A direct evaluation gives

$$\Im m f(s_1, \vec{k}^2, s') = -4p^0 m^2 (2\pi)^3 \frac{d^3 \sigma_{\text{diff}}^{\pi N}(\vec{k})}{d^3 \vec{k}}, \tag{16}$$

where $\sigma_{\text{diff}}^{\pi N}$ is the cross section of all diffractive processes ($\pi N \rightarrow XN$) with a small momentum transfer \vec{k} to the nucleon. Note that $\Im m f < 0$ since each of the Pomeron exchange amplitudes is purely imaginary.

Applying the optical theorem to the pion-deuteron scattering amplitude at $q = 0$ and using Eqs. (9) and (16), we obtain the total pion-deuteron cross section,

$$\sigma_{\text{tot}}^{\pi D} = 2\sigma_{\text{tot}}^{\pi N} - 2 \int d\vec{k}^2 \rho(4\vec{k}^2) \frac{d\sigma_{\text{diff}}^{\pi N}(\vec{k})}{d\vec{k}^2}. \tag{17}$$

Equation (17) expresses the shadowing correction to the total hadron-deuteron cross section in terms of the hadron-nucleon diffractive cross section.

As derived by Gribov, Eq. (17) assumes that the real part of the scattering amplitude f is zero (this corresponds to the intercept of the Pomeron trajectory $\alpha_P(0) = 1$.) However, this assumption is not necessary and Eq. (17) can be straightforwardly generalized:

$$\sigma_{\text{tot}}^{\pi D} = 2\sigma_{\text{tot}}^{\pi N} - 2\frac{1-\eta^2}{1+\eta^2} \int d\vec{k}^2 \rho(4\vec{k}^2) \frac{d\sigma_{\text{diff}}^{\pi N}(\vec{k})}{d\vec{k}^2}, \quad (18)$$

where η is the ratio of the real to imaginary parts of the scattering amplitude f . The fast convergence of the integral over $d\vec{k}^2$ in Eq. (18) allows us to neglect a weak dependence of η on k^2 .

It should be noted that the graphs in Fig. 2 give the complete answer for the pion-deuteron scattering amplitude at high pion momenta. Other contributions, for instance, the diagram presented in Fig. 6, vanish as $p \rightarrow \infty$ [112]. The physical reason for the negligibly small

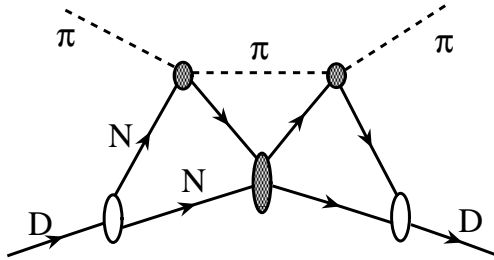


Fig. 6. An example of the contribution to the pion-deuteron cross section that vanishes at large energies.

contribution of the diagram in Fig. 6 is that during the short time required for the pion to cover the distance between the two nucleons, the slow nucleons in the deuteron cannot (do not have enough time to) interact.

It is possible to extend the Gribov analysis to include the relativistic motion of the nucleons using the light-cone formalism. One finds that the corrections due to the nucleon Fermi motion are very small due to the dominance of the pn intermediate states in the deuteron wave function up to the internal momenta ~ 500 MeV/c. Note here that a small value of the admixture of non-nucleonic states in the nucleus wave function is confirmed by the smallness of the EMC effect due to hadronic effects up to $x \sim 0.55$, see the discussion in Sec. 5.17.

2.3 Comparison of Gribov and Glauber results for nuclear shadowing

Originally the nuclear shadowing correction to the pion-deuteron cross section was calculated by Glauber in 1955 [113] for the energy range $E_\pi \sim 1$ GeV, where the Lorentz

dilation was not important. In the Glauber approach, the pion-deuteron scattering amplitude receives contributions from the impulse approximation term and from the term corresponding to the subsequent interactions of the pion with the two nucleons of the target; the both terms are presented in Fig. 7.

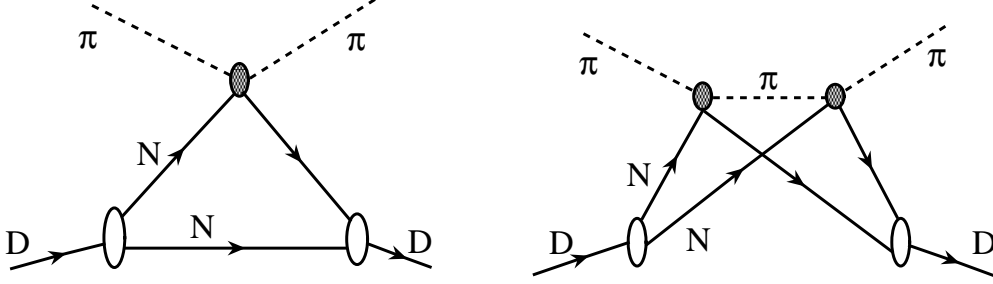


Fig. 7. Graphs for pion-deuteron scattering in the Glauber approach.

The corresponding expression for the total pion-deuteron cross section reads [113]:

$$\sigma_{\text{tot}}^{\pi D} = 2\sigma_{\text{tot}}^{\pi N} - \frac{(\sigma_{\text{tot}}^{\pi N})^2}{4\pi} \left\langle \frac{1}{r^2} \right\rangle_D, \quad (19)$$

where $\langle 1/r^2 \rangle_D$ is the average inverse radius squared of the deuteron,

$$\left\langle \frac{1}{r^2} \right\rangle_D = \int d^3\vec{r} |\psi_D(\vec{r})|^2 \frac{1}{r^2}, \quad (20)$$

with $\psi_D(\vec{r})$ the deuteron wave function.

The Gribov formula for the nuclear shadowing correction (17) is the generalization of that of Glauber (19) to high energies. Noticing that in Eq. (17), the $|\vec{k}|^2$ dependence of the deuteron form factor is much faster than that of the diffractive cross section and assuming that only the elastic intermediate state contributes, Eq. (17) can be written as

$$\sigma_{\text{tot}}^{\pi D} \approx 2\sigma_{\text{tot}}^{\pi N} - \left. \frac{d\sigma_{\text{el}}^{\pi N}(\vec{k})}{d\vec{k}^2} \right|_{|\vec{k}|^2=0} 2 \int d\vec{k}^2 \rho(4\vec{k}^2). \quad (21)$$

Using the S -matrix unitarity condition,

$$\left. \frac{d\sigma_{\text{el}}^{\pi N}(\vec{k})}{d\vec{k}^2} \right|_{|\vec{k}|^2=0} = \frac{(\sigma_{\text{tot}}^{\pi N})^2}{16\pi}, \quad (22)$$

and the expression for $\langle 1/r^2 \rangle_D$ in the momentum representation,

$$\int d\vec{k}^2 \rho(4\vec{k}^2) = 2 \left\langle \frac{1}{r^2} \right\rangle_D, \quad (23)$$

one readily sees that the Gribov (21) and Glauber (19) formulas coincide, if the intermediate state is purely elastic. However, when inelastic diffraction is important, the Gribov formula leads to larger shadowing.

Despite the similarity of the results obtained within the Gribov and Glauber approaches, the two approaches are based on very different pictures of high-energy hadron-nucleus scattering. The Glauber approach neglects the Lorentz time dilation effects related to the hadron production. Indeed, the method is essentially quantum-mechanical and the creation of particles in the intermediate states is not possible. As a result, the incoming hadron is formed after each interaction and scatters *successively* on the target nucleons, see Fig. 7.

More generally, in the $p \rightarrow \infty$ limit, the shadowing correction in the Glauber approach (the right graph in Fig. 7) vanishes. This can be proven by exact calculations in any quantum field theory which accounts for particle production. Using analytic properties of the scattering amplitude with respect to the mass squared of the produced state, one can demonstrate the exact cancellation of the diagrams with the eikonal topology [112,114] (the right graph in Fig. 7 is an example of such diagrams). The physical reason for this cancellation is that during the finite time it takes for the partonic fluctuation to traverse the nucleus, the fluctuation does not have enough time (which is of the order of $l_c \propto p$) to form back into the projectile.

In the Gribov approach, the projectile interacts with the target as a superposition of different configurations that interact with different strengths, but which evolve very little during the passage through the nucleus. These configurations emerge behind the nucleus as a distorted—but still a coherent—superposition of configurations, which, when decomposed over the eigenstates of the strong Hamiltonian, contains both the original hadron (elastic scattering) as well as diffractively excited states (coherent diffraction). The Gribov approach is essentially field-theoretical and the creation of particles in the intermediate state is properly taken into account, see Figs. 2 and 5. Hence, although the final answer for nuclear shadowing in the Glauber and Gribov approaches is expressed through topologically different diagrams, it has the structure of the sum of the eikonal term and the same-sign term corresponding to the contribution of other diffractive states.

Comment. A simple picture of the scattering eigenstates by Feinberg and Pomeranchuk [104] and Good and Walker [115] provides an s -channel model for the picture of high-energy scattering employed in the Gribov approach. In particular, a projectile being in different eigenstates interacts with the two nucleons of the deuteron. The contribution of this interactions to the elastic scattering amplitude at $t = 0$ is given by the overlapping integral

between the final state and projectile wave functions. When expressed through the cross section of diffractive hN scattering at $t = 0$ with help of the Miettinen-Pumplin relation [116], one finds [117] the same expression as found by Gribov, see Eq. (17). We will further discuss the Good–Walker picture later on.

It is worth noting that in the Gribov-Glauber approximation, the nucleus is treated as a dilute system. Namely, it is assumed that the characteristic impact parameters for the projectile-nucleon interaction are much smaller than the typical transverse distance between the interacting nucleon and its neighbor. The corrections to this approximation are difficult to estimate in a model-independent way, although they may become important at the LHC energies, where the typical impact parameters in the pp interaction are as large as 1.5 fm, which is close to the average distance to the nearest neighbor. However, phenomenological analyses indicate that the Gribov-Glauber approximation works well for fixed-target energies in nucleon-nucleus scattering at the beam energies $E_N \leq 400$ GeV, for a recent analysis, see Ref. [118]. Since in the energy range that we discuss in the present review the impact parameters in γ^*p diffraction do not exceed those in NN scattering at fixed-target energies, we will neglect these effects in our analysis.

2.4 The AGK cutting rules and nuclear shadowing

In the Gribov approach, the nuclear shadowing correction to the total pion-deuteron cross section is given by the diffractive cut of the graph, where the fast pion exchanges two Pomerons with the target, see Fig. 5. The resulting shadowing correction is negative and given in terms of the pion-nucleon diffractive cross section. These two features of the Gribov result can be understood using the Abramovsky-Gribov-Kancheli (AGK) cutting rules in the Reggeon field theory [119].

Let us consider the part of the pion-deuteron scattering amplitude that gives rise to the shadowing correction by assuming that the high-energy pion interacts with the target nucleons by the Pomeron exchanges. In the symbolic form (omitting the integration over the transverse momentum of exchanged Pomerons in the loop which does not change the AGK rules), the amplitude reads:

$$F_{np} = -iN(iD_1)N(iD_2), \quad (24)$$

where $D_{1,2}$ denote the complex Reggeon amplitudes; N is the real-valued particle-Reggeon vertex function which is an operator in the space of diffractively produced particles (see below). The imaginary part of F_{np} is then readily found:

$$\Im F_{np} = -2N^2 (\Im D_1 \Im D_2 - \Re D_1 \Re D_2), \quad (25)$$

where $N^2 = \sum_n \langle i|N|n\rangle \langle n|N|f\rangle d\tau_n$ (in this expression, $|n\rangle$ denotes the diffractively produced state; $d\tau_n$ is its phase volume). The additional factor of two originates from the fact that the deuteron consists of two nucleons.

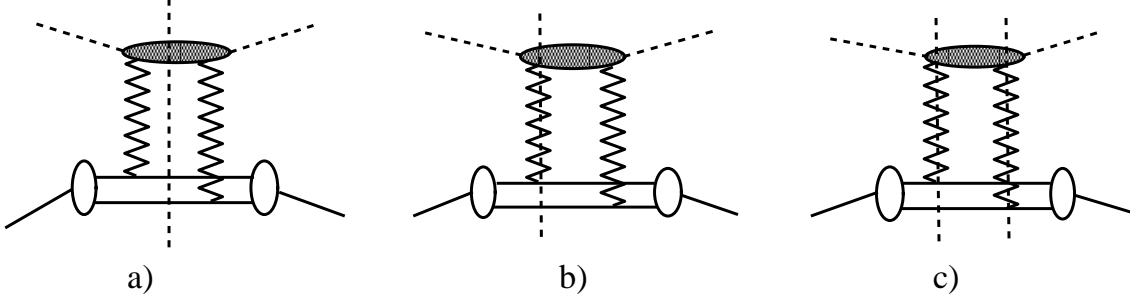


Fig. 8. The cuts of F_{np} that contribute to $\Im m F_{np}$.

Alternatively, the imaginary part of F_{np} can be evaluated by summing all possible cuts of the diagram corresponding to F_{np} , see Fig. 8. Graph *a* corresponds to the diffractive final state in the $\pi N \rightarrow XN$ reaction, when the pion diffractively dissociates into the hadronic states X . Hence, this cut is called diffractive. Graph *b* corresponds to the single multiplicity of the final state Y in the $\pi D \rightarrow Y$ reaction; graph *c* corresponds to the double multiplicity in the $\pi D \rightarrow Y$ reaction.

Denoting the results of the cutting of graphs *a*, *b* and *c* in Fig. 8 as $\Im m F_{np}^a$, $\Im m F_{np}^b$ and $\Im m F_{np}^c$, respectively, a direct evaluation gives [119]:

$$\begin{aligned}\Im m F_{np}^a &= 2N^2 (\Im m D_1 \Im m D_2 + \Re e D_1 \Re e D_2) = 2N^2 |D_1 D_2^*|, \\ \Im m F_{np}^b &= -8N^2 \Im m D_1 \Im m D_2, \\ \Im m F_{np}^c &= 4N^2 \Im m D_1 \Im m D_2.\end{aligned}\tag{26}$$

The sum of these contributions leads to Eq. (25). Indeed,

$$\begin{aligned}\Im m F_{np} &\equiv \Im m F_{np}^a + \Im m F_{np}^b + \Im m F_{np}^c = -2N^2 (\Im m D_1 \Im m D_2 - \Re e D_1 \Re e D_2) \\ &= -2 \frac{1 - \eta^2}{1 + \eta^2} N^2 |D_1 D_2^*|,\end{aligned}\tag{27}$$

where $\eta \equiv \Re e D_{1,2} / \Im m D_{1,2}$.

Equation (27) demonstrates that the shadowing correction, which is proportional to $\Im m F_{np}$, is negative and expressed in terms of the pion-nucleon diffractive cross section (the latter is proportional to $|D_1 D_2^*|$). The real part of the pion-nucleon scattering amplitude is accounted for by the factor $(1 - \eta^2)/(1 + \eta^2)$, see also Eq. (18).

A different derivation of the AGK cutting rules for hadron-nucleus scattering was proposed in [120]. Assuming validity of the eikonal (Glauber) approximation, the following expression for the total inelastic hadron-nucleus cross section, $\sigma_{\text{summed}}^{hA,\text{inel}}$, was derived,

$$\sigma_{\text{summed}}^{hA,\text{inel}} = \sum_{n=1}^A \sigma_n, \quad (28)$$

where σ_n is the inelastic cross section that corresponds to inelastic production on n nucleons and no inelastic absorption on $A - n$ nucleons. Further, one can show that in any multiple scattering theory which is unitary,

$$\sum_{n=1}^A n\sigma_n = A\sigma_{\text{inel}}, \quad (29)$$

where σ_{inel} is the hadron-nucleon inelastic cross section. Equation (29) gives an example of the so-called AGK cancellation.

3 Leading twist theory of nuclear shadowing for quark and gluon nuclear parton distribution functions

The derivation of the leading twist theory of nuclear shadowing is based on combining the Gribov technique (discussed in the previous chapter), the factorization theorem for diffraction in DIS [59,121], and the QCD analyses of the HERA data on diffraction in lepton-nucleon DIS [60–73]. The name *leading twist nuclear shadowing* derives from the fact that the model-independent contribution to nuclear shadowing coming from the interaction with two nucleons of the target is given in terms of the diffractive structure functions which are leading twist quantities that were determined in a series of the analyses of the HERA data on diffraction in DIS. In this section, we discuss each component of the leading twist theory of nuclear shadowing separately and in detail and present the derivation of the master equation for nuclear shadowing in nuclear PDFs.

3.1 Derivation of the master equation for nuclear parton distribution functions

In this subsection, we give the derivation of the equation that expresses nuclear shadowing in nuclear parton distribution functions (nPDFs) in the small x shadowing region in terms of the proton (nucleon) diffractive PDFs (DPDFs). The derived master equation constitutes the key expression of the theory of leading twist nuclear shadowing. The leading twist theory of nuclear shadowing was proposed and developed by Frankfurt and

Strikman in 1998 [57] by exploring the topology of the AGK cutting rules and was further elaborated later on in [74–76].

3.1.1 Contributions of the interaction with one and two nucleons of the target

The starting point of the derivation is the generalization of the Gribov theory of nuclear shadowing in hadron-deuteron scattering to the case of inclusive deep inelastic scattering (DIS) of leptons off an arbitrary nucleus with A nucleons. According to the space-time picture of the strong interactions presented in the Introduction, the virtual photon with the large momentum $|\vec{q}|$ interacts with the target by fluctuating into strongly interacting states. The lifetime of such fluctuations, which is called the coherence length l_c , can be estimated in the limit of small x using Eq. (1) by assuming that the invariant mass squared of the fluctuation, M_X^2 , approximately equals the virtuality of the photon Q^2 ,

$$\Delta E = \sqrt{\vec{q}^2 + M_X^2} - \sqrt{\vec{q}^2 - Q^2} \approx \frac{M_X^2 + Q^2}{2|\vec{q}|} \approx \frac{Q^2}{|\vec{q}|} \simeq 2m_N x,$$

$$l_c \equiv \frac{1}{\Delta E} = \frac{1}{2m_N x}, \quad (30)$$

where m_N is the nucleon mass; x is the usual Bjorken variable, $x = Q^2/(2m_N q_0)$ in the laboratory frame. Note that in this derivation, we used the estimate of the aligned jet model that $\langle M_X^2 \rangle = Q^2$ and also that $|\vec{q}| \approx q_0$ at small x . At very small x corresponding to $l_c \gg 2R_A$, $\langle M_X^2 \rangle / Q^2$ gradually increases with a decrease of x , see also the discussion in Sec. 8.

When l_c is larger than the diameter of the nucleus, $2R_A$, the virtual photon coherently (“simultaneously”) interacts with all nucleons of the target located at the same impact parameter. For instance, for the nucleus of ^{40}Ca , this happens for $x \leq 0.01$. On the other hand, when l_c decreases and becomes compatible to the average distance between two nucleons in the nucleus, $r_{NN} \approx 1.7$ fm, all effects associated with large l_c are expected to disappear. Therefore, the nuclear effects of shadowing and antishadowing disappear for $x > 0.2$ (see also the discussion in Sec. 3.2 where this is discussed in the reference frame of the fast moving nucleus).

The wave function of the projectile virtual photon is characterized by the distribution over components (fluctuations) that widely differ in the strength of the interaction with the target: the fluctuations of a small transverse size correspond to the small interaction strength and the large phase volume, while the fluctuations of a large transverse size correspond to the large interaction strength but the small phase volume. A proper account of the interplay between the phase volume of different configurations and their strength of interactions shows [122] that these components lead to the contributions characterized by

the same power of Q^2 : $\sigma_{\gamma^*T} \propto 1/Q^2$.¹ Hence, at moderately small x , nuclear shadowing is a predominantly non-perturbative QCD phenomenon complicated by the leading twist Q^2 evolution. At extremely small x , perturbative QCD (pQCD) interactions become strong which leads to a change of the dynamics of nuclear shadowing, see the discussion in Sec. 8.

At sufficiently high energies (small Bjorken x), when the virtual photon interacts with many nucleons of the target, the lepton-nucleus scattering amplitude receives contributions from the graphs presented in Fig. 9. Considering the forward scattering and taking the imaginary part of the graphs in Fig. 9 (presented by the vertical dashed lines), one obtains the graphical representation for the total virtual photon-nucleus cross section, σ_{γ^*A} . Note that there are other graphs, corresponding to the interaction with four and more nucleons of the target, which are not shown in Fig. 9; the contribution of these graphs to σ_{γ^*A} is insignificant. However, they appear to be important in the case of the events with the multiplicity significantly larger than the average.

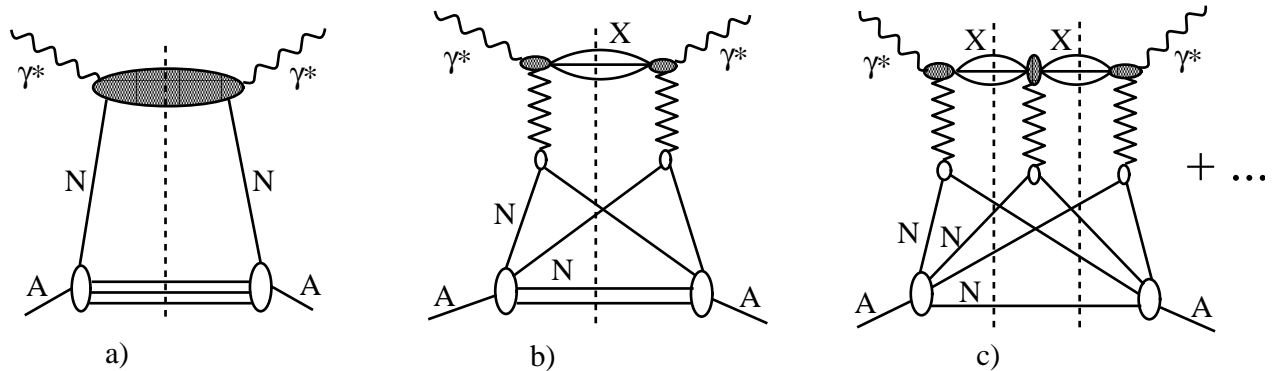


Fig. 9. Graphs for to the total virtual photon-nucleus cross section, σ_{γ^*A} . Graph *a* gives the impulse approximation; graphs *b* and *c* give the shadowing correction arising from the interaction with two and three nucleons of the target, respectively.

Graph *a* in Fig. 9, which is a generalization of the left graph in Fig. 2 to the case of DIS, corresponds to the interaction with one nucleon of the target (the impulse approximation). The contribution of graph *a* to σ_{γ^*A} , which we denote $\sigma_{\gamma^*A}^{(a)}$, is

$$\sigma_{\gamma^*A}^{(a)} = A\sigma_{\gamma^*N}, \quad (31)$$

where σ_{γ^*N} is the total virtual photon-nucleon cross section. The proton and neutron

¹ This parton-model reasoning is modified in QCD where the configurations with almost on-mass-shell quarks are suppressed at large Q^2 by the Sudakov form factor. An account of radiation (Q^2 evolution) leads to the appearance of hard gluons (in addition to the near on-mass-shell quarks) in the wave function of the virtual photon. This property of QCD is important for the theoretical analysis of hard diffractive processes considered in Sec. 6.

total cross sections (structure functions) are very close at small x , and, therefore, unless specified, we shall not distinguish between protons and neutrons. Also, in Eq. (31), we employed the non-relativistic approximation for the nucleus wave function. A more accurate treatment would involve the light-cone many-nucleon approximation for the description of nuclei which leads to tiny corrections to Eq. (31) for small x due to the Fermi motion effect, see Sec. 3.2. The good accuracy of this approximation has been tested by numerous studies of elastic and total hadron-nucleus scattering cross sections at intermediate energies.

The total cross section in Eq. (31) corresponds to the sum of the cross sections with the transverse ($\sigma_{\gamma_T^*N}$) and longitudinal ($\sigma_{\gamma_L^*N}$) polarizations of the virtual photon. These cross sections can be expressed in terms of the isospin-averaged inclusive (unpolarized) structure function $F_{2N}(x, Q^2)$ and longitudinal structure function $F_L(x, Q^2)$, see, e.g. [101]:

$$\begin{aligned}\sigma_{\gamma_T^*N} + \sigma_{\gamma_L^*N} &= \sigma_{\gamma^*N} = \frac{4\pi^2\alpha_{\text{em}}}{Q^2(1-x)} F_{2N}(x, Q^2), \\ \sigma_{\gamma_L^*N} &= \frac{4\pi^2\alpha_{\text{em}}}{Q^2(1-x)} F_L(x, Q^2),\end{aligned}\tag{32}$$

where α_{em} is the fine-structure constant. The structure functions $F_{2N}(x, Q^2)$ and $F_L(x, Q^2)$ parameterize the unpolarized lepton-hadron cross section, $d^2\sigma/(dx dQ^2)$, using the standard expression [58]:

$$\frac{d^2\sigma}{dx dQ^2} = \frac{2\pi\alpha_{\text{em}}^2}{xQ^4} \left[(1 + (1-y)^2) F_2(x, Q^2) - y^2 F_L(x, Q^2) \right],\tag{33}$$

where $y = (p \cdot q)/(p \cdot k)$, p is the momentum of the hadron, k is the momentum of the initial lepton, and q is the momentum of the exchanged virtual photon. Note that the contribution of $F_L(x, Q^2)$ to the cross section is generally significantly smaller than that of $F_2(x, Q^2)$.

Using Eqs. (31) and (32), we obtain the following connection between the structure functions:

$$F_{2A}^{(a)}(x, Q^2) = A F_{2N}(x, Q^2),\tag{34}$$

where $F_{2A}^{(a)}(x, Q^2)$ is the contribution of graph a in Fig. 9 (impulse approximation) to the nuclear structure function $F_{2A}(x, Q^2)$. A similar relation is also valid for the longitudinal structure functions.

Graph b in Fig. 9 is the generalization of the right graph in Fig. 2 (see also Fig. 5) to the case of DIS off an arbitrary nucleus. The intermediate state X denotes the diffractive final

state of the $\gamma^*N \rightarrow XN$ reaction. Therefore, the answer for the contribution of graph b to σ_{γ^*A} , which we shall call $\sigma_{\gamma^*A}^{(b)}$, should have the structure of the shadowing term in the Gribov formula (17). The generalization to the case of the photon interaction with more than two nucleons will be considered in Sec. 3.1.2.

The calculation of graph b in Fig. 9 is significantly simplified if one observes that the nuclear part of this interaction (graph) weakly depends on energy and has the same structure as in the Glauber multiple scattering formalism [113]. Indeed, restricting the projectile-nucleon intermediate states by the diffractive ones and taking into account that at high energies the interaction with the target nucleons depends only on the transverse part of the momentum transfer, the expression for graph b in Fig. 9 should have the same form as that in the multiple scattering formalism, except for the additional effect of the longitudinal momentum transfer to the nucleons which cuts off the contribution of large-mass intermediate states [the last factor in Eq. (35) below]. The effects of Fermi motion and the dependence of the amplitudes of diffractive processes on energy can be easily taken into account within light-cone quantum mechanics of nuclei; these effects lead to small corrections [123].

However, in contrast to the Glauber multiple scattering formalism, QCD predicts the existence of the contribution of the diffractively produced inelastic states relevant for the color coherent phenomena and triple Pomeron diagrams. Besides one needs to implement another QCD phenomenon, namely, energy-momentum conservation, which is impossible to enforce within the eikonal approximation, see the discussion in Sec. 5.14. At sufficiently large energies, where the pQCD interaction becomes strong (possibly, at the LHC), the nuclear part of graph b in Fig. 9 will lose its universality and one would need to explore the approximation of the black disk limit in order to do the calculations in a model-independent way.

In summary, for the calculation of graph b in Fig. 9, at moderately small x , one can use the Glauber multiple scattering formalism generalized to include inelastic diffractive intermediate states, i.e., coherent phenomena and energy-momentum conservation. Expressing the scattering amplitude corresponding to graph b in Fig. 9 in the momentum representation and performing the Fourier transform to the coordinate space, one obtains an operator whose matrix element between the initial and final nuclear states integrated over the positions of nucleons gives the contribution to σ_{γ^*A} that we seek [80,111,124] (an account of the energy-momentum conservation will be discussed in Sec. 5):

$$\sigma_{\gamma^*A}^{(b)} = -2\Re e \int d^2\vec{b} \sum_X A(A-1) \left\langle \Theta(z_2 - z_1) \Gamma_{\gamma^*X}(\vec{b} - \vec{r}_{1\perp}) \Gamma_{X\gamma^*}(\vec{b} - \vec{r}_{2\perp}) e^{i(z_1 - z_2)\Delta_{\gamma^*X}} \right\rangle, \quad (35)$$

where \sum_X denotes the sum over all diffractive intermediate states (see Fig. 9); $A(A-1)$ is the number of the nucleon pairs; $(\vec{r}_{i\perp}, z_i)$ are the transverse and longitudinal (with

respect to the direction of the momentum of γ^* , \vec{q}) coordinates of the involved nucleons; $\Theta(z_2 - z_1)$ is the step-function reflecting the underlying space-time evolution of the process; Γ_{γ^*X} is the $\gamma^*N \rightarrow XN$ scattering amplitude in the space of the impact-parameter \vec{b} ; the brackets denote the matrix element between the nuclear ground-states; Δ_{γ^*X} is the longitudinal momentum transfer, or, equivalently, the inverse coherence length for the $\gamma^* \rightarrow X$ fluctuation,

$$\Delta_{\gamma^*X} = \frac{M_X^2 + Q^2}{2|\vec{q}|}. \quad (36)$$

For sufficiently heavy nuclei, the t dependence of the $\gamma^*N \rightarrow XN$ scattering amplitude is much slower than that of the nuclear form factor and, hence, can be safely neglected. Therefore, Γ_{γ^*X} in Eq. (35) can be used in the following approximate form, see e.g., [80,125]:

$$\Gamma_{\gamma^*X}(\vec{b} - \vec{r}_{1\perp}) = \frac{1 - i\eta}{2} \sqrt{\frac{16\pi \frac{d\sigma_{\gamma^*N \rightarrow XN}}{dt}(t_{\min})}{1 + \eta^2}} \delta^2(\vec{b} - \vec{r}_{1\perp}), \quad (37)$$

where $d\sigma_{\gamma^*N \rightarrow XN}/dt$ is the differential cross section of the $\gamma^* + N \rightarrow X + N$ process; $t_{\min} \approx -x^2 m_N^2 (1 + M_X^2/Q^2)^2$ is the minimal momentum transfer defined by kinematics; η is the ratio of the real to the imaginary parts of the $\gamma^*N \rightarrow XN$ scattering amplitude. The normalization of Γ_{γ^*X} in Eq. (37) is fixed by the S-matrix unitarity condition for the hadronic fluctuation X of the virtual photon,

$$\frac{d\sigma_{XN \rightarrow XN}}{dt}(t_{\min}) = (1 + \eta^2) \frac{\sigma_{XN \rightarrow NX}^2}{16\pi}. \quad (38)$$

Note that for DIS on deuterium and other light nuclei such as e.g., ^3He and ^4He , one cannot neglect the t dependence of the elementary $\gamma^*N \rightarrow XN$ amplitude, see Sec. 4.

Unless specified, we consider sufficiently large nuclei, whose ground-state wave function squared can be approximated by the product of independent, one-particle nuclear densities ρ_A ,

$$|\psi_A(\vec{r}_1, \vec{r}_2, \dots, \vec{r}_A)|^2 = \prod_{i=1}^A \rho_A(\vec{r}_i). \quad (39)$$

The nuclear density ρ_A is normalized to unity, $\int d^3r \rho_A(\vec{r}) = 1$. The approximation of independent nucleons is used only for simplification: nucleon-nucleon correlations can be straightforwardly introduced and this will not noticeably change our results. For instance, corrections due to short-range correlations between nucleons is a few percent effect for

the total hadron-nucleus cross sections [126]. For the case of the deuteron target, we use directly the deuteron wave function, see details in Sec. 4.

Substituting Eq. (37) in Eq. (35) and integrating over the nucleon coordinates using Eq. (39), we obtain:

$$\begin{aligned} \sigma_{\gamma^*A}^{(b)} &= -8\pi A(A-1) \Re e \int d^2\vec{b} \sum_X \frac{(1-i\eta)^2}{1+\eta^2} \\ &\times \frac{d\sigma_{\gamma^*N \rightarrow XN}}{dt}(t_{\min}) \int_{-\infty}^{\infty} dz_1 \int_{z_1}^{\infty} dz_2 \rho_A(\vec{b}, z_1) \rho_A(\vec{b}, z_2) e^{i(z_1-z_2)\Delta_{\gamma^*X}}. \end{aligned} \quad (40)$$

The $d\sigma_{\gamma^*N \rightarrow XN}/dt$ differential cross section can be expressed in terms of the diffractive structure functions $F_2^{D(4)}$ and $F_L^{D(4)}$ [compare to Eq. (32)] which parameterize the cross section of inclusive diffraction $ep \rightarrow e + p + X$ [compare to Eq. (33)]:

$$\frac{d^4\sigma_{ep}^D}{dx_{\mathcal{P}} dt dx dQ^2} = \frac{2\pi\alpha_{\text{em}}^2}{xQ^4} \left[(1+(1-y)^2) F_2^{D(4)}(x, Q^2, x_{\mathcal{P}}, t) - y^2 F_L^{D(4)}(x, Q^2, x_{\mathcal{P}}, t) \right]. \quad (41)$$

The diffractive structure functions depend on the virtuality Q^2 , Bjorken x , the invariant momentum transfer t , and the light-cone fraction $x_{\mathcal{P}}$,

$$x_{\mathcal{P}} = \frac{M_X^2 + Q^2}{W^2 + Q^2}, \quad (42)$$

where $W^2 = (q+p)^2$. For a mini-review of hard diffraction in lepton-nucleon DIS, we refer the reader to Sec. 3.5 and 3.6.

Using the connection between the total and diffractive cross sections and the corresponding structure functions [Eqs. (32), (33), and (41)] and replacing the sum over the diffractive states X in Eq. (40) by the integration over $x_{\mathcal{P}}$, we obtain our final expression for the contribution of graph b in Fig. 9 to the nuclear structure function $F_{2A}(x, Q^2)$, which we denote $F_{2A}^{(b)}(x, Q^2)$:

$$\begin{aligned} F_{2A}^{(b)}(x, Q^2) &= -8\pi A(A-1) \Re e \frac{(1-i\eta)^2}{1+\eta^2} \int_x^{0.1} dx_{\mathcal{P}} F_2^{D(4)}(x, Q^2, x_{\mathcal{P}}, t_{\min}) \\ &\times \int d^2\vec{b} \int_{-\infty}^{\infty} dz_1 \int_{z_1}^{\infty} dz_2 \rho_A(\vec{b}, z_1) \rho_A(\vec{b}, z_2) e^{i(z_1-z_2)x_{\mathcal{P}}m_N}. \end{aligned} \quad (43)$$

The lower limit of integration over $x_{\mathcal{P}}$ corresponds to $M_X = 0$ [see Eq. (42)]; the upper limit of integration is defined by the typical cut on the diffractively produced masses

$M_X^2 \leq 0.1W^2$. The contribution of large diffractive masses, $M_X^2 \gtrsim 0.1W^2$, is automatically suppressed by the $e^{i(z_1-z_2)x_{\mathcal{P}}m_N}$ factor in the above integrand. A similar expression is also valid for the longitudinal structure functions:

$$F_L^{A(b)}(x, Q^2) = -8\pi A(A-1) \Re e \frac{(1-i\eta)^2}{1+\eta^2} \int_x^{0.1} dx_{\mathcal{P}} F_L^{D(4)}(x, Q^2, x_{\mathcal{P}}, t_{\min}) \\ \times \int d^2\vec{b} \int_{-\infty}^{\infty} dz_1 \int_{z_1}^{\infty} dz_2 \rho_A(\vec{b}, z_1) \rho_A(\vec{b}, z_2) e^{i(z_1-z_2)x_{\mathcal{P}}m_N}. \quad (44)$$

It is important to point out that Eqs. (43) and (44) give the complete and model-independent answer for the shadowing correction for the interaction with two nucleons of the target, which is the case in the low nuclear density limit and in the case of the deuteron target. One should also note that Eqs. (43) and (44) do not require the decomposition over twists. The only requirement is that the nucleus is a system of color neutral objects—nucleons. The data on the EMC ratio $F_{2A}(x, Q^2)/[AF_{2N}(x, Q^2)]$ for $x > 0.1$ indicate that the corrections to the multinucleon picture of the nucleus do not exceed few percent for $x \leq 0.5$, see the discussion in Sec. 3.2.

The next crucial step in the derivation of our master equation for nuclear PDFs is the use of the QCD factorization theorems for inclusive DIS and hard diffraction in DIS. According to the QCD factorization theorem for inclusive DIS (for a review, see, e.g., [58]) the inclusive structure function $F_2(x, Q^2)$ (of any target) is given by the convolution of hard scattering coefficients C_j with the parton distribution functions of the target f_j (j is the parton flavor):

$$F_2(x, Q^2) = x \sum_{j=q, \bar{q}, g} \int_x^1 \frac{dy}{y} C_j\left(\frac{x}{y}, Q^2\right) f_j(y, Q^2). \quad (45)$$

Since the coefficient functions C_j do not depend on the target, Eq. (34) leads to the relation between nuclear PDFs of flavor j , which are evaluated in the impulse approximation, $f_{j/A}^{(a)}$, and the nucleon PDFs $f_{j/N}$,

$$x f_{j/A}^{(a)}(x, Q^2) = A x f_{j/N}(x, Q^2). \quad (46)$$

In the graphical form, $f_{j/A}^{(a)}$ is given by graph a in Figs. 10 and 11.

Note also that one can take into account the difference between the proton and neutron PDFs by replacing $A f_{j/N} \rightarrow Z f_{j/p} + (A-Z) f_{j/n}$, where Z is the number of protons, and

the subscripts p and n refer to the free proton and neutron, respectively.

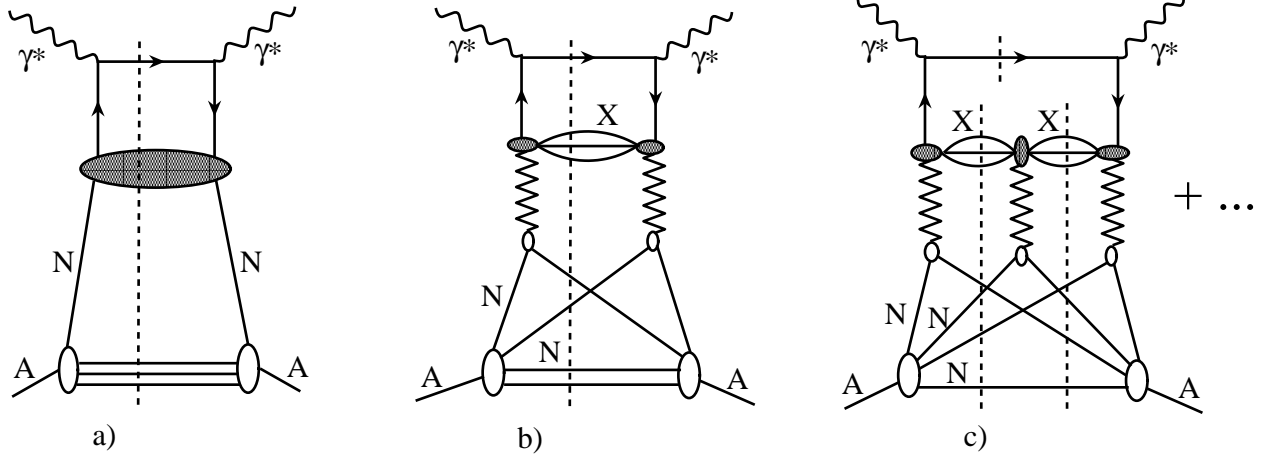


Fig. 10. Graphs corresponding to sea quark nuclear PDFs. Graphs a , b , and c correspond to the interaction with one, two, and three nucleons, respectively. Graph a gives the impulse approximation; graphs b and c contribute to the shadowing correction.

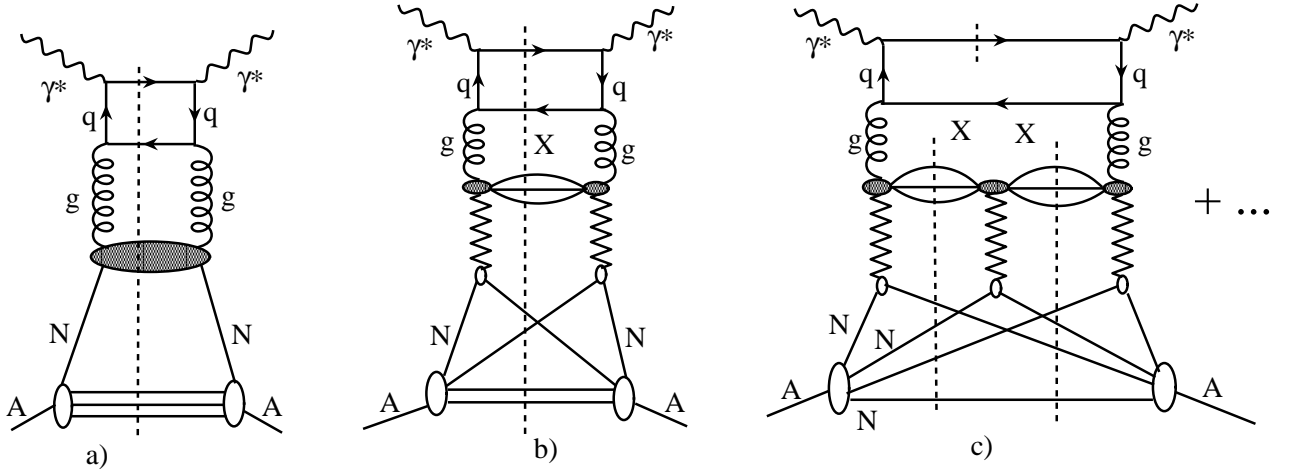


Fig. 11. Graphs corresponding to the gluon nuclear PDF. For the legend, see Fig. 10.

Similarly to the inclusive case, the factorization theorem for hard diffraction in DIS states that, at given fixed t and x_P and in the leading twist (LT) approximation, the diffractive structure function $F_2^{D(4)}$ can be written as the convolution of the same hard scattering coefficient functions C_j with universal diffractive parton distributions $f_j^{D(4)}$:

$$F_2^{D(4)}(x, Q^2, x_P, t) = \beta \sum_{j=q, \bar{q}, g} \int_{\beta}^1 \frac{dy}{y} C_j\left(\frac{\beta}{y}, Q^2\right) f_j^{D(4)}(y, Q^2, x_P, t), \quad (47)$$

where $\beta = x/x_P$. The diffractive PDFs $f_j^{D(4)}$ are conditional probabilities to find a parton

of flavor j with a light-cone fraction β in the proton that undergoes diffractive scattering characterized by the longitudinal momentum fraction $x_{\mathcal{P}}$ and the momentum transfer t , see Sec. 3.5 and 3.6 for details.

Since the inclusive and diffractive structure functions in Eq. (43) are given by the convolution of the corresponding PDFs with the same hard scattering coefficients C_j , Eq. (43) can be turned into the relation between nuclear PDFs, $f_{j/A}^{(b)}$, and the diffractive PDFs of the nucleon, $f_j^{D(4)}$:

$$x f_{j/A}^{(b)}(x, Q^2) = -8\pi A(A-1) \Re e \frac{(1-i\eta)^2}{1+\eta^2} \int_x^{0.1} dx_{\mathcal{P}} \beta f_j^{D(4)}(\beta, Q^2, x_{\mathcal{P}}, t_{\min}) \\ \times \int d^2\vec{b} \int_{-\infty}^{\infty} dz_1 \int_{z_1}^{\infty} dz_2 \rho_A(\vec{b}, z_1) \rho_A(\vec{b}, z_2) e^{i(z_1-z_2)x_{\mathcal{P}}m_N}. \quad (48)$$

In the graphical form, $f_{j/A}^{(b)}$ is given by graph b in Figs. 10 and 11 (the superscript (b) indicates that we took into account only the contribution of graph b in Figs. 9, 10, and 11). Again, similarly to the case of Eq. (43), it is important to note that Eq. (48) gives the complete answer for the shadowing correction to nuclear PDFs when the interaction with only two nucleons of the target is important (see the discussion above). Since according to the factorization theorem diffractive PDFs have the same anomalous dimensions as the usual PDFs, the left-hand and right-hand sides of Eq. (48) satisfy the same evolution equations at any order in the strong coupling constant α_s . We also simplified the expression in Eq. (48) by pulling $(1-i\eta)^2/(1+\eta^2)$ out of the integral over $x_{\mathcal{P}}$. This can be done because, experimentally, η is practically $x_{\mathcal{P}}$ -independent and the $(1-i\eta)^2/(1+\eta^2)$ factor itself is rather close to unity. This follows from the Gribov-Migdal formula which was derived within the Pomeron exchange framework [127]:

$$\eta \equiv \frac{\Re e A_{\gamma^*N \rightarrow XN}}{\Im m A_{\gamma^*N \rightarrow XN}} = \frac{\pi}{2} \frac{\partial \ln \Im m A_{\gamma^*N \rightarrow XN}}{\partial \ln(1/x)} \approx \frac{\pi}{2} (\alpha_{\mathcal{P}}(0) - 1) = 0.174, \quad (49)$$

where in the last step we used the relation between the energy dependence of the imaginary part of the diffractive amplitude $\Im m A_{\gamma^*N \rightarrow XN}$ and the intercept of the Pomeron trajectory, $\alpha_{\mathcal{P}}(0)$, for which we used the phenomenological value $\alpha_{\mathcal{P}}(0) = 1.111$, see the detailed discussion in Sec. 3.6 and Sec. 5.

The derivation of the expressions for $f_{j/A}^{(a)}$ and $f_{j/A}^{(b)}$ is general and model-independent: we only made a simplifying approximation neglecting nucleon correlations in the nuclear wave function and a small correction associated with the t dependence of the elementary diffractive $\gamma^*N \rightarrow XN$ amplitude. (For the deuteron target, the latter two approximations are not used, see Sec. 4.) By the virtue of the factorization theorem the derived results do not depend on the specific current used to probe nuclear PDFs and are valid for any kind of

current: transversely and longitudinally polarized virtual photons γ_T^* and γ_L^* , respectively, gauge boson Z^0 , or any leading twist operator that couples directly to gluons.

3.1.2 *Contribution to nuclear shadowing of the interactions with $N \geq 3$ nucleons of the target: the cross section (color) fluctuation formalism*

We derived the model-independent expressions for the interaction of the virtual photon with one and two nucleons of the nuclear target and expressed them in terms of measurable quantities, see Eqs. (46) and (48). To generalize the above results to the interaction with three and more nucleons of the target, graph *c* in Figs. 10 and 11, requires invoking additional ideas. (The A -dependence of the contributions of the interaction with a given number of nucleons can still be calculated in a model-independent way). Below we explain the problem and how to resolve it. We suggest an approximation for treating the interactions with $N > 2$ nucleons that circumvents the problem, takes into account main features of the diffractive dynamics and enables us to express the shadowing correction in terms of the parton distributions.

The problem of nuclear shadowing in DIS can be reformulated as the problem of propagation of QCD color singlet states in a nuclear medium. While at each step of our calculations we are dealing with colorless objects, the strength of the interactions of the virtual photon with the nucleons and, in particular, the presence of point-like configurations, is an unambiguous consequence of the QCD color dynamics. The QCD factorization theorem for diffraction in DIS is also valid for the interactions with $N = 3$ nucleons (graph *c* of Figs. 10 and 11) and $N > 3$ nucleons. Hence, one can easily derive the general expression for the nuclear shadowing correction for a heavy nucleus. However, this expression is not calculable in terms of DIS diffraction off a nucleon since the configurations in the photon wave function, which lead to diffractive final states and those which do not, enter in a different proportion in the interactions with $N = 2$ and $N \geq 3$ nucleons. Therefore, we have to elaborate further our approach.

In order to take into account the sum over diffractively produced states in DIS, we use the formalism of cross section fluctuations [104,115,128,129]. In this formalism, the wave function of a fast projectile (virtual photon) is represented as a superposition of the eigenstates of the scattering operator, $|\sigma\rangle$. Each eigenstate interacts with a target nucleon with a certain cross section σ . The usefulness of such a decomposition follows from the well understood property of QCD that the wave function of a virtual photon (hadron) is a superposition of quark-gluon configurations of different transverse sizes whose interaction is proportional the transverse area occupied by color, see, e.g., [130]. The existence and important role of small transverse size configurations in the wave functions of photons and pions has been confirmed by the observation of the color transparency phenomenon in a variety of different processes; for a review, see [130]. The probability of the incoming virtual photon to fluctuate into a given eigenstate is given by the distribution $P_j(\sigma)$. We explicitly show the dependence of $P_j(\sigma)$ on parton flavor j as a reminder that DIS

probes a particular parton distribution of the target. In soft hadron interactions, the formalism of cross section fluctuations provides a good description of the total hadron-nucleus cross sections and the coherent inelastic diffraction in hadron-nucleus scattering, for a review and references, see Ref. [129]. The latter is far less trivial as the coherent inelastic diffraction would have been absent if the fluctuations were not present.

Note also that the validity of the formalism of cross section fluctuations for the virtual photon is supported by the observation of the low value of the intercept of the Pomeron trajectory, $\alpha_P(0) = 1.111 \pm 0.007$, see Sec. 3.6. The closeness of $\alpha_P(0)$ extracted from the HERA data on diffraction in DIS to $\alpha_P(0) = 1.0808$ extracted from the fits to soft hadron-hadron cross sections [131] and to $\alpha_P(0) \approx 1.08$ extracted from the energy dependence of elastic ρ_0 photoproduction at HERA [132] indicates that our approximation should work in lepton-nucleus DIS approximately as well as in high-energy hadron-nucleus scattering [133,134].

The entire series of the interactions with the target nucleons shown in Figs. 10 and 11 can be summed as in the standard Glauber formalism, with the substitution of σ^k in the term corresponding to the interaction with k nucleons by $\langle \sigma^k \rangle_j$,

$$\langle \sigma^k \rangle_j = \int_0^\infty d\sigma P_j(\sigma) \sigma^k, \quad (50)$$

which accounts for the color fluctuations of the strength of the interaction, see, e.g., Ref. [129]. Assuming that $A \gg 1$ such that the interactions can be exponentiated, one obtains [135]:

$$\begin{aligned} x f_{j/A}(x, Q^2) &= \frac{x f_{j/N}(x, Q^2)}{\langle \sigma \rangle_j} 2 \Re e \int d^2b \left\langle \left(1 - e^{-\frac{A}{2}(1-i\eta)\sigma T_A(b)} \right) \right\rangle_j \\ &= A x f_{j/N}(x, Q^2) - x f_{j/N}(x, Q^2) \frac{A^2 \langle \sigma^2 \rangle_j}{4 \langle \sigma \rangle_j} \Re e (1 - i\eta)^2 \int d^2b T_A^2(b) \\ &\quad - x f_{j/N}(x, Q^2) 2 \Re e \int d^2b \frac{\sum_{k=3}^\infty \left(-\frac{A}{2}(1-i\eta) T_A(b) \right)^k \langle \sigma^k \rangle_j}{k! \langle \sigma \rangle_j}, \end{aligned} \quad (51)$$

where $T_A(b) = \int_{-\infty}^\infty dz \rho_A(b, z)$. In the second and third lines of Eq. (51), we made an expansion in the number of the interactions with the target nucleons. The interaction with k nucleons of the nuclear target probes the k -th moment of the distribution $P_j(\sigma)$. Note that the above equation has no evident problems with energy-momentum conservation and causality that are characteristic for the eikonal approximation since the energy is split between the constituents of the projectile well before the interaction and different configurations are practically frozen during the propagation of the wave packet through the nucleus.

Equation (51) is valid at high energies (small x), when the effect of the finite coherence length (the coherence length is proportional to the lifetime of the fluctuations $|\sigma\rangle$) is unimportant. In this case, all factors associated with the space-time development of the scattering, such as, e.g., the $e^{i(z_1-z_2)m_N x_P}$ factor, should be set to unity. Note that our numerical analysis shows that the $e^{i(z_1-z_2)m_N x_P}$ factor can be safely set to unity for $x \leq 10^{-2}$, see Fig. 44.

In Eq. (51), the first term corresponds to the interaction with one nucleon of the target, and, hence, is equal to $Ax f_{j/N}^{(a)}(x, Q^2)$. The second term describes the interaction with two nucleons, and, hence, should be equal to $x f_{j/N}^{(b)}(x, Q^2)$ after $e^{i(z_1-z_2)m_N x_P}$ is set to unity in Eq. (48). [Note that we take into account the effect of the finite coherence length in our final expression below, see Eq. (61).] Indeed, as follows from the formalism of cross section fluctuations, the second moment $\langle \sigma^2 \rangle_j$ is proportional to the differential cross section of diffractive dissociation [128]. In the case of DIS and in our notation (normalization), $\langle \sigma^2 \rangle_j$ is related to the diffractive parton distribution $f_j^{D(4)}$ [57,76]:

$$\frac{\langle \sigma^2 \rangle_j}{\langle \sigma \rangle_j} \equiv \sigma_2^j(x, Q^2) = \frac{16\pi}{(1 + \eta^2)x f_{j/N}(x, Q^2)} \int_x^{0.1} dx_P \beta f_j^{D(4)}(\beta, Q^2, x_P, t_{\min}). \quad (52)$$

Equation (52) is similar to the Miettinen-Pumplin relation [116] generalized to include the real part of the diffractive amplitude.

Also, one notices that $\int_{-\infty}^{\infty} dz_1 \int_{z_1}^{\infty} dz_2 \rho_A(\vec{b}, z_1) \rho_A(\vec{b}, z_2) = (1/2)T_A^2(\vec{b})$. Therefore, in the discussed high-energy limit, we obtain from Eq. (48):

$$x f_{j/A}^{(b)}(x, Q^2) = -x f_{j/N}(x, Q^2) \frac{A^2}{4} \sigma_2^j(x, Q^2) \Re e (1 - i\eta)^2 \int d^2b T_A^2(b), \quad (53)$$

which coincides with the second term in Eq. (51).

The last term in Eq. (51) describes the interaction with three and more nucleons of the target. It corresponds to graph c and implied (not shown) higher rescattering terms in Figs. 10 and 11. Denoting the contribution of the last term in Eq. (51) by $x f_{j/A}^{(c)}(x, Q^2)$, we obtain:

$$\begin{aligned} x f_{j/A}^{(c)}(x, Q^2) &= -x f_{j/N}(x, Q^2) \sigma_2^j(x, Q^2) 2 \Re e \int d^2b \frac{\sum_{k=3}^{\infty} \left(-\frac{A}{2}(1-i\eta)T_A(b)\right)^k \langle \sigma^k \rangle_j}{k! \langle \sigma^2 \rangle_j} \\ &= -x f_{j/N}(x, Q^2) \sigma_2^j(x, Q^2) 2 \Re e \int d^2b \\ &\times \frac{\left\langle \left(e^{-\frac{A}{2}(1-i\eta)\sigma T_A(b)} - 1 + \frac{A}{2}(1-i\eta)\sigma T_A(b) - \frac{1}{2} \left[\frac{A}{2}(1-i\eta)\sigma T_A(b) \right]^2 \right) \right\rangle_j}{\langle \sigma^2 \rangle_j}. \end{aligned} \quad (54)$$

Therefore, the full expression for the nuclear parton distribution, $xf_{j/A} = xf_{j/A}^{(a)} + xf_{j/A}^{(b)} + xf_{j/A}^{(c)}$, is

$$xf_{j/A}(x, Q^2) = Ax f_{j/N}(x, Q^2) - xf_{j/N}(x, Q^2) \sigma_2^j(x, Q^2) 2 \Re e \int d^2b \frac{\left\langle \left(e^{-\frac{A}{2}(1-i\eta)\sigma T_A(b)} - 1 + \frac{A}{2}(1-i\eta)\sigma T_A(b) \right) \right\rangle_j}{\langle \sigma^2 \rangle_j}. \quad (55)$$

To cast Eq. (55) into the more standard form, which reflects the space-time development of the scattering process [76], we reintroduce the dependence on the longitudinal coordinates z_1 and z_2 , use the definition of $\sigma_2^j(x, Q^2)$ from Eq. (52), and equivalently rewrite Eq. (55) in the following form:

$$xf_{j/A}(x, Q^2) = Ax f_{j/N}(x, Q^2) - 8\pi A^2 \Re e \frac{(1-i\eta)^2}{1+\eta^2} \int_x^{0.1} dx_{\mathcal{P}} \beta f_j^{D(4)}(\beta, Q^2, x_{\mathcal{P}}, t_{\min}) \times \int d^2b \int_{-\infty}^{\infty} dz_1 \int_{z_1}^{\infty} dz_2 \rho_A(\vec{b}, z_1) \rho_A(\vec{b}, z_2) \frac{\left\langle \sigma^2 e^{-\frac{A}{2}(1-i\eta)\sigma \int_{z_1}^{z_2} dz' \rho_A(\vec{b}, z')} \right\rangle_j}{\langle \sigma^2 \rangle_j}. \quad (56)$$

Equation (56) is derived in the limit of high energies when the coherence length l_c is infinite. To derive the formula applicable for moderately small x corresponding to $l_c \sim R_A$, we need to take into account the effect of the finite l_c , which was correctly included in Eq. (48) for $f_{j/A}^{(b)}$. Therefore, we restore the effect of the finite coherence length by reintroducing the $e^{i(z_1-z_2)x_{\mathcal{P}}m_N}$ factor in the integral over $x_{\mathcal{P}}$. In addition, we replace A^2 by $A(A-1)$ to account for the well-understood $1/A$ corrections in the double scattering term [cf. Eq. (35)]. Our resulting expression for the nuclear parton distribution reads:

$$xf_{j/A}(x, Q^2) = Ax f_{j/N}(x, Q^2) - 8\pi A(A-1) \Re e \frac{(1-i\eta)^2}{1+\eta^2} \int_x^{0.1} dx_{\mathcal{P}} \beta f_j^{D(4)}(\beta, Q^2, x_{\mathcal{P}}, t_{\min}) \times \int d^2b \int_{-\infty}^{\infty} dz_1 \int_{z_1}^{\infty} dz_2 \rho_A(\vec{b}, z_1) \rho_A(\vec{b}, z_2) e^{i(z_1-z_2)x_{\mathcal{P}}m_N} \frac{\left\langle \sigma^2 e^{-\frac{A}{2}(1-i\eta)\sigma \int_{z_1}^{z_2} dz' \rho_A(\vec{b}, z')} \right\rangle_j}{\langle \sigma^2 \rangle_j}. \quad (57)$$

It is important to note here that the key input in Eq. (57) is the diffractive PDFs $f_j^{D(4)}(\beta, Q^2, x_{\mathcal{P}}, t_{\min})$ evaluated at $t = t_{\min}$ because the slope of the t dependence of the nuclear form factor is much larger than the slope of the diffractive structure function. In

the cases when the t dependence of the diffractive structure functions (diffractive PDFs) was measured at HERA, it was fitted to the exponential form (see Sec. 3.6.2),

$$f_j^{D(4)}(\beta, Q^2, x_P, t) = e^{B_{\text{diff}}(t-t_{\text{min}})} f_j^{D(4)}(\beta, Q^2, x_P, t_{\text{min}}), \quad (58)$$

where $B_{\text{diff}} \approx 6 \text{ GeV}^{-2}$ [62]. Note that the recent ZEUS analysis reports a rather close value, $B_{\text{diff}} \approx 7 \pm 0.3 \text{ GeV}^{-2}$ [72]. Integrating Eq. (58) over t , one obtains the simple relation between $f_j^{D(4)}(\beta, Q^2, x_P, t_{\text{min}})$ and the diffractive PDFs $f_j^{D(3)}(\beta, Q^2, x_P)$ obtained from the fits to the t -integrated diffractive structure function $F_2^{D(3)}(\beta, Q^2, x_P)$,

$$f_j^{D(4)}(\beta, Q^2, x_P, t_{\text{min}}) = B_{\text{diff}} f_j^{D(3)}(\beta, Q^2, x_P), \quad (59)$$

where

$$f_j^{D(3)}(\beta, Q^2, x_P) \equiv \int_{-1 \text{ GeV}^2}^{t_{\text{min}}} dt f_j^{D(4)}(\beta, Q^2, x_P, t). \quad (60)$$

The use of $f_j^{D(3)}$ enables us to express the shadowing correction in terms of the quantities known to date from the QCD analysis of diffraction in ep DIS. The final expression for $x f_{j/A}(x, Q^2)$ obtained with help of the color fluctuation formalism reads:

$$\begin{aligned} x f_{j/A}(x, Q^2) &= A x f_{j/N}(x, Q^2) \\ &- 8\pi A(A-1) \Re e \frac{(1-i\eta)^2}{1+\eta^2} B_{\text{diff}} \int_x^{0.1} dx_P \beta f_j^{D(3)}(\beta, Q^2, x_P) \\ &\times \int d^2b \int_{-\infty}^{\infty} dz_1 \int_{z_1}^{\infty} dz_2 \rho_A(\vec{b}, z_1) \rho_A(\vec{b}, z_2) e^{i(z_1-z_2)x_P m_N} \frac{\left\langle \sigma^2 e^{-\frac{A}{2}(1-i\eta)\sigma} \int_{z_1}^{z_2} dz' \rho_A(\vec{b}, z') \right\rangle_j}{\langle \sigma^2 \rangle_j}. \end{aligned} \quad (61)$$

3.1.3 The color fluctuation approximation within the color fluctuation formalism

The distribution $P_j(\sigma)$ that enters Eq. (61) is restricted by the general properties of QCD. For small σ , it is calculable in pQCD and leads to a singular behavior $P_j(\sigma) \propto 1/\sigma$ [136,137]. Such a behavior follows from the factorization theorem, the value of the cross section for the spatially small wave packet of quarks and gluons, and the form of the light-cone wave function of the virtual photon in the case of large transverse momenta of the constituents. For large σ , $P_j(\sigma)$ has to decrease with an increase of σ to ensure the convergence of the moments. In contrast to DIS, in the case of hadron projectiles, the

small- σ behavior of the corresponding distribution $P_h(\sigma)$ is not singular. For example, for pions (mesons), $P_\pi(\sigma)|_{\sigma \rightarrow 0} \rightarrow \text{const}$. Also, in the case of hadrons, several first moments of $P_h(\sigma)$ can be extracted from the data and used to model $P_\pi(\sigma)$ and $P_N(\sigma)$. These models could in turn be tested using coherent nuclear diffraction data (see the discussion and references in Sec. 7).

In the case of hadrons, color fluctuations are known to lead only to small corrections to the total cross section of hadron-nucleus scattering [74,118,130]. In the case of virtual photons, we are faced with a new situation since in this case $P_j(\sigma)$ is very broad and includes the states $|\sigma\rangle$ that correspond to both small and large cross sections σ [136,137]. The states (fluctuations) with small cross sections constitute the perturbative contribution to the photon-nucleon cross section; the fluctuations with large cross sections correspond to the hadronic component of the virtual photon. In practice, only hadronic-size configurations contribute to $\langle\sigma^2\rangle$. This expectation is based on the QCD-improved aligned jet model which takes into account the Q^2 evolution [138] and agrees well with the final analyses of the HERA data on diffraction in DIS that find that the energy dependence of the diffractive amplitudes is practically the same as in the soft QCD processes [131] and is given by $\alpha_{\mathcal{P}}(t=0) = 1.111 \pm 0.007$ [61,62]. Hence, the diffractive state X in Figs. 9, 10 and 11 is dominated by the large- σ hadron-like fluctuations. At the same time, weakly interacting configurations give an important contribution to $\langle\sigma\rangle$ down to very small values of x . One of the sources of such weakly interacting configurations is the QCD evolution which generates small- x partons at $Q^2 \sim \text{few GeV}^2$ from the configurations with $x \geq 0.1$ and $Q_0^2 \sim 1 \text{ GeV}^2$ which do not lead to diffractive states since in such processes production of nucleons with $x_{\mathcal{P}} < 0.1$ is kinematically forbidden.

The key feature of Eq. (61) is that it separates the contributions of the small and large cross sections [it was the main purpose of rewriting Eq. (51) in the form of Eq. (55) which led to Eq. (61)]. While the fluctuations with large cross sections contribute to all moments $\langle\sigma^k\rangle$, the fluctuations with small cross sections contribute significantly only to $\langle\sigma\rangle$ and $\langle\sigma^2\rangle$, i.e., to the $Ax f_{j/N}(x, Q^2)$ term and the double scattering term proportional to $f_j^{D(3)}$. Therefore, since the last term in Eq. (61) proportional to

$$\frac{\left\langle \sigma^2 e^{-\frac{A}{2}(1-i\eta)\sigma} \int_{z_1}^{z_2} dz' \rho_A(\vec{b}, z') \right\rangle_j}{\langle\sigma^2\rangle_j} \equiv \eta_j \quad (62)$$

probes the higher moments of $P_j(\sigma)$, $\langle\sigma^k\rangle/\langle\sigma^2\rangle$ with $k \geq 3$, it can be evaluated with the distribution $P_j(\sigma)$ that neglects the small- σ perturbative contribution and uses only the information on cross section fluctuations from soft hadron-hadron scattering.

The factor η_j in Eqs. (61) and (62) can be identically expanded in terms of $\langle\sigma^k\rangle_j/\langle\sigma^2\rangle_j$ with $k \geq 3$. We have just explained that the required component of the distribution $P_j(\sigma)$ is dominated by soft hadron-like fluctuations. Similarly to the case of such fluctuations

for the total hadron-nucleus cross sections mentioned above, the dispersion of $P_j(\sigma)$ does not lead to significant modifications of η_j in Eq. (61). In particular, our numerical studies using $P_j(\sigma) \propto P_\pi(\sigma)$ have found that it is a good approximation to use $\langle \sigma^k \rangle_j / \langle \sigma^2 \rangle_j = (\langle \sigma^3 \rangle_j / \langle \sigma^2 \rangle_j)^{k-2}$ for all $k \geq 3$, which we shall call the *color fluctuation approximation*. Therefore, the η_j term in Eqs. (61) and (62) can be expressed in terms of a single cross section, $\sigma_{\text{soft}}^j(x, Q^2)$,

$$\sigma_{\text{soft}}^j(x, Q^2) \equiv \langle \sigma^3 \rangle_j / \langle \sigma^2 \rangle_j = \left(\langle \sigma^k \rangle_j / \langle \sigma^2 \rangle_j \right)^{1/(k-2)}, \text{ for } k \geq 3. \quad (63)$$

We can estimate $\sigma_{\text{soft}}^j(x, Q^2)$ based on the analysis of the inelastic diffraction in the pion-nucleon scattering. In our numerical predictions for nuclear shadowing, we will use two models for $\sigma_{\text{soft}}^j(x, Q^2)$, which are based on the assumption that soft physics dominates the interaction of the configurations leading to diffraction, see the discussion in Sec. 5.1.2. It is also worth emphasizing here that for realistic nuclei, a typical number of interactions even at small impact parameters does not exceed three. As a result, the uncertainties in the predictions (which are quite small in the case of nuclear PDFs) are dominated by the uncertainties in the value of σ_{soft}^j rather than by the color fluctuation approximation for the $k \geq 4$ moments (63).

Note that the factor $1 - \sigma_2^j(x, Q^2) / \sigma_{\text{soft}}^j(x, Q^2)$ can be interpreted as the fraction of the DIS cross section (PDF) originating from the point-like configurations—it is the parameter λ of the QCD-improved aligned jet model [57,81]. As one can see from our numerical studies described below, λ decreases with decreasing x , which reflects the onset of the strong interaction regime for the increasing fraction of the configurations contributing to the PDFs.

We shall postpone the detailed discussion of σ_{soft}^j until Sec. 5.1.2. At this point, to get the feeling about the meaning and magnitude of σ_{soft}^j , we note that if diffraction were described by the aligned jet model, we would expect the typical strength of the interaction of a large-size $q\bar{q}$ configuration with the nucleon to be compatible to that for pions (ρ mesons, etc.), i.e., $\sigma_{\text{aligned jet-N}} \approx 25$ mb at $x = 0.01$ and $\sigma_{\text{aligned jet-N}} \approx 40$ mb at $x = 10^{-5}$.

Applying the color fluctuation approximation to Eq. (61), we obtain our final expression for the nuclear parton distribution modified by nuclear shadowing,

$$\begin{aligned} x f_{j/A}(x, Q_0^2) &= A x f_{j/N}(x, Q_0^2) \\ &- 8\pi A(A-1) \Re e \frac{(1-i\eta)^2}{1+\eta^2} B_{\text{diff}} \int_x^{0.1} dx_{\mathcal{P}} \beta f_j^{D(3)}(\beta, Q_0^2, x_{\mathcal{P}}) \\ &\times \int d^2b \int_{-\infty}^{\infty} dz_1 \int_{z_1}^{\infty} dz_2 \rho_A(\vec{b}, z_1) \rho_A(\vec{b}, z_2) e^{i(z_1-z_2)x_{\mathcal{P}}m_N} e^{-\frac{A}{2}(1-i\eta)\sigma_{\text{soft}}^j(x, Q_0^2) \int_{z_1}^{z_2} dz' \rho_A(\vec{b}, z')}, \quad (64) \end{aligned}$$

where $Af_{j/N} \equiv Zf_{j/p} + (A - Z)f_{j/n}$; Q_0^2 is a low scale at which the color fluctuation approximation is applicable (see below). The nuclear PDFs $f_{j/A}$ given by Eq. (64) are next-to-leading (NLO) PDFs since the nucleon diffractive PDFs $f_j^{D(3)}$ are obtained from the NLO QCD fit.

Our master equation (64) determines the nuclear PDFs $f_{j/A}$ at a particular input scale $Q^2 = Q_0^2$, which is explicitly present in $f_{j/N}$, $f_j^{D(3)}$ and σ_{soft}^j . The color fluctuation approximation is more accurate if the fluctuations are more hadron-like, i.e., when the contribution of the point-like configurations (PLCs) is small. This demands that Q_0^2 is not too large. At the same time, we would like to stay within the perturbative regime, where higher twist contributions to the diffractive structure functions are still small and where the fits to diffractive PDFs do not have to be extrapolated too strongly. (In the extraction of the diffractive PDFs from the HERA data on diffraction, only the data with $Q^2 > 8.5 \text{ GeV}^2$ were used [61]. However, it has been checked that the extrapolation down to $Q^2 = 4 \text{ GeV}^2$ works with a good accuracy.) Accordingly, in our numerical analysis, we use $Q_0^2 = 4 \text{ GeV}^2$. We will demonstrate that our results depend weakly on the choice of Q_0^2 , even if we keep σ_{soft}^j fixed. This is because the approximations discussed above are needed only for the interactions with three and more nucleons of the target; the double rescattering contribution is evaluated in a model-independent way.

It is important to emphasize that while Eq. (61) gives a general expression for the effect of cross section (color) fluctuations on the multiple interactions, Eq. (64) presents a particular approximation—the color fluctuation approximation. In this approximation, the interaction cross section with $N \geq 3$ nucleons is $\sigma_{\text{soft}}^j(x, Q^2) = \langle \sigma^3 \rangle_j / \langle \sigma^2 \rangle_j$, see Eq. (63). Equation (64) allows for a simple interpretation: the factor $B_{\text{diff}} \int_x^{0.1} dx_{\mathcal{P}} \beta f_j^{D(3)}(\beta, Q^2, x_{\mathcal{P}})$ describes the probability for a photon to diffract into diffractive states in the interaction with a target nucleon at point (z_1, \vec{b}) and to be absorbed in the interaction with another nucleon at point (z_2, \vec{b}) , while the factor in the third line of Eq. (64) describes the interaction of the diffractive states with other nucleons of the nucleus with the cross section σ_{soft}^j between points z_1 and z_2 .

It is important to note that $\sigma_{\text{soft}}^j(x, Q^2)$ can be determined experimentally by measuring nuclear shadowing with a light nucleus, for instance, with ^4He . Alternatively, $\sigma_{\text{soft}}^j(x, Q^2)$ can be extracted directly from coherent diffraction in DIS on deuterium [128]. After $\sigma_{\text{soft}}^j(x, Q^2)$ will have been determined, the leading twist theory will contain no model-dependent parameters and can be used to predict nuclear shadowing for an arbitrary nucleus in a completely model-independent way. The discussed measurements can be carried out at a future Electron-Ion Collider.

In the treatment of multiple rescatterings in the leading twist theory of nuclear shadowing in Ref. [76], we used the so-called quasi-eikonal approximation, which neglects color fluctuations and, hence, uses $\sigma_{\text{soft}}^j(x, Q^2) = \sigma_2^j(x, Q^2) \equiv \langle \sigma^2 \rangle_j / \langle \sigma \rangle_j$ in Eq. (64). Such an approximation gives the results identical to Eq. (64) for the interaction with one and

two nucleons of the nuclear target. However, it neglects the presence of point-like configurations in the virtual photon wave function and, hence, overestimates shadowing at $x \sim 10^{-3}$, where the contribution of the interactions with $N > 2$ is already important, while the contribution of the point-like configurations is still significant. We will use a comparison between the color fluctuation and quasi-eikonal approximations to illustrate the role of color fluctuations in Sec. 5.8. (Note that the quasi-eikonal approximation is popular in the literature in spite of its deep shortcomings discussed above and also in Sec. 3.1.4.)

In the very small- x limit, which for practical purposes means $x < 10^{-2}$ (see Fig. 44), the factor $e^{i(z_1 - z_2)x_{\mathcal{P}MN}}$ in Eq. (64) can be safely neglected. This results in a significant simplification of the master formula after the integration by parts two times (cf. [80]):

$$\begin{aligned}
x f_{j/A}(x, Q_0^2) &= A x f_{j/N}(x, Q_0^2) - 8\pi A(A-1) B_{\text{diff}} \Re e \frac{(1-i\eta)^2}{1+\eta^2} \int_x^{0.1} dx_{\mathcal{P}} \beta f_j^{D(3)}(\beta, Q_0^2, x_{\mathcal{P}}) \\
&\times \int d^2\vec{b} \frac{e^{-LT_A(b)} - 1 + LT_A(b)}{L^2}, \tag{65}
\end{aligned}$$

where $L = A/2(1-i\eta)\sigma_{\text{soft}}^j(x, Q_0^2)$; $T_A(b) = \int_{-\infty}^{\infty} dz \rho_A(z)$.

We will discuss the energy and A dependence of nuclear shadowing in nuclear PDFs and structure functions in Sec. 5. At this point, we note that in the limit of $x = \text{const}$ and $A \rightarrow \infty$, Eq. (65) predicts that nuclear shadowing tends to a constant, i.e.,

$$\frac{x f_{j/A}(x, Q_0^2)}{A x f_{j/N}(x, Q_0^2)} = 1 - \frac{\sigma_2^j(x, Q_0^2)}{\sigma_{\text{soft}}^j(x, Q_0^2)} \equiv \lambda, \tag{66}$$

where $\lambda = 0 - 0.13$ for gluons and $\lambda = 0.25 - 0.50$ for quarks, and decreasing with a decrease of x for fixed $Q^2 = Q_0^2$, see our results in Sec. 5. This is a consequence of the fact that in our approach, we effectively allow for the presence of unshadowed PLCs in the virtual photon wave function and the $A \rightarrow \infty$ limit chooses only those. Note that the PLCs can be present even in this limit due to the QCD evolution from larger $x \geq 0.01$ at the input scale Q_0^2 , see the discussion of the evolution trajectories in Sec. 5.15. In any case, the $A \rightarrow \infty$ limit is far from the realistic one for realistic nuclei, where very few nucleons are involved in the shadowing and, consequently, the suppression due to nuclear shadowing does not exceed approximately a factor of three, even for small impact parameters, see our predictions in Sec. 5.

The color fluctuation pattern is changing with an increase of Q^2 : the configuration that interacted with the strength σ at the resolution Q_0^2 at x_0 , at higher Q^2 will interact with the same strength at smaller x . As a result, the strength of the fluctuations at fixed x grows with an increase of Q^2 . In particular, it leads to an increase of the contribution of

the PLCs. These effects are automatically taken into account by the QCD evolution and they could be visualized by inspecting the trajectories of the QCD evolution which we present in Sec. 5.15.

3.1.4 Eikonal approximation violates constraints due to energy-momentum conservation

In this section we explain caveats of the eikonal approximation to QCD amplitudes of high energy processes and how they are resolved within the color fluctuation approach. As a consequence of the Lorentz dilation, transitions between different configurations in the wave function of the energetic projectile occur in the target rest frame at the distances comparable to the scale characterized by the coherence length,

$$l_c = \frac{2E_h}{M_n^2 - M_h^2}, \quad (67)$$

where E_h is the energy of the projectile; M_n is the mass of the intermediate state $|n\rangle$; M_h is the projectile mass. At sufficiently large E_h , when coherence length exceeds internucleon distances in nuclei, the approximation of consecutive multiple collisions (the Glauber approximation) becomes inapplicable, see the discussion in Sec. 2. Instead, the projectile interacts at the same time with all nucleons located at the same impact parameter (the Gribov approximation). Thus, the quark-gluon configurations in the wave function of the projectile are frozen during collisions.

At high energies, diffractive processes are a shadow of inelastic ones. Indeed, the Abramovsky-Gribov-Kancheli cutting rules [119] allow one to calculate the amplitudes of diffractive processes in terms of inelastic ones. This relationship allows one to visualize the exact constraints imposed by energy-momentum conservation and also suggests how to satisfy them.

To visualize the constraints due to energy-momentum conservation, let us consider the double and triple scattering of a colorless dipole of the projectile off a nucleus target. Each constituent of the dipole carries either the fraction z or $1 - z$ of the projectile momentum. In the case of the double inelastic collision, the dipole scatters off different nucleons. The total energy released into the final state is $z s + (1 - z) s = s$, where s is the total invariant energy of the initial state, i.e., the energy-momentum constraint is fulfilled. In the case of the triple scattering, the invariant energy of the final state is $z s + (1 - z) s + z s = (1 + z) s$ or $(1 - z) s + (1 - z) s + z s = (2 - z) s$, i.e., the eikonal approximation neglects the energy lost by the projectile during the collision. Thus, the eikonal approximation has fundamental problems in the application to the high-energy processes when inelastic processes dominate. The constraint imposed by the energy-momentum conservation is stronger and more specific than the cancellation of the eikonal term due to causality found in [112,114].

The resolution of this puzzle is that the projectile dipole develops other components containing more partons which participate in the triple, quadruple, etc. collisions. However, this quantum field theory effect is beyond the framework of the eikonal approximation, but it is well consistent with the color fluctuation approach, which also includes large-mass diffraction (contribution of the triple Pomeron limit).

3.2 Space-time picture of leading twist shadowing in the nucleus infinite momentum frame and the transverse structure of the nuclear wave function

As we already mentioned above, the starting point of the discussion of nuclear shadowing in DIS is the observation that, to a very good approximation, a nucleus can be described as a many-nucleon nonrelativistic system. This condition is easier to implement in the reference frame where the nucleus is at rest. Hence, many calculations, including those of Sec. 3.1, are performed in that frame. However, in the rest frame, one does not explicitly use quark and gluon degrees of freedom in the nucleus. Hence, in order to explain what processes lead to leading twist shadowing, it is instructive to consider the frame where the target nucleus is fast (the infinite momentum frame).

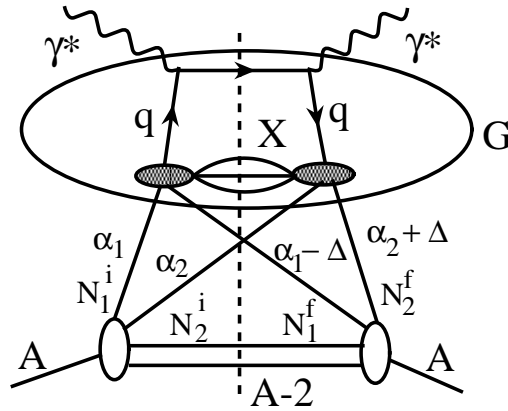


Fig. 12. The interchange (interference) diagram corresponding to the leading twist contribution to the diffractive final state.

For certainty, we will consider the interaction with two nucleons of the target, see Fig. 12. Since γ^* 's are attached to the same quark, it appears at the first glance that it is impossible to break the additivity of the interaction since, naively, the quark should belong to the same nucleon in the $|in\rangle$ and $\langle out|$ states (similarly to graph *a* of Fig. 10). Let us determine the necessary conditions to avoid this conclusion. In Fig. 12, the nucleon that interacts in the $|in\rangle$ state is denoted as N_1^i and the one that interacts in the final state as N_2^f . For each nucleon in Fig. 12, we introduce the light-cone fractions $\alpha \equiv Ap_N^+/p_A^+$, where p_N^+ and p_A^+ are the plus-momenta of the nucleon and the nucleus, respectively (the plus-momentum is defined as $p^+ = (p^0 + p^3)/\sqrt{2}$). For the nucleon at rest, $\alpha = 1$. It follows from the DIS kinematics that

$$\begin{aligned}\alpha_1^f &\leq \alpha_1^i - x, \\ \alpha_2^i &\leq \alpha_2^f - x,\end{aligned}\tag{68}$$

where x is the Bjorken x . Since $\alpha - 1 \approx p_3/m_N$, where p_3 is the projection of the nucleon momentum on the reaction axis, and typical momenta of nucleons are less than $k_F \sim 250$ MeV/c, the interference (interchange) diagram in Fig. 12 is automatically suppressed for $x \geq 0.1$ since this requires scattering off nucleons with very large momenta. Also, there is an additional suppression since only a small fraction of nucleons is produced with Feynman $x_F = \alpha/(1-x)$ close to unity. In fact, one expects that the $\gamma^*N \rightarrow NX$ inclusive cross section behaves as [123,139]:

$$\begin{aligned}\frac{d\sigma^{\gamma^*N \rightarrow NX}(x_F)}{dx_F/x_F} \Big|_{x_F \rightarrow 1} &\propto (1-x_F)^{n(x)}, \\ n(x \geq 0.2) &\sim 1, \quad n(0.02 < x < 0.1) \sim 0, \quad n(x < 0.01) \sim -1,\end{aligned}\tag{69}$$

which further suppresses the contribution of the $x \geq 0.05$ region and leads to the dominance of the diffractive contribution for $x \leq 0.01$.

The above analysis demonstrates that the interference effects are restricted to the region of small x and any deviations from the additivity for $x \geq 0.2$ should be due to the presence of non-nucleonic degrees of freedom in the nucleus wave function. These effects have indeed been observed—the EMC effect for this kinematics—but they become significant only for rare configurations of quarks in the nucleons with $x \geq 0.5$.

Introducing the light-cone wave function of the nucleus, ψ_A , we can write the contribution due to the diffractive cut of the interference diagram to the total cross section as (see Fig. 12):

$$\begin{aligned}\Delta^{\text{diff}} F_{2A}(x, Q^2) &= \frac{1}{16\pi} \int \prod_{i=1,2} \frac{d\alpha_i}{\alpha_i} d^2 p_{\perp i} d\Delta d^2 q_{\perp} G(\alpha_1, \alpha_2, \Delta, p_{\perp 1}, p_{\perp 2} + q_{\perp}, x, Q^2) \\ &\times \psi_A(\alpha_i, p_{\perp i}) \psi_A^*(\alpha_1 - \Delta, \alpha_2 + \Delta, \alpha_3, \dots, p_{\perp 1} + q_t, p_{\perp 2} - q_{\perp}, p_{\perp 3}, \dots),\end{aligned}\tag{70}$$

where Δ is related to the invariant mass of the system produced in the intermediate state, $M_X^2 = -Q^2 + \Delta W^2$; q_{\perp} is the transverse momentum of the intermediate state; G describes the upper part of the diagram associated with the $\gamma^*NN \rightarrow \gamma^*NN$ interaction. Note that $\Delta = x_{\mathcal{P}}$ [see Eq. (42)].

Since the nucleon momenta are small, the integration is symmetric with respect to the $p_3 \rightarrow -p_3$ transformation, and G only weakly depends on the incident energy, we can neglect the dependence of the factor G on α_1 , α_2 , $p_{\perp 1}$ and $p_{\perp 2}$. In this approximation (implicit in the Gribov derivation of shadowing for hadron-deuteron scattering, see Sec. 2.2), if we neglect the Fermi motion and take $\alpha_i \simeq 1$ and $\Delta \ll 1$, $G \equiv G(x, Q^2, \Delta, q_{\perp})$ is the

cross section of the nucleon production for $x_F \sim 1$. Indeed, the Fermi motion leads to the rescaling of the invariant energy \hat{s} in the diffractive amplitude by the factor $\alpha_1^n (\alpha_2 + \Delta)^n$, where $n \approx 0.11$. Since Δ is small, the correction factor for $\alpha_1 \simeq \alpha_2 \simeq 1$ is $(1 + n\Delta)$ in the integrand where $G \equiv G(x, Q^2, \Delta, q_\perp)$. The terms proportional to $(\alpha_i - 1)$ cancel out due to the $\alpha \rightarrow 2 - \alpha$ symmetry for $\alpha \sim 1$. As a result, the Fermi motion correction is proportional to $n \langle p^2 \rangle / (3m_N^2)$ and is smaller than 1%. Hence, overall the approximation of Eq. (71) is accurate to better than 1%.

As a result, we can rewrite Eq. (70) as

$$\Delta^{\text{diff}} F_{2A}(x, Q^2) = \frac{1}{16\pi} \int d\Delta d^2q_\perp G(x, Q^2, \Delta, q_\perp) F_A(\Delta m_N, q_\perp), \quad (71)$$

where F_A is the two-nucleon form factor of the nucleus. In the case of the calculation of the nuclear shadowing phenomenon, it is sufficient to have F_A in the non-relativistic limit:

$$F_A(\Delta m_N, q_\perp) = \int d^3k_i \psi_A(k_i) \psi_A^*(k_1 + \vec{q}, k_2 - \vec{q}, k_3, \dots), \quad (72)$$

where $\vec{q} = (\Delta m_N, q_\perp)$. The application of the AGK cutting rules allows one to connect $\Delta^{\text{diff}} F_{2A}(x, Q^2)$ with the shadowing contribution to the nuclear structure function $F_{2A}(x, Q^2)$. The result is

$$\Delta^{\text{diff}} F_{2A}(x, Q^2) = -F_{2A}^{(b)}(x, Q^2), \quad (73)$$

where $F_{2A}^{(b)}(x, Q^2)$ is derived in the nucleus rest frame and is given by Eq. (43).

The main contribution to nuclear shadowing originates from diffraction at small t , which is dominated by non-spin-flip hadron production. The spin-flip contribution is small for $t \sim 0$ (due to the helicity conservation at $t = 0$), becoming important for larger t and leading to the slope of the inelastic diffractive cross section, which is smaller than that of the elastic cross section. Hence, the slope of the non-spin-flip term, B , is likely to be somewhat larger than $B_{\text{diff}} \sim 6 \text{ GeV}^2$, probably closer to the slope of the elastic meson-nucleon cross section, $B \sim 10 \text{ GeV}^2$. One can express the average distance in the transverse plane between the centers of the two nucleons which contribute to nuclear shadowing as

$$\langle (r_{\perp 1} - r_{\perp 2})^2 \rangle = 4B. \quad (74)$$

Therefore, the average transverse distance between the nucleon centers contributing to nuclear shadowing is of the order of 1–1.2 fm, so that the nucleons overlap rather strongly in the transverse plane.

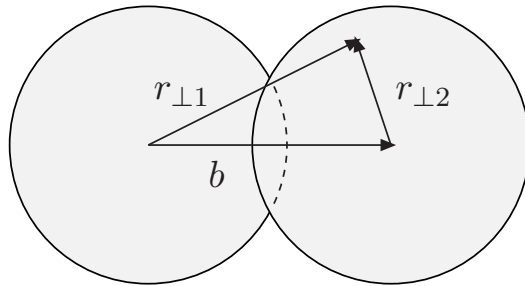


Fig. 13. Geometry of the parton overlap in the transverse plane.

As Bjorken x is decreased, the strength of the interaction increases, and an increasing number of nucleons screen each other within the cylinder of the radius of $\sim \sqrt{2B} \approx 0.9$ fm (although this radius should slowly increase with decreasing x for $x \leq 10^{-3}$, the current data does not find a significant change of the slope in the HERA range of energies). Therefore, a transverse slice of the wave function of a heavy nucleus for $x \sim 5 \times 10^{-3}$ looks like as a system of colorless (white) clusters with some clusters ($\sim 30\%$ – cf. a numerical study below) built of two rather than of one nucleon, with a gradual increase of the number of two-nucleon, three-nucleon, etc. clusters with decreasing x .

The microscopic picture of nuclear shadowing described above allows one to address also the question of at what transverse distances from the centers of two nucleons, $\rho_1 = r_{\perp 1}$ and $\rho_2 = r_{\perp 2}$, for a given transverse internucleon distance, b , shadowing occurs, see Fig. 13. First we observe that experimentally the t dependence of inclusive diffraction and deeply virtual Compton scattering (DVCS) for similar values of x and Q^2 are very close, $B_{\text{DVCS}} = 6.02 \pm 0.35 \pm 0.39$ GeV $^{-2}$ in the H1 2005 analysis [140] and $B_{\text{DVCS}} = 5.45 \pm 0.19 \pm 0.34$ GeV $^{-2}$ in the H1 2007 analysis [141], so that $|B_{\text{DVCS}} - B| < 2$ GeV $^{-2}$. This implies that the parton removed from the initial nucleon and the parton in the final nucleon are located at very close impact parameters. As a result, the screening effect occurs very locally in the transverse plane, mostly in the region along the axis between the two nucleons. If we neglect the small difference between the slopes of DVCS and diffraction, we obtain:

$$f(b) = \int p(r_{\perp 1}) p(r_{\perp 2}) \delta(r_{\perp 1} - r_{\perp 2} - b) d^2 r_{\perp 1} d^2 r_{\perp 2}, \quad (75)$$

where $f(b)$ is the Fourier transform of the t dependence of the diffractive cross section; $p(r_{\perp i})$ are transverse distributions of partons.

In our derivations, the global and local color neutrality are satisfied at every step. This is very different from the approaches where the nucleus is initially built from free quarks and the color neutrality is achieved by imposing additional conditions at a later stage.

3.3 On nuclear shadowing of valence quark parton distributions

In this subsection we discuss nuclear shadowing effects in the parton distributions in the channels with non-vacuum quantum numbers in the crossed channel, like the structure function $F_{3A}(x, Q^2)$ which could be measured for example in the $\nu(\bar{\nu})A$ scattering.

In the case of soft QCD dynamics, the shadowing of cross sections with non-vacuum quantum numbers in the crossed channel is significantly stronger than in the vacuum channel. Indeed, let us consider the difference of the scattering cross sections of a particle h ($h = p, K, \dots$) and its antiparticle \bar{h} off a nucleus, $\Delta\sigma_{hA} = \sigma_{hA} - \sigma_{\bar{h}A}$. It is straightforward to derive within the eikonal approximation [81,142] (neglecting inelastic screening effects):

$$\Delta\sigma_{hA} = \Delta\sigma_{hN} \int d^2b AT_A(b) e^{-A/2\langle\sigma\rangle T_A(b)}. \quad (76)$$

Here we introduced the notation $\langle\sigma\rangle = (\sigma_{hA} + \sigma_{\bar{h}A})/2$ and took the limit $\Delta\sigma_{hA} \ll \langle\sigma\rangle$. It is easy to see from Eq. (76) that the shadowing for $\Delta\sigma_{hA}$ is much larger than for the total cross sections of hA scattering, see also Fig. 14. The physical reason for the enhancement of shadowing in the non-vacuum channel is that scattering at small impact parameters does not contribute to the difference since the interaction is essentially black (i.e., equal) for small $|\vec{b}|$. In terms of the Gribov Reggeon Calculus, the reason is that for the $\mathbb{R} - n\mathbb{P}$ exchange, the factor $1/n!$ is changed to $1/(n-1)!$ since only $n-1$ exchanges are identical.

A qualitative difference of the nuclear shadowing in the LT limit from that in soft QCD is that in the former case the masses produced by a current, which typically contribute to shadowing, are at least of the order of Q^2 and increasing with energy. Moreover, the spectrum of masses produced in the valence and vacuum channels are vastly different. For the non-vacuum channel, $N(z) = (d\sigma(z)/dz)/\sigma \propto (1-z)^n$ with $n \geq 0$ in difference from the vacuum exchange where $n \sim -1$. (Here z is the fraction of nucleon momentum carried by the interacting parton.) Thus, shadowing given by the overlapping integral between the diffractive amplitudes in the non-vacuum and vacuum channels should be suppressed.

As we discussed in Sec. 3.2 only the final states, where a small momentum is transferred to the target nucleon of the nucleus, can contribute to shadowing. Only in this case an effective interference between scattering off one nucleon in the $|in\rangle$ state and another nucleon in the $\langle out|$ state is possible. In the infinite momentum frame this corresponds to the requirement that $1-z \leq 0.03$. This is because in the case of the removal of a valence quark, one expects that $N(z) = (d\sigma(z)/dz)/\sigma \propto (1-z)^n$ with $n \geq 0$.

To estimate the suppression factor for nuclear shadowing of the valence quark distribution we may explore qualitative properties of parton distributions. Although there are no measurements of $N(z)$ for the $e+p \rightarrow e+p+X$ cross section where the electron interacts with a valence quark, we use as a guide the cross section of the process $e+p \rightarrow e+n+X$,

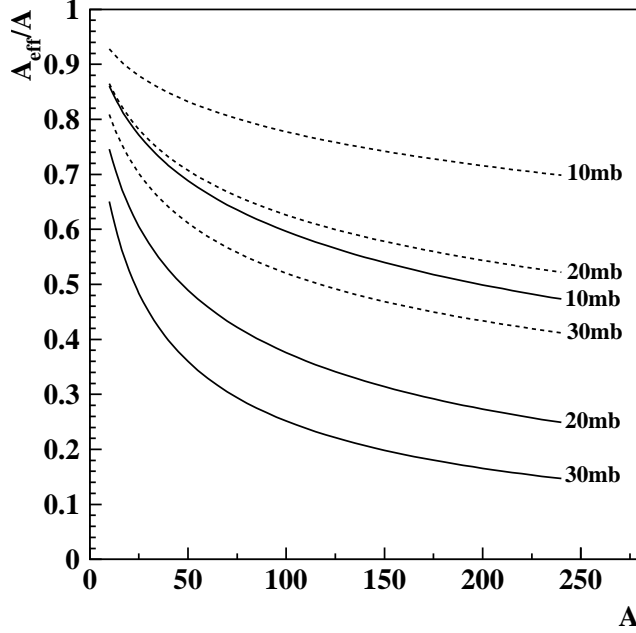


Fig. 14. Comparison of shadowing in the non-vacuum channel (solid curves) and vacuum channel (dashed curves) for different values of $\langle\sigma\rangle$.

which is dominated for small x by the scattering off the sea quarks. The HERA data [143] indicate that the neutron spectrum dN/dz in the ep DIS scattering is nearly constant for $z < 0.80$. For larger z , it drops and the z dependence is consistent with $\propto (1 - z)$ (which corresponds to the QCD quark counting rules). If we assume a similar dN/dz for the valence quark removal case, we find that the ratio of the probability to produce a proton (neutron) in the scattering off a valence quark of the proton (neutron) and the corresponding probability for the scattering off a sea quark, $r_{v/s}$, is of the order $\sim 10^{-2}$. This estimate does not include an additional small factor due to the contribution of the spin-flip processes to the nucleon spectrum since such a contribution to the shadowing is strongly suppressed by the nuclear overlapping integral. Since we are considering here the interference of the production in the valence and sea channels, the relevant suppression factor for the ratio of LT shadowing in the vacuum and non-vacuum channels is $\sqrt{r_{v/s}}$.

As a result, we obtain an estimate for the suppression of the valence quark shadowing in the double scattering approximation (in the approximation of the interaction with two nucleons of the nuclear target):

$$\frac{1 - V_A/AV_N}{1 - F_{2A}/AF_{2N}} \leq 2\sqrt{r_{v/s}}, \quad (77)$$

where V_A and V_N are the valence quark distributions in the nucleus and nucleon, respectively; the factor of two comes from combinatorics [cf. Eq. (76)]. Thus we conclude that

nuclear shadowing in the valence quark channel (for the double scattering contribution) is strongly suppressed as compared to the sea channel in spite of the combinatorial factor of two.

Therefore, we expect a rather small shadowing for V_A for realistic nuclei ($\leq 10\%$ for $A \sim 200$), though the A dependence of $1 - V_A/(AV_N)$ should be stronger than that for the sea quark distribution due to combinatorial factors similar to the one we discussed in relation to Eq. (76).

At the same time, no such suppression is expected for the higher twist (HT) effects due to transitions to the low mass intermediate states which are not suppressed for $Q^2 \leq 1 \div 2$ GeV²; these contributions would result in an enhanced HT shadowing in the non-vacuum channel. Note also that the HT shadowing may extend to higher x than the leading twist shadowing. Indeed, the characteristic coherence length in the case of the vector meson contribution, $l_c = 2\nu/(Q^2 + m_V^2)$, is somewhat larger than the average $l_c = 2\nu/(Q^2 + M^2)$ for $Q^2 > m_V^2$, where $M^2 \approx Q^2$.

Comment. There exists another example where nuclear shadowing effects in neutrino and electron interactions should be different. Indeed, it follows from the Adler theorem [144] that, in the limit of very small Q^2 ,

$$\frac{\sigma^{\nu+A \rightarrow \mu+X}(E_\nu, Q^2)}{\sigma^{\nu+N \rightarrow \mu+X}(E_\nu, Q^2)} = \frac{\sigma_{\text{tot}}(\pi A)}{\sigma_{\text{tot}}(\pi N)}. \quad (78)$$

Since shadowing for $\sigma_{\text{tot}}(\gamma A)$ is known to be smaller than for $\sigma_{\text{tot}}(\pi A)$ by about $20 \div 30\%$, we conclude that for sufficiently low Q^2 neutrino scattering, the higher twist shadowing in νA scattering is likely to be significantly larger than in the photon case.

3.4 The upper limit on nuclear shadowing in nuclear PDFs

We discussed in Sec. 3.2 that the leading twist shadowing is dominated by the interaction of partons which are located at close impact parameters. In this approximation, the use of the infinite momentum nuclear frame allows one to derive a lower limit for the nuclear PDFs (the maximal value of nuclear shadowing) [145]. Below we sketch the derivation and present the final results.

Our starting point is the observation that nuclear shadowing in the scattering off the deuteron cannot reduce the cross section to the value smaller than the cross section of scattering off one nucleon. This is basically because one nucleon can screen another one, but not itself.

Similarly, it is natural to expect that the gluon density (the quark case can be worked out

similarly) at a given impact parameter b , $g_A(x, b, Q^2)$, cannot be less than the maximum of the gluon densities of the nucleon, $g_N(x, \rho, Q^2)$. Therefore,

$$g_A(x, b, Q^2) \geq \langle \max_{i=1,A} \{g_N^{(i)}(x, r_\perp - b, Q^2)\} \rangle, \quad (79)$$

where $\rho = r_\perp - b$ are the transverse coordinates of partons in the c.m. of the corresponding nucleons, see Fig. 13; the brackets denote taking the average over the nucleon configurations. While at the moment the physical meaning of the impact parameter dependent PDFs $g_A(x, b, Q^2)$ and $g_N(x, \rho, Q^2)$ is intuitively clear, they will be defined and discussed in Sec. 5.5. Those PDFs are nothing else but the generalized parton distributions (GPDs) in the $\xi = 0$ limit in the mixed momentum-coordinate (impact parameter) representation.

In the $A \rightarrow \infty$ limit, at a fixed b there will be at least one nucleon with $\rho = r_\perp - b$ close to zero. Hence, in this limit, Eq. (79) gives:

$$g_A(x, b, Q^2)|_{\min} \geq g_N(x, \rho = 0, Q^2). \quad (80)$$

It is convenient to analyze the gluon GPD of the nucleon in the factorized form, $g_N(x, \rho, Q^2) = g_N(x, Q^2)F_g(x, \rho, Q^2)$, where $g_N(x, Q^2)$ is the usual forward gluon distribution and $F_g(x, \rho, Q^2)$ is the so-called two-gluon form factor defining the skewness of the gluon GPD. The onset of the limiting behavior depends on the transverse shape of the gluon GPD. In Ref. [146], two parameterizations of the two-gluon form factor $F_g(x, \rho, Q^2)$ were discussed and fitted to the J/ψ photoproduction data [147], which were taken in the form of an exponential and a dipole, respectively. The corresponding transverse spatial distributions of the gluon GPD are

$$\begin{aligned} F_g^{(1)}(\vec{\rho}, Q^2) &= \frac{1}{2\pi B_g(Q^2)} e^{-\rho^2/(2B_g(Q^2))}, \\ F_g^{(2)}(\vec{\rho}, Q^2) &= \frac{m_g^2 m_g(Q^2) \rho}{2\pi} K_1(m_g(Q^2) \rho), \end{aligned} \quad (81)$$

where $B_g(Q^2) = 3.24/m_g^2(Q^2)$; K_1 is the modified Bessel function; $m_g^2(Q^2 = 3 \text{ GeV}^2) = 0.6 \text{ GeV}^2$ for $x \sim 10^{-4}$. The average over the nucleon configurations in a nucleus was calculated using the Monte Carlo generator of [145] and taking into account short-range correlations of nucleons (this effect is numerically small for the quantities discussed here).

The described procedure allows one to determine the maximal value of the gluon shadowing at a given b , $R_g(b)$, which is given by the ratio of the lower limit on $g_A(x, b)$ to its value in the impulse approximation, $g_A(x, b) = g_N(x)T_A(b)$:

$$R_g(b) = \frac{g_A(x, b, Q^2)|_{\min}}{g_N(x)T_A(b)}. \quad (82)$$

The results for $R_g(b)$ for ^{16}O and ^{208}Pb and the two models of the gluon GPD of Eq. (81) are presented in Figs. 15 and 16. The dotted curves correspond to the calculation with $F_g^{(1)}(\vec{\rho})$ (Gaussian form); the solid curves correspond to $F_g^{(2)}(\vec{\rho})$ (dipole form). Figure 15 presents $R_g(b)$ as a function of the impact parameter b and plotted for $m_g^2 = 0.6 \text{ GeV}^2$.

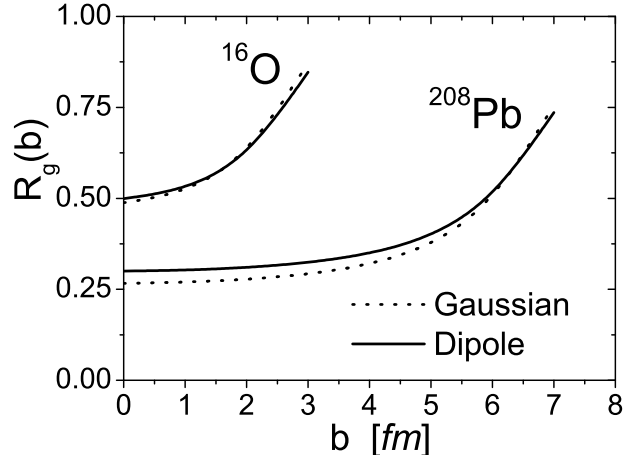


Fig. 15. The maximal value of nuclear shadowing in the gluon channel, $R_g(b)$, see Eq. (82), for ^{16}O and ^{208}Pb calculated using the Gaussian (dotted curves) and dipole (solid curves) forms for the gluon density distribution and correlated configurations. $R_g(b)$ is plotted as a function of the impact parameter b for $m_g^2 = 0.6 \text{ GeV}^2$ corresponding to $x \sim 10^{-4}$ and $Q^2 = 4 \text{ GeV}^2$.

Figure 16 presents $R_g(b)$ as a function of m_g^2 at $b = 0$. [Note that m_g^2 is a parameter in Eq. (82); its variation matches the change of x .]

In the $A \rightarrow \infty$ limit, the results of the two parameterizations differ by $F_g^{(1)}(0)/F_g^{(2)}(0) = 2/3.24 = 0.62$. However, this limit is reached at extremely large $A \gg 10^3$. The reasons for this are a rather small radius of the gluon density in the transverse plane, $r_g^{\text{tr}} \leq 0.5 \text{ fm}$, and low nuclear density, which in combination lead to a small probability for more than three nucleons to significantly screen each other up to very large A .

It is important to point out that the results of our calculations of nuclear shadowing in the impact parameter dependent nuclear gluon PDF discussed in Sec. 5.5 are consistent with the upper limit on nuclear shadowing, $R_g(b)$, discussed in this subsection and presented in Figs. 15 and 16. Indeed, at $Q^2 \sim 4 \text{ GeV}^2$ and for $x \sim 10^{-4}$, where $m_g^2 \sim 0.6 \text{ GeV}^2$, the limit for ^{208}Pb from Fig. 15 is $R_g(x = 10^{-4}, b = 0) \geq 0.3$. At the same time, our calculation for ^{208}Pb in the framework of the leading twist theory of nuclear shadowing predicts for $x = 10^{-4}$ and $b = 0$ that $g_A(x, b, Q^2)/[AT_A(b)g_N(x, Q^2)] = 0.33$ (FGS10_H) and $g_A(x, b, Q^2)/[AT_A(b)g_N(x, Q^2)] = 0.51$ (FGS10_L), see Fig. 41.

The discussed results give another illustration of the observation that realistic nuclei can

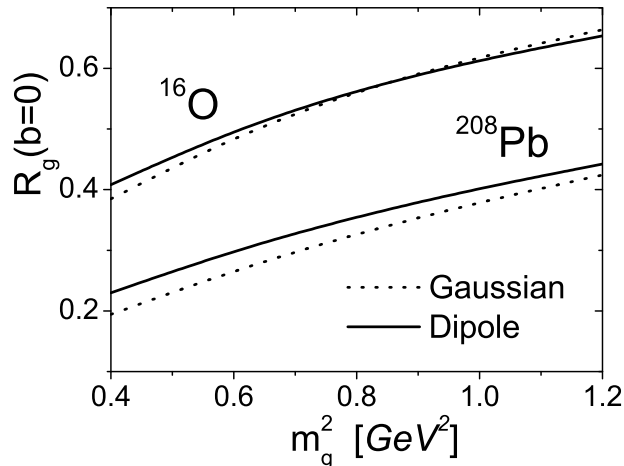


Fig. 16. $R_g(b)$ as a function of m_g^2 at $b = 0$. For the details, see the caption of Fig. 15.

be treated as rather dilute systems in the processes involving nuclear shadowing with large fluctuations of the number of involved nucleons, even at small impact parameters.

3.5 Diffraction in DIS and the QCD factorization theorem

3.5.1 Nucleon fragmentation in DIS

In DIS a struck parton is removed from the nucleon and moves with a large momentum relative to the spectator system. The struck parton and spectator system fragment into separate groups of hadrons. (Hadrons at the central rapidities may belong to either of the groups.) It is convenient to consider the process in the Breit frame where the nucleon momentum $P \rightarrow \infty$ and the photon momentum is aligned along the same axis: $\vec{q} = -2x\vec{P}$ and $q_\mu = 0$ for all other components. In the parton model approximation, the final quark flies with the momentum $-xP$ in the opposite direction with respect to the residual system that carries the momentum $(1-x)P$. As a result, a hadron in the target fragmentation region can be produced with the maximal light-cone fraction z relative to the incident nucleon: $z \leq (1-x)$. For large $x \geq 0.1$, the process corresponds to the removal of the valence quark from the nucleon and creation of a color flow between the current and target fragmentation regions. As a result, for such x , the distribution in the variable $x_F = z/(1-x)$ should go to zero at the kinematic limit $x_F \rightarrow 1$ [123,139]. (This kinematic limit follows from the requirement that the minus component of the four momentum of the system X should be positive. The actual dependence on x_F follows from details of the QCD dynamics and is often parameterized in terms of quark counting rules.) With a decrease of x , the dynamics changes; hence, the shape of the distribution $z(x_F)$ should

depend on x .

3.5.2 Diffractive structure functions and diffractive PDFs

Most of the HERA experimental studies were performed at small x . In this case, one often uses the variable $x_P = 1 - z$. The cross section for the process $ep \rightarrow e + p + X$ (or production of any other hadron), see Fig. 17, is usually parameterized in the following form:

$$\frac{d^4\sigma_{ep}^D}{dx_P dt dx dQ^2} = \frac{2\pi\alpha^2}{xQ^4} \left[(1 + (1 - y)^2) F_2^{D(4)}(x, Q^2, x_P, t) - y^2 F_L^{D(4)}(x, Q^2, x_P, t) \right], \quad (83)$$

where Q^2 is the virtuality of the exchanged photon; $x = Q^2/(2p \cdot q)$ is the Bjorken variable; $y = (p \cdot q)/(p \cdot k)$ is the fractional energy loss of the incoming lepton. We follow here the

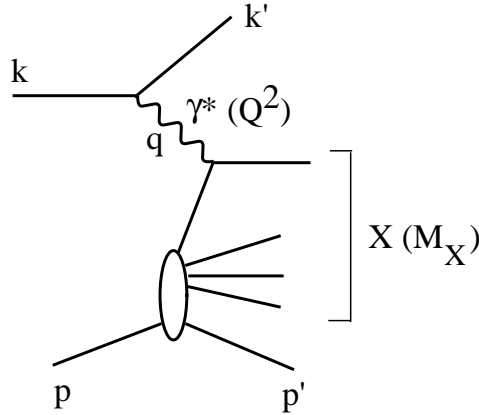


Fig. 17. Diffractive production of a hadron with momentum p' in the nucleon fragmentation region in DIS.

notations commonly used for the description of phenomena in the small x kinematics; in order to emphasize the role of small x_P processes, one introduces the superscript " D " denoting $F_2^{D(4)}$ and $F_L^{D(4)}$ as the diffractive structure functions (the superscript " (4) " denotes that the structure functions depend on four variables). (Note that in the case of generic x and z , these quantities are often referred to as fracture functions [148].) The variables x_P and t are expressed through the experimentally measured quantities:

$$\begin{aligned} t &= (p' - p)^2, \\ x_P &= \frac{q \cdot (p - p')}{q \cdot p} \approx \frac{M_X^2 + Q^2}{W^2 + Q^2}, \\ \beta &= \frac{Q^2}{2q \cdot (p - p')} = \frac{x}{x_P} \approx \frac{Q^2}{Q^2 + M_X^2}, \end{aligned} \quad (84)$$

where M_X is the invariant mass of the produced final state; W^2 is the invariant mass squared of the γ^*p system (see Fig.17). The variable $x_{\mathcal{P}}$ describes the fractional loss of the proton longitudinal momentum; we also defined here β which is the longitudinal momentum fraction with respect to $x_{\mathcal{P}}$ carried by the interacting parton (to the leading order in α_s). Note that the contribution of the term proportional to $F_L^{D(4)}$ in Eq. (83) is kinematically suppressed and usually neglected in the analysis of diffraction.

In pQCD a parton with a virtuality Q_0^2 is resolved at higher Q^2 leading to the scaling violations. If a parton at the resolution scale (x, Q^2) is removed, the final state in the fragmentation region will be changed as compared to the removal of a parent parton at the scale (x_0, Q_0^2) . The difference is due to the emission of partons in the evolution process and fragmentation of the struck quark. However, partons produced in the hard process of the evolution from scale Q_0 to scale Q have the transverse momenta $\geq Q_0$ and, hence, their overlapping integral with a low p_t and finite z hadron is suppressed by a power of Q_0^2 [121]. The quark-gluon system produced in the hard interaction is well localized in the transverse directions and, hence, should interact with the target in the same way as the parton at (x_0, Q_0^2) . As a result, the Q^2 evolution of the fragmentation functions for fixed t and z is given by the same DGLAP equations as those for the nucleon PDFs [59,121]. This result follows from the fact that QCD evolution occurs in both cases off a single parton. The kinematical window appropriate for the onset of the applicability of the QCD factorization theorem depends on the interplay between z and x : (i) the selection of smaller x increases the contribution of higher-twist effects, and (ii) the products of the hard parton fragmentation tend to fill the rapidity gap between the photon and target fragmentation regions, especially in the case when this parton carries a small fraction z of the photon momentum. Thus, larger Q_0 is necessary to suppress the both effects.

Similarly to the inclusive case, the factorization theorem for diffraction (production of a hadron with fixed z and t) in DIS states that, at given fixed t and $x_{\mathcal{P}}$ and in the leading twist approximation, the diffractive structure function $F_2^{D(4)}$ is given by the convolution of the same hard scattering coefficient functions C_j with universal diffractive parton distributions $f_j^{D(4)}$:

$$F_2^{D(4)}(x, Q^2, x_{\mathcal{P}}, t) = \beta \sum_{j=q,\bar{q},g} \int_{\beta}^1 \frac{dy}{y} C_j\left(\frac{\beta}{y}, Q^2\right) f_j^{D(4)}(y, Q^2, x_{\mathcal{P}}, t), \quad (85)$$

where $\beta = x/x_{\mathcal{P}}$. The diffractive PDFs $f_j^{D(4)}$ are conditional probabilities to find a parton of flavor j with a light-cone fraction β in the proton that undergoes diffractive scattering characterized by the longitudinal momentum fraction $x_{\mathcal{P}}$ and the momentum transfer t , see Sec. 3.5 and 3.6 for details.

3.5.3 Diffractive dynamics in DIS

DIS at finite x creates a color flow between the current and target fragmentation regions leading to a strong break-up of the nucleon since a typical nucleon carries a relatively small light-cone fraction of the initial nucleon momentum (remember that $z > 1 - x$ is kinematically forbidden in this case). Hence, the HERA observation of the significant diffraction in DIS at small x came as a surprise to the theorists not used to the small x dynamics since pQCD and the confinement of color do not allow rapidity gaps.

The key to resolving this puzzle has been provided long time ago by the aligned jet model (AJM) [122]. The model was proposed to address the Gribov paradox consisting in the observation that if all configurations in the virtual photon wave function interacted with large hadronic strengths with nuclei, the Bjorken scaling would be grossly violated at small x . Bjorken has demonstrated that if one follows the spirit of the parton model and allows only the interactions of the partons with small k_t , the scaling is restored. The dominant configurations in the photon wave function are the $q\bar{q}$ pairs with the invariant masses of the order of Q^2 and transverse momenta k_{soft} . In the rest frame of the target, the partons carry the momenta $p_1 \sim q_0$ and $p_2 = k_{\text{soft}}^2/(2xm_N)$. In coordinate space, the process proceeds as follows: γ^* transforms into a $q\bar{q}$ pair with the momenta $\pm k_{\text{soft}}$ at a large distance $1/(2m_N x)$ from the target. After covering this distance to the target, the $q\bar{q}$ pair has the transverse separation which is of the order of $1/k_{\text{soft}}$ and the system can interact with the typical hadronic strength.

In QCD one needs to modify the AJM to account for two effects [81]. One is the Sudakov form factor: γ^* cannot transform into a $q\bar{q}$ pair with small k_t without gluon radiation. This effect is taken into account by the pQCD evolution (change of x of the parton). It does not change the transverse size of the system and, as a result, the system interacts with the same strength at large Q^2 . The second modification is the presence of large k_t configurations that have small transverse sizes. Their interaction is suppressed by the factor $\alpha_s(k_t)^2/k_t^2$ —the color transparency effect. However, due to a large phase volume, these configurations give a contribution comparable to that of the AJM. (The estimate of [81,82] suggested that the AJM contributes about 70% to $F_{2p}(x \sim 10^{-2}, Q_0^2 \sim 2 \div 3 \text{ GeV}^2)$.)

While diffraction for the AJM configurations is expected to be comparable to that of hadrons, it is strongly suppressed for small size configurations for moderate $x > 10^{-3}$ since the strength of the interaction enters quadratically in the diffractive cross section.

The dominance of the AJM configurations leads to the expectation that the W dependence of diffraction at fixed Q^2 and M_X^2 should be close to that for soft processes [138]. Another important contribution to diffraction is due to large size color octet dipoles ($q\bar{q}g$ configurations in the virtual photon). These predictions are in a good agreement with the current HERA data, see below.

It is also instructive to consider diffraction in the Breit frame. It is easy to see that

the AJM contribution corresponds to the following process: a parton with the light-cone fraction x absorbs γ^* and turns around so that it has the momentum $(xP, -xP)$. To produce a color neutral system with the typical mass squared $M_X^2 \approx Q^2$, it has to pick up a parton with the momentum $(x'P, x'P)$ leading to $M_X^2 = Q^2(x'/x)$ and pull it out of the nucleon. This implies that although the diffraction involves the absorption of γ^* by one parton, it requires the presence of a strong short-range correlation in rapidity between the partons in the nucleon light-cone wave function [138]. A nearly hadron-level strength of the diffraction indicates that a strong color screening takes place in the proton wave function for small x *locally* in x (in rapidity $\Delta Y = \ln x'/x$).

3.6 Summary of QCD analysis of the data on hard diffraction at HERA

3.6.1 Diffractive structure function $F_2^{D(3)}$

The bulk of the data on diffraction in DIS at HERA comes from inclusive measurements performed by H1 and ZEUS collaborations [60–73]. When the t dependence of the diffractive cross section is not measured [60,61,67,71,73], the data are analyzed in terms of the diffractive structure function $F_2^{D(3)}$:

$$F_2^{D(3)}(x, Q^2, x_P) = \int_{-1 \text{ GeV}^2}^{t_{\min}} dt F_2^{D(4)}(x, Q^2, x_P, t), \quad (86)$$

where $F_2^{D(4)}$ is defined by Eq. (83); $t_{\min} = -m_N^2 x_P^2 / (1 - x_P) \approx -m_N^2 x^2 (1 + M_X^2 / Q^2)^2$ with m_N the nucleon mass.

The weak (logarithmic) Q^2 dependence of $F_2^{D(3)}$, which follows from the QCD evolution equations for diffractive PDFs, was observed experimentally, see, e.g., Fig. 21 below.

As we discussed above the diffractive structure function $F_2^{D(3)}$ is given in terms of the diffractive PDFs $f_j^{D(3)}$:

$$F_2^{D(3)}(x, Q^2, x_P) = \beta \sum_{j=q,\bar{q},g} \int_{\beta}^1 \frac{dy}{y} C_j\left(\frac{\beta}{y}, Q^2\right) f_j^{D(3)}(y, Q^2, x_P). \quad (87)$$

Extensive studies of hard inclusive diffraction at HERA were performed both by H1 and ZEUS collaborations [60–73]. Within the normalization uncertainties, the measurements of the two collaborations are in good agreement, see, e.g., the comparison in Ref. [72].

It was suggested in [149] that diffraction in hard process can be treated as scattering off a t -channel exchange—Pomeron—which has the same properties for different x_P . We have

argued above that the dominant source of the diffraction in DIS is the AJM-like configurations in the virtual photon. In a wide energy range, these hadron-like configurations should interact through a coupling to a soft ladder. The properties of such a ladder (or a multiladder system), which are local in rapidity, should weakly depend on its length in rapidity proportional to $\ln(x_0/x_{\mathcal{P}})$, where $x_0 \sim 0.01$.

In line with the suggestion of [149], the QCD analyses of the HERA diffractive data make an additional *soft / Regge factorization* assumption (which does not contradict the data) that DPDFs $f_j^{D(3)}$ can be presented as a sum of the leading Pomeron-exchange term and the subleading Reggeon-exchange term (the latter plays a role only at large $x_{\mathcal{P}}$). Each of the terms is given as the product of the corresponding flux factors and the parton distribution functions,

$$f_j^{D(3)}(\beta, Q^2, x_{\mathcal{P}}) = f_{\mathcal{P}/p}(x_{\mathcal{P}})f_{j/\mathcal{P}}(\beta, Q^2) + n_{\mathcal{R}}f_{\mathcal{R}/p}(x_{\mathcal{P}})f_{j/\mathcal{R}}(\beta, Q^2), \quad (88)$$

where $f_{\mathcal{P}/p}(x_{\mathcal{P}})$ is the Pomeron flux factor; $f_{\mathcal{R}/p}$ is the Reggeon flux factor; $f_{j/\mathcal{P}}(\beta, Q^2)$ can be interpreted as the PDF of flavor j of the Pomeron; $f_{j/\mathcal{R}}(\beta, Q^2)$ are PDFs of the subleading Reggeon; $n_{\mathcal{R}}$ is a small free parameter determined from the fit to the data. The Q^2 dependence of $f_{j/\mathcal{P}}(\beta, Q^2)$ is given by the DGLAP evolution equations.

Note that Eq. (88) does not follow from the QCD factorization theorem, but it is rather a hypothesis of the soft matching to the non-perturbative QCD, which is supported by the data (see the discussion below).

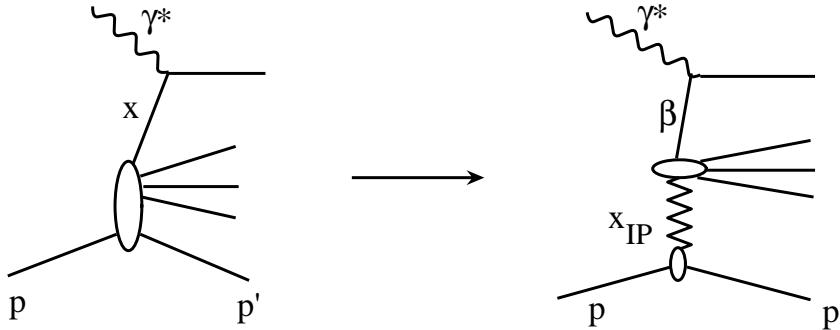


Fig. 18. A schematic representation of the factorization of the diffractive PDFs into the product of the Pomeron or Reggeon flux factor and the corresponding PDFs, see Eq. (88).

The schematic view of the separation of $f_j^{D(3)}$ into the flux factors and the corresponding PDFs used in Eq. (88) is presented in Fig. 18. The figure also illustrates the physical interpretation of the variable β : β is the light-cone fraction of the Pomeron (or Reggeon) momentum carried by the interacting parton.

It is important to emphasize that the words "Pomeron" and "Reggeon" are used in the analysis of the hard diffraction in DIS only as bookkeeping terms since those terms are

reserved for soft hadron-hadron interactions. The parameters (intercepts, slopes, etc.) of the Pomeron and Reggeon exchanges as determined from the phenomenology of soft hadron-hadron interactions may differ from the parameters obtained from the fits to the hard diffractive data at HERA.

In Eq. (88), the Pomeron and Reggeon flux factors have the following form:

$$\begin{aligned}
f_{\mathbb{P}/p}(x_{\mathbb{P}}) &= \int_{-1 \text{ GeV}^2}^{t_{\min}} dt A_{\mathbb{P}} \frac{e^{B_{\mathbb{P}}t}}{x_{\mathbb{P}}^{2\alpha_{\mathbb{P}}(t)-1}}, & \alpha_{\mathbb{P}}(t) &= \alpha_{\mathbb{P}}(0) + \alpha'_{\mathbb{P}}t, \\
f_{\mathbb{R}/p}(x_{\mathbb{P}}) &= \int_{-1 \text{ GeV}^2}^{t_{\min}} dt A_{\mathbb{R}} \frac{e^{B_{\mathbb{R}}t}}{x_{\mathbb{P}}^{2\alpha_{\mathbb{R}}(t)-1}}, & \alpha_{\mathbb{R}}(t) &= \alpha_{\mathbb{R}}(0) + \alpha'_{\mathbb{R}}t.
\end{aligned} \tag{89}$$

In the following, we concentrate on the result of the QCD analysis of the hard inclusive diffraction at HERA by the H1 collaboration [61,62] since we used the H1 Fit B as an input for our calculations of nuclear shadowing (the QCD analysis of hard diffraction by the ZEUS collaboration will be discussed in the end of this subsection).

The H1 QCD fit gives $B_{\mathbb{P}} = 5.5 \text{ GeV}^{-2}$; $\alpha'_{\mathbb{P}} = 0.06 \text{ GeV}^{-2}$; $B_{\mathbb{R}} = 1.6 \text{ GeV}^{-2}$; $\alpha_{\mathbb{R}}(0) = 0.5$; $\alpha'_{\mathbb{R}} = 0.3 \text{ GeV}^{-2}$. The coefficients $A_{\mathbb{P}}$ and $A_{\mathbb{R}}$ are found from the conditions $x_{\mathbb{P}}f_{\mathbb{P}/p}(x_{\mathbb{P}}) = 1$ and $x_{\mathbb{P}}f_{\mathbb{R}/p}(x_{\mathbb{P}}) = 1$ at $x_{\mathbb{P}} = 0.003$. The intercept of the Pomeron trajectory, $\alpha_{\mathbb{P}}(0)$, is a free parameter of the fit to the data.

The fit to the HERA data on hard diffraction in DIS is carried out as follows. One assumes a particular shape of $f_{j/\mathbb{P}}$ at a certain value of $Q^2 = Q_0^2$ ($Q_0^2 = 1.75 - 2.5 \text{ GeV}^2$),

$$\beta f_{j/\mathbb{P}}(\beta, Q_0^2) = A_j \beta^{B_j} (1 - \beta)^{C_j}, \tag{90}$$

where A_j , B_j and C_j are free parameters. Since the Pomeron exchange is a flavor-singlet, it is assumed that $f_{u/\mathbb{P}} = f_{\bar{u}/\mathbb{P}} = f_{d/\mathbb{P}} = f_{\bar{d}/\mathbb{P}} = f_{s/\mathbb{P}} = f_{\bar{s}/\mathbb{P}}$. The theoretical prediction for the diffractive structure function $F_2^{D(3)}$ at given x , Q^2 and $x_{\mathbb{P}}$ is obtained using Eqs. (87), (88), (89) and (90). The χ^2 fit to the experimental values of $F_2^{D(3)}$ determines the free parameters of the fit: $n_{\mathbb{R}}$, $\alpha_{\mathbb{P}}(0)$, A_j , B_j and C_j .

The 2006 H1 data on diffraction in $ep \rightarrow eXY$ DIS (Y denotes products of the proton dissociation) [61,62] covers the following kinematics: $3.5 \leq Q^2 < 1600 \text{ GeV}^2$, $0.0003 < x_{\mathbb{P}} < 0.03$, $0.0017 < \beta < 0.8$, $|t| < 1 \text{ GeV}^2$. Since the diffractive events were reconstructed using the rapidity gap selection method, the proton was allowed to dissociate into states with a low invariant mass, $M_Y < 1.6 \text{ GeV}$. In order to avoid the kinematic regions which are most likely to be influenced by higher twist contributions, only the data with $Q^2 \geq 8.5 \text{ GeV}^2$ and $M_X^2 > 2 \text{ GeV}^2$ were included in the QCD analysis (fit).

The results of the H1 QCD fit in terms of the diffractive quark and gluon PDFs, $f_{u/\mathcal{P}}(\beta, Q^2)$ and $f_{g/\mathcal{P}}(\beta, Q^2)$, at $Q^2 = 2.5 \text{ GeV}^2$ as functions of β are presented in Fig. 19. The solid curves correspond to fit B; the dotted curves correspond to fit A. The difference between fits A and B is that while the parameters A_j , B_j and C_j in Eq. (90) are free in fit A, $C_g = 0$ for the gluon PDF in Fit B.

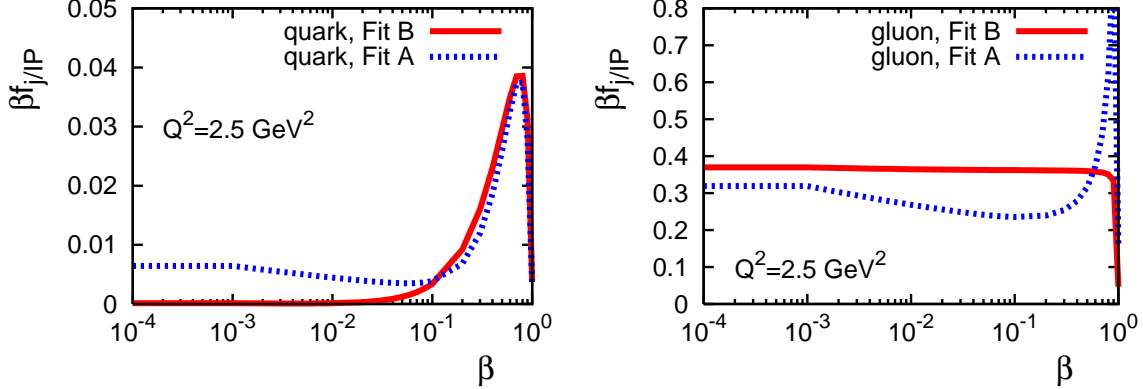


Fig. 19. The diffractive quark and gluon PDFs $f_{j/\mathcal{P}}(\beta, Q^2)$ at $Q^2 = 2.5 \text{ GeV}^2$ as functions of β .

The need to have two types of fits is explained by the fact that the gluon diffractive PDF is determined from the scaling violations of $F_2^{D(3)}$. However, at large β , the scaling violations of $F_2^{D(3)}$ are predominantly determined by the quark diffractive PDFs. Therefore, the gluon diffractive PDF at large β is very weakly constrained by the data, which allows one (requires) to consider two scenarios (fits A and B) of the gluon diffractive PDFs with a different behavior in the large- β limit, see the right panel of Fig. 19.

Note that the large support of the diffractive PDFs at large β means that the diffraction is enhanced in the $M_X^2/Q^2 \sim 1$ region, resulting in a smaller relative contribution of the triple Pomeron contribution to diffraction, see Sec. 5.1.3.

One should mention that both fits A and B correspond to very similar values of $\alpha_{\mathcal{P}}(0)$ and $n_{\mathcal{R}}$:

$$\begin{aligned} \text{Fit A : } \alpha_{\mathcal{P}}(0) &= 1.118 \pm 0.008, & n_{\mathcal{R}} &= (1.7 \pm 0.4) \times 10^{-3}, \\ \text{Fit B : } \alpha_{\mathcal{P}}(0) &= 1.111 \pm 0.005, & n_{\mathcal{R}} &= (1.4 \pm 0.4) \times 10^{-3}. \end{aligned} \quad (91)$$

It is important to note that these values of the Pomeron intercept $\alpha_{\mathcal{P}}(0)$ are very close to the one observed for soft hadron-hadron interactions, $\alpha_{\mathcal{P}}(0) = 1.0808$ [131]. As we explained in Sec. 3.1, this justifies the use of the color fluctuation approximation for the interaction with three and more nucleons of the nuclear target.

As seen from Fig. 19, the gluon diffractive PDF is much larger than the quark one. We shall later show that this will lead to the prediction that the leading twist nuclear shadowing

for the gluon nuclear PDF is larger than that for the quark nuclear PDFs.

In the analyses [61,62], the PDFs of the subleading Reggeon exchange, $f_{j/R}$, are taken to be those of the pion [150]. The β and Q^2 dependence of $f_{j/R}(\beta, Q^2)$ are given by the fit to the $\pi N \rightarrow J/\Psi X$ and $\pi N \rightarrow \mu^+ \mu^- X$ data.

Both fits A and B provide a good description of the H1 data on hard inclusive diffraction in DIS over the entire kinematic range [61]. The subleading Reggeon contribution is required only at the large- x_P end of the covered range: $x_P > 0.01$. An example of the good agreement between the H1 data [61] and its perturbative QCD description is presented in Fig. 20 (taken from Ref. [61]). The figure shows the reduced cross section multiplied by x_P , $x_P \sigma_r^{D(3)} \approx x_P F_2^{D(3)}$, as a function of β at fixed $x_P = 0.001$ for a wide range of Q^2 . The solid curves correspond to fit A in the kinematic region used in the fit, $Q^2 > 8.5 \text{ GeV}^2$ and $\beta < 0.8$. The dotted curves correspond to the extrapolation of fit A beyond the kinematic region used in the fit. As one can see from Fig. 20, the QCD fits provide not

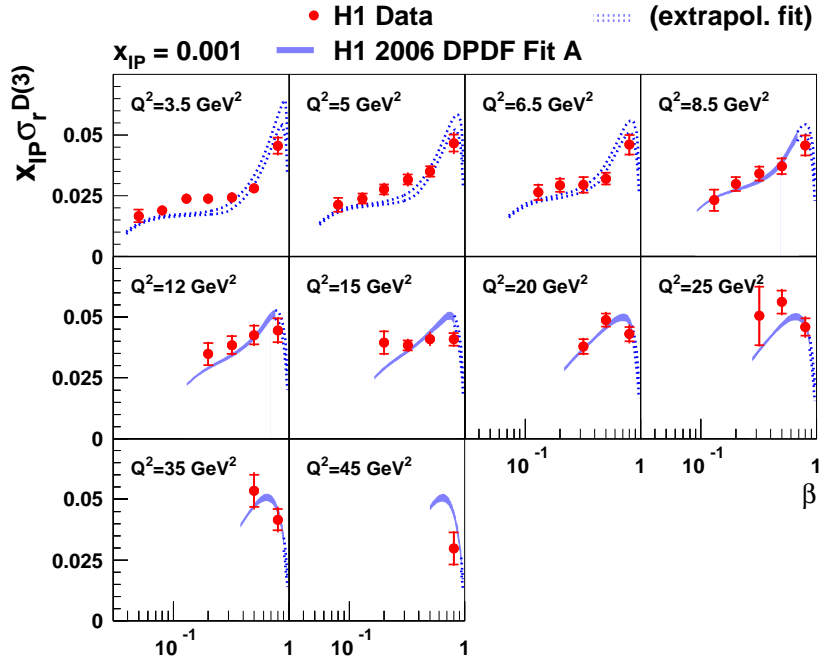


Fig. 20. The perturbative QCD description of the H1 LRG diffractive data on $x_P \sigma_r^{D(3)} \approx x_P F_2^{D(3)}$. The figure is from Ref. [61]. Reproduced with the kind permission of the H1 Collaboration and Springer.

only a good description of the data used in the fit ($Q^2 \geq 8.5 \text{ GeV}^2$), but also of the H1 data with $Q^2 < 8.5 \text{ GeV}^2$ that were not used in the QCD fit.

One should note that the pattern of the scaling violations at large β presented in Fig. 20 is opposite to that of the inclusive structure function $F_2(x, Q^2)$: it is a consequence of the large gluon diffractive PDF.

Besides the diffractive PDFs obtained by the H1 collaboration that we have just discussed, the ZEUS collaboration performed the next-to-leading order QCD analysis [73] of their own data on inclusive diffraction in DIS [72]. As a result, several sets of diffractive PDFs were obtained using essentially the same method as we discussed above. The resulting diffractive PDFs describe well the ZEUS data sample for $Q^2 > 5 \text{ GeV}^2$ (only this part of the data was used in the QCD analysis). For $Q^2 < 5 \text{ GeV}^2$, the predictions are extrapolated and underestimate the data.

In addition, the ZEUS collaboration performed a QCD fit using both the inclusive diffractive and diffractive dijet data [70]. An explicit comparison of the predictions of this fit to the H1 fit B shows that while both fits are consistent with each other and the ZEUS data on $x_{\mathcal{P}}\sigma_r^{D(3)}$, the normalization of the predictions of the H1 fit B is somewhat smaller than that of the ZEUS fit [73].

One should also mention that the value of $\alpha_{\mathcal{P}}(0)$ at low virtualities Q^2 obtained by the H1 and ZEUS analyses are very close: the H1 value of $\alpha_{\mathcal{P}}(0)$ in Eq. (91) should be compared to $\alpha_{\mathcal{P}}(0) = 1.11 - 1.12 \pm 0.02$ obtained by ZEUS [73].

3.6.2 Diffractive structure function $F_2^{D(4)}$

The measurement of the t dependence of hard inclusive diffraction and the structure function $F_2^{D(4)}$ can be performed by detecting the final state proton. This was done using the forward proton spectrometer (FPS) by the H1 collaboration [62] and the leading proton spectrometer (LPS) by the ZEUS collaboration [72]. In the following, we focus on the H1 results since we used the H1 Fit B as an input for our calculations of nuclear shadowing.

In the kinematic range $2 < Q^2 < 50 \text{ GeV}^2$ and $x_{\mathcal{P}} < 0.02$, the t dependence of $F_2^{D(4)}$ was parameterized in a simple exponential form with a constant slope,

$$F_2^{D(4)}(x, Q^2, x_{\mathcal{P}}, t) = e^{B_{\text{diff}}(t-t_{\text{min}})} F_2^{D(4)}(x, Q^2, x_{\mathcal{P}}, t_{\text{min}}), \quad (92)$$

where $B_{\text{diff}} \approx 6 \text{ GeV}^{-2}$ [62]. Note that this value is somewhat lower (but still consistent) than the ZEUS LPS result, $B_{\text{diff}} = 7.0 \pm 0.3 \text{ GeV}^{-2}$ [72].

After the integration over t , the FPS data on $\sigma_r^{D(3)}$ [62] can be compared to the LRG data [61]. A point-by-point comparison shows that

$$\frac{\sigma_r^{D(3)}(\text{LRG})}{\sigma_r^{D(3)}(\text{FPS})} = 1.23 \pm 0.03 (\text{stat.}) \pm 0.16 (\text{syst.}). \quad (93)$$

Equation (93) is interpreted as that the excess of events in the LRG method compared to

the FPS method must come from the proton dissociation into the states with the invariant mass $M_Y < 1.6$ GeV.

The FPS method also allows one to find the relation between the sub-leading cross sections obtained in the two methods:

$$\frac{n_{\mathcal{R}}(\text{LRG})}{n_{\mathcal{R}}(\text{FPS})} = 1.39 \pm 0.48 (\text{exp.}) \pm 0.29 (\text{model}). \quad (94)$$

Equations (93) and (94) mean that the QCD prediction for the diffractive structure function $F_2^{D(3)}$, which would be consistent with the H1 FPS data [62], is obtained by scaling down fits A and B for the Pomeron PDFs by the factor 1.23 and the constant $n_{\mathcal{R}}$ by the factor 1.39. This is illustrated in Fig. 21 (taken from Ref. [62]), where the scaled QCD predictions are compared to the H1 FPS data. The solid curves correspond to fit A in the kinematic region used in the fit (see comments for Fig. 20); the dashed curves correspond to fit A extrapolated beyond the kinematic region used in the fit; the dotted curves correspond to the Pomeron contribution only. Since the FPS data extend to larger values of $x_{\mathcal{P}}$, Figure 21 clearly indicates the need for the sub-leading Reggeon contribution for $x_{\mathcal{P}} > 0.01$.

3.6.3 Tests of the QCD factorization using other diffractive DIS processes

The diffractive parton distributions (DPDFs) $f_j^{D(4)}$ are process-independent universal quantities that enter the pQCD description of such diffractive processes as inclusive DIS diffraction [60–62,66,67,69,71–73], diffractive electroproduction of jets [63,64,70], diffractive photoproduction of jets [64,151,152], diffractive electroproductions of heavy quarks [65,153], and diffractive photoproduction of heavy quarks [154]. The Q^2 dependence of $f_j^{D(4)}$ is given by the DGLAP equations with the same splitting functions as in the case of inclusive DIS. Hence, a wide range of processes (some of them are mentioned above) can be described from the first principles in the framework of perturbative QCD using universal non-perturbative DPDFs as input.

Measurements of diffractive DIS processes serve as stringent tests of the QCD factorization for hard diffraction and further constrain diffractive PDFs. One example of such a diffractive process, which predominantly probes the gluon diffractive PDF, is diffractive production of dijets, see Fig. 22. The figure depicts diffractive production of dijets in DIS. Replacing the virtual photon by the real (quasi-real) one, it is possible to study diffractive photoproductions of dijets. In the latter process, the hard scale is given by the transverse momenta of the jets.

Both H1 and ZEUS collaborations measured diffractive dijet production. In detail, the H1 collaboration measured diffractive dijet production in DIS ($4 < Q^2 < 80$ GeV²) and photoproduction ($Q^2 < 0.01$ GeV²) in the reaction $ep \rightarrow e \text{jet}_1 \text{jet}_2 XY$ [64,151]. It was

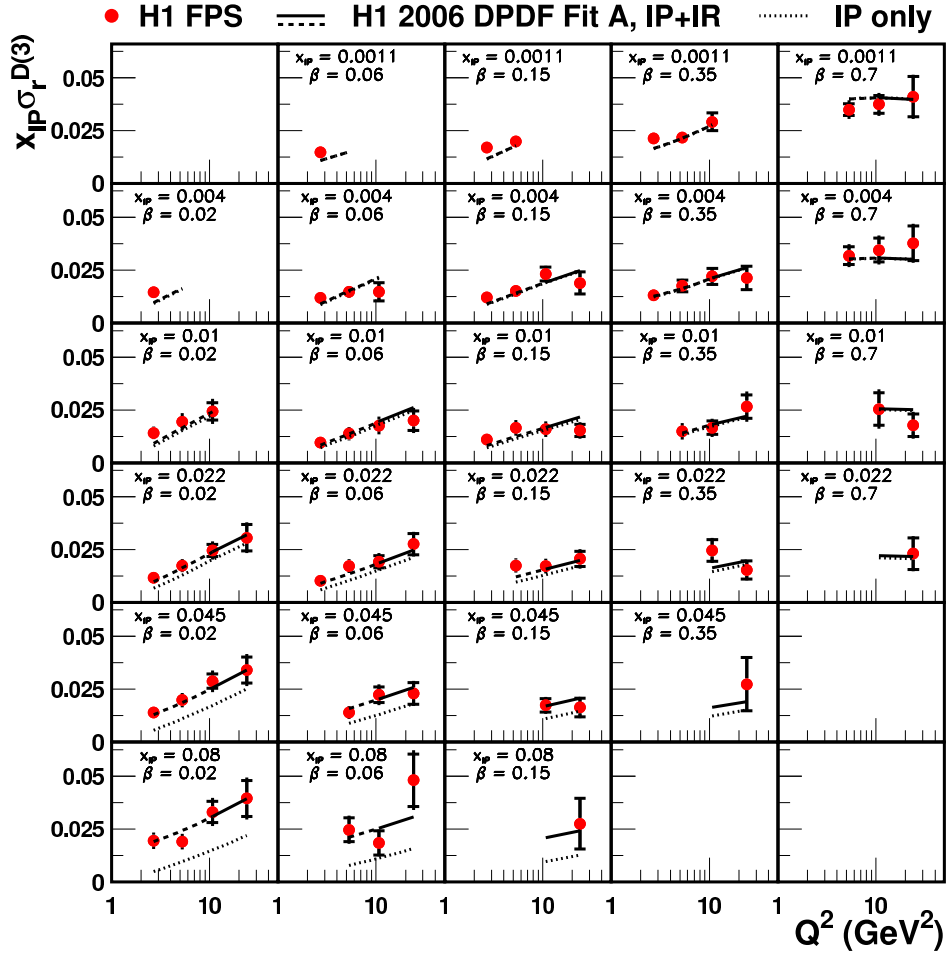


Fig. 21. The perturbative QCD description of the H1 FPS diffractive data on $x_{\mathbb{P}}\sigma_r^{D(3)} \approx x_{\mathbb{P}}F_2^{D(3)}$. The figure is from Ref. [62]. Reproduced with the kind permission of the H1 Collaboration and Springer.

found that, in DIS, the data are described well by diffractive PDFs extracted from the fits to the H1 data on inclusive diffraction in DIS [61,62]. The dijet data clearly favors fit B, which corresponds to a smaller (compared to fit A) gluon diffractive PDF $f_{g/\mathbb{P}}(\beta, Q^2)$ in the large β limit, see Fig. 19.

In photoproduction of dijets, theoretical predictions based on fit B overestimate the data by approximately a factor of two (both for the direct and resolved contributions). This indicates the breakdown of the QCD factorization theorem for the photoproduction, similarly to the case of factorization breaking in hadron-induced diffractive dijet production, see e.g., [155]. One should note that while the factorization breaking is expected for the resolved component of the real photon (since the resolved component consists of hadronic fluctuations interacting with the target with typical, large hadronic cross sections), it is surprising that the factorization is similarly violated for the direct component of the real

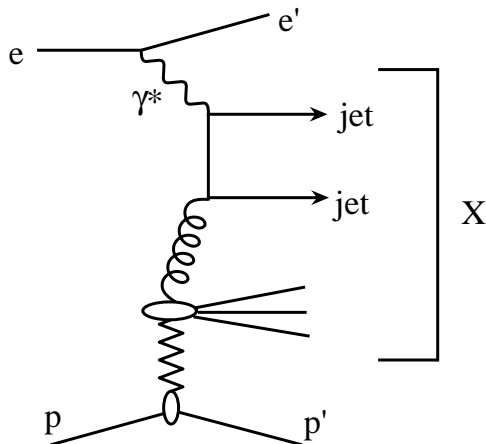


Fig. 22. Diffractive productions of dijets in DIS.

photon up to the large transverse momenta $\sim 7 \text{ GeV}/c$ [64].

The ZEUS collaboration performed a combined QCD fit to the data on inclusive diffraction and diffractive dijet production in DIS [70]. The resulting fit provides a good description of the dijet data throughout the whole kinematic region [73]. The application of the fit to the ZEUS diffractive dijet photoproduction data [152] shows an adequate description of the data over the whole x_γ^{obs} and E_T^{obs} ranges [73]. Hence, the ZEUS collaboration does not observe the suppression of the resolved component (or both the resolved and direct components), which appears to be in conflict with the H1 findings [64] (see our discussion above). Further theoretical analyses are necessary, including a more accurate definition of the direct and resolved processes at the next-to-leading (NLO) accuracy. Note that the recent analysis of Klasen and Kramer has shown that the large majority of the H1 and ZEUS points lay below their NLO pQCD predictions [156].

Diffractive open charm production is another example of diffractive processes, where the factorization theorem is expected to be valid. The underlying mechanism of open charm production is given by Fig. 22 after the replacement of the two jets by c and \bar{c} quarks. The measurement of diffractive open charm (D^* meson) production at HERA by the H1 collaboration [65] found a good agreement between the data and perturbative QCD predictions based on the H1 fits A and B, both in DIS and in photoproduction. Diffractive photoproduction of D^* mesons was also measured by the ZEUS collaboration at HERA [154]. A good agreement between pQCD calculations and the data was found. Also, the pQCD predictions based on the ZEUS diffractive PDFs [73] provide a fair description of the charm contribution to the diffractive structure function [68].

To summarize, the considered examples of diffractive dijet production and diffractive open charm production illustrate the validity of the factorization theorem for diffraction and of the concept of universal diffractive PDFs [59].

Comment. While the validity of the Regge factorization supports the dominance of the

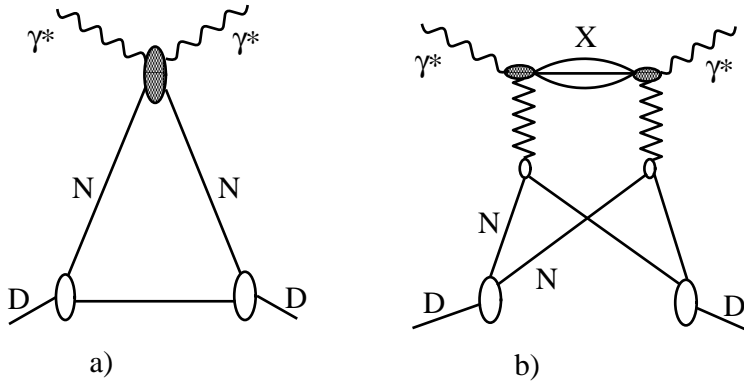


Fig. 23. Graphs depicting the contributions to the zero angle γ^*D scattering amplitude: (a) the impulse approximation, (b) the nuclear shadowing correction.

soft AJM-type configurations in diffraction, it is hardly consistent with the dominance of the pQCD Pomeron at the HERA energies. The latter hypothesis leads to $\alpha_{\mathbb{P}} \sim 1.25$, which is much larger than that found experimentally, see Eq. (91).

4 Nuclear shadowing in DIS on deuterium

In this section, we present the application of the leading twist theory of nuclear shadowing to inclusive and tagged DIS on deuterium. Numerical results presented in this section update our predictions made in [157,158].

4.1 Nuclear shadowing for unpolarized deuteron structure functions

The deuteron inclusive structure function $F_{2D}(x, Q^2)$ is proportional to the imaginary part of the forward γ^*D scattering amplitude, which, in the graphical form, receives contributions from graphs *a* and *b* in Fig. 23: graph *a* is the impulse approximation contribution; graph *b* is the nuclear shadowing correction. These graphs should be compared to the corresponding ones in Fig. 9. Note also that graph *c* in Fig. 9, which corresponds to the interaction with three and more nucleons, is naturally absent in the deuteron case.

It is important to understand and appreciate the fact that the shadowing correction for the total cross section as given by graph *b* in Fig. 23 corresponds to several distinguishable final states which could be described as a result of the application of the Abramovsky-Gribov-Kancheli (AGK) cutting rules, see Sec. 2.4. Indeed, the imaginary part of the double scattering contribution to the forward γ^*D scattering amplitude is given by the sum of all possible cuts, see Fig. 24. In this figure, graph *a* contributes to the diffractive final state in the reaction $\gamma^*N \rightarrow XN$ (the diffractive cut); graphs *b* and *c* correspond to

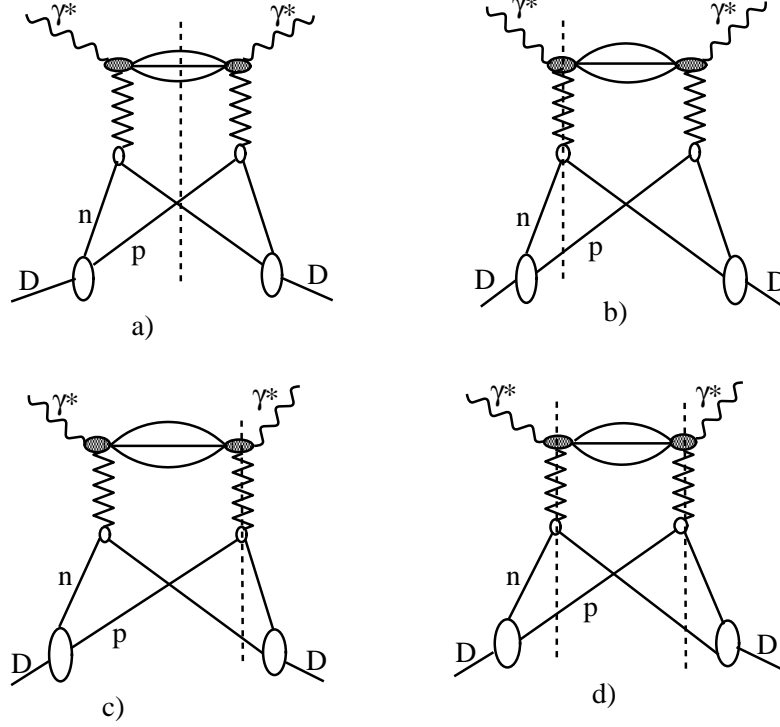


Fig. 24. Unitarity cuts of the imaginary part of the double scattering contribution to the forward γ^*D scattering amplitude: (a) diffractive cut, (b) and (c) single multiplicity cuts, (d) double multiplicity cut.

the processes with single multiplicity in the reaction $\gamma^*N \rightarrow Y$ (Y denotes all possible final states); graph d corresponds to the double multiplicity in the reaction $\gamma^*N \rightarrow Y$. Denoting the shadowing correction to the deuteron structure function $F_{2D}(x, Q^2)$ as $\delta F_{2D}(x, Q^2) = F_{2D}(x, Q^2) - F_{2p}(x, Q^2) - F_{2n}(x, Q^2)$, we find the corresponding contributions of the graphs in Fig. 24 (see also Sec. 2.4):

$$\begin{aligned}
\delta F_{2D}^a(x, Q^2) &\propto 2 (\Im D_1 \Im D_2 + \Re D_1 \Re D_2) = 2 |D_1 D_2^*|, \\
\delta F_{2D}^{b+c}(x, Q^2) &\propto -8 \Im D_1 \Im D_2, \\
\delta F_{2D}^d(x, Q^2) &\propto 4 \Im D_1 \Im D_2,
\end{aligned} \tag{95}$$

where $D_{1,2}$ denote the amplitude of the $\gamma^* + N \rightarrow X + N$ diffractive process. Here the ratio of the contributions of the diagrams is $a : b : c : d = 1 : -2 : -2 : 2$, which is due to the lack of the identity of two exchanges with vacuum quantum numbers for diagrams b , c , and d . Therefore,

$$\begin{aligned}
\delta F_{2D}(x, Q^2) &= \delta F_{2D}^a(x, Q^2) + \delta F_{2D}^{b+c}(x, Q^2) + \delta F_{2D}^d(x, Q^2) \\
&= -2 \frac{1 - \eta^2}{1 + \eta^2} |D_1 D_2^*| = -\frac{1 - \eta^2}{1 + \eta^2} \delta F_{2D}^a(x, Q^2),
\end{aligned} \tag{96}$$

where $\eta = \Re e D_{1,2}/\Im m D_{1,2}$.

As we discussed in Sec. 3, the shadowing correction to the nuclear structure function $F_{2A}(x, Q^2)$ is given by Eq. (43) in the approximation when the nucleons in the nuclear wave function are not correlated. However, in the deuteron case, the nucleons are strongly correlated. To calculate the contribution of graph b of Fig. 23, it is convenient to recall our previous discussion that the soft (nuclear) part of graph b coincides with that in the shadowing correction to hadron-deuteron scattering considered in Sec. 2. The complete expression for the deuteron structure function $F_{2D}(x, Q^2)$ in the shadowing region reads [157,158]:

$$\begin{aligned}
F_{2D}(x, Q^2) &= F_{2p}(x, Q^2) + F_{2n}(x, Q^2) \\
&- 2 \frac{1 - \eta^2}{1 + \eta^2} \int_x^{0.1} dx_{\mathcal{P}} dk_t^2 F_2^{D(4)}(\beta, Q^2, x_{\mathcal{P}}, t) \rho_D(4k_t^2 + 4(x_{\mathcal{P}}m_N)^2) \\
&= F_{2p}(x, Q^2) + F_{2n}(x, Q^2) \\
&- 2 \frac{1 - \eta^2}{1 + \eta^2} B_{\text{diff}} \int_x^{0.1} dx_{\mathcal{P}} dk_t^2 F_2^{D(3)}(\beta, Q^2, x_{\mathcal{P}}) e^{-B_{\text{diff}} k_t^2} \rho_D(4k_t^2 + 4(x_{\mathcal{P}}m_N)^2), \quad (97)
\end{aligned}$$

where the $F_{2p}(x, Q^2) + F_{2n}(x, Q^2)$ term is the impulse approximation (graph a of Fig. 9); the term proportional to $F_2^{D(4)}$ and $F_2^{D(3)}$ is the nuclear shadowing correction (graph b of Fig. 9). In Eq. (97), k_t is the transverse component of the momentum transfer; $|t| = k_t^2 + (x_{\mathcal{P}}m_N)^2$; ρ_D is the deuteron charge form factor of the double argument, which can be written as an overlap between the initial and final state deuteron wave functions:

$$\begin{aligned}
\rho_D(4k_t^2 + 4(x_{\mathcal{P}}m_N)^2) &= \int d^3\vec{p} \left[u(\vec{p})u(\vec{p} + \vec{k}) \right. \\
&\quad \left. + w(\vec{p})w(\vec{p} + \vec{k}) \left(\frac{3}{2} \frac{(\vec{p} \cdot (\vec{p} + \vec{k}))^2}{p^2(p+k)^2} - \frac{1}{2} \right) \right], \quad (98)
\end{aligned}$$

where u and w are the S -wave and D -wave components of the deuteron wave function, respectively; $\vec{k} = \vec{k}_t + (x_{\mathcal{P}}m_N)e_z$. In our analysis, we use the deuteron wave function that corresponds to the Paris nucleon-nucleon potential [159]. Note that the double argument of the deuteron form factor is the consequence of the correct treatment of the deuteron center of mass. One should also note that the t dependence of $F_2^{D(4)}$ cannot be neglected compared to that of the deuteron form factor: since the t dependence of ρ_D is rather moderate (compared to heavier nuclei), the integral in Eq. (97) is sensitive to $F_2^{D(4)}(t)$ up to $-t \leq 0.05 \text{ GeV}^2$.

The results of the calculation of leading twist nuclear shadowing for the deuterium structure function $F_{2D}(x, Q^2)$ are presented in Fig. 25, where we plot the ratio of $F_{2D}(x, Q^2)$

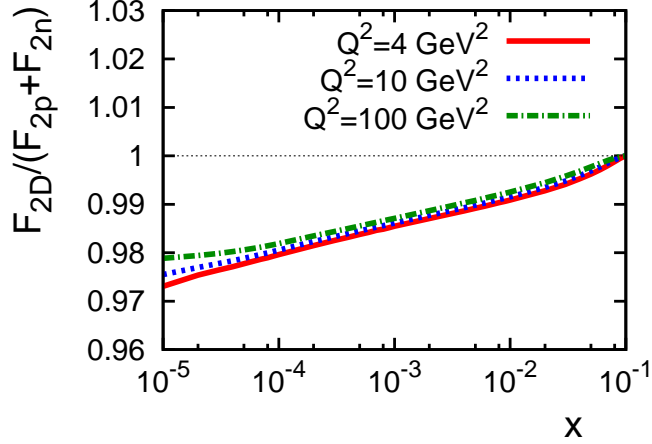


Fig. 25. Leading twist nuclear shadowing for the deuteron structure function $F_{2D}(x, Q^2)$, see Eq. (97). The ratio of the deuteron $F_{2D}(x, Q^2)$ to the sum of the free proton and neutron structure functions, $F_{2D}/(F_{2p} + F_{2n})$, as a function of Bjorken x for different values of Q^2 .

given by Eq. (97) to the sum of the free proton and neutron structure functions, $F_{2D}/(F_{2p} + F_{2n})$, as a function of Bjorken x for different values of Q^2 . The suppression of $F_{2D}/(F_{2p} + F_{2n})$ compared to unity is given by the nuclear shadowing correction in Eq. (97). For the calculation of the free proton and neutron structure functions, we used as input the next-to-leading (NLO) CTEQ5M parameterization [160]. The nucleon PDFs are evolved to the required values of Q^2 using the QCDNUM package [161]. Note that our predictions for the magnitude of the nuclear shadowing correction are in a very good agreement with the earlier calculation of [162], which considered the range of intermediate values of Q^2 where the contribution of low diffractive masses M_X to nuclear shadowing is important.

As we explained in Sec. 3, the use of the QCD factorization theorems for inclusive and hard diffractive DIS allows one to generalize the shadowing correction for the nuclear structure function $F_{2A}(x, Q^2)$ to individual nuclear parton distributions $f_{j/A}(x, Q^2)$. In the case of the deuteron, we obtain from Eq. (97):

$$f_{j/D}(x, Q^2) = f_{j/p}(x, Q^2) + f_{j/n}(x, Q^2) - 2 \frac{1 - \eta^2}{1 + \eta^2} B_{\text{diff}} \int_x^{0.1} dx_P dk_t^2 f_2^{D(3)}(\beta, Q^2, x_P) e^{-B_{\text{diff}} k_t^2} \rho_D(4k_t^2 + 4(x_P m_N)^2). \quad (99)$$

Our predictions for the leading twist nuclear shadowing for the deuteron PDFs $f_{j/D}(x, Q^2)$ are presented in Fig. 26. In this figure, we plot the ratio $f_{j/D}/(f_{j/p} + f_{j/n})$, where $f_{j/p}$ and $f_{j/n}$ are flavor j PDFs of the free proton and neutron, respectively, as a function of Bjorken x for different values of Q^2 . The left panel corresponds to \bar{u} quarks; the right panel corresponds to gluons. Since the ratio of the gluon diffractive PDF to the usual gluon PDF is much larger than that for quarks, see Fig. 19, we predict the larger nuclear

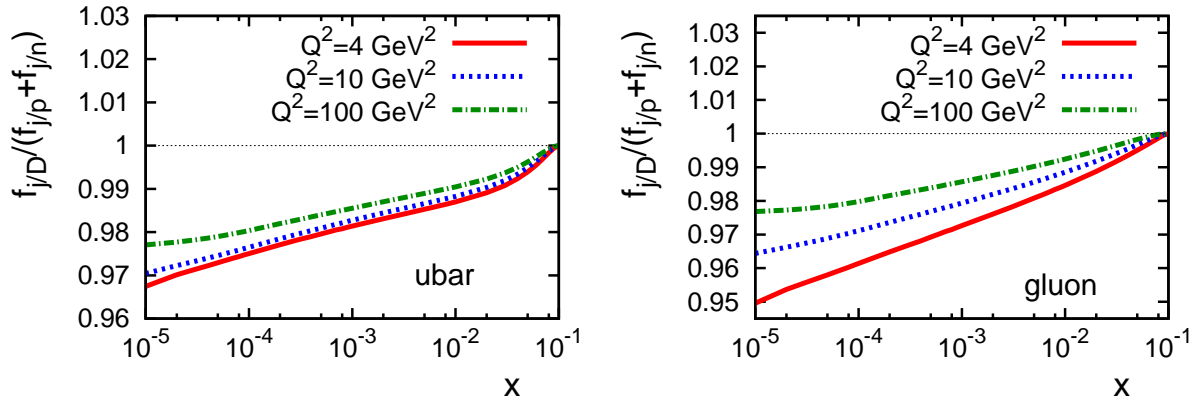


Fig. 26. Leading twist nuclear shadowing for deuteron PDFs $f_{j/D}(x, Q^2)$, see Eq. (99). The ratio of $f_{j/D}(x, Q^2)$ to the sum of the free proton and neutron PDFs, $f_{j/D}/(f_{j/p} + f_{j/n})$, as a function of Bjorken x for different values of Q^2 . The left panel corresponds to \bar{u} quarks; the right panel corresponds to gluons.

shadowing effect for the gluon nuclear PDFs compared to that for the quark nuclear PDFs which reflects the stronger interaction in the gluon channel.

The case of DIS on deuterium presents a very important testing ground for the leading twist theory of nuclear shadowing since the shadowing correction can be calculated in a model-independent way, without the necessity to model multiple scatterings. Conversely, precise measurements of the deuteron structure function $F_{2D}(x, Q^2)$ at low x and Q^2 of the order of a few GeV^2 will constrain the nucleon diffractive structure function $F_2^{D(4)}$.

DIS on deuterium is the main source of information on the neutron structure function $F_{2n}(x, Q^2)$. The measurement of $F_{2n}(x, Q^2)$ using the deuteron beams is one of the important components of the planned physics program of the future Electron-Ion Collider [36,37]. The main goal of such a measurement is to study the flavor dependence of parton distributions in a wide kinematic region, including small x . The correct extraction of $F_{2n}(x, Q^2)$ from the deuteron data requires an account of the nuclear shadowing correction. The effect of nuclear shadowing on the extraction of $F_{2n}(x, Q^2)$ from $F_{2D}(x, Q^2)$ can be estimated as follows. Since the diffractive structure function $F_2^{D(4)}$ is known with the accuracy of approximately 20%, the accuracy of our calculations of nuclear shadowing is $20 \times 0.025 = 0.5\%$ at the smallest values of x . Correspondingly the theoretical uncertainty of the F_{2n}/F_{2p} ratio extracted from the deuteron data will be $2 \times 0.5 = 1\%$, which is likely to be smaller than possible experimental systematic errors (the additional factor of two comes from the fact that the calculated shadowing correction is per nucleon).

In this review, we concentrate on unpolarized scattering, singlet nuclear parton distributions (unpolarized sea quarks and gluons) and nuclear shadowing driven by the vacuum exchange. The leading twist theory of nuclear shadowing can be generalized to non-singlet structure functions and parton distributions, where the shadowing correction is given by

the interference between the vacuum and non-vacuum exchanges, see Sec. 3.3. However, the corresponding diffractive PDFs are not known and one has to model them. Important examples of the processes, where nuclear shadowing is given by the interference between the vacuum and non-vacuum exchanges, include shadowing in the valence quark channels and polarized DIS. If one uses an eikonal-type approximation for these channels, one finds the much stronger nuclear shadowing for the non-vacuum channels since the scattering off the nucleus at small impact parameters does not contribute to the difference of the two cross sections, for instance, the W^+A and W^-A cross sections [81]. However, large shadowing for the valence quarks combined with the baryon charge sum rule may lead to a substantial enhancement of the valence quark distribution around $x \sim 0.1$, which is probably not supported by the data.

For light nuclei, the eikonal-type approximation just mentioned leads to the shadowing correction in the non-singlet case which is approximately the factor of two as large as that in the singlet case. Examples of such calculations of nuclear shadowing for various non-singlet observables include the difference between the ${}^3\text{He}$ and ${}^3\text{H}$ structure functions, $F_2^{{}^3\text{He}} - F_2^{{}^3\text{H}}$, with the application to the Gottfried sum rule [163], polarized structure functions of deuterium [158,162], the difference between the ${}^3\text{He}$ and ${}^3\text{H}$ polarized structure functions and the Bjorken sum rule [164], the polarized structure functions of ${}^3\text{He}$ [164–166], ${}^7\text{Li}$ [165] and ${}^6\text{LiD}$ [167].

The discussion in Sec. 3.3 suggests that the eikonal approximation is likely to overestimate the nuclear shadowing effects in the scaling limit in non-singlet channels, although these effects could be large at moderate Q^2 corresponding to enhanced higher twist effects. Clearly further experimental studies of nuclear shadowing in non-vacuum channels are highly desirable.

4.2 Nuclear shadowing in tagged DIS processes on deuterium

In the previous subsection, we discussed the extraction of the neutron structure function $F_{2n}(x, Q^2)$ from the deuteron inclusive structure function $F_{2D}(x, Q^2)$. A strategy complementary to the inclusive measurement of $F_{2D}(x, Q^2)$ is the use of the neutron tagging by detecting a slow spectator proton. Conversely, the proton structure function $F_{2p}(x, Q^2)$ can be studied by the proton tagging. The usefulness of the tagged DIS on deuterium for the extraction of $F_{2n}(x, Q^2)$ at large x was discussed in [168]. In our analysis, we concentrate on the small x region of nuclear shadowing.

By tagging the final proton in DIS on deuterium, one measures the $\gamma^*D \rightarrow pX$ cross section, $d\sigma^{\gamma^*D \rightarrow pX}/d^3p$, which can be expressed in terms of the tagged deuteron structure function $F_{2D}(x, Q^2, \vec{p})$, where \vec{p} is the momentum of the final proton. The kinematic proportionality factor between $d\sigma^{\gamma^*D \rightarrow pX}/d^3p$ and $F_{2D}(x, Q^2, \vec{p})$ is the same as the one between $\sigma^{\gamma^*D \rightarrow X}$ and $F_{2D}(x, Q^2)$.

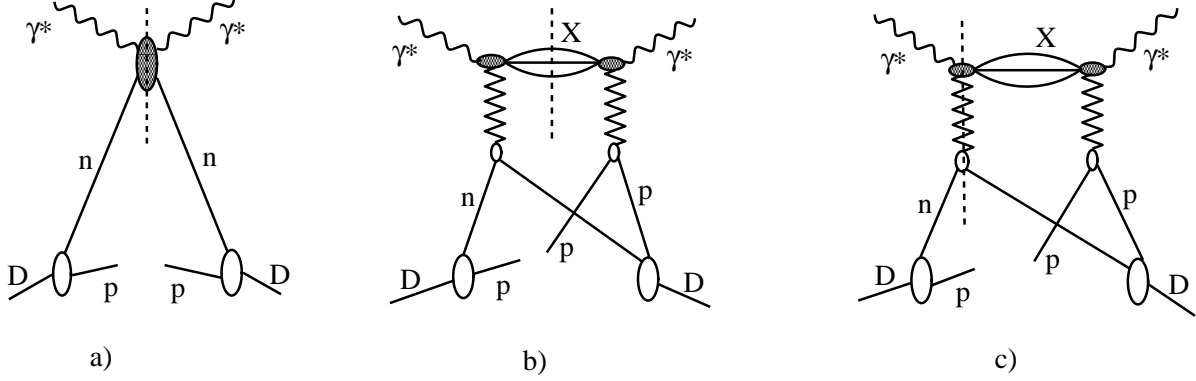


Fig. 27. Graphs depicting the contributions to the deuteron tagged structure function $F_{2D}(x, Q^2, \vec{p})$: (a) the impulse contribution, (b)+(c) the nuclear shadowing correction.

In the graphical form, the tagged deuteron structure function is presented in Fig. 27: graph *a* gives the impulse approximation; graphs *b* and *c* is the nuclear shadowing correction. The expression for $F_{2D}(x, Q^2, \vec{p})$ corresponding to the sum of graphs *a*, *b*, and *c* in Fig. 27 reads [157,158] [compare to Eq. (97)]:

$$\begin{aligned}
F_{2D}(x, Q^2, \vec{p}) &= \left(1 + \frac{q_z}{q_0} \frac{p_z}{m_N}\right)^{\alpha_P(0)-1} [u^2(p) + w^2(p)] F_{2n}(\tilde{x}, Q^2) \\
&\quad - \frac{3 - \eta^2}{1 + \eta^2} \int_x^{0.1} dx_P \frac{d^2 \vec{k}_t}{\pi} F_2^{D(4)}(\beta, Q^2, x_P, t) \left[u(\vec{p}) u(\vec{p} + \vec{k}) \right. \\
&\quad \left. + w(\vec{p}) w(\vec{p} + \vec{k}) \left(\frac{3 (\vec{p} \cdot (\vec{p} + \vec{k}))^2}{2 p^2 (p+k)^2} - \frac{1}{2} \right) \right], \tag{100}
\end{aligned}$$

where $\tilde{x} = (1 - p_z/m_N)x$ which takes into account the effect of Fermi motion. Since the second term in Eq. (100) is a correction, the effect of Fermi motion can be safely neglected there. In Eq. (100), the first line is the impulse approximation to $F_{2D}(x, Q^2, \vec{p})$; the second and third lines is the shadowing correction. The $(1 + q_z/q_0 p_z/m_N)^{\alpha_P(0)-1}$ factor reflects the different invariant energies of the virtual photon-deuteron and the virtual photon-neutron interactions— $(1 + q_z/q_0 p_z/m_N)^{\alpha_P(0)-1}$ is the flux factor of the interacting neutron (q_0 and q_z are the energy and momentum [along the z -axis] of the virtual photon, respectively; p_z is the z -component of the neutron momentum). In our derivation, we neglected corrections of the order of $\mathcal{O}(p^2/m_N^2)$ and higher, which is standard for the non-relativistic treatment of the deuteron wave function.

The coefficient $(3 - \eta^2)/(1 + \eta^2)$, which determines the weight of the shadowing correction, is a direct consequence of the application of the AGK rules. Indeed, in the case of the proton tagging, only the diffractive cut (graph *b* in Fig. 27) and single unitarity cut (graph *c* in Fig. 27) are allowed. (If both ladders are cut, the hadron final state contains no slow nucleons, and there are no spectators from the deuteron wave function.) The respective

contributions of these graphs to the shadowing correction $\delta F_2^D(x, Q^2, \vec{p})$ read [compare to the case of inclusive structure function, see Eq. (95)]:

$$\begin{aligned}\delta F_{2D}^{(b)}(x, Q^2, \vec{p}) &\propto (\Im m D_1 \Im m D_2 + \Re e D_1 \Re e D_2) = |D_1 D_2^*|, \\ \delta F_{2D}^{(c)}(x, Q^2, \vec{p}) &\propto -4 \Im m D_1 \Im m D_2.\end{aligned}\quad (101)$$

Therefore,

$$\begin{aligned}\delta F_{2D}(x, Q^2, \vec{p}) &= \delta F_{2D}^{(b)}(x, Q^2, \vec{p}) + \delta F_{2D}^{(c)}(x, Q^2, \vec{p}) \\ &= -\frac{3 - \eta^2}{1 + \eta^2} |D_1 D_2^*| = -\frac{3 - \eta^2}{1 + \eta^2} \delta F_{2D}^{(b)}(x, Q^2, \vec{p}).\end{aligned}\quad (102)$$

One has to note that, in general, the tagged deuteron structure function receives additional contributions from the triple and quadruple interactions with the target nucleons (not shown in Fig. 27). However, at small values of the spectator nucleon momentum, $p \leq \sqrt{\epsilon m_N} = 64 \text{ MeV}/c$, where $\epsilon = 2.2 \text{ MeV}$ is the deuteron binding energy, it is legitimate to keep only the single and double scattering terms shown in Fig. 27. At larger spectator momenta, the contributions of the triple and quadruple interactions with the target are no longer suppressed by the small parameter $p/\sqrt{\epsilon m_N}$ and, hence, should be included. This will introduce a certain model dependence since those terms are not simply related to the elementary diffractive structure function $F_2^{D(4)}$. One should emphasize that this is only the case for the tagged structure function: the triple and quadruple interaction terms cancel in the inclusive structure function, which is unambiguously expressed in terms of the nucleon diffractive structure function, see Eq. (97).

As one can see from Eq. (100), nuclear shadowing suppresses the spectrum of the produced protons. We quantify this effect by considering the ratio $R(x, Q^2, \vec{p})$:

$$R(x, Q^2, \vec{p}) = \frac{F_{2D}(x, Q^2, \vec{p})}{F_{2D}^{\text{IA}}(x, Q^2, \vec{p})}, \quad (103)$$

where $F_{2D}(x, Q^2, \vec{p})$ is given by Eq. (100), and $F_{2D}^{\text{IA}}(x, Q^2, \vec{p})$ is the impulse approximation to $F_{2D}(x, Q^2, \vec{p})$ [the first line of Eq. (100)],

$$F_{2D}^{\text{IA}}(x, Q^2, \vec{p}) = \left(1 + \frac{q_z p_z}{q_0 m_N}\right)^{\alpha_P(0)-1} [u^2(p) + w^2(p)] F_{2n}(\tilde{x}, Q^2). \quad (104)$$

For the neutron structure function $F_{2n}(x, Q^2)$, we use the next-to-leading order CTEQ5M parameterization [160]; $\alpha_P(0) = 1.111$.

Figure 28 presents the ratio $R(x, Q^2, \vec{p})$ of Eq. (103) as a function of Bjorken x at fixed $Q^2 = 4 \text{ GeV}^2$. The left panel corresponds to the case of the zero longitudinal momentum

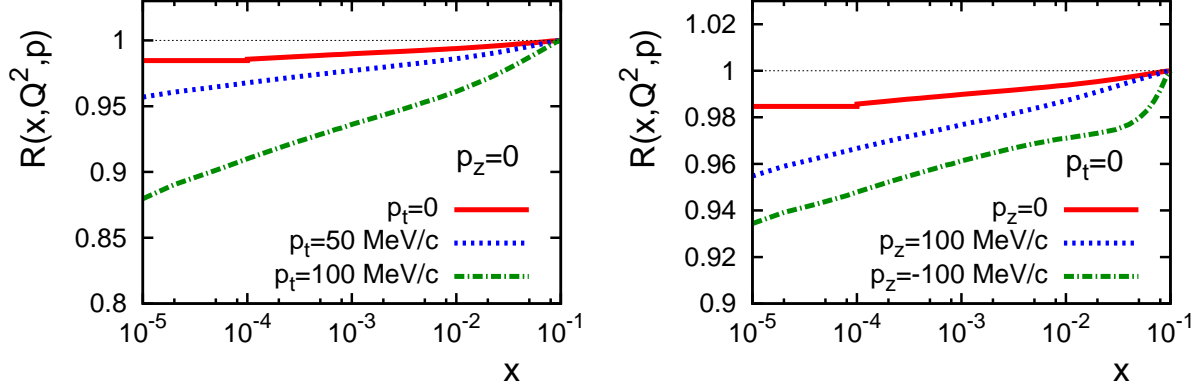


Fig. 28. Nuclear shadowing in the tagged deuteron structure function $F_{2D}(x, Q^2, \vec{p})$. The ratio $R(x, Q^2, \vec{p})$ of Eq. (103) as a function of Bjorken x at fixed $Q^2 = 4 \text{ GeV}^2$. The left panel corresponds to $p_z = 0$ and $|\vec{p}_t| = 0, 50, \text{ and } 100 \text{ MeV/c}$; the right panel corresponds to $|\vec{p}_t| = 0$ and $p_z = \pm 100 \text{ MeV/c}$.

of the final proton, $p_z = 0$, and different values of the transverse momentum, $|\vec{p}_t| = 0, 50, \text{ and } 100 \text{ MeV/c}$; the right panel corresponds to $|\vec{p}_t| = 0$ and $p_z = \pm 100 \text{ MeV/c}$. As one can see from Fig. 28, nuclear shadowing decreases the ratio $R(x, Q^2, \vec{p})$ as p_\perp is increased. Larger values of p_t correspond to smaller transverse distances between the proton and neutron, which leads to larger nuclear shadowing.

A comparison of Figs. 28 and 25 shows that the shadowing correction to the tagged deuteron structure function is much larger than that for the inclusive structure function. This happens because of the following two features of the tagged case. First, the weight of the shadowing correction is larger because of the AGK cutting rules (see the discussion above). Second, the impulse approximation decreases with increasing $|\vec{p}|$ faster than the shadowing term, which enhances the relative magnitude of nuclear shadowing.

In addition to nuclear shadowing, the spectrum of the produced protons is also modified by the proton-neutron final state interactions (FSI). FSI partially cancel the effect of nuclear shadowing and decrease the deviation of the ratio $R(x, Q^2, \vec{p})$ from unity [158].

From the experimental point of view, several strategies of the extraction of the neutron structure function $F_{2n}(x, Q^2)$ from the deuteron data using the proton tagging are possible. As our analysis above shows, by selecting only very low p_t protons, the distortion of the proton spectrum by the nuclear shadowing and FSI effects will be minimal. However, the drawback of this approach is the gross loss of statistics. The other, more promising approach is to measure the p_t dependence of the spectrum up to $p_t \sim 200 \text{ MeV/c}$, which will allow one to use most of the spectator protons. Provided the good momentum resolution of the proton spectrometer, one would be able to make (longitudinal) momentum cuts to suppress/increase the shadowing effect and, thus, one would have an opportunity to independently study the enhanced nuclear shadowing. In general, the tagged method will allow one to extract $F_{2n}(x, Q^2)$ from deuteron data with an accuracy at the level of

the fraction of a percent.

Note also that, in general, the proton spectrum receives an additional contribution that predominantly originates from the diffractive scattering off the proton with large p_t , $|\vec{p}_t| \geq 300$ MeV/c. As a result of the AGK cancellation, this contribution is given by the corresponding impulse approximation. The contribution has a broad p_t distribution, $\propto \exp(-Bp_t^2)$ with $B \approx 7$ GeV², and can be subtracted using the measurement at, for instance, $|\vec{p}_t| \geq 300$ MeV/c.

One can also use the simultaneous tagging of protons and neutrons, when both the neutron and proton are detected in the reactions $\gamma^*D \rightarrow nX$ and $\gamma^*D \rightarrow pX$. In this case, the effects of nuclear shadowing and FSI cancel in the ratio $\sigma^{\gamma^*D \rightarrow nX} / \sigma^{\gamma^*D \rightarrow pX}$ and the main errors in the measurement of $F_{2n}(x, Q^2)$ will come from the determination of relative efficiencies of the proton and neutron taggers.

Another possibility to extract the $F_{2n}(x, Q^2)/F_{2p}(x, Q^2)$ ratio is from comparing the rate of the tagged proton scattering events with the neutron spectator to inclusive eD scattering. Such a strategy has certain merits as it avoids the issue of luminosity and does not require a leading proton spectrometer. The disadvantage of this method is the sensitivity to the nuclear shadowing and FSI effects and errors in the acceptance of the neutron detector. One possible way to deal with the latter problem will be to perform measurements at very small x and large energies, where the ep and en cross sections are equal to better than a fraction of 1% and, hence, one would be able to cross-check the acceptances of the proton and neutron detectors. Note also that taking proton data from an independent run will potentially lead to another set of issues such as relative luminosity, the use of different beam energies, etc., which will likely introduce additional systematic error at the level of 1%.

In our analysis, we neglected possible non-nucleonic components of the deuteron wave function such as kneaded (six-quark) components, etc. Current estimates put an upper limit on the probability of such components at the level of less than one percent, and they are expected to modify predominantly the high-momentum component of the deuteron wave function. Hence, the non-nucleonic components should give a very small (less than one percent) correction for the spectator momenta ≤ 200 MeV/c. Moreover, the experiments at the future Electron-Ion Collider looking for production of baryons such as Δ and N^* in the spectator kinematics (the spectator Feynman $x_L(\Delta, N^*) \geq 0.5$) would allow one to put a more stringent upper limit on (or to discover) non-nucleonic components of the deuteron wave function.

Finally, we would like to mention that similarly to the tagged deuteron structure function $F_{2D}(x, Q^2, \vec{p})$, nuclear shadowing and final-state interactions modify the cross section of diffractive deuteron disintegration $\gamma^*D \rightarrow Xpn$.

5 Phenomenology of nuclear shadowing for nuclear structure functions and parton distributions for medium and heavy nuclei

In this section, we present predictions of the leading twist theory of nuclear shadowing for the nuclear PDFs and nuclear structure functions for a wide range of nuclei. We discuss theoretical uncertainties of our predictions as well as the uncertainties due the experimental knowledge of diffraction in ep DIS. (The largest experimental uncertainty is associated with the uncertainty in the t dependence of the proton diffractive structure function $F_2^{D(4)}$.) We also present predictions for impact parameter dependent nPDFs, which are required in the description of hard processes in hadron-nucleus and nucleus-nucleus scattering.

We compare our predictions for nPDFs to those resulting from the global fits to fixed-target data on DIS on nuclei. We also make a comparison between our results on $F_{2A}(x, Q^2)$ and the nuclear longitudinal structure function $F_L^A(x, Q^2)$ with the predictions obtained within the eikonal approximation.

Also, we compare our results with the available fixed-target data on DIS off various nuclear targets. We demonstrate that the data contain a significant higher twist component, which might invalidate the extraction of leading-twist nuclear PDFs from the fixed-target data.

5.1 Predictions for nuclear parton distributions

5.1.1 General remarks

Nuclear parton distributions (nPDFs) at a fixed low scale Q_0^2 ($Q_0^2 = 4 \text{ GeV}^2$ in our case) and for small values of Bjorken x , $x \leq 0.1$, $f_{j/A}(x, Q_0^2)$, are given by Eq. (64). This equation defines the input for the subsequent next-to-leading order (NLO) DGLAP evolution of nPDFs to arbitrary high $Q^2 > Q_0^2$. In the numerical analysis of Eq. (64), we used the following input.

For diffractive PDFs $f_j^{D(3)}$, we used the H1 diffractive fit B [61,62]. We assumed that the leading Pomeron and the subleading Reggeon contribute *independently* to nuclear shadowing. Note that the latter contribution is small and contributes sizably only for $x_{\mathcal{P}} > 0.05$. As explained in Sect. 3.6, the FPS H1 data requires that the Pomeron contribution is reduced by the factor 1.23 and the Reggeon contribution is reduced by the factor 1.39. For the slope of the t dependence of the quark and gluon diffractive PDFs, we used $B_{\text{diff}} = 6 \text{ GeV}^{-2}$, see Eq. (58) and the corresponding discussion.

Our numerical analysis shows that the subleading Reggeon contribution to the shadowing correction is negligible. Not only the Reggeon contribution is numerically small by itself

[see Eq. (91)], but it is also additionally suppressed by the $(1 - i\eta)^2/(1 + \eta^2)$ factor in Eq. (64) because $|\eta| \approx 1$ for the Reggeon trajectory [76]. Therefore, only the leading Pomeron term contributes to the resulting nuclear PDFs.

We would like to point out that our present conclusion about the smallness of the nuclear shadowing correction coming from the subleading Reggeon trajectory differs from our original findings [76]. In Ref. [76], we used the results of the older H1 analysis of inclusive diffraction at HERA, which did not report the normalization constant of the Reggeon contribution, n_R , see Eq. (91), and, as a result, we significantly overestimated n_R in [76].

In the present calculation, for the ratio of the real to imaginary parts of the diffractive amplitude, η , we use its relation to the intercept of the effective Pomeron trajectory, $\alpha_P(0)$, using the Gribov-Migdal relationship [127] between the imaginary and real parts of the scattering amplitude at high energies,

$$\eta \approx \frac{\pi}{2}(\alpha_P(0) - 1) = 0.174, \quad (105)$$

where the H1 Fit B value for $\alpha_P(0) = 1.111$ was employed, see Eq. (91).

For the nuclear density $\rho_A(r)$, we used the two-parameter Fermi parameterization [169]. For the usual nucleon PDFs, $f_{j/N}$, we used the NLO CTEQ5M parameterization [160].

Two important remarks are in order. First, while the leading twist theory of nuclear shadowing is applicable to partons of all flavors, at present we are unable to make quantitative predictions for nuclear shadowing of valence quarks since the subleading Reggeon contribution, which gives rise to nuclear shadowing of nuclear valence PDFs, is essentially unknown, but it is strongly suppressed (see the discussion above) since inclusive diffraction is dominated by the C -even Pomeron exchange. In principle, a significant Reggeon contribution could arise from the Reggeon-Reggeon-Pomeron (RRP) interference term. However, the magnitude of such a contribution is not known, although it was included in the fits to the HERA diffractive data. In any case, the absence of diffractive final states in γ^* -“valence quark” interactions leads to a strong suppression of nuclear shadowing in this channel, see the discussion in Sec. 3.3. In practical terms, all this means that Eq. (64) should be applied to evaluate nuclear shadowing for the sea quarks and gluons only.

Second, since diffractive PDFs of the nucleon, $f_j^{D(4)}$, represent next-to-leading order (NLO) distributions, our predictions for nuclear PDFs $f_{j/A}$ are also NLO predictions, which correspond to QCD observables calculated to the NLO accuracy.

5.1.2 Color fluctuation approximation for multiple interactions in leading twist theory of nuclear shadowing

In the derivation of our master equation (64), we used the color fluctuation approximation, which enabled us to express the interaction with $N \geq 3$ nucleons of the nuclear target in terms of a single cross section $\sigma_{\text{soft}}^j(x, Q^2)$. In our numerical analysis, we use two different models for $\sigma_{\text{soft}}^j(x, Q^2)$ that we present below. They can be interpreted as giving the higher and lower values of nuclear shadowing in our approach. This reflects the objective reality that currently the value of $\sigma_{\text{soft}}^j(x, Q^2)$ has large uncertainties. However, as we pointed out in Sec. 3, one possible strategy could be that once nuclear shadowing is measured on one nucleus, $\sigma_{\text{soft}}^j(x, Q^2)$ can be extracted from that measurement and predictions for other nuclei can be made with very little theoretical uncertainty. Note also that $\sigma_{\text{soft}}^j(x, Q^2)$ can be fixed from the studies of coherent diffraction with nuclei, see Sec. 6.

Model 1 (FGS10_H): Larger nuclear shadowing

In the first model for $\sigma_{\text{soft}}^j(x, Q^2)$, we use as a reference the effective cross section $\sigma_2^j(x, Q^2)$, see Eq. (52). The resulting model for the gluon and quark channels reads:

$$\sigma_{\text{soft}}^{g(\text{H})}(x, Q_0^2) = \begin{cases} \sigma_2^g(x, Q_0^2), & x \leq x_4 = 10^{-4}, \\ \sigma_2^g(x_4, Q_0^2) \left(\frac{x_4}{x}\right)^{0.06}, & 10^{-4} \leq x \leq x_2 = 10^{-2}, \\ \sigma_2^g(x_4, Q_0^2) \left(\frac{x_4}{x_2}\right)^{0.06} \left(\frac{0.1-x}{0.1-x_2}\right), & 10^{-2} \leq x \leq 0.1, \end{cases}$$

$$\sigma_{\text{soft}}^{q(\text{H})}(x, Q_0^2) = \begin{cases} \kappa(x) \sigma_2^q(x, Q_0^2), & x \leq 10^{-4}, \\ \kappa(x_0) \sigma_2^q(x_0, Q_0^2) \left(\frac{x_0}{x}\right)^{0.06}, & 10^{-4} \leq x \leq 10^{-2}, \\ \kappa(x_0) \sigma_2^q(x_0, Q_0^2) \left(\frac{x_0}{x_2}\right)^{0.06} \left(\frac{0.1-x}{0.1-x_2}\right), & 10^{-2} \leq x \leq 0.1, \end{cases} \quad (106)$$

where $x_4 = 10^{-4}$ and $x_2 = 10^{-2}$. The superscript "(H)" indicates that the resulting nuclear shadowing corresponds to the higher value of shadowing in our approach. In the following, predictions for nuclear shadowing made with the effective cross section $\sigma_{\text{soft}}^{j(\text{H})}$ will be referred to and labeled as "FGS10_H".

Below we explain the motivation and building blocks used in Eq. (106). In the gluon channel, the interaction at $Q^2 = Q_0^2 = 4 \text{ GeV}^2$ and $x \leq 10^{-4}$ is rather close to the maximally allowed by unitarity (the black disk regime, see Sec. 8). Therefore, the cross section (color) fluctuations are small and it is a good approximation to use $\sigma_{\text{soft}}^{g(\text{H})}(x, Q_0^2) \approx \sigma_2^g(x, Q_0^2)$. For the larger values of x , $10^{-2} > x > 10^{-4}$, we impose the soft energy dependence for $\sigma_{\text{soft}}^{g(\text{H})}(x, Q_0^2)$. The exponent 0.06 is taken to be equal to the exponent of the energy dependence of the $\sigma_{\text{soft}}^{j(\text{L})}$ cross section [see the details below when we discuss the second model for $\sigma_{\text{soft}}^j(x, Q^2)$]. For even larger values of x , $x > 0.01$, the cross section fluctuation formalism is not applicable since different fluctuations are not coherent. However, for $x > 0.01$, the

interaction with $N \geq 3$ nucleons gives a negligible correction to nuclear shadowing and, hence, the issue of modeling of $\sigma_{\text{soft}}^j(x, Q^2)$ is unimportant. Therefore, we simply assume that $\sigma_{\text{soft}}^{j(\text{H})}(x, Q^2)$ linearly decreases on the interval $10^{-2} \leq x \leq 0.1$ and vanishes at $x = 0.1$.

In the quark channel, the interaction has not reached the black disk regime, the color fluctuations are sizable, and $\sigma_{\text{soft}}^{q(\text{H})}(x, Q_0^2) > \sigma_2^q(x, Q_0^2)$ because of the dispersion of the distribution over cross section $P_j(\sigma)$. This is modeled by the dimensionless coefficient κ ($\kappa > 1$) that we evaluate within the dipole model,

$$\kappa(x) = \frac{\langle \sigma_{q\bar{q}N}^3(x, d_{\perp}^2, m_i) \rangle}{\langle \sigma_{q\bar{q}N}^2(x, d_{\perp}^2, m_i) \rangle} \bigg/ \frac{\langle \sigma_{q\bar{q}N}^2(x, d_{\perp}^2, m_i) \rangle}{\langle \sigma_{q\bar{q}N}(x, d_{\perp}^2, m_i) \rangle}, \quad (107)$$

where the brackets denote the integration with the weight given by the square of the virtual photon wave function:

$$\langle \sigma_{q\bar{q}N}^n(x, d_{\perp}^2, m_i) \rangle = \int d\alpha d^2d_{\perp} \sum_i |\Psi(\alpha, Q^2, d_{\perp}^2, m_i)|^2 \sigma_{q\bar{q}N}^n(x, d_{\perp}^2, m_i), \quad (108)$$

where $|\Psi|^2$ is the square of the virtual photon wave function (the probability for the virtual photon to fluctuate into a $q\bar{q}$ state); $\sigma_{q\bar{q}N}$ is the $q\bar{q}$ -nucleon cross section. For the details of the dipole formalism relevant for the present results, see Sec. 5.14. In the considered kinematics, $1.37 \leq \kappa \leq 1.55$.

Model 2 (FGS10_L): Lower nuclear shadowing

In the second model for $\sigma_{\text{soft}}^j(x, Q^2)$, we assume that the relevant distribution $P_j(\sigma)$ is given by the distribution over cross sections for the pion, $P_{\pi}(\sigma)$, i.e., $P_j(\sigma) \approx P_{\pi}(\sigma)$. The form of $P_{\pi}(\sigma)$ is rather well-known [135,170]:

$$P_j(\sigma) = P_{\pi}(\sigma) = N e^{-\frac{(\sigma-\sigma_0)^2}{(\Omega\sigma_0)^2}}. \quad (109)$$

The parameters N , σ_0 and Ω are constrained by following requirements:

$$\begin{aligned} \int_0^{\infty} d\sigma P_{\pi}(\sigma) &= 1, \\ \int_0^{\infty} d\sigma P_{\pi}(\sigma) \sigma &\equiv \langle \sigma \rangle = \sigma_{\text{tot}}^{\pi N}(W^2), \\ \int_0^{\infty} d\sigma P_{\pi}(\sigma) \sigma^2 &\equiv \langle \sigma^2 \rangle = \left(\sigma_{\text{tot}}^{\pi N}(W^2) \right)^2 \left(1 + \omega_{\sigma}^{\pi N}(W^2) \right), \end{aligned} \quad (110)$$

where $\sigma_{\text{tot}}^{\pi N}$ is the total pion-nucleon cross section. The parameter $\omega_{\sigma}^{\pi N}$ characterizes the dispersion of the distribution $P_{\pi}(\sigma)$:

$$\omega_{\sigma}^{\pi N} = \frac{\langle \sigma^2 \rangle - \langle \sigma \rangle^2}{\langle \sigma \rangle^2}, \quad (111)$$

Both $\sigma_{\text{tot}}^{\pi N}$ and $\omega_{\sigma}^{\pi N}$ depend on the pion-nucleon invariant energy squared W^2 , $W^2 = Q^2/x - Q^2 + m_N^2$. In our numerical analysis, we used the Donnachie-Landshoff parameterization for $\sigma_{\text{tot}}^{\pi N}$ [131]:

$$\sigma_{\text{tot}}^{\pi N}(W^2) = \frac{1}{2} \left(\sigma_{\text{tot}}^{\pi^+ N} + \sigma_{\text{tot}}^{\pi^- N} \right) = 13.63 (W^2)^{0.0808} + 31.79 (W^2)^{-0.4525} \text{ mb}. \quad (112)$$

Note that in our calculations, we effectively use only the first term in Eq. (112), see also Fig. 29.

The parameter $\omega_{\sigma}^{\pi N}$ decreases with an increase of energy [134]. At the pion beam energy of $E_{\pi} \approx 300$ GeV (which corresponds to $W^2 \approx 600$ GeV²), one has $\omega_{\sigma} \approx 0.4$ [128,170]. At the CDF energy of $W^2 = (546 \text{ GeV})^2 \approx 3 \times 10^5$ GeV², we take $\omega_{\sigma}^{\pi N} \approx 0.16 \times (3/2) = 0.24$. In this estimate, we used the relation between $\omega_{\sigma}^{\pi N}$, the parameter ω_{σ}^{pp} for the proton projectile, and the total pion-nucleon and proton-proton cross sections,

$$\omega_{\sigma}^{\pi N} = \frac{\sigma_{\text{tot}}^{pp}}{\sigma_{\text{tot}}^{\pi N}} \omega_{\sigma}^{pp}, \quad (113)$$

as well as the result that $\omega_{\sigma}^{pp} = 0.16$ at the CDF energy [128], and the constituent quark model counting rule $\sigma_{\text{tot}}^{pp}/\sigma_{\text{tot}}^{\pi N} = 3/2$ [170]. Assuming a simple linear interpolation between the two energies, we arrive at the following model for $\omega_{\sigma}^{\pi N}$ (for $W_2^2 \geq W^2 \geq W_1^2$):

$$\omega_{\sigma}^{\pi N}(W^2) = 0.4 - 0.16 \frac{W^2 - W_1^2}{W_2^2 - W_1^2}, \quad (114)$$

where $W_1^2 = 600$ GeV² and $W_2^2 = 3 \times 10^5$ GeV². Equations (110), (112) and (114) fully determine $P_{\pi}(\sigma)$ and its energy (Bjorken x) dependence. In summary, the second model for the effective rescattering cross section reads [see also Eq. (63)]:

$$\sigma_{\text{soft}}^{j(L)}(W^2) = \frac{\int_0^{\infty} d\sigma P_{\pi}(\sigma) \sigma^3}{\int_0^{\infty} d\sigma P_{\pi}(\sigma) \sigma^2}. \quad (115)$$

The superscript "(L)" indicates that the resulting nuclear shadowing corresponds to the lower limit on nuclear shadowing predicted in our leading twist approach. Predictions

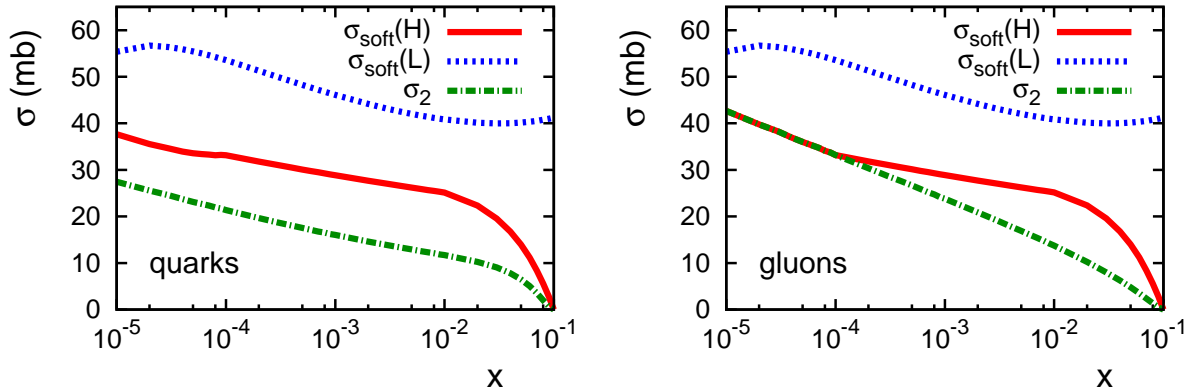


Fig. 29. The cross sections $\sigma_{\text{soft}}^{j(\text{H})}$, $\sigma_{\text{soft}}^{j(\text{L})}$, and $\sigma_2^j(x, Q_0^2)$ as functions of Bjorken x at fixed $Q_0^2 = 4$ GeV 2 . The left panel corresponds to the \bar{u} -quark; the right panel corresponds to gluons.

for nuclear shadowing made with the effective cross section $\sigma_{\text{soft}}^{j(\text{L})}$ will be referred to as "FGS10_L".

Figure 29 presents $\sigma_{\text{soft}}^{j(\text{H})}(x, Q_0^2)$ (model 1) and $\sigma_{\text{soft}}^{j(\text{L})}(W^2)$ (model 2) as functions of Bjorken x at fixed $Q_0^2 = 4$ GeV 2 . (Note that for the latter cross section, $W^2 = Q_0^2/x - Q_0^2 + m_N^2$.) For comparison and completeness, we also give $\sigma_2^j(x, Q_0^2)$ which is relevant for the calculation of nuclear shadowing in the quasi-eikonal approximation (see Fig. 45). The left panel of Fig. 29 corresponds to the \bar{u} -quark; the right panel corresponds to gluons. Note that $\sigma_{\text{soft}}^{j(\text{L})}(W^2)$ is flavor-independent.

The difference between the approximation when one uses $\sigma_2^j(x, Q_0^2)$ as the effective rescattering cross section and the color fluctuation approximation (models 1 and 2) is the amount of point-like (very weakly interacting) configurations (PLC) in the virtual photon wave function. The both approximations can be considered as generalizations of the QCD-improved aligned jet model (AJM), where one has two components—the strongly interacting AJM component and a PLC. Note also that in general the fraction of PLC decreases with increasing energy.

5.1.3 Large β diffraction dominates nuclear shadowing down to $x \sim 10^{-4}$

The effective cross section $\sigma_2^j(x, Q^2)$ determines the magnitude of nuclear shadowing when only the interaction with two nucleons of the target is important. This is the case for the deuteron and heavy nuclei in the low-nuclear density limit. In the following, we examine what values of the diffractive masses M_X , or what values of $\beta = Q^2/(Q^2 + M_X^2)$, dominate the integrand of the expression for $\sigma_2^j(x, Q^2)$ in Eq. (52). This question is important in relation to the issue of the applicability of our leading twist approach based on the DGLAP evolution.

To quantify the contributions of different regions of integration over β to $\sigma_2^j(x, Q^2)$, we

introduce the ratio R defined as follows:

$$R(\beta_{\max}, x) \equiv \frac{\int_x^{0.1} dx_{\mathbb{P}} \beta f_{j/N}^{D(3)}(\beta, Q_0^2, x_{\mathbb{P}}) \Theta(\beta_{\max} - \beta)}{\int_x^{0.1} dx_{\mathbb{P}} \beta f_{j/N}^{D(3)}(\beta, Q_0^2, x_{\mathbb{P}})}. \quad (116)$$

The ratio R for the \bar{u} -quark and gluon channels at $Q_0^2 = 4 \text{ GeV}^2$ is presented in Fig. 30. In the figure, the solid curves correspond to $\beta_{\max} = 0.5$; the dotted curves correspond to $\beta_{\max} = 0.1$; the dot-dashed curves correspond to $\beta_{\max} = 0.01$; the short-dashed curves correspond to $\beta_{\max} = 0.001$.

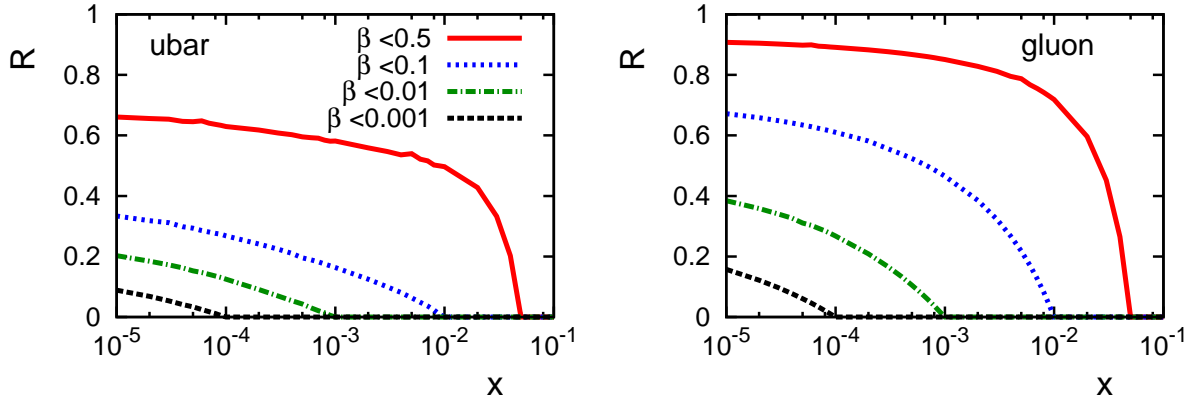


Fig. 30. The ratio R of Eq. (116) at $Q_0^2 = 4 \text{ GeV}^2$. The solid curves correspond to $\beta_{\max} = 0.5$; the dotted curves correspond to $\beta_{\max} = 0.1$; the dot-dashed curves correspond to $\beta_{\max} = 0.01$; the short-dashed curves correspond to $\beta_{\max} = 0.001$.

One can infer from Fig. 30 the relative contributions of different β -regions to $\sigma_2^j(x, Q^2)$ and, hence, to nuclear shadowing. For instance, for $x \leq 10^{-5}$, the $\beta \leq 0.001$ -region contributes to nuclear shadowing at most 9% in the quark channel and 16% in the gluon channel. This estimate suggests that even for such small values of Bjorken x , various small- x effects, which are not included in the DGLAP picture, should not lead to significant corrections in the evaluation of nuclear PDFs.

Another conclusion is that the diffractively produced masses $M_X^2 \approx Q^2(1 - \beta)/\beta$ can be large. At very high energies (small x), one enters the regime analogous to the triple Pomeron limit of hadronic physics, which allows for $\beta \ll 1$. This contribution (neglecting the large- β contribution) to the nuclear structure functions at extremely small x was evaluated in the Color Glass Condensate framework, see, e.g., Ref. [171].

5.1.4 Nuclear antishadowing and DGLAP evolution

By construction, Eq. (64) does not describe nuclear modifications of PDFs for $x > 0.1$, where such effects as nuclear antishadowing and the EMC effect take place. However, we

need to know nuclear PDFs at our chosen input scale $Q_0^2 = 4 \text{ GeV}^2$ for a wide range of the values of Bjorken x' , $x \leq x' \leq 1$, since we use those nPDFs as an input for the Dokshitzer-Gribov-Lipatov-Altarelli-Parisi (DGLAP) evolution to higher $Q^2 > Q_0^2$.

The DGLAP evolution equations for PDFs f_j of any target (we use the nucleus) read [77]:

$$\begin{aligned} \frac{d f_{j/A}^{ns}(x, Q^2)}{d \log Q^2} &= \frac{\alpha_s(Q^2)}{2\pi} \int_x^1 \frac{dx'}{x'} P_{qq} \left(\frac{x}{x'} \right) f_{j/A}^{ns}(x', Q^2), \\ \frac{d}{d \log Q^2} \begin{pmatrix} f_A^s(x, Q^2) \\ f_{g/A}(x, Q^2) \end{pmatrix} &= \frac{\alpha_s(Q^2)}{2\pi} \int_x^1 \frac{dx'}{x'} \begin{pmatrix} P_{qq} \left(\frac{x}{x'} \right) & P_{qg} \left(\frac{x}{x'} \right) \\ P_{gq} \left(\frac{x}{x'} \right) & P_{gg} \left(\frac{x}{x'} \right) \end{pmatrix} \begin{pmatrix} f_A^s(x', Q^2) \\ f_{g/A}(x', Q^2) \end{pmatrix} \end{aligned} \quad (117)$$

where $\alpha_s(Q^2)$ is the QCD running coupling constant; P_{ij} are the splitting functions, which give the probability for parton j with the longitudinal momentum fraction x' to radiate parton i with the momentum fraction x . The so-called non-singlet and singlet combinations of PDFs are denoted as $f_{j/A}^{ns}$ and f_A^s , respectively.

Equations (117) are integro-differential equations, which can be numerically solved by, e.g., the so-called brute force method. In this method, starting from the input $f_{j/A}(x, Q_0^2)$ at the initial evolution scale Q_0^2 , one obtains $f_{j/A}(x, Q^2)$ at $Q^2 = Q_0^2 + \Delta Q^2$ (ΔQ^2 is small) by integrating the right-hand side of Eqs. (117). The procedure is repeated until the desired value of Q^2 is reached. In our numerical analysis, we use the QCDNUM Fortran program which uses the brute force method [161].

It is clear from the above discussion and from Eqs. (117) that in order to determine $f_{j/A}(x, Q^2)$ at any Q^2 , one needs to know $f_{j/A}(x', Q_0^2)$ for all $x \leq x' < 1$. In other words, we need to extend our calculations for nPDFs beyond the $x < 0.1$ region and also to adopt an external model for the nuclear valence PDFs.

In our analysis, we adopt the general qualitative picture of nuclear modification of PDFs developed in [81,82,172], which was later confirmed by the results of global fits to fixed-target DIS on nuclei data [39–52]. In our implementation, the picture of nuclear PDFs at the initial scale $Q_0^2 = 4 \text{ GeV}^2$ looks as follows. Antiquarks (sea quarks) in nuclei are shadowed for $x \leq 0.1$ according to Eq. (64). For $x > 0.1$, we take $f_{\bar{q}/A}/(A f_{\bar{q}/N}) = 1$. Gluons in nuclei are also shadowed for $x \leq 0.1$ according to Eq. (64). In addition to nuclear shadowing, the nuclear gluon PDF is enhanced (antishadowed). The antishadowing of gluons is constrained using the momentum sum rule,

$$\sum_{j=q,\bar{q},g} \int_0^1 dx x f_{j/A}(x, Q^2) = 1. \quad (118)$$

In our numerical analysis, we model the gluon antishadowing at the initial scale $Q_0^2 = 4$

GeV² in the interval $0.03 \leq x \leq 0.2$ using the following simple form,

$$\frac{f_{g/A}(x, Q_0^2)}{Af_{g/N}(x, Q_0^2)} = \frac{f_{g/A}(x, Q_0^2)}{Af_{g/N}(x, Q_0^2)} [\text{given by Eq.(64)}] + \Theta(0.03 \leq x \leq 0.2) N_{\text{anti}} (0.2 - x)(x - 0.03), \quad (119)$$

where the free parameter N_{anti} is found by requiring the conservation of the momentum sum rule, see Eq. (118). Table 1 summarizes the used numerical values of N_{anti} for different nuclei. Note that Eq. (118) constrains N_{anti} rather weakly: large variations of N_{anti} lead to insignificant changes in the momentum sum rule. Hence, the values of N_{anti} in Table 1 should not be taken too literally—the momentum sum rule is a poor way to constrain antishadowing.

Nucleus	N_{anti}
¹² C	5
⁴⁰ Ca	20
¹¹⁰ Pd	25
¹⁹⁷ Au	30
²⁰⁸ Pb	30

Table 1

The parameter N_{anti} that controls the magnitude of antishadowing, see Eq. (119), as a function of the nuclear atomic number A .

In Eq. (119), the first term is evaluated using Eq. (64); on the $0.1 \leq x \leq 0.2$ interval, it is set to unity. In addition, we assume that the gluon PDF is not modified for $x > 0.2$, $f_{g/A}/(Af_{g/N}) = 1$.

As was mentioned above, we do not attempt to give numerical predictions for valence nuclear PDFs. Instead, we use the results of the global QCD fit of Eskola and collaborators [39,40].

5.1.5 Input nuclear charm quark PDF

The QCD analysis of the H1 diffractive data [67,60–62] assumes that the charm quark diffractive PDF is zero at the initial scale Q_0 . As a result, the naive application of our master Eq. (64) for the calculation of nuclear shadowing for charm quarks gives no nuclear shadowing in this channel, $f_{c/A}(x, Q_0^2)/[Af_{c/N}(x, Q_0^2)] = 1$. However, there is no reason for such an approximation.

At small values of Bjorken x , charm quarks are mostly produced via the QCD evolution because of the $g \rightarrow c\bar{c}$ splitting. Thus, nuclear shadowing for the charm quarks at some

x and $Q^2 = Q_0^2$ originates from nuclear shadowing of gluons at larger x and a certain $Q_{\text{eff}}^2 > Q_0^2$. In our analysis, we use the following model [75]:

$$\frac{f_{c/A}(x, Q_0^2)}{Af_{c/N}(x, Q_0^2)} = \frac{f_{g/A}(2x, Q_{\text{eff}}^2)}{Af_{g/N}(2x, Q_{\text{eff}}^2)}, \quad (120)$$

where $Q_{\text{eff}}^2 = 4m_c^2 + Q_0^2 = 11 \text{ GeV}^2$ ($m_c = 1.3 \text{ GeV}$).

In practice, the following procedure was performed. First, using Eq. (64) and the QCD evolution, we find the gluon PDF, assuming no nuclear shadowing for charm quarks. Second, we use Eq. (120) to determine the charm nuclear PDF at the input scale Q_0^2 . Third, we repeat the QCD evolution, this time with the shadowed charm quarks, which gives us the final result for nuclear PDFs of all flavors and for all scales.

5.1.6 Predictions for nuclear PDFs

We present the results of our calculations of nuclear PDFs in terms of the following ratios:

$$\begin{aligned} R_j &= \frac{f_{j/A}(x, Q^2)}{Af_{j/N}(x, Q^2)}, \\ R_{F_2} &= \frac{F_{2A}(x, Q^2)}{AF_{2N}(x, Q^2)}, \end{aligned} \quad (121)$$

where $Af_{j/N} \equiv Zf_{j/p} + Nf_{j/n}$; $AF_{2N} \equiv ZF_{2p} + NF_{2n}$; the subscripts p and n refer to the proton and neutron, respectively. For the PDFs and structure functions of the neutron, we used the charge symmetry, e.g., $f_{u/n}(x, Q^2) = f_{d/p}(x, Q^2)$.

Figures 31, 32, 33, and 34 present our predictions for R_j and R_{F_2} for the nuclei of ^{40}Ca and ^{208}Pb .

In Figs. 31 and 32, we compare predictions made using the two models for the effective cross section σ_{soft}^j that we discussed in Sec. 5.1.2. The curves labeled "FGS10_H" correspond to the calculation with $\sigma_{\text{soft}}^{j(\text{H})}(x, Q_0^2)$ given by Eq. (106); the curves labeled "FGS10_L" correspond to the calculation with $\sigma_{\text{soft}}^{j(\text{L})}(x, Q_0^2)$ of Eq. (115). (The effective cross sections $\sigma_{\text{soft}}^{j(\text{H})}(x, Q_0^2)$ and $\sigma_{\text{soft}}^{j(\text{L})}(x, Q_0^2)$ are compared in Fig. 29.) The curves in Fig. 31 correspond to the input scale $Q_0^2 = 4 \text{ GeV}^2$; the curves in Fig. 32 correspond to $Q_0^2 = 100 \text{ GeV}^2$. The four upper panels are for ^{40}Ca ; the four lower panels are for ^{208}Pb . One can see from Fig. 31 that the difference in the predictions of nuclear shadowing in the two models is not large (it is smaller than the uncertainty associated with the diffractive slope B_{diff}). Moreover, as one can see from Fig. 32, the difference between the two models decreases with increasing Q^2 .

In Figs. 33 and 34, R_j and R_{F_2} are given as functions of Bjorken x for $Q^2 = 4 \text{ GeV}^2$ (input) and $Q^2 = 10, 100$ and $10,000 \text{ GeV}^2$ (after the QCD evolution). For the R_j ratio, the predictions are given for the \bar{u} and c quarks and gluons. For R_{F_2} , next-to-leading (NLO) nuclear and nucleon structure functions are used.

Several features of our predictions need to be pointed out. First, at the input scale, $Q_0^2 = 4 \text{ GeV}^2$, and also after the evolution to not very large Q^2 , nuclear shadowing in the gluon channel is larger than in the quark channel. This is a natural consequence of the fact that the gluon diffractive PDF is much larger than the quark ones, see Fig. 19. As one increases Q^2 , nuclear shadowing in the gluon channel decreases faster than in the quark channel and rapidly becomes compatible to that in the quark channel. This is the effect of antishadowing for the gluon nPDF, which feeds into the QCD evolution equations and reduces nuclear shadowing in the gluon channel for $Q^2 > Q_0^2$.

Second, the Q^2 evolution of R_j and R_{F_2} is slow. This is a manifestation of the leading twist nature of nuclear shadowing in our approach.

Third, nuclear shadowing is larger for heavier nuclei.

Figures 33 and 34 give just several examples of our predictions for nuclear PDFs and nuclear structure functions. The complete set of predictions, which involve the nuclei of ^{12}C , ^{40}Ca , ^{110}Pd , ^{197}Au and ^{208}Pb and cover the wide kinematics range of $10^{-5} \leq x \leq 0.95$ and $4 \leq Q^2 \leq 10,000 \text{ GeV}^2$, can be found at <http://www.jlab.org/~vguzey>. In addition, these predictions and the predictions of all groups performing global fits to nuclear PDFs can be conveniently and easily obtained using the online generator of nuclear PDFs at <http://laphth.in2p3.fr/npdfgenerator>.

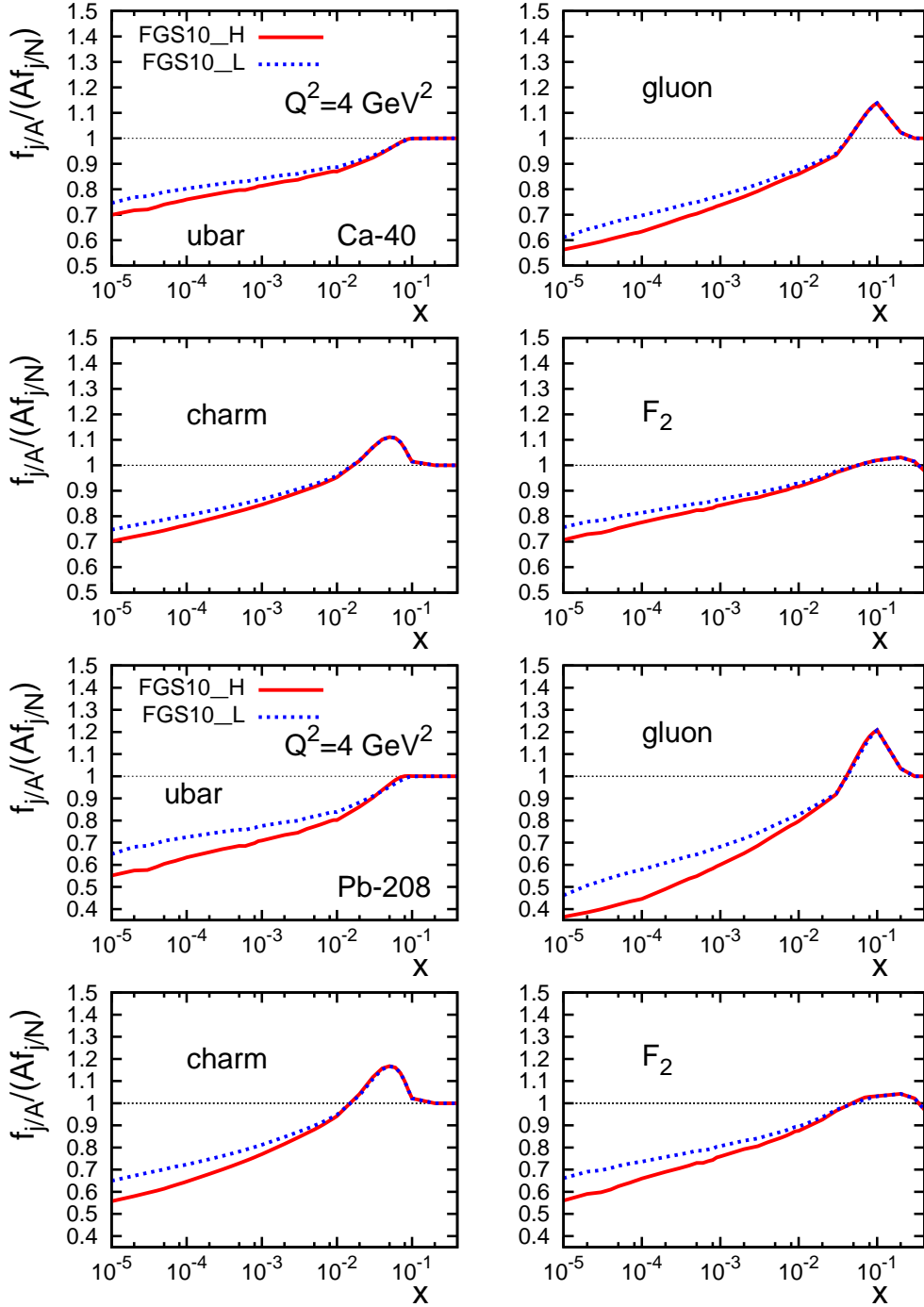


Fig. 31. Predictions for nuclear shadowing at the input scale $Q_0^2 = 4 \text{ GeV}^2$. The ratios R_j (\bar{u} and c quarks and gluons) and R_{F_2} as functions of Bjorken x at $Q^2 = 4$. The four upper panels are for ^{40}Ca ; the four lower panels are for ^{208}Pb . Two sets of curves correspond to models FGS10_H and FGS10_L (see the text).

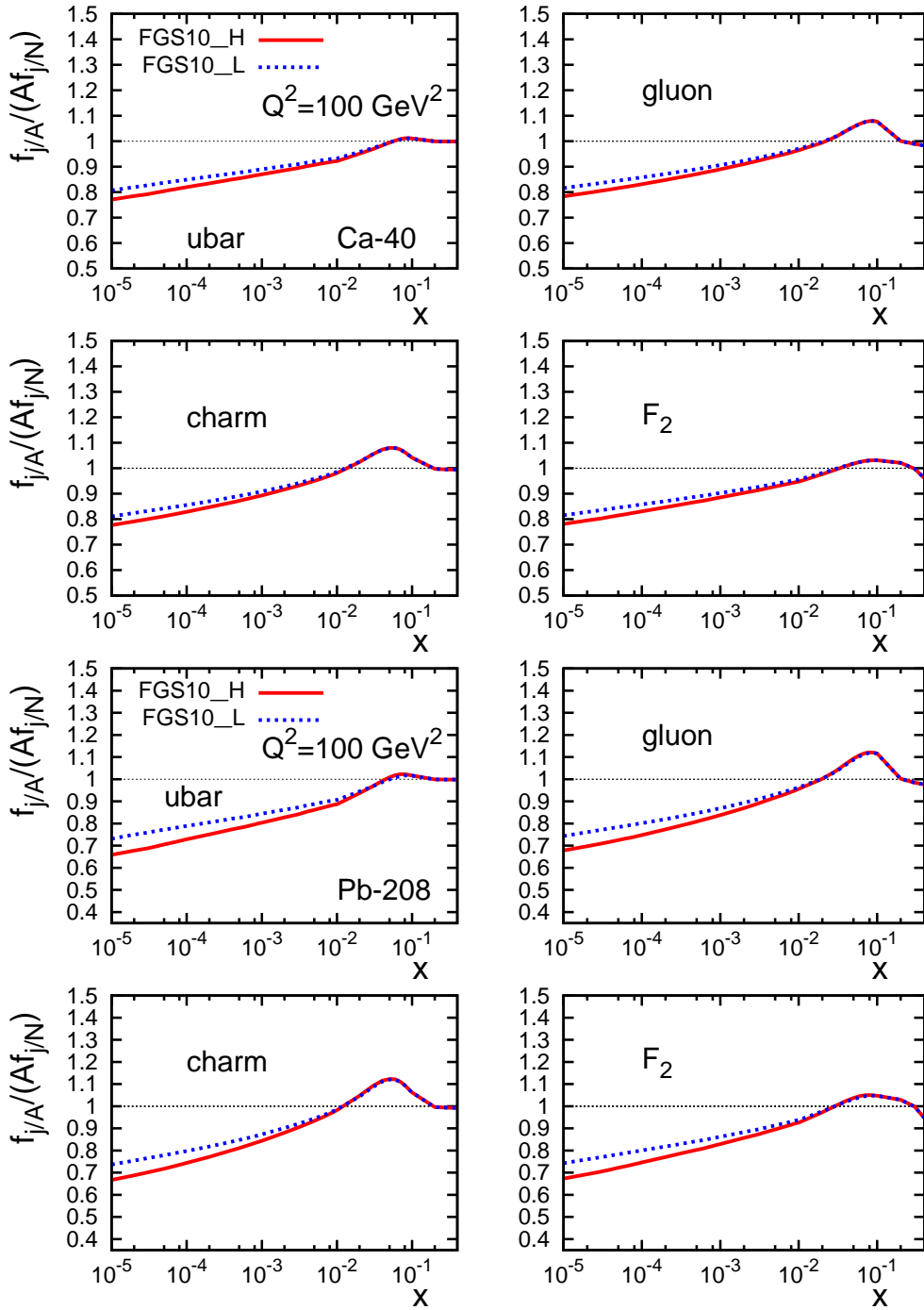


Fig. 32. The same as in Fig. 31, but the ratios are evaluated at $Q^2 = 100 \text{ GeV}^2$.

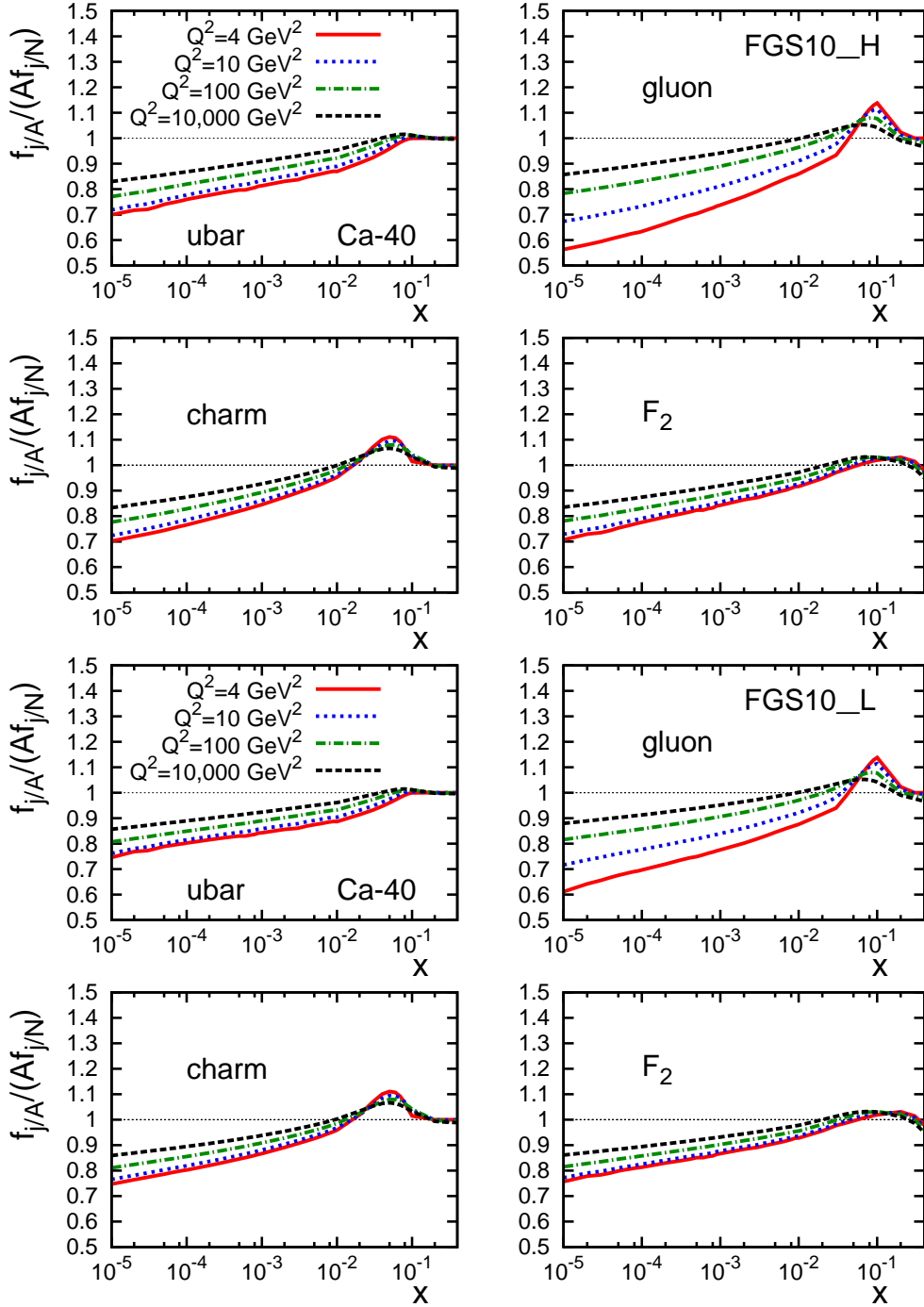


Fig. 33. Prediction for nuclear PDFs and structure functions for ^{40}Ca . The ratios R_j (\bar{u} and c quarks and gluons) and R_{F_2} as functions of Bjorken x at $Q^2 = 4, 10, 100$ and $10,000 \text{ GeV}^2$. The four upper panels correspond to FGS10_H; the four lower panels correspond to FGS10_L.

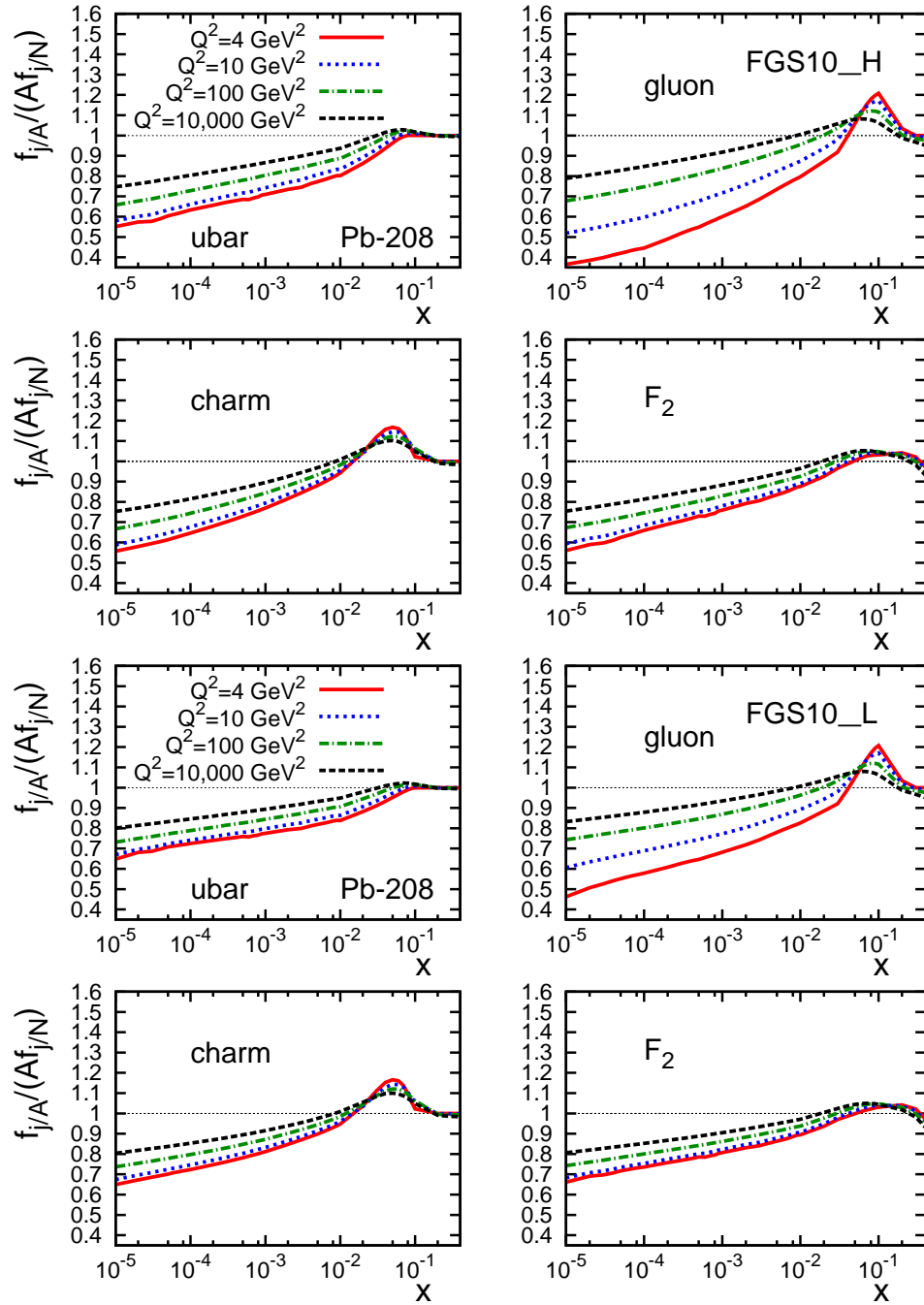


Fig. 34. Prediction for nuclear PDFs and structure functions for ^{208}Pb . The ratios R_j (\bar{u} and c quarks and gluons) and R_{F_2} as functions of Bjorken x at $Q^2 = 4, 10, 100$ and $10,000 \text{ GeV}^2$. The four upper panels correspond to FGS10_H; the four lower panels correspond to FGS10_L.

5.2 Nuclear shadowing in longitudinal structure function $F_L^A(x, Q^2)$

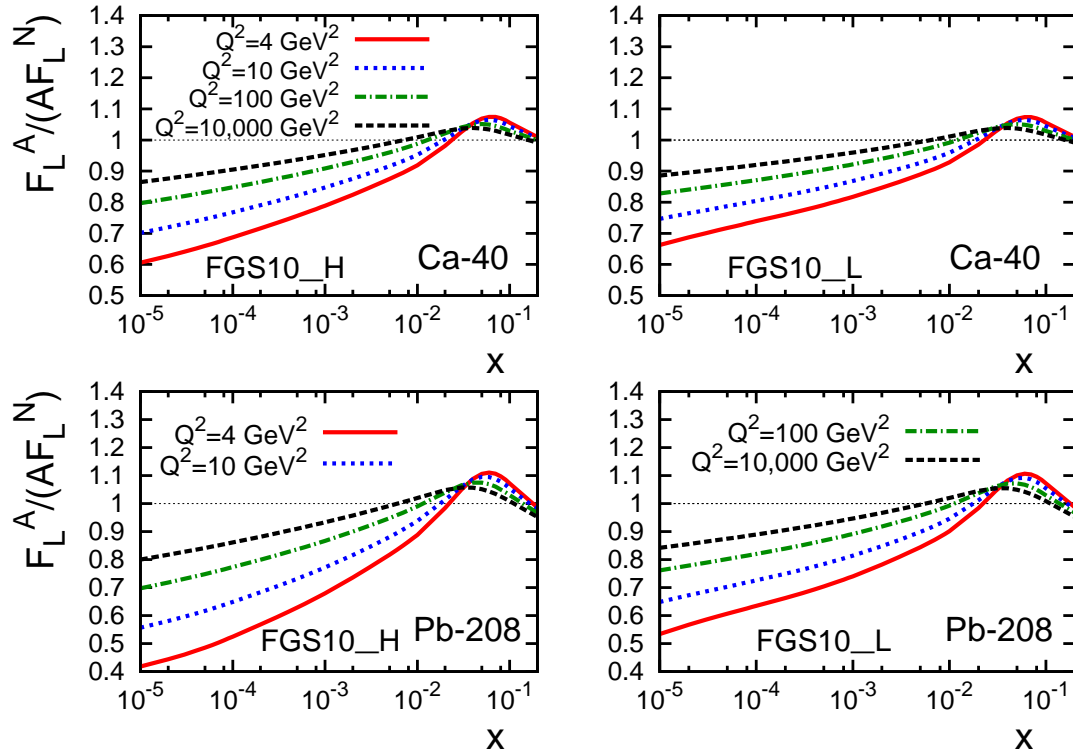


Fig. 35. Nuclear shadowing for the longitudinal structure function $F_L(x, Q^2)$. The ratio of the nuclear to nucleon longitudinal structure functions, $F_L^A(x, Q^2)/[AF_L^N(x, Q^2)]$, as a function of Bjorken x for different values of Q^2 . The upper row of panels corresponds to ^{40}Ca ; the lower row is for ^{208}Pb . Two sets of curves correspond to models FGS10_H and FGS10_L.

The longitudinal structure function $F_L(x, Q^2)$ is sensitive to the gluon distribution at small x . To the leading order in the strong coupling constant α_s , it reads [58]:

$$F_L(x, Q^2) = \frac{2\alpha_s(Q^2)}{\pi} \int_x^1 \frac{dy}{y} \left(\frac{x}{y}\right)^2 \sum_q^{n_f} e_q^2 \left[\left(1 - \frac{x}{y}\right) yg(y, Q^2) + \frac{2}{3} \left(yq(y, Q^2) + y\bar{q}(y, Q^2)\right) \right], \quad (122)$$

where the sum runs over quark flavors; n_f is the number of active flavors at given Q^2 .

Figure 35 presents our predictions for the ratio of the nuclear to nucleon longitudinal structure functions, $F_L^A(x, Q^2)/[AF_L^N(x, Q^2)]$, as a function of Bjorken x at different values of Q^2 . The upper row of panels corresponds to ^{40}Ca ; the lower row is for ^{208}Pb . The two sets of curves correspond to models FGS10_H and FGS10_L. As one can see from the figure, the amount of nuclear shadowing for $F_L^A(x, Q^2)$ is compatible with that of the

nuclear gluon PDF, see Figs. 33 and 34.

As we explained in the Introduction, the measurement of the longitudinal structure function in inclusive DIS with nuclei presents a new and promising opportunity to determine the nuclear gluon parton distribution.

Large nuclear shadowing effects in the nuclear longitudinal structure function, which are similar in magnitude to the large nuclear shadowing in the nuclear gluon distribution, were also predicted in the approach based on nPDFs extracted from the global QCD fits to the available data for $x \geq 10^{-2}$ and various guesses about the behavior of nPDFs at smaller x [173].

Another important quantity related to the longitudinal structure function is the ratio of the virtual photon-target cross sections for the longitudinal and transverse polarizations of the virtual photon,

$$R \equiv \frac{\sigma_L}{\sigma_T} = \frac{F_L(x, Q^2)}{F_2(x, Q^2) - F_L(x, Q^2)}. \quad (123)$$

Below we present our predictions for the super-ratio R_A/R_N , which is the ratio of the nuclear to the nucleon ratios R :

$$\begin{aligned} \frac{R_A}{R_N} &\equiv \frac{F_L^A(x, Q^2)}{F_{2A}(x, Q^2) - F_L^A(x, Q^2)} \frac{F_{2N}(x, Q^2) - F_L^N(x, Q^2)}{F_L^N(x, Q^2)} \\ &= \frac{F_L^A(x, Q^2)}{AF_L^N(x, Q^2)} \frac{AF_{2N}(x, Q^2)}{F_{2A}(x, Q^2)} \frac{1 - F_L^N(x, Q^2)/F_{2N}(x, Q^2)}{1 - F_L^A(x, Q^2)/F_{2A}(x, Q^2)}. \end{aligned} \quad (124)$$

The advantage of considering the super-ratio R_A/R_N is that this quantity is essentially insensitive to the value of the elementary ratio R_N .

Figure 36 presents our predictions for R_A/R_N of Eq. (124) for ^{40}Ca and ^{208}Pb for four different values of Q^2 as a function of Bjorken x . Both models FGS10.H and FGS10.L give numerically indistinguishable predictions for R_A/R_N . Also, as one can see from Fig. 36, the predicted A dependence of R_A/R_N is rather weak, but still non-negligible. (This also naturally applies to the ratio R_A .)

The trend of the x behavior of R_A/R_N can be understood as follows. For small x , $x \leq 10^{-3}$, and not too large Q^2 , $Q^2 \leq 10 \text{ GeV}^2$, the suppression of $F_L^A/(AF_L^N)$ due to nuclear shadowing is larger than that of $F_{2A}/(AF_{2N})$ (the nuclear gluon PDF is shadowed more than the quark nuclear PDFs), which makes $R_A/R_N < 1$. As one increases x , antishadowing begins to play a role, which makes $F_L^A/(AF_L^N) > 1$, see Fig. 35. As a result, $R_A/R_N > 1$ for approximately $5 \times 10^{-3} \leq x \leq 0.2$.

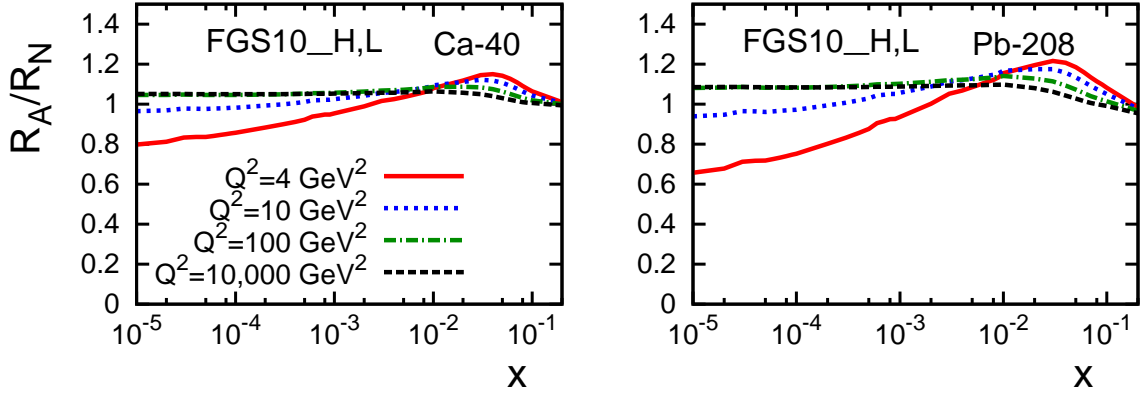


Fig. 36. The super-ratio R_A/R_N of Eq. (124) as a function of Bjorken x for different values of Q^2 . Models FGS10_H and FGS10_L give numerically indistinguishable predictions.

One has to note that as an input for our calculation of the R factor, we use the nucleon longitudinal structure function $F_L^N(x, Q^2)$ that we calculate using the CTEQ5M parton distributions. A comparison of our predictions for $F_L^N(x, Q^2)$ to the ZEUS [174] and H1 [175] data on $F_L^N(x, Q^2)$ shows that our predictions somewhat overestimate the data. At the same time, NLO and NNLO predictions made with contemporary parton distributions describe the data reasonably well [175]. An inspection shows that the CTEQ5M gluon distribution at small x is significantly larger than, e.g., the CT10 gluon distribution [176] which explains our overestimate of the HERA data on $F_L^N(x, Q^2)$.

5.3 Energy and Q^2 dependence of nuclear shadowing

It is also important to study the energy dependence (the dependence on Bjorken x) and Q^2 dependence of nuclear shadowing. In the following, we consider the shadowing corrections to the structure function $F_{2A}(x, Q^2)$ and to the gluon distribution $g_A(x, Q^2)$ defined respectively as

$$\begin{aligned}\delta F_{2A}(x, Q^2) &\equiv F_{2A}(x, Q^2) - ZF_{2p}(x, Q^2) - (A - Z)F_{2p}(x, Q^2), \\ \delta xg_A(x, Q^2) &\equiv xg_A(x, Q^2) - Axg_N(x, Q^2).\end{aligned}\tag{125}$$

These quantities are less sensitive to uncertainties in the nucleon PDFs at $x \sim 10^{-4}$ and $Q^2 \sim 4 \text{ GeV}^2$. Figure 37 presents $\delta F_{2A}(x, Q^2)/A$ and $\delta xg_A(x, Q^2)/A$ as a function of Bjorken x at two values of Q^2 , $Q^2 = 4 \text{ GeV}^2$ and $Q^2 = 100 \text{ GeV}^2$. The two top rows of panels correspond to ^{40}Ca ; the two bottom rows correspond to ^{208}Pb . The solid curves correspond to FGS10_H; the dotted curves correspond to FGS10_L.

For small values of x , $x < 10^{-3}$, the curves in Fig. 37 can be economically parameterized by a simple analytical expression:

$$\begin{aligned}
\delta F_{2A}(x, Q^2)/A &\approx \delta N_{F_2} \left(\frac{0.00001}{x} \right)^{0.25}, \\
\delta x g_A(x, Q^2)/A &\approx \delta N_g \left(\frac{0.00001}{x} \right)^{0.25},
\end{aligned} \tag{126}$$

with the coefficients δN_{F_2} and δN_g summarized in Table 2.

	⁴⁰ Ca	⁴⁰ Ca	²⁰⁸ Pb	²⁰⁸ Pb
$Q^2 = 4 \text{ GeV}^2$	FGS10_H	FGS10_L	FGS10_H	FGS10_L
δN_{F_2}	-0.37	-0.31	-0.56	-0.43
δN_g	-6.0	-5.3	-8.7	-7.4
$Q^2 = 100 \text{ GeV}^2$	FGS10_H	FGS10_L	FGS10_H	FGS10_L
δN_{F_2}	-1.48	-1.25	-2.21	-1.74
δN_g	-17.8	-15.2	-26.5	-21.1

Table 2

The parameters δN_{F_2} and δN_g of Eq. (126).

The numerical value of the exponent $\lambda = 0.25$ in Eq. (126) can be understood as follows. The x dependence of nuclear shadowing at small x is primarily driven by the x_P dependence of the Pomeron flux $f_{P/p}(x_P) \propto 1/x_P^{(2\alpha_P-1)} \propto 1/x_P^{1.22}$. Therefore, in the very small x limit, one expects from Eq. (64) that, approximately,

$$\begin{aligned}
\delta F_{2A}(x, Q^2)/A &\propto \left(\frac{1}{x} \right)^{0.22}, \\
\delta x g_A(x, Q^2)/A &\propto \left(\frac{1}{x} \right)^{0.22},
\end{aligned} \tag{127}$$

which is consistent with our numerical result in Eq. (126).

When we present our predictions for nuclear shadowing in the form of the ratios of the nuclear to nucleon PDFs, it is somewhat difficult to see the leading twist nature of the predicted nuclear shadowing because of the rapid Q^2 dependence of the free nucleon structure functions and PDFs. In order to see the leading twist nuclear shadowing more explicitly, one should examine the absolute values of the shadowing corrections.

Figure 38 presents $|\delta F_{2A}(x, Q^2)/A|$ and $|\delta x g_A(x, Q^2)/A|$ as functions of Q^2 at fixed $x = 10^{-4}$ (first and third rows) and $x = 10^{-3}$ (second and fourth rows) for ⁴⁰Ca (four upper panels) and ²⁰⁸Pb (four lower panels). The solid curves correspond to FGS10_H; the dotted curves correspond to FGS10_L. Also, for comparison, presented by the dot-dashed curves, we give the impulse (unshadowed) contributions to $F_{2A}(x, Q^2)/A$ and $x g_A(x, Q^2)/A$, which are equal to $F_{2N}(x, Q^2)$ and $x g_N(x, Q^2)$, respectively.

One can draw several conclusions by examining the curves in Fig. 38. First, at $x = 10^{-4}$ and $x = 10^{-3}$, the difference in the predicted nuclear shadowing in models FGS10_H and FGS10_L (the difference between the solid and dotted curves) is essentially zero. Second, $|\delta F_{2A}(x, Q^2)|$ and $|\delta xg_A(x, Q^2)|$ do not disappear as Q^2 is increased, which means that the considered nuclear shadowing is not a higher twist ($1/Q^2$ power-suppressed) phenomenon. Third, the deviation of the dot-dashed curves from the solid and dotted curves increases as Q^2 is increased. This, again, points to the leading twist nature of nuclear shadowing, which may not be clearly seen in the ratios of the nuclear to nucleon structure functions and PDFs.

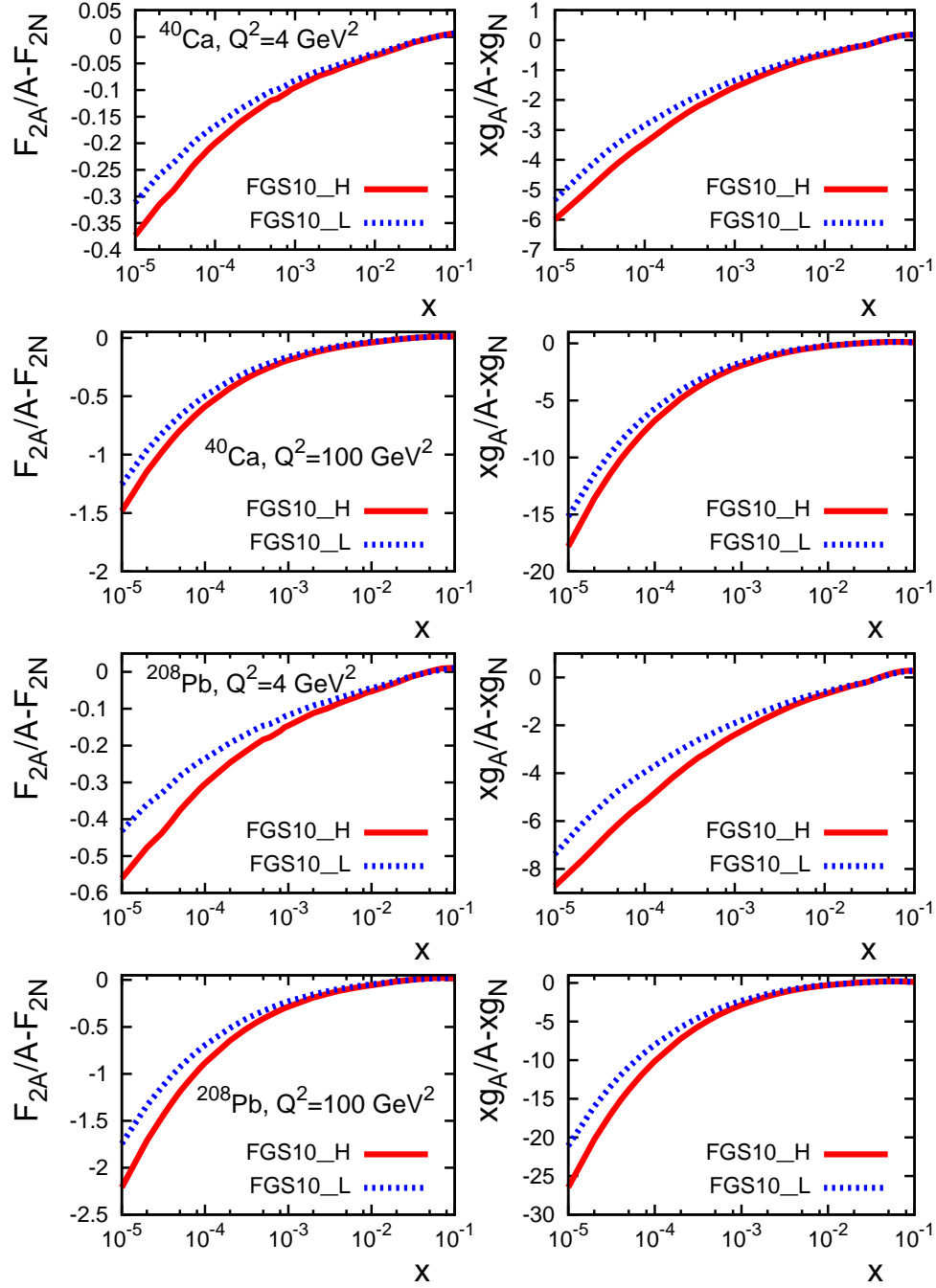


Fig. 37. The Bjorken x dependence of nuclear shadowing. The shadowing corrections per nucleon, $\delta F_{2A}(x, Q^2)/A$ and $\delta g_A(x, Q^2)/A$, see Eq. (125), as functions of Bjorken x at $Q^2 = 4 \text{ GeV}^2$ and $Q^2 = 100 \text{ GeV}^2$ for ^{40}Ca (four upper panels) and ^{208}Pb (four lower panels). The two sets of curves correspond to models FGS10_H and FGS10_L.

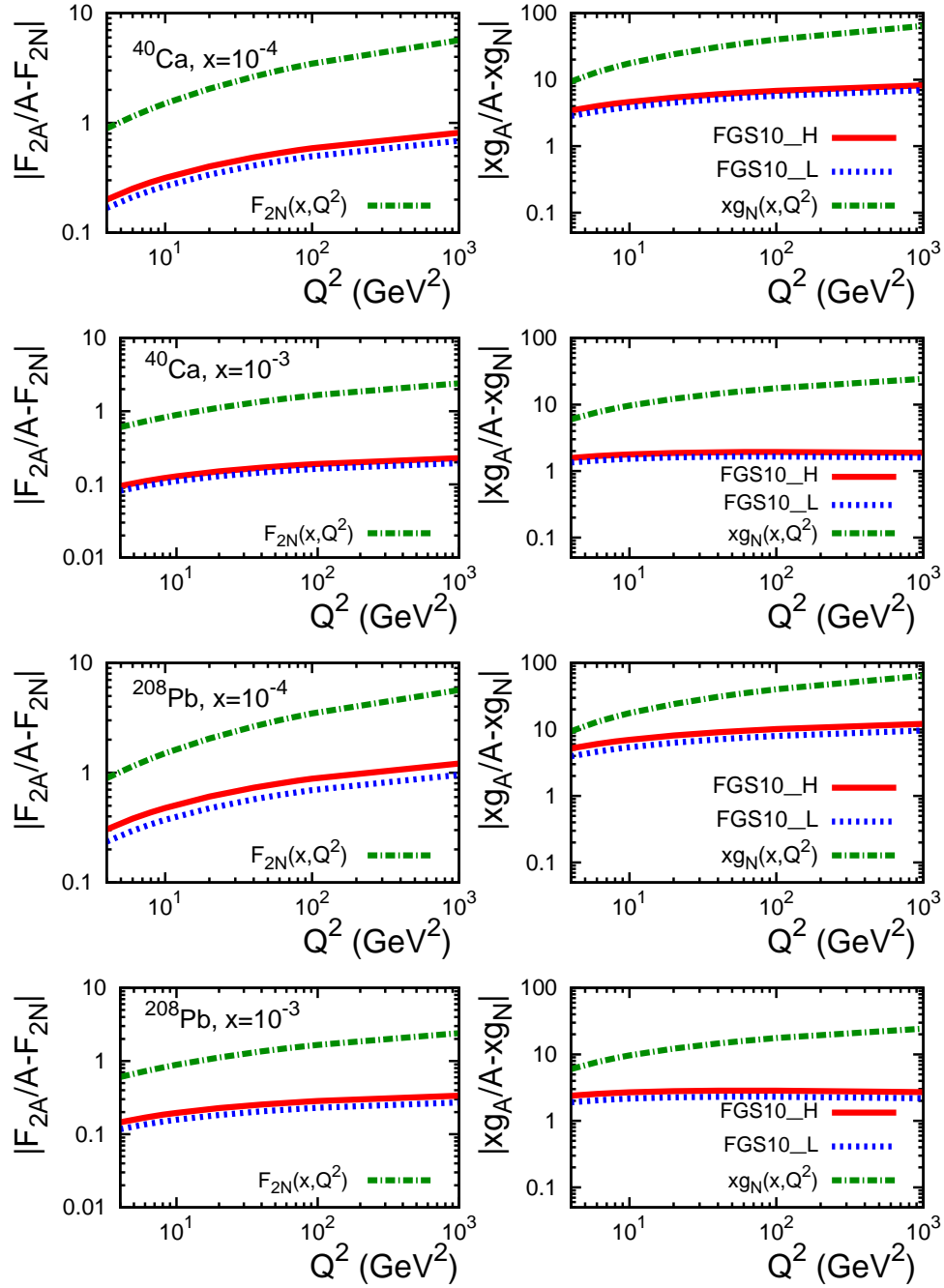


Fig. 38. The Q^2 dependence of nuclear shadowing. The shadowing corrections per nucleon, $\delta F_{2A}(x, Q^2)/A$ and $\delta g_A(x, Q^2)/A$, see Eq. (125), as functions of Q^2 at fixed $x = 10^{-4}$ and $x = 10^{-3}$ for ^{40}Ca (four upper panels) and ^{208}Pb (four lower panels). The solid curves is the result of FGS10_H; the dotted curves correspond to FGS10_L. For comparison, the dot-dashed curves present the impulse (unshadowed) contributions to $F_{2A}(x, Q^2)/A$ and $xg_A(x, Q^2)/A$, which are equal to $F_{2N}(x, Q^2)$ and $xg_N(x, Q^2)$, respectively.

5.4 The A dependence of nuclear shadowing

Using our predictions for nuclear PDFs, one can also examine the resulting A dependence of nuclear shadowing. An example of this is presented in Fig. 39, where we plot the $f_{j/A}(x, Q^2)/[Af_{j/N}(x, Q^2)]$ ratio as a function of the atomic mass number A for two values of x : $x = 10^{-4}$ and $x = 10^{-3}$. All curves correspond to our input scale $Q^2 = Q_0^2 = 4 \text{ GeV}^2$. The points (squares for $x = 10^{-4}$ and open circles for $x = 10^{-3}$) are the results of our calculations for $f_{j/A}(x, Q^2)/[Af_{j/N}(x, Q^2)]$ for ^{12}C , ^{40}Ca , ^{110}Pd , and ^{208}Pb ; the smooth curves is a two-parameter fit (for $A \geq 12$) in the form [81]:

$$\frac{f_{j/A}(x, Q^2)}{Af_{j/N}(x, Q^2)} = \lambda + a(1 - \lambda)/A^{1/3}, \quad (128)$$

where λ and a are free parameters of the fit; they are summarized in Table 3. Note that the fit in Eq. (128) is designed for $A \geq 12$. The form of the fit in Eq. (128) corresponds to the simple physical picture that assumes that the virtual photon wave function contains only two essential components: a point-like configuration (PLC) that has a small cross section and, hence, cannot be shadowed, and an effective large-size configuration, which is a subject to full-fledged nuclear shadowing.

	λ_{gluon}	a_{gluon}	λ_{ubar}	a_{ubar}
$x = 10^{-4}$				
FGS10_H	0.28	1.53	0.52	1.55
FGS10_L	0.46	1.38	0.65	1.40
$x = 10^{-3}$				
FGS10_H	0.48	1.54	0.62	1.58
FGS10_L	0.59	1.43	0.70	1.46

Table 3

The parameters λ and a of Eq. (128) that fits the A dependence of the $f_{j/A}(x, Q^2)/[Af_{j/N}(x, Q^2)]$ ratio.

The magnitude of the parameter λ is related to the size of the unshadowed PLC in the virtual photon wave function: the larger λ corresponds to the higher probability of the PLC. It is larger for the quark channel than for the gluon one. Also, as one increases energy (decreases x), the probability of the PLC expectedly decreases. One can also see that model FGS10_H corresponds to the smaller λ compared to model FGS10_L, which is understandable since FGS10_H provides larger nuclear shadowing than FGS10_L (the probability of the PLC in FGS10_H is suppressed compared to FGS10_L).

The second term in Eq. (128) is related to the probability of large-size configurations in the virtual photon wave function. These configurations are strongly shadowed and one expects

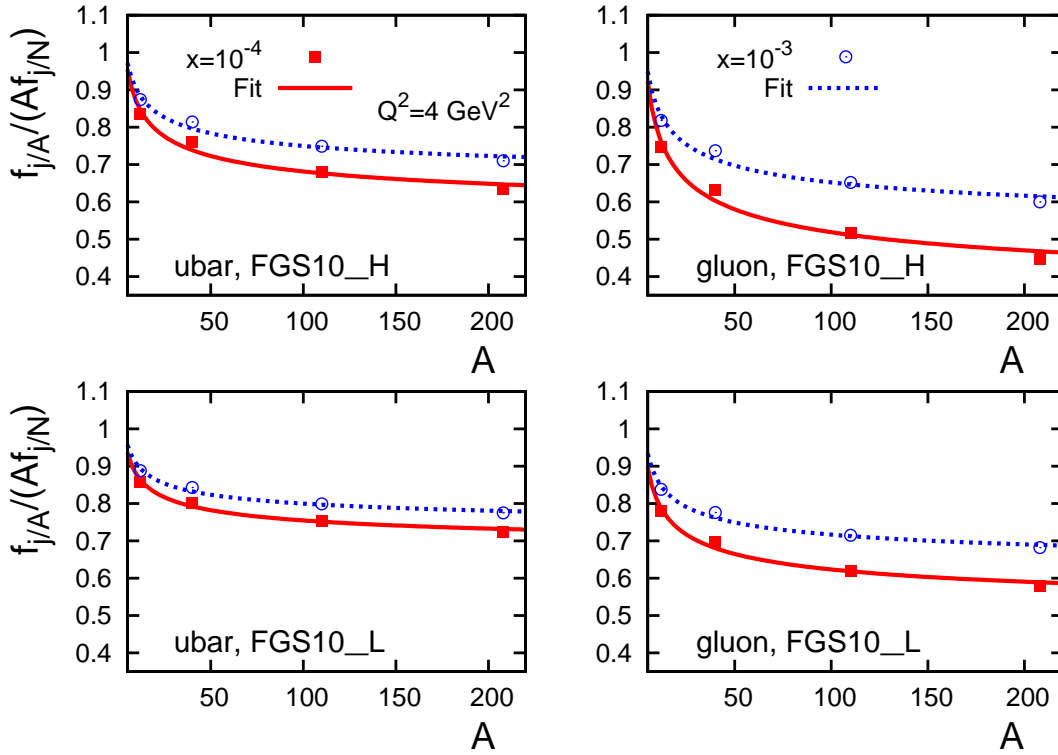


Fig. 39. The A dependence of nuclear shadowing. The points (squares for $x = 10^{-4}$ and open circles for $x = 10^{-3}$) are the results of our calculations for $f_{j/A}(x, Q^2)/[Af_{j/N}(x, Q^2)]$ for ^{12}C , ^{40}Ca , ^{110}Pd , and ^{208}Pb ; the smooth curves is a two-parameter fit of Eq. (128).

that the resulting shadowing correction should behave as $A^{2/3}$, i.e., the A dependence of the second term in the $f_{j/A}(x, Q^2)/[Af_{j/N}(x, Q^2)]$ ratio should behave as $1/A^{1/3}$.

5.5 Impact parameter dependent nuclear PDFs

Predictions of the leading twist theory of nuclear shadowing for nPDFs can be readily generalized to predict the dependence of nuclear PDFs on the impact parameter b . The impact parameter dependent nPDFs, $f_{j/A}(x, Q^2, b)$, can be introduced by the following relation [75]:

$$\int d^2\vec{b} f_{j/A}(x, Q^2, b) = f_{j/A}(x, Q^2). \quad (129)$$

Removing the integration over the impact parameter \vec{b} in our master equation (64), one immediately obtains the nuclear PDFs as functions of x and b :

$$\begin{aligned}
& x f_{j/A}(x, Q_0^2, b) = A T_A(b) x f_{j/N}(x, Q_0^2) \\
& - 8\pi A(A-1) B_{\text{diff}} \Re e \frac{(1-i\eta)^2}{1+\eta^2} \int_x^{0.1} dx_{\mathcal{P}} \beta f_j^{D(3)}(\beta, Q_0^2, x_{\mathcal{P}}) \\
& \times \int_{-\infty}^{\infty} dz_1 \int_{z_1}^{\infty} dz_2 \rho_A(\vec{b}, z_1) \rho_A(\vec{b}, z_2) e^{i(z_1-z_2)x_{\mathcal{P}}m_N} e^{-\frac{A}{2}(1-i\eta)\sigma_{\text{soft}}^j(x, Q_0^2) \int_{z_1}^{z_2} dz' \rho_A(\vec{b}, z')}, \quad (130)
\end{aligned}$$

where $T_A(b) = \int_{-\infty}^{\infty} dz \rho_A(\vec{b}, z)$. Note that the presence of the factor $T_A(b)$ in Eq. (130) is required by the condition of Eq. (129). The impact parameter dependent nPDFs, $f_{j/A}(x, Q^2, b)$, have the meaning of the probability to find parton j at the impact parameter b at the resolution scale Q^2 . In deriving Eq. (130) the finite size of the nucleon was neglected as compared to the nucleus size.

As we will discuss in Sec. 6.2, our impact parameter dependent nuclear PDFs are nothing else but the diagonal nuclear generalized parton distributions,

$$f_{j/A}(x, Q^2, b) = H_A^j(x, \xi = 0, b, Q^2). \quad (131)$$

Let us now discuss the spatial image of nuclear shadowing. This can be done by considering the ratio $R^j(x, b, Q^2)$:

$$R^j(x, b, Q^2) = \frac{f_{j/A}(x, Q^2, b)}{A T_A(b) f_{j/N}(x, Q^2)} = \frac{H_A^j(x, \xi = 0, b, Q^2)}{A T_A(b) f_{j/N}(x, Q^2)}. \quad (132)$$

The ratio $R^j(x, b, Q^2)$ of Eq. (132) for ^{40}Ca (upper green surfaces) and ^{208}Pb (lower red surfaces) as a function of x and $|\vec{b}|$ is presented in Fig. 40. The top panel corresponds to \bar{u} quarks; the bottom panel corresponds to gluons. All surfaces correspond to $Q^2 = 4 \text{ GeV}^2$ and to model FGS10_H of nuclear shadowing (see the previous discussion). Note that in the absence of nuclear shadowing, $R^j(x, b, Q^2) = 1$.

Several features of Fig. 40 deserve a discussion. First, as one can see from Fig. 40, the amount of nuclear shadowing—the suppression of $R^j(x, b, Q^2)$ compared to unity—increases as one decreases x and b . Second, nuclear shadowing for gluons is larger than for quarks. Third, nuclear shadowing induces non-trivial correlations between x and b in the nuclear GPD $H_A^j(x, 0, \vec{b}, Q^2)$, even if such correlations were absent in the free nucleon GPD. [In Eq. (130) we neglected the x - b correlations in the nucleon GPDs by neglecting the t dependence of $H_N^j(x, 0, t, Q^2)$ and using $H_N^j(x, 0, t, Q^2) \approx f_{j/N}(x, Q^2)$.]

To make the discussed features of the spatial image of nuclear GPDs presented in Fig. 40 more transparent, it is instructive to consider various two-dimensional slices of Fig. 40. In Fig. 41, we present $f_{j/A}/(A T_A(b) f_{j/N})$ as a function of x at the central impact parameter ($b = 0$) by the solid curves. For comparison, the dotted curves present the corresponding

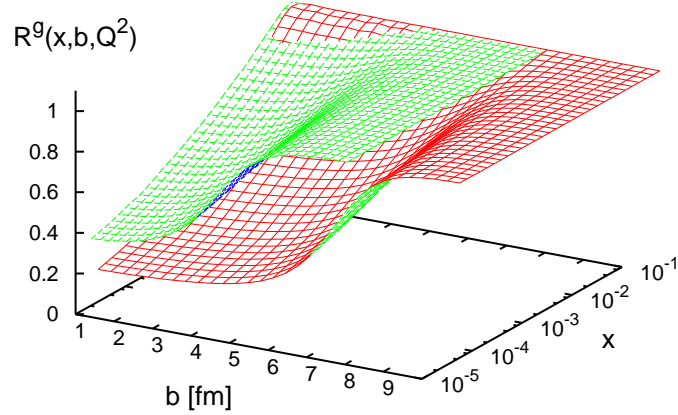
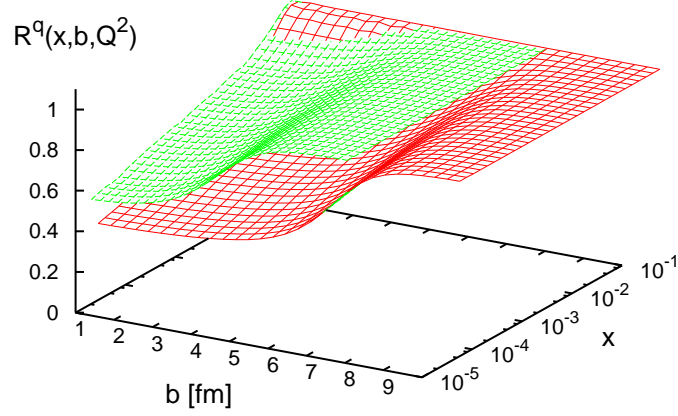


Fig. 40. Impact parameter dependence of nuclear shadowing for ^{40}Ca (upper green surfaces) and ^{208}Pb (lower red surfaces). The graphs show the ratio $R^j(x, b, Q^2)$ of Eq. (132) as a function of x and the impact parameter $|\vec{b}|$ at $Q^2 = 4 \text{ GeV}^2$. The top panel corresponds to \bar{u} -quarks; the bottom panel corresponds to gluons. For the evaluation of nuclear shadowing, model FGS10_H was used (see the text).

results for the b -integrated nPDFs (i.e., usual nPDFs), see Figs. 33 and 34. All curves correspond to our input scale $Q_0^2 = 4 \text{ GeV}^2$ and to model FGS10_H. Note that since nuclear shadowing depends on the impact parameter, so should antishadowing. We constrain the amount of antishadowing by requiring the conservation of the momentum sum rule locally in the impact parameter b [compare to Eq. (118)]:

$$\sum_{j=q,\bar{q}} \int_0^1 dx x f_{j/A}(x, Q^2, b) + \int_0^1 dx x g_A(x, Q^2, b) = 1. \quad (133)$$

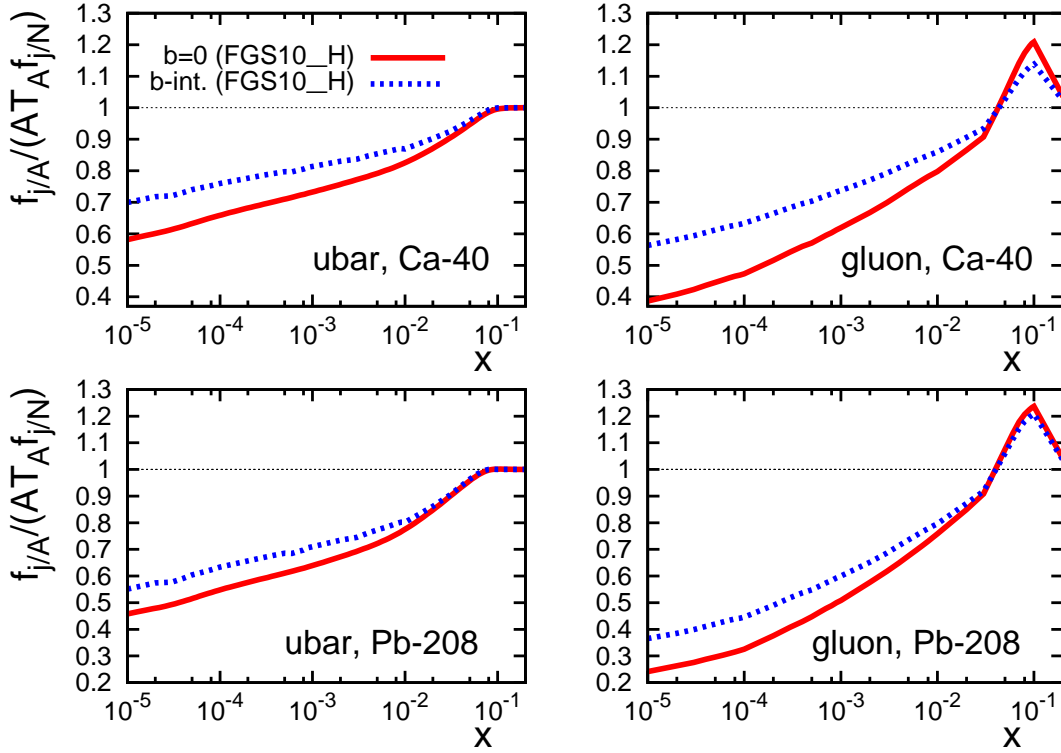


Fig. 41. The ratio $f_{j/A}/(AT_A(b)f_{j/N})$ as a function of x . The solid curves correspond to the central impact parameter ($b = 0$); the dotted curves are for the nPDFs integrated over all b (the same as in Figs. 33 and 34). All curves correspond to $Q_0^2 = 4 \text{ GeV}^2$ and to model FGS10_H.

As a result, the parameter N_{anti} that controls the amount of antishadowing [see Eq. (119)] depends on b : N_{anti} decreases from its maximal value at $b = 0$ (the corresponding values of N_{anti} are numerically close to those given in Table 1) to $N_{\text{anti}} = 0$ for large b .

As can be seen from Fig. 41, nuclear shadowing is larger at small impact parameters than that in the case when one integrates over all b . This is a natural consequence of the fact that the density of nucleons is larger in the center of the nucleus.

In Fig. 42, we plot $f_{j/A}/(AT_A(b)f_{j/N})$ as a function of the impact parameter b for three different values of x , $x = 10^{-4}$, $x = 10^{-3}$, and $x = 0.005$. All curves correspond to model FGS10_H and $Q_0^2 = 4 \text{ GeV}^2$. As one see from the figure, nuclear shadowing for gluons is larger than for quarks in essentially an entire region of b .

DIS off nuclear targets involves usual nPDFs that are integrated over all impact parameters b . However, using the fact the nuclear shadowing is local in the impact parameter [nuclear shadowing depends only on the nuclear density at a given b and will be same for two different nuclei, A_1 and A_2 , for the range of impact parameters satisfying the condition $A_1 T_{A_1}(b_1) = A_2 T_{A_2}(b_2)$], one can enhance the contribution of small b by considering special linear combinations of the structure functions (parton distributions) of different nuclei. In particular, one can effectively eliminate the contribution of single and

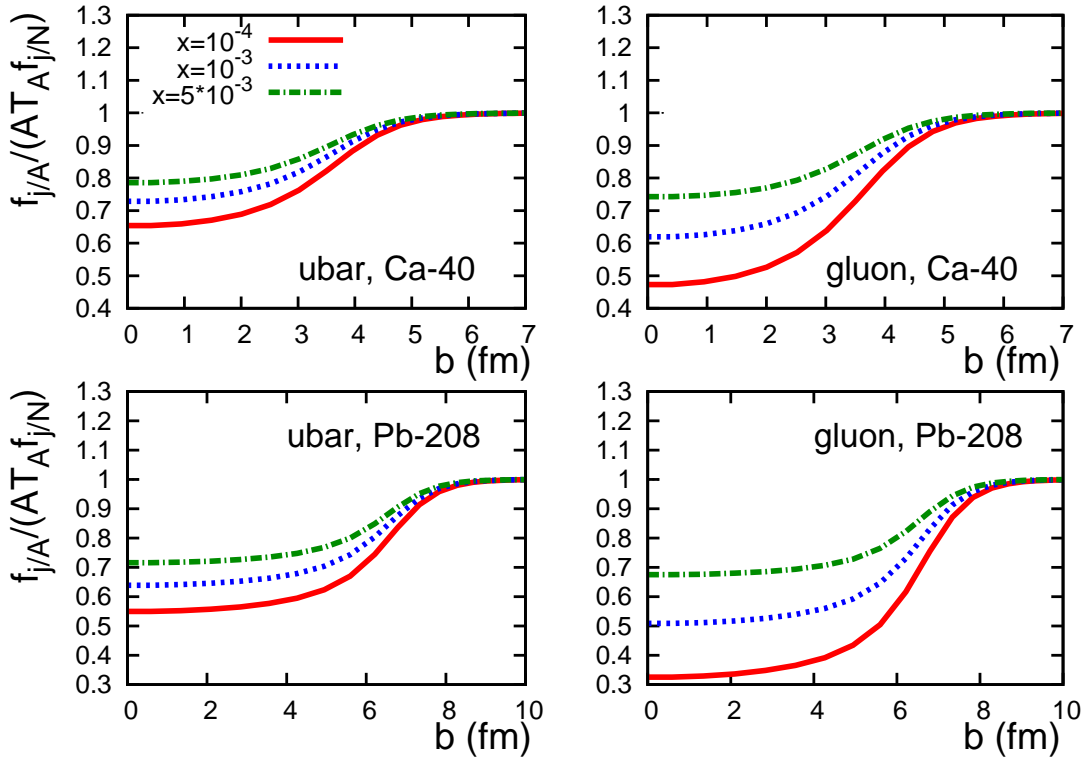


Fig. 42. The ratio $f_{j/A}/(AT_A(b)f_{j/N})$ as a function of the impact parameter b for fixed values of $x = 10^{-4}$, $x = 10^{-3}$, and $x = 0.005$. All curves correspond to FGS10_H and $Q_0^2 = 4 \text{ GeV}^2$.

double scattering, and, thus, essentially subtract the contribution of the nuclear edge (leave in mostly the contribution of the nuclear center) by considering, e.g., the following combination:

$$F_{2A}(x, Q^2) - \lambda_{A/A_0} F_{2A_0}(x, Q^2) - (A - \lambda_{A/A_0} A_0) F_{2N}(x, Q^2), \quad (134)$$

where A refers to a heavy nucleus; A_0 refers to a light nucleus (such as ^4He and ^{12}C); the parameter λ_{A/A_0} is defined as

$$\lambda_{A/A_0} \equiv \frac{\int d^2b A^2 T_A^2(b)}{\int d^2b A_0^2 T_{A_0}^2(b)}. \quad (135)$$

Since the expansion of the expression in Eq. (134) in the number of interactions with the target nucleons starts from the term proportional to $T_A^3(b)$, the combination in Eq. (134) has the support for the values of b that are more central (smaller) than those for the unsubtracted $F_{2A}(x, Q^2)$.

The dependence of nPDFs on the impact parameter and, thus, our predictions for nuclear shadowing as a function of the impact parameter b can be probed in proton-nucleus (pA) and nucleus-nucleus (AA) collisions, where the centrality (the impact parameter b) is

defined by the multiplicity of binary collisions. Examples of the application of the impact parameter dependent nPDFs involve inclusive production of pions [177] and J/ψ [178,179] in dA and AA collisions at RHIC and in pA and AA collisions at the LHC [180], where collisions with different centrality are selected using, e.g., the number of wounded nucleons.

Another opportunity to study the impact parameter dependence of nuclear shadowing is provided by hard exclusive processes with nuclei such as deeply virtual Compton scattering (DVCS) and vector meson electroproduction (see the detailed discussion in Sec. 6.2). The amplitudes of these reactions are expressed in terms of the convolution of the corresponding hard scattering coefficient functions and nuclear generalized parton distributions (GPDs). While in general those GPDs are complicated unknown distributions, at high energies (small Bjorken x), it is a good approximation [181] to use the (nuclear) GPDs in the $\xi = 0$ limit as the initial condition for the Q^2 evolution. This is because the initial condition is dominated by the large parton light-cone fractions $x_i \gg \xi$ and the dependence on ξ is not evolved; the off-diagonal effects (the effects of $\xi \neq 0$) are accounted for by the off-diagonal modifications of the QCD evolution kernels.

The leading twist nuclear shadowing in nuclear GPDs was analyzed in Ref. [182]. It was found that nuclear shadowing leads to clear experimental signatures: the shift toward smaller $|t|$ of the DVCS differential cross section and dramatic oscillations of the beam-spin DVCS asymmetry. These effects can be interpreted as the fact that the transverse size of parton distributions—as probed by hard probes—increases in nuclei. We shall address this issue in some detail in the following section.

Figures 40, 41, and 42 present only several examples of our predictions for impact-parameter dependent nuclear PDFs. The complete set of predictions for a wide range of nuclei (^{12}C , ^{40}Ca , ^{110}Pd , ^{197}Au and ^{208}Pb) and the kinematics range $10^{-5} \leq x \leq 0.95$ and $4 \leq Q^2 \leq 10,000 \text{ GeV}^2$ can be found at <http://www.jlab.org/~vguzey>.

5.6 *The transverse size of parton distributions in nuclei*

As we discussed in Sec. 5.5, the leading twist nuclear shadowing, which increases with decreasing the impact parameter b , leads to distinct experimental signatures that can be interpreted as the increase of the transverse size of the parton distributions in nuclei compared to the free nucleon. To quantify the effect, one can introduce the average transverse size of the parton distribution of flavor j in terms of the corresponding impact parameter dependent nuclear PDFs:

$$\langle b_j^2 \rangle \equiv \frac{\int d^2b b^2 f_{j/A}(x, Q^2, b)}{\int d^2b f_{j/A}(x, Q^2, b)}. \quad (136)$$

For comparison, the transverse size of the nuclear PDFs in the absence of nuclear shadowing (in the impulse approximation) is

$$\langle b_j^2 \rangle_{\text{imp}} = \frac{\int d^2b b^2 AT_A(b) f_{j/N}(x, Q^2)}{\int d^2b AT_A(b) f_{j/N}(x, Q^2)} = \int d^2b b^2 T_A(b) = \frac{R_A^2}{6}. \quad (137)$$

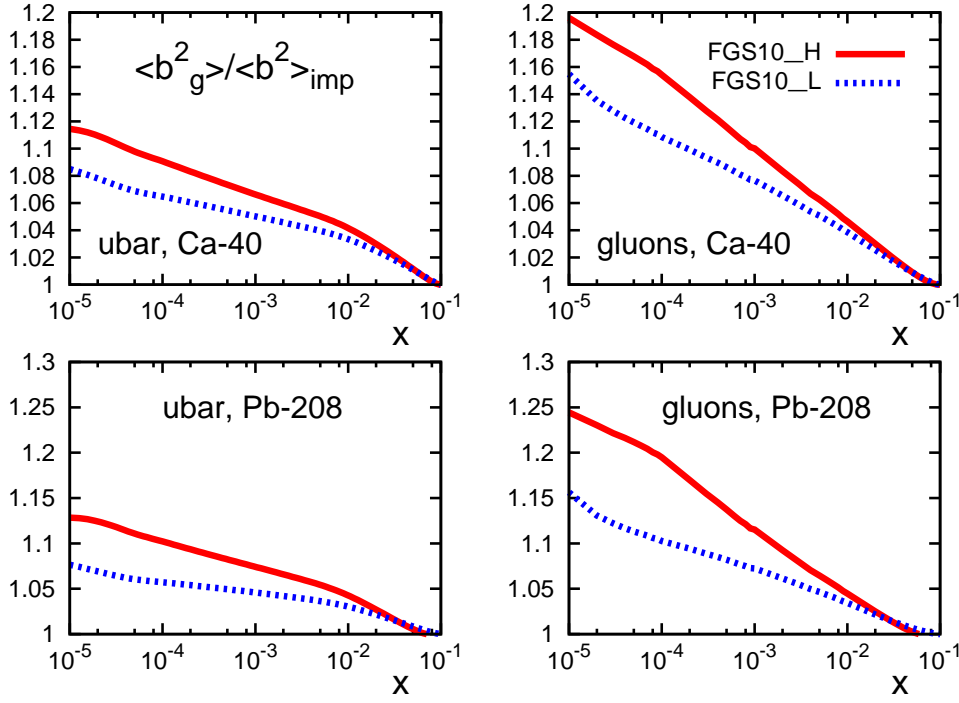


Fig. 43. The ratio $\langle b_j^2 \rangle / \langle b_j^2 \rangle_{\text{imp}}$ for the \bar{u} quarks and gluons in ^{40}Ca and ^{208}Pb as a function of Bjorken x at $Q^2 = 4 \text{ GeV}^2$. The two sets of curves correspond to models FGS10_H and FGS10_L.

The last equality follows from the relation between $T_A(b)$ and the nuclear radius R_A that parameterizes the nuclear form factor at small t , $F_A(t) = \exp(-R_A^2 t/6)$. It is given as a reference point—in our analysis we used $T_A(b)$ obtained from the nuclear density $\rho_A(r)$ [169]. Note that in deriving Eq. (137) we neglected the weak t dependence of the free nucleon GPDs compared to the strong t dependence of the nuclear form factor. In this approximation, $\langle b_j^2 \rangle_{\text{imp}}$ is flavor-independent.

The ratio $\langle b_j^2 \rangle / \langle b_j^2 \rangle_{\text{imp}}$ for the \bar{u} -quarks and gluons in ^{40}Ca and ^{208}Pb as a function of Bjorken x at $Q^2 = 4 \text{ GeV}^2$ is presented in Fig. 43. The solid curves correspond to model FGS10_H; the dashed curves correspond to model FGS10_L. As one can see from the figure, the leading twist nuclear shadowing leads to an increase of the transverse size of shadowed parton distributions in nuclei.

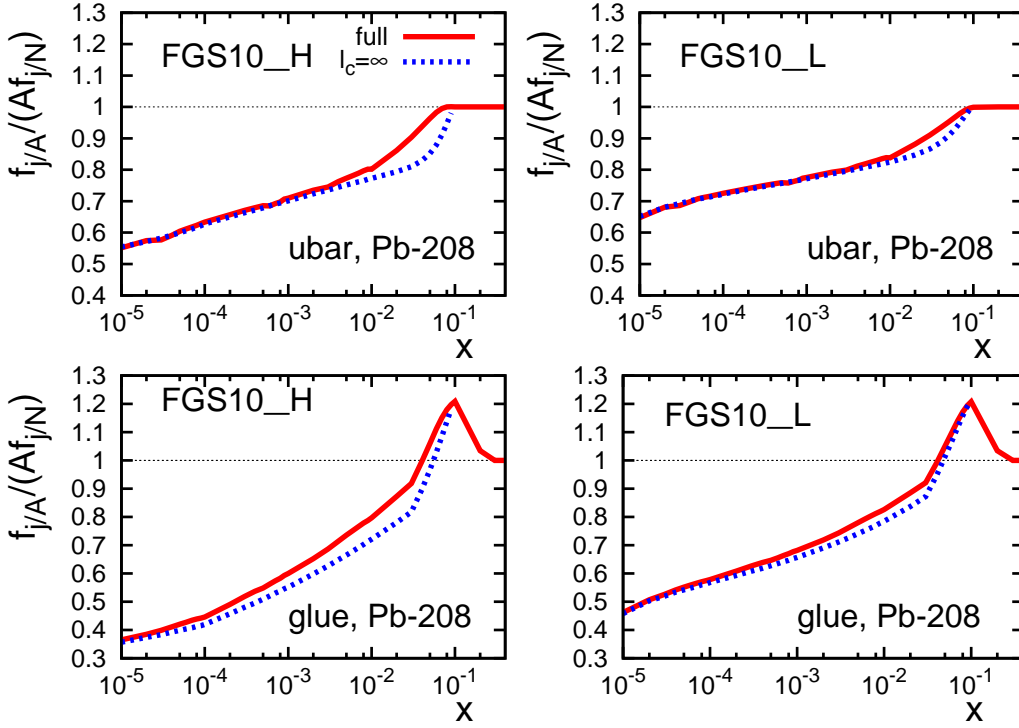


Fig. 44. The ratios of \bar{u} -quark and gluon PDFs in ^{208}Pb at $Q^2 = 4 \text{ GeV}^2$. The solid curves correspond to the full calculation using Eq. (64); the dashed curves correspond to the calculation with $e^{i(z_1-z_2)x_{\mathbb{P}m_N}} = 1$ in Eq. (64) or, equivalently, to the calculation using Eq. (65).

5.7 The role of the finite coherence length

The effect of the non-zero longitudinal momentum transfer Δ_{γ^*X} , see Eq. (36), or, in other words, the effect of the finite coherence length $l_c \propto 1/\Delta_{\gamma^*X} \neq \infty$, on nuclear shadowing is given by the factor $e^{i(z_1-z_2)x_{\mathbb{P}m_N}}$ in Eq. (64). At small values of Bjorken x , this factor can be neglected and after the integration by parts two times, Eq. (64) can be cast in a much simpler form, see Eq. (65).

Figure 44 compares the results of the full calculation using Eq. (64) (solid curves, same as in Figs. 34) with the calculation using the approximate expression of Eq. (65) (dashed curves). The presented results correspond to the ratios of \bar{u} -quark and gluon PDFs in ^{208}Pb at $Q^2 = 4 \text{ GeV}^2$. The effect of antishadowing is added as explained in Sect. 5.1.4. As one can see from Fig. 44, the effect of the finite coherence length l_c ($l_c \neq \infty$) can be safely neglected all the way up to at least $x = 10^{-2}$ for quarks. For gluons, the effect of the finite l_c is somewhat larger, though it is still a small correction for $x \leq 5 \times 10^{-3}$.

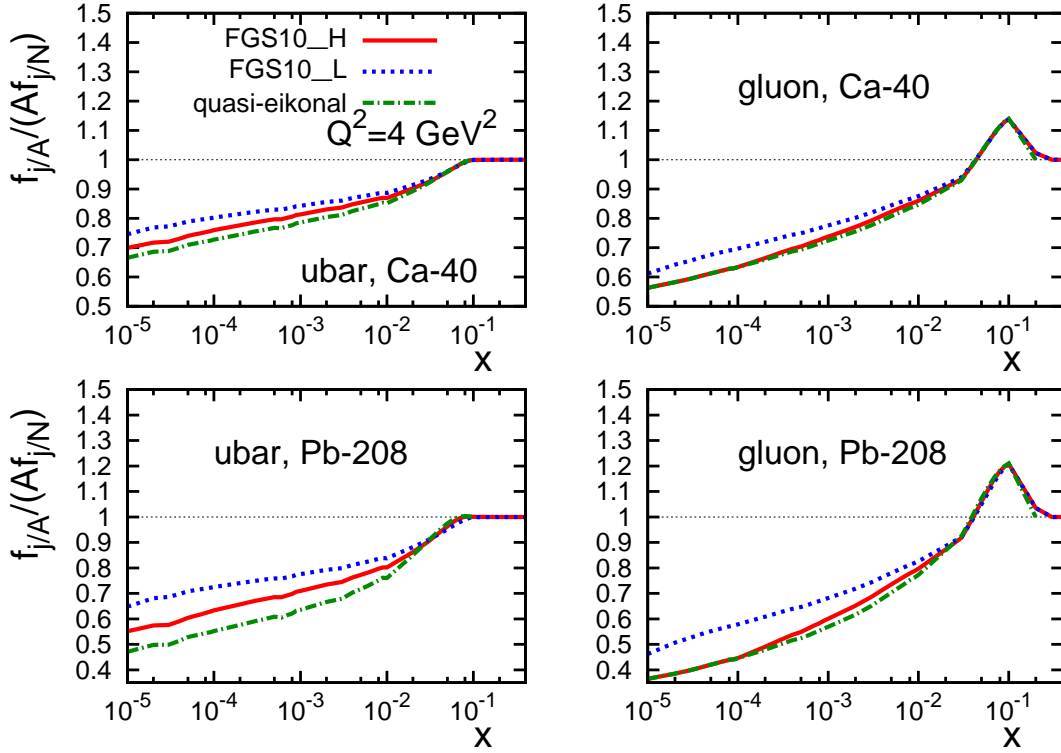


Fig. 45. Comparison of the color fluctuation and quasi-eikonal approximations. The solid and dotted curves correspond to the color fluctuation approximation (same as in Figs. 33 and 34); the dot-dashed curves correspond to the quasi-eikonal approximation.

5.8 Comparison of the color fluctuation and quasi-eikonal approximations

Our predictions for nuclear PDFs, which are based on the color fluctuation approximation for multiple interactions (models FGS10_H and FGS10_L), see Eq. (64), can be compared to the calculation of nuclear PDFs in the quasi-eikonal approximation [the approximation when one uses σ_2^j instead of σ_{soft}^j in Eq. (64)]. This is presented in Fig. 45, where the results of models FGS10_H and FGS10_L (the same curves as in Figs. 33 and 34) are compared to the dot-dashed curves corresponding to the quasi-eikonal approximation. All curves correspond to $Q^2 = 4 \text{ GeV}^2$.

To understand the results presented in Fig. 45, it is useful to recall the relative magnitude of the effective cross sections $\sigma_{\text{soft}}^{j(\text{H})}$, $\sigma_{\text{soft}}^{j(\text{L})}$ and σ_2^j presented in Fig. 29. In the quark channel, $\sigma_{\text{soft}}^{j(\text{L})} > \sigma_{\text{soft}}^{j(\text{H})} > \sigma_2^j$, and, hence, $f_{j/A}^{\text{FGS10-L}} > f_{j/A}^{\text{FGS10-H}} > f_{j/A}^{\text{qe}}$. In the gluon channel, the trend is quite similar with the only exception that for small x , $\sigma_{\text{soft}}^{j(\text{H})}$ and σ_2^j are very close ($\sigma_{\text{soft}}^{j(\text{H})} = \sigma_2^j$ for $x \leq 10^{-4}$ by construction), which means that $f_{j/A}^{\text{FGS10-H}} \approx f_{j/A}^{\text{qe}}$ ($f_{j/A}^{\text{FGS10-H}} = f_{j/A}^{\text{qe}}$ for $x \leq 10^{-4}$ by construction).

5.9 Uncertainties of predictions of the leading twist theory of nuclear shadowing

Our predictions for nuclear PDFs obtained in the framework of the leading twist theory of nuclear shadowing contain certain uncertainties. They include:

- (i) The experimental uncertainty in the slope of the t dependence of the diffractive structure function $F_2^{D(4)}$ reported by the H1 collaboration, $B_{\text{diff}} = 6 \pm 1.6 \text{ GeV}^{-2}$ [62] (Note that the ZEUS LPS value of B_{diff} is somewhat larger, $B_{\text{diff}} = 7.0 \pm 0.3 \text{ GeV}^{-2}$ [72].);
- (ii) The theoretical uncertainty related to the choice of the input scale Q_0^2 ;
- (iii) The uncertainty related to the color-fluctuation approximation for the interaction with $N \geq 3$ nucleons. This uncertainty manifests itself in the necessity to use two different models for the rescattering cross section σ_{soft}^j , which we called $\sigma_{\text{soft}}^{j(\text{H})}$ and $\sigma_{\text{soft}}^{j(\text{L})}$. This leads to the spread in the predictions for nuclear shadowing for small values of x (scenarios FGS10_H and FGS10_L), see the discussion and results in Sec. 5.1.2, 5.1.6, and 5.8.
- (iv) The uncertainty related to the choice of the nucleon PDFs, primarily the gluon PDF, at $x \sim 10^{-4}$ and $Q^2 = 4 \text{ GeV}^2$.

The largest uncertainty among the first three that we just mentioned is the statistical error in the value of B_{diff} , $B_{\text{diff}} = 6 \pm 1.6 \text{ GeV}^{-2}$, extracted from the H1 data taken with the forward proton spectrometer [62]. (Note that this value of B_{diff} is somewhat lower than the ZEUS LPS result, $B_{\text{diff}} = 7.0 \pm 0.3 \text{ GeV}^{-2}$ [72]. The two values are still consistent with each other within errors.) To assess the uncertainty of our predictions related to the experimental uncertainty in B_{diff} , we vary the used value of B_{diff} and repeat our calculations of nuclear PDFs using $B_{\text{diff}} = 6 - 1 = 5 \text{ GeV}^{-2}$ and $B_{\text{diff}} = 6 + 1 = 7 \text{ GeV}^{-2}$. In Fig. 46, we present the resulting nuclear PDFs in FGS10_H model: the central solid curves correspond to our standard choice $B_{\text{diff}} = 6 \text{ GeV}^{-2}$ (same as in Figs. 33 and 34); the shaded areas represent the theoretical uncertainty related to the experimental uncertainty in B_{diff} and fill in the area between the predictions with $B_{\text{diff}} = 5 \text{ GeV}^{-2}$ (upper boundary) and $B_{\text{diff}} = 7 \text{ GeV}^{-2}$ (lower boundary). The effect of the variation of B_{diff} in the calculation with model FGS10_L is similar to the one presented in Fig. 46.

Next we turn to the uncertainty related to our choice of the input evolution scale Q_0^2 . This uncertainty can be assessed as follows. Instead of taking the initial scale $Q_0^2 = 4 \text{ GeV}^2$, the leading twist nuclear PDFs can be evaluated at a different low input scale, for instance, at $Q_0^2 = 2.5 \text{ GeV}^2$. Then one can perform the QCD evolution from $Q_0^2 = 2.5 \text{ GeV}^2$ to $Q^2 = 4 \text{ GeV}^2$ and compare the result with the direct calculation at $Q_0^2 = 4 \text{ GeV}^2$. Potential differences between the two results characterize the theoretical uncertainty related to the choice of Q_0^2 . Since our results for the double scattering term ($N = 2$) do not depend on the choice of Q_0^2 , this analysis effectively checks how strongly the higher order terms ($N \geq 3$) are modified by the DGLAP evolution. This provides another way to access the role of the color fluctuations due to the interplay between the small-size and large-size configurations in the virtual photon wave function.

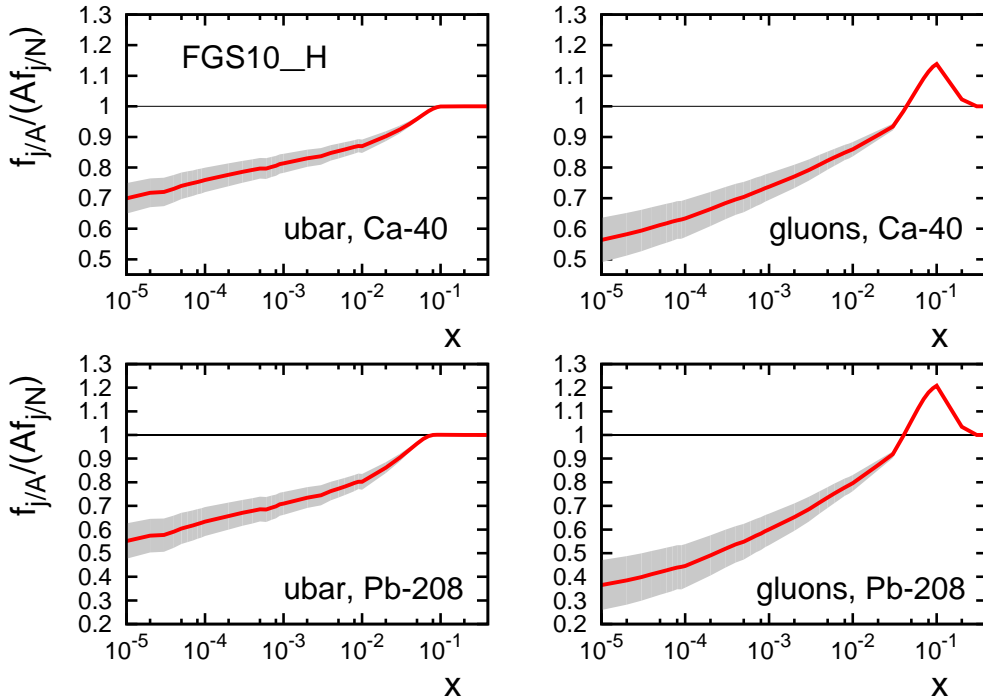


Fig. 46. Nuclear PDFs calculated with our standard choice $B_{\text{diff}} = 6 \text{ GeV}^{-2}$ (solid curves) and with $B_{\text{diff}} = 5 \text{ GeV}^{-2}$ and $B_{\text{diff}} = 7 \text{ GeV}^{-2}$ that correspond to the upper and lower boundaries of the shaded areas, respectively. All curves correspond to model FGS10_H and $Q_0^2 = 4 \text{ GeV}^2$.

The results of this procedure are presented in Fig. 47. In this figure, the solid and dot-dashed curves present the results of the direct calculation of nuclear PDFs at $Q_0^2 = 4 \text{ GeV}^2$ and $Q_0^2 = 2.5 \text{ GeV}^2$, respectively. One can see that the Q_0^2 dependence of quark PDFs is very weak for the $Q_0^2 = 2.5 \div 4 \text{ GeV}^2$ range, while the gluon shadowing changes quite significantly in this Q^2 interval. Performing the QCD evolution from $Q_0^2 = 2.5 \text{ GeV}^2$ to $Q^2 = 4 \text{ GeV}^2$, one obtains the dotted curves, which are indistinguishable from the solid ones. Therefore, the uncertainty related to our choice of Q_0^2 is negligibly small. All curves in Fig. 47 correspond to model FGS10_L.

The fact that nuclear shadowing in the gluon channel rather rapidly decreases after a very short Q^2 evolution is a consequence of the presence of antishadowing and large- x non-shadowed region (which corresponds to point-like configurations in the virtual photon). Indeed, because of the character of QCD evolution, nPDFs at small x and $Q^2 > Q_0^2$ originate from the larger values of Bjorken x , $x_0 > x$, at the input scale Q_0^2 . Therefore, the effects of antishadowing and the presence of non-shadowed point-like configurations (for $x > 0.2$ in our approach) feed into the QCD evolution and decrease nuclear shadowing after a few steps of the QCD evolution. For an addition discussion of QCD evolution of nPDFs, see Sect. 5.15.

We also stress that in the limit of the low nuclear density when the interaction with only two nucleons of the target is important (the deuteron target is the best example),

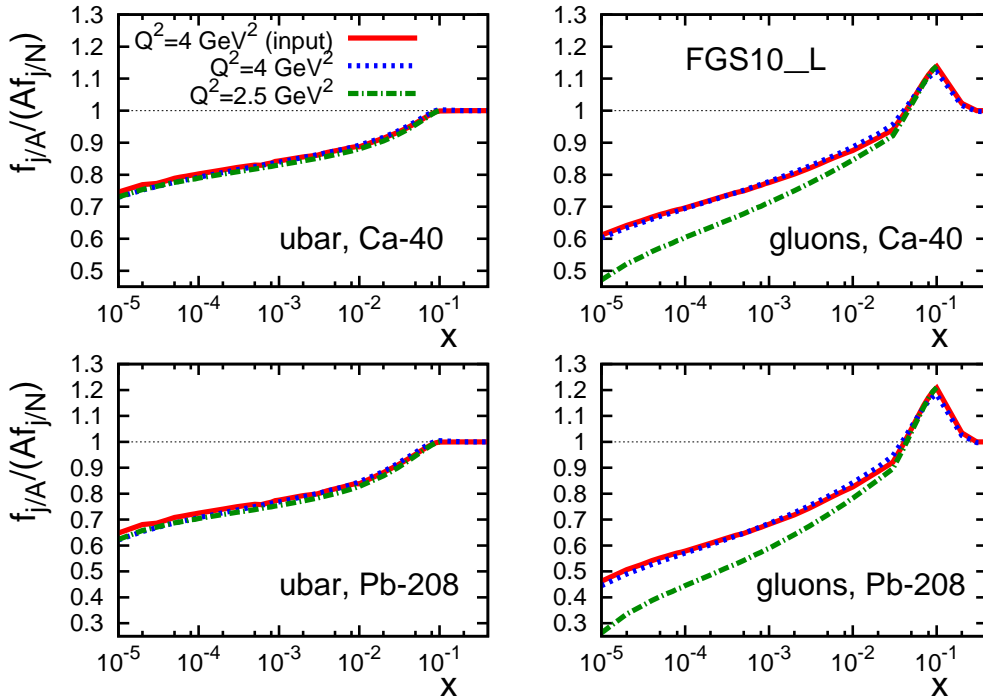


Fig. 47. Theoretical uncertainty associated with the choice of the input evolution scale Q_0^2 . The solid and dot-dashed curves are the results of the direct calculation of nuclear PDFs using Eq. (64) at $Q_0^2 = 4 \text{ GeV}^2$ and $Q_0^2 = 2.5 \text{ GeV}^2$, respectively. Performing the QCD evolution from $Q_0^2 = 2.5 \text{ GeV}^2$ to $Q_0^2 = 4 \text{ GeV}^2$, one obtains the dotted curves, which are indistinguishable from the solid curves. All curves correspond to model FGS10_L.

the modeling of multiple rescatterings using the color fluctuation approximation is not needed, and, as a result, one can evaluate nuclear PDFs using Eq. (64) at any scale Q^2 without the need of QCD evolution.

The HERA experiments do not cover a sufficiently large range of Q^2 for $x \sim 10^{-4}$ to extract the nucleon gluon PDF for $Q^2 \sim 4 \text{ GeV}^2$. (In the sea quark channel, the kinematic coverage of small x region is much better and, hence, the quark PDFs are known with much higher precision.) This can be seen from a comparison of the current fits to the data (CTEQ5M [160], CTEQ6.6 [183], HERAPDF1.0 [184], and NLO MSTW2008 [185]), see Fig. 48, where they are presented as functions of x at $Q^2 = 4 \text{ GeV}^2$. While the choice of the nucleon gluon PDF does not impact very strongly the difference of nuclear and nucleon PDFs (see Eq. (125)) since it only affects the value of $\sigma_{\text{soft}}^{j(\text{H})}$, the effect is more significant for the ratios of the gluon PDFs in nuclei and the nucleon. This happens because the leading twist theory of nuclear shadowing leads to different shadowing for the same diffractive PDFs and different nucleon PDFs and, hence, the use of our nuclear shadowing ratios requires specifying the parameterization of the nucleon PDFs. An example of this is presented in Fig. 49, where we compare our predictions for $g_A(x, Q_0^2)/[Ag_N(x, Q_0^2)]$ for ^{208}Pb at $Q_0^2 = 4 \text{ GeV}^2$ calculated using CTEQ5M (upper band, our standard choice in this review) and CTEQ6.6 (lower band) parameterizations of the proton gluon PDF.

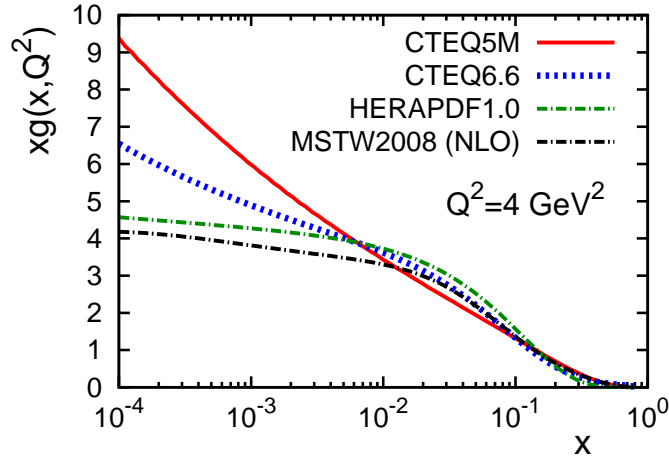


Fig. 48. Comparison of several current parameterizations of the gluon PDF in the nucleon at $Q^2 = 4 \text{ GeV}^2$ as a function of x . The solid curve is CTEQ5M [160] (used in this review); the dotted curve is CTEQ6.6 [183]; the green dot-dashed curve is HERAPDF1.0 [184]; the black dot-dashed curve is NLO MSTW2008 [185].

The upper boundary of each band corresponds to model FGS10_L; the lower boundary corresponds to FGS10_H. As one can see from Fig. 49, the uncertainty associated with the choice of the gluon PDF is not large (it is smaller than the uncertainty in the slope B_{diff} —compare Fig. 49 to Fig. 46) and essentially disappears for $x \geq 10^{-3}$. For the quark

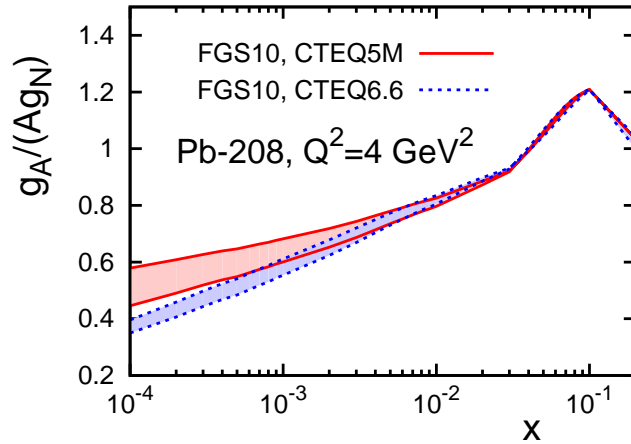


Fig. 49. Predictions for $g_A(x, Q_0^2)/[A g_N(x, Q_0^2)]$ for ^{208}Pb at $Q_0^2 = 4 \text{ GeV}^2$ as a function of x calculated using CTEQ5M (upper band, our standard choice in this review) and CTEQ6.6 (lower band) parameterizations of the proton gluon PDF.

case, the discussed uncertainty is practically absent for all x .

In summary, theoretical uncertainties of our predictions for the leading twist nuclear shadowing in nPDFs, which are related to the structure of color fluctuations, appear to be smaller than the uncertainty of the experimental input due to the experimental uncer-

tainty in the value of the diffractive slope B_{diff} and, in the case of gluons, the uncertainties in the nucleon gluon PDF at $x \sim 10^{-4}$.

5.10 Predictions for leading twist nuclear shadowing at the leading-order accuracy

In this review, our predictions for nuclear PDFs and structure functions are given at the next-to-leading order (NLO) accuracy in the strong coupling constant α_s . However, since the QCD factorization theorems that we used are valid at any order, we can also make predictions at the leading-order (LO) accuracy. Indeed, using LO diffractive PDFs of the proton [186] in conjunction with LO free proton PDFs in our master Eq. (64), we can readily make predictions for LO nuclear PDFs. An example of this is shown in Fig. 50 where the solid curves present the $f_{j/A}(x, Q_0^2)/[Af_{j/N}(x, Q_0^2)]$ ratios of LO nuclear and free proton PDFs for ^{208}Pb at $Q_0^2 = 4 \text{ GeV}^2$. The left panels correspond to \bar{u} quarks; the right panels correspond to the gluon channel; the upper row of panels is for model FGS10_H, while the lower row is for FGS10_L. For the free proton PDFs, we used the CTEQ5L parameterization [160]. For comparison, our predictions for $f_{j/A}(x, Q_0^2)/[Af_{j/N}(x, Q_0^2)]$ at the NLO accuracy are given by the dotted curves (same curves as in Fig. 31).

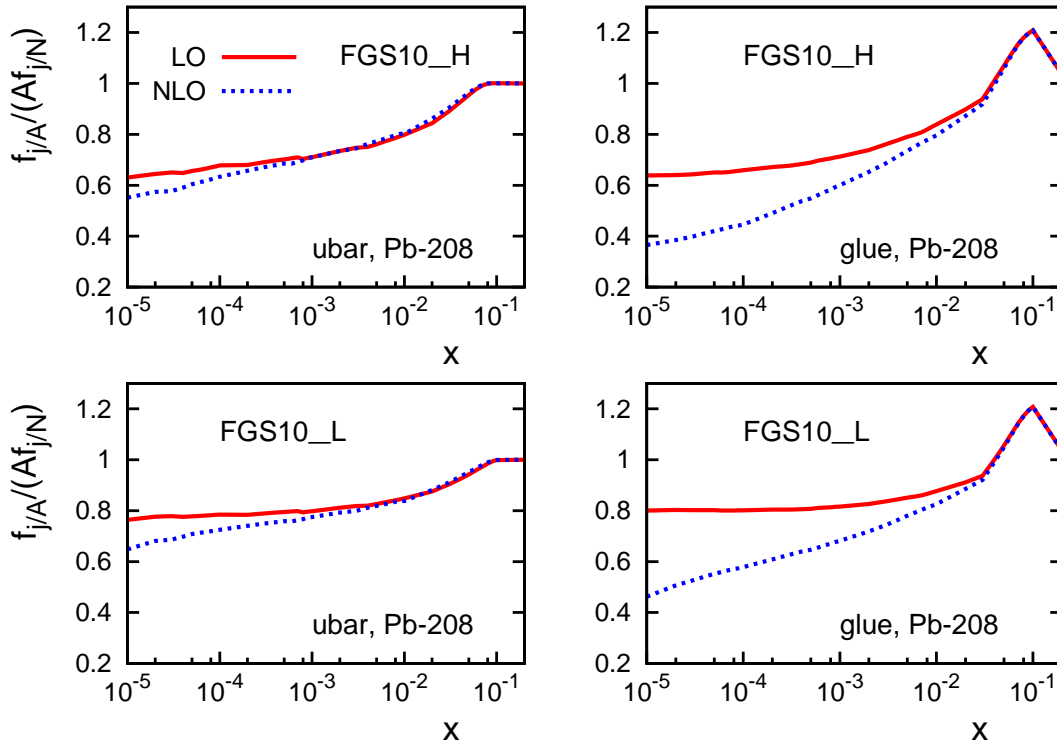


Fig. 50. Predictions for $f_{j/A}(x, Q_0^2)/[Af_{j/N}(x, Q_0^2)]$ for ^{208}Pb at $Q_0^2 = 4 \text{ GeV}^2$ at LO (solid curves) and NLO (dotted curves).

As one can see from Fig. 50, the predicted shadowing is somewhat smaller at the LO

accuracy. An inspection reveals that this is mostly due to the fact that the LO CTEQ5L \bar{u} quark and gluon PDFs are larger than the corresponding NLO CTEQ5M ones.

One should note that while the difference between the LO and NLO predictions for the $f_{j/A}(x, Q_0^2)/[Af_{j/N}(x, Q_0^2)]$ ratio for different parton flavors presented in Fig. 50 is sizable, it is much smaller for the ratio of the structure functions $F_{2A}(x, Q_0^2)/[AF_{2N}(x, Q_0^2)]$, see Fig. 51. This is due to the facts that i) the values of the proton structure function $F_{2N}(x, Q_0^2)$ at LO and NLO accuracy are very close because both fits reproduce the same inclusive data, ii) the values of the proton diffractive structure function $F_{2N}^{D(3)}(x, Q_0^2, x_P)$ at LO and NLO are numerically close since, like in the inclusive case, the LO and NLO fits are constrained to reproduce the same diffractive DIS data.

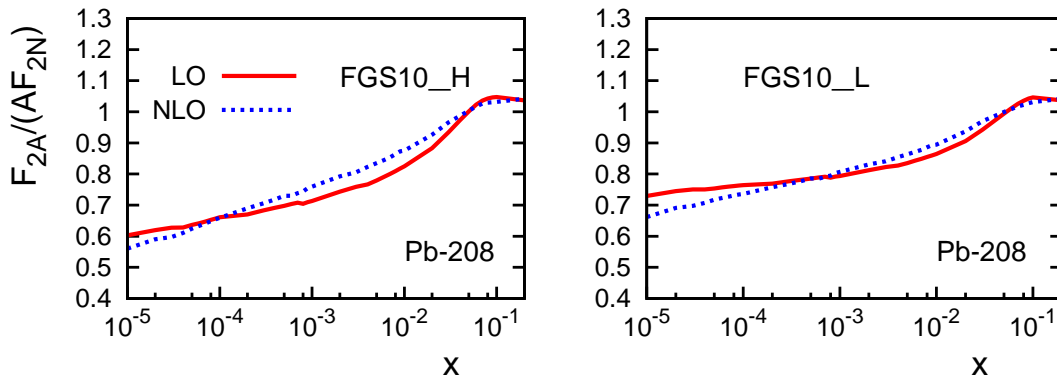


Fig. 51. Predictions for $F_{2A}(x, Q_0^2)/[AF_{2N}(x, Q_0^2)]$ for ^{208}Pb at $Q_0^2 = 4 \text{ GeV}^2$ at LO (solid curves) and NLO (dotted curves) accuracy.

While for many observables the NLO (and higher) accuracy is the state of the art, there are situations when one cannot avoid using LO nuclear PDFs. One notable example is the application of the dipole formalism to processes with nuclear targets which requires LO nuclear PDFs as input.

5.11 The double scattering contribution to nuclear shadowing vs. the full result

To better understand the theoretical uncertainty associated with modeling the multiple interactions using the color-fluctuation approximation, it is important to compare the full calculation of nuclear shadowing to the calculation, where only the double rescattering contribution to nuclear shadowing is retained. The latter corresponds to setting $\sigma_{\text{soft}}^j(x, Q^2) = 0$ in Eq. (64). This comparison is presented in Fig. 52. All curves correspond to $Q^2 = 4 \text{ GeV}^2$. The solid (FGS10_H) and dotted (FGS10_L) curves are the results of the full calculation using the color-fluctuation approximation for the interaction with $N \geq 3$ nucleons, the same as in Figs. 33 and 34. The dot-dashed curves are obtained by keeping only the interaction with two nucleons in the calculation of the shadowing correction. Naturally, the results presented by the dashed curves are model-independent

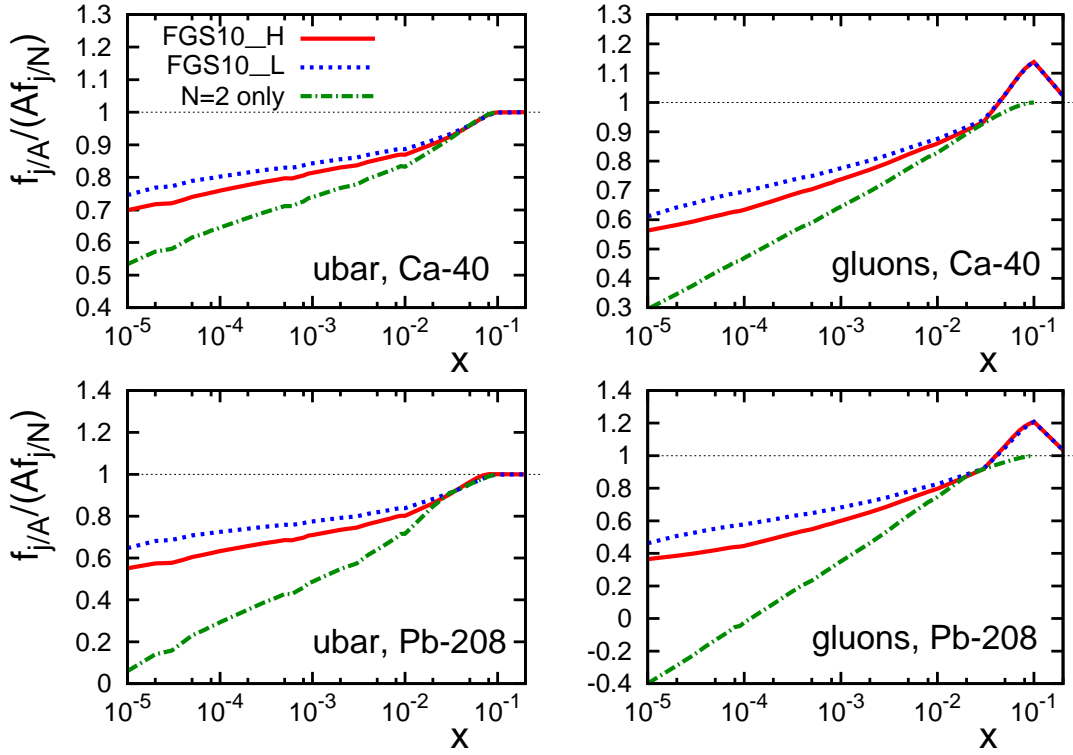


Fig. 52. Comparison of the full calculation of $f_{j/A}(x, Q_0^2)/[Af_{j/N}(x, Q_0^2)]$ using the color-fluctuation approximation (solid and dotted curves, same as in Figs. 33 and 34) to the calculation when only the interaction with two nucleons is retained (dot-dashed curves). All curves correspond to $Q_0^2 = 4 \text{ GeV}^2$.

and do not rely on any approximations to model the interaction with $N \geq 3$ nucleons.

As one can see from Fig. 52, since $\sigma_{\text{soft}}^j(x, Q^2)$ decreases with increasing x very slowly and remains large, the effect of the interaction with $N \geq 3$ nucleons remains important up to rather large values of x . One can approximate the full result by the interaction with only two nucleons of the nuclear target only for $x > 0.01$.

5.12 Comparison with the nPDFs obtained from the DGLAP fits to the data

Our predictions for the leading twist next-to-leading (NLO) order nPDFs can be compared to those obtained from the DGLAP fits to the available data [39–52], see also the discussion in Sec. 1. An example of such a comparison is presented in Fig. 53. In this figure, we compare our predictions for the \bar{u} -quark and gluon distributions in ^{208}Pb in the leading twist theory of nuclear shadowing [the shaded area bound by the two solid curves corresponding to models FGS10_H (lower boundary) and FGS10_L (upper boundary)], the EPS09 fit (dotted curves and the corresponding shaded error bands) [51], and the HKN07 fit (dot-dashed curves) [45]; all curves correspond to the NLO accuracy. The

ratios of the nuclear to nucleon PDFs are plotted as a function of x at two fixed values of Q^2 : $Q^2 = 4 \text{ GeV}^2$ (upper panels) and $Q^2 = 10 \text{ GeV}^2$ (lower panels).

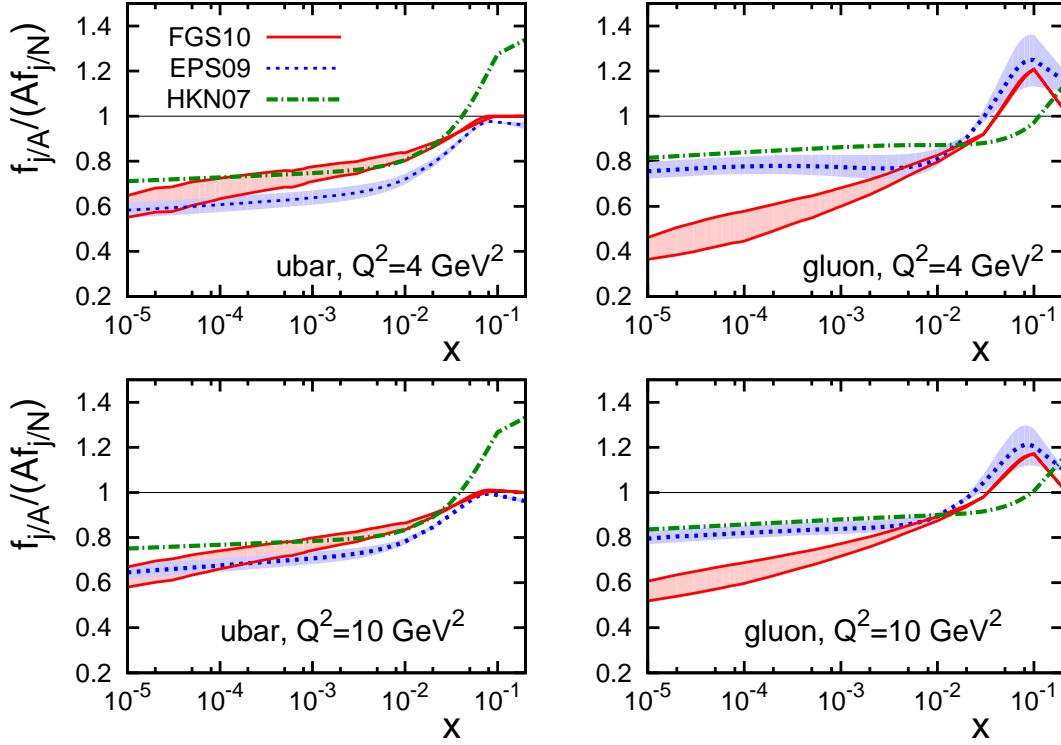


Fig. 53. Comparison of predictions of the leading twist theory of nuclear shadowing [the area bound by the two solid curves corresponding to models FGS10_H (lower boundary) and FGS10_L (upper boundary)], the EPS09 fit (dotted curves and the corresponding shaded error bands) [51], and the HKN07 fit (dot-dashed curves) [45]. The NLO $f_{j/A}(x, Q^2)/[Af_{j/N}(x, Q^2)]$ ratios for the \bar{u} -quark and gluon distributions in ^{208}Pb are plotted as functions of x at $Q^2 = 4 \text{ GeV}^2$ (upper panels) and $Q^2 = 10 \text{ GeV}^2$ (lower panels).

As one can see from Fig. 53, the three compared approaches give rather close values for nuclear shadowing in the sea-quark channel for a wide range of x , $10^{-5} \leq x \leq 0.02 - 0.03$. For larger x , the HKN07 fit deviates from the other two due to the assumed antishadowing for the sea quarks.

In the gluon channel, our approach suggests much larger shadowing at $Q^2 = 4 \text{ GeV}^2$ than that suggested by the extrapolation of the EPS09 and HKN07 results. Here, however, one has to make a distinction. While the shadowing in the gluon channel is insignificant in the HKN07 fit for all Q^2 scales, at the input scale $Q_0^2 = 1.69 \text{ GeV}^2$, the EPS09 fit suggests very large gluon shadowing with the very large theoretical uncertainty [51]. This is a consequence of the fact that the available data cannot constrain the nuclear gluon PDF at small x . (Note also that the large gluon shadowing in the EPS09 fit is mostly driven by the RHIC data which are not in the kinematics where the leading twist pQCD is applicable, see the discussion in Sec. 8.) Indeed, since the relevant nuclear data for

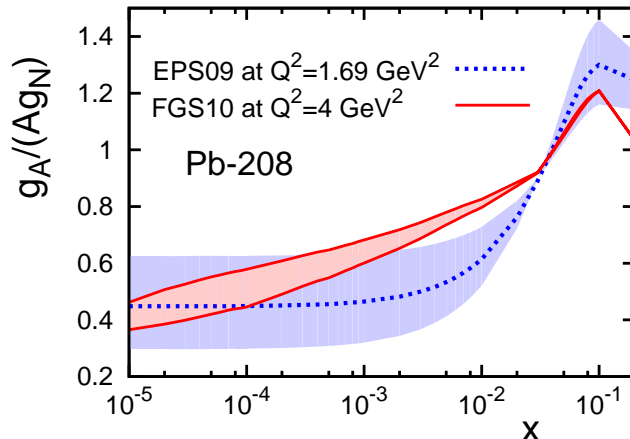


Fig. 54. The ratio of the gluon distributions in ^{208}Pb and the nucleon, $g_A(x, Q^2)/[Ag_N(x, Q^2)]$, as a function of x for the EPS09 fit at $Q^2 = 1.69 \text{ GeV}^2$ (the dotted curve with the shaded error band) and in the leading twist theory of nuclear shadowing at $Q^2 = 4 \text{ GeV}^2$ (the shaded area spanned by the two solid curves, the same as in Fig. 53).

$Q^2 \geq 4 \text{ GeV}^2$ exist only for $x \geq 10^{-2}$, one is forced to assume the dominance of the LT approximation down to $Q^2 \approx 1 \text{ GeV}^2$ and use ad hoc assumptions about nuclear PDFs for smaller x where they are not constrained by the data. When these data are not included in the fit, the resulting error band is huge.

To illustrate this point, in Fig. 54 we present the ratio of the gluon distributions in ^{208}Pb and in the nucleon, $g_A(x, Q^2)/[Ag_N(x, Q^2)]$, as a function of x for the EPS09 fit at $Q^2 = 1.69 \text{ GeV}^2$ (the dotted curve with the shaded error band) and for our leading twist theory of nuclear shadowing at $Q^2 = 4 \text{ GeV}^2$ (the shaded area spanned by the two solid curves, the same as in Fig. 53). As one can see from Fig. 54, the predicted amounts of nuclear shadowing in the gluon channel for $x < 10^{-3}$ are similar in the two approaches. However, after short evolution in Q^2 from $Q_0^2 = 1.69 \text{ GeV}^2$ to $Q^2 = 4 \text{ GeV}^2$, the shadowing in the gluon channel in the EPS09 fit significantly reduces and becomes noticeably smaller than in our LT approach (compare the solid and dotted curves in the right column of panels in Fig. 53).

We point out, again, that nuclear shadowing in the gluon channel is essentially unconstrained by the fixed-target data. The future Electron-Ion Collider, with its deep reach in the nuclear shadowing region and a large lever arm in Q^2 should significantly improve our knowledge of the gluon parton distribution in nuclei.

Recently nuclear PDFs have also been extracted using neutrino DIS data and combining the neutrino and lepton DIS data [52,187–192]. At the moment, the results of such extractions are controversial: while the analyses of Refs. [52,187–189] seem to indicate that the nuclear corrections are different between the charged and neutral lepton DIS, the analyses of Refs. [190–192] find no such difference.

5.13 Comparison to the soft QCD model of [97–99]

An approach to nuclear shadowing that is based on the Gribov-Glauber theory of nuclear shadowing and that has certain similarity to our leading twist approach has been proposed and developed in Refs. [97–99]. It also starts with the Gribov relation between diffraction and shadowing for $F_{2A}(x, Q^2)$ for the interaction with two nucleons and employs the phenomenological Regge-motivated model for the diffractive structure function $F_2^{D(3)}$ which contains both the leading twist and higher twist contributions. Since the approach effectively includes both leading and higher twist contributions to nuclear shadowing (via the use of the all-twist parameterization of diffraction), it provides a good description of the fixed-target data on nuclear shadowing which is predominantly in the kinematics where only interactions with two nucleons contribute, see the discussion in Sec. 5.16.

To sum up the multiple interactions with $N \geq 3$ nucleons of the nuclear target, the fan diagram approximation is used (the Schwimmer model [193]). Such a model assumes the dominance of large-mass diffraction, $M^2 \gg Q^2$, while we find that $M^2 \sim Q^2$ dominate in a wide range of x . Also, the use of this model for large Q^2 results in the expressions which do not satisfy DGLAP equations even for large Q^2 and do not allow one to determine nuclear PDFs for individual parton flavors.

In the recent paper [99], the authors adopted to some extent our QCD factorization approach and used diffractive PDFs to calculate nuclear PDFs. However, to evaluate nuclear shadowing as a function of Q^2 , the authors of [97–99] apply an equation similar in the spirit to our master Eq. (64) for all Q^2 . As we explain in Sec. 3, the application of Eq. (64) at large Q^2 violates the QCD evolution because one then ignores the increase of the color fluctuations induced by the QCD evolution. [We use Eq. (64) only at an input scale $Q_0^2 = 4 \text{ GeV}^2$; the subsequent Q^2 dependence of nuclear PDFs is given by the usual DGLAP equations.] In addition, neglecting proper QCD evolution, one neglects the contribution of larger x effects—antishadowing and EMC effects—to the small- x region.

5.14 The leading twist theory of nuclear shadowing vs. dipole model eikonal approximation

5.14.1 The dipole model eikonal approximation

Besides the leading twist theory of nuclear shadowing, there is a broad class of models of nuclear shadowing, which are based on the so-called eikonal approximation [83,194–198]. The eikonal approximation in nuclear DIS is based on the assumption that the virtual photon-nucleus cross section can be written as the convolution of the probability of the transition of the virtual photon into a quark-antiquark pair ($q\bar{q}$ dipole) with the (exponential) factor describing the $q\bar{q}$ dipole-nucleus scattering. The exponential factor is

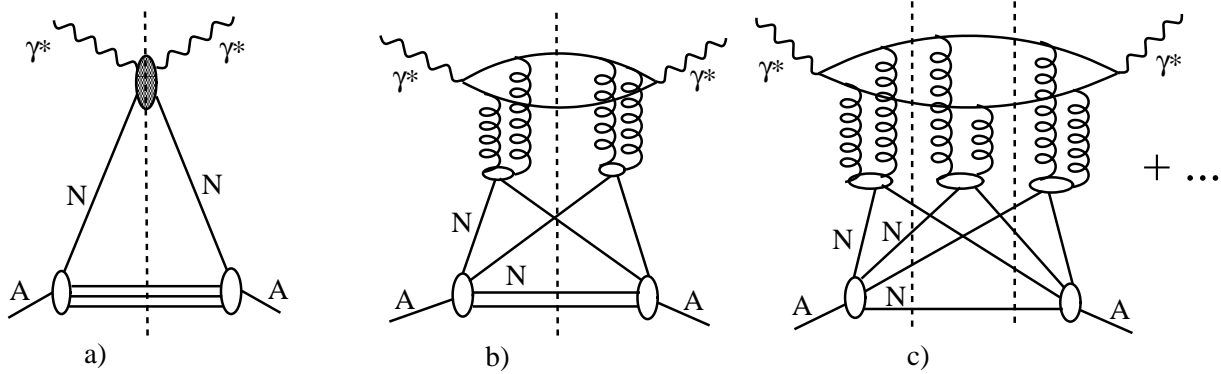


Fig. 55. Graphs corresponding to the virtual photon-nucleus cross section in the eikonal approximation. Graph *a* gives the impulse approximation; graphs *b* and *c* give the shadowing correction arising from the interaction with two and three nucleons of the target, respectively.

a result of the eikonalization of the multiple $q\bar{q}$ -nucleon scattering series, which is done in the spirit of the Glauber model.

The graphical representation of the virtual photon-nucleus cross section in the eikonal approximation is given in Fig. 55 (the vertical dashed lines denote the unitary cuts). The graphs in Fig. 55 should be compared to the corresponding graphs of the leading twist theory of nuclear shadowing in Fig. 9. In Fig. 55, graph *a* is the impulse approximation, which is the same as in the leading twist approach. Graphs *b* and *c* give the shadowing correction arising from the interaction with two and three nucleons of the target, respectively. The two-gluon exchange is the symbolic notation for the $q\bar{q}$ dipole-nucleon interaction. Graphs corresponding to the interaction with four and more nucleons are not shown, but are assumed. Note that the dipole model approximation violates the energy-momentum conservation in the case of the interaction with more than two nucleons, see the discussion in Sec. 3.1.4.

Within the eikonal approximation, the expression for the nuclear inclusive structure function $F_{2A}(x, Q^2)$ reads, see, e.g., [75],

$$\begin{aligned}
F_{2A}(x, Q^2) &= AF_{2N}(x, Q^2) - \frac{Q^2}{4\pi^2\alpha_{\text{em}}} \Re \left[\int_0^1 d\alpha \, d^2d_{\perp} \sum_i |\Psi(\alpha, Q^2, d_{\perp}^2, m_i)|^2 \right. \\
&\times \frac{A(A-1)}{2} (1-i\eta)^2 \int d^2\vec{b} \int_{-\infty}^{\infty} dz_1 \int_{z_1}^{\infty} dz_2 [\sigma_{q\bar{q}N}(x, Q^2, d_{\perp}^2, m_i)]^2 \rho_A(\vec{b}, z_1) \rho_A(\vec{b}, z_2) \\
&\times e^{i(z_1-z_2)2xm_N} e^{-\frac{A}{2}(1-i\eta)\sigma_{q\bar{q}N}(x, Q^2, d_{\perp}^2, m_i) \int_{z_1}^{z_2} dz \rho_A(z)} \left. \right]. \quad (138)
\end{aligned}$$

In Eq. (138), α_{em} is the fine-structure constant; α is the fraction of the photon longitudinal momentum carried by q or \bar{q} ; d_{\perp} is the transverse diameter of the $q\bar{q}$ -system; m_i is the

mass of the constituent quark of flavor i ; η is the ratio of the real to imaginary parts of $q\bar{q}$ -nucleon scattering amplitude; $|\Psi|^2$ is the probability of the virtual photon- $q\bar{q}$ transition (the square of the effective light-cone wave functions of the virtual photon); $\sigma_{q\bar{q}N}$ is the $q\bar{q}$ -nucleon cross section, which is schematically denoted by the two-gluon exchange in Fig. 55.

The square of the effective unpolarized light-cone wave function of the virtual photon, $|\Psi|^2$, can be written as the sum of the squares of the wave function for the transversely-polarized photon, $|\Psi_T|^2$, and the effective wave function for the longitudinally-polarized photon, $|\Psi_L|^2$, i.e., $|\Psi|^2 = |\Psi_T|^2 + |\Psi_L|^2$, where

$$\begin{aligned} |\Psi_T(\alpha, Q^2, d_\perp^2, m_i)|^2 &= \frac{6}{4\pi^2} \frac{\alpha_{\text{em}}}{e_i^2} \left[(\alpha^2 + (1-\alpha)^2) \epsilon_i^2 K_1^2(\epsilon_i d_\perp) + m_i^2 K_0^2(\epsilon_i d_\perp) \right], \\ |\Psi_L(\alpha, Q^2, d_\perp^2, m_i)|^2 &= \frac{6}{\pi^2} \frac{\alpha_{\text{em}}}{e_i^2} Q^2 \alpha^2 (1-\alpha)^2 K_0^2(\epsilon_i d_\perp). \end{aligned} \quad (139)$$

In Eq. (139), K_0 and K_1 are the modified Hankel functions; $\epsilon_i^2 = Q^2 \alpha(1-\alpha) + m_i^2$. Following the analysis in Ref. [75], we include four quark flavors and take $m_u = m_d = m_s = 300$ MeV and $m_c = 1.5$ GeV. Note that the effective Ψ_L differs from the light-cone wave function of the longitudinal photon. The additional factor of Q results from the exact cancellation of the components of the longitudinal photon polarization vector that increase with energy, which follows from the conservation of the electromagnetic current for the whole amplitude. (For the discussion of conceptual differences between the leading twist and dipole model eikonal approximations to nuclear shadowing, see Sec. 5.14.4.)

Taking the longitudinally-polarized virtual photon, one readily obtains the expression for the longitudinal nuclear structure function $F_L^A(x, Q^2)$:

$$\begin{aligned} F_L^A(x, Q^2) &= A F_L^N(x, Q^2) - \frac{Q^2}{4\pi^2 \alpha_{\text{em}}} \Re e \left[\int_0^1 d\alpha \, d^2 d_\perp \sum_i |\Psi_L(\alpha, Q^2, d_\perp^2, m_i)|^2 \right. \\ &\times \frac{A(A-1)}{2} (1-i\eta)^2 \int_{-\infty}^{\infty} d^2 \vec{b} \int_{z_1}^{\infty} dz_1 \int_{z_1}^{\infty} dz_2 \left[\sigma_{q\bar{q}N}(x, Q^2, d_\perp^2, m_i) \right]^2 \rho_A(\vec{b}, z_1) \rho_A(\vec{b}, z_2) \\ &\left. \times e^{i(z_1 - z_2)2xm_N} e^{-\frac{A}{2}(1-i\eta)\sigma_{q\bar{q}N}(x, Q^2, d_\perp^2, m_i) \int_{z_1}^{z_2} dz \rho_A(z)} \right]. \end{aligned} \quad (140)$$

For comparison and completeness, we also give the expressions for the free nucleon structure functions in the dipole approximation [83]:

$$F_{2N}(x, Q^2) = \frac{Q^2}{4\pi^2 \alpha_{\text{em}}} \int_0^1 d\alpha \, d^2 d_\perp \sum_i |\Psi(\alpha, Q^2, d_\perp^2, m_i)|^2 \sigma_{q\bar{q}N}(x, Q^2, d_\perp^2, m_i),$$

$$F_L^N(x, Q^2) = \frac{Q^2}{4\pi^2\alpha_{\text{em}}} \int_0^1 d\alpha d^2d_\perp \sum_i |\Psi_L(\alpha, Q^2, d_\perp^2, m_i)|^2 \sigma_{q\bar{q}N}(x, Q^2, d_\perp^2, m_i). \quad (141)$$

In Eqs. (138) and (140), we take $\eta = 0.25$, see, e.g., [80]. In addition, the model includes the simplifying assumption that the invariant mass of all $q\bar{q}$ dipoles is the same and approximately equals Q . Therefore, the diffractive light-cone fraction $\beta = Q^2/(Q^2 + M_X^2) \approx 0.5$ and, hence, $x_P \approx 2x$. This explains the argument of the first exponential factor in Eqs. (138) and (140).

In the very low- x limit, the expressions for $F_{2A}(x, Q^2)$ and $F_L^A(x, Q^2)$ in the eikonal approximation can be simplified. Neglecting the $e^{i(z_1 - z_2)2xm_N}$ factor in Eqs. (138) and (140), integrating these equations by parts two times, and using the dipole formalism expressions for $F_{2N}(x, Q^2)$ and $F_L^N(x, Q^2)$, one obtains [compare to Eqs. (51) and (65)]:

$$\begin{aligned} F_{2A}(x, Q^2) &= \frac{Q^2}{4\pi^2\alpha_{\text{em}}} \Re e \left[\int_0^1 d\alpha d^2d_\perp \sum_i |\Psi(\alpha, Q^2, d_\perp^2, m_i)|^2 \right. \\ &\quad \left. \times 2 \int d^2b \left(1 - e^{-\frac{A}{2}(1-i\eta)\sigma_{q\bar{q}N}(x, Q^2, d_\perp^2, m_i)T_A(b)} \right) \right], \\ F_L^A(x, Q^2) &= \frac{Q^2}{4\pi^2\alpha_{\text{em}}} \Re e \left[\int_0^1 d\alpha d^2d_\perp \sum_i |\Psi_L(\alpha, Q^2, d_\perp^2, m_i)|^2 \right. \\ &\quad \left. \times 2 \int d^2b \left(1 - e^{-\frac{A}{2}(1-i\eta)\sigma_{q\bar{q}N}(x, Q^2, d_\perp^2, m_i)T_A(b)} \right) \right]. \end{aligned} \quad (142)$$

5.14.2 The dipole cross section

The dipole cross section $\sigma_{q\bar{q}N}$ plays a central role in the dipole formalism and in the quasi-eikonal approximation. We use the dipole model of McDermott, Frankfurt, Guzey and Strikman (MFGS) [199]. In this approach, the $q\bar{q}$ -nucleon dipole cross section is constructed in a piecewise form, where each piece corresponds to the particular range of the dipole transverse size d_\perp with the corresponding physics motivation. For small dipole sizes, the dipole cross section is dictated by perturbative QCD. As one increases the dipole size, the dynamics becomes non-perturbative and it is no longer reasonable to think of d_\perp as a size of a simple $q\bar{q}$ pair. Instead, it is better to think of it as corresponding to the typical transverse size of a complicated non-perturbative system, which in general contains many constituents. When the dipole size becomes as large as the transverse separation of quarks in a pion, $d_\perp = d_\pi \approx 0.65$ fm, one expects that the dipole cross section should be comparable to the soft pion-nucleon cross section, $\sigma_{\text{tot}}^{\pi N}$. The intermediate region between

the small dipole sizes and $d_{\perp} = 0.65$ fm is least known. For the lack of the physical motivation, the dipole cross section in this region is modeled by the smooth interpolation between the small- d_{\perp} perturbative and the large- d_{\perp} non-perturbative regions.

The explicit expression for the dipole cross section, $\sigma_{q\bar{q}N}$, has the following form [199]:

$$\sigma_{q\bar{q}N}(x, Q^2, d_{\perp}, m_i) = \begin{cases} \frac{\pi^2}{3} d_{\perp}^2 \alpha_s(\frac{\lambda}{d_{\perp}^2}) x' g(x', \frac{\lambda}{d_{\perp}^2}), & d_{\perp} \leq \min\{d_{\text{crit}}, d_{Q_0}\} \\ (\sigma_{\pi N}(x) - \sigma_{q\bar{q}}(x', Q^2, d_{\text{crit}})) H(d_{\perp}) \\ \quad + \sigma_{q\bar{q}}(x', Q^2, d_{\text{crit}}), & \min\{d_{\text{crit}}, d_{Q_0}\} \leq d_{\perp} \leq d_{\pi} \\ \sigma_{\pi N}(x) \frac{1.5 d_{\perp}^2}{d_{\perp}^2 + d_{\pi}^2/2}, & d_{\perp} \geq d_{\pi}. \end{cases} \quad (143)$$

In Eq. (143), the perturbative dipole cross section in the region $d_{\perp} \leq \min\{d_{\text{crit}}, d_{Q_0}\}$ is proportional to the dipole size squared d_{\perp}^2 , the gluon density of the target (nucleon or nucleus) $g(x', \lambda/d_{\perp}^2)$, and the strong coupling constant $\alpha_s(\lambda/d_{\perp}^2)$. (The result that $\sigma_{q\bar{q}N} \approx \text{const} \cdot d_{\perp}^2$ was first obtained by F. Low in the two-gluon exchange model in 1975 [200].) The gluon density and the strong coupling constant are probed at the effective scale $Q_{\text{eff}}^2 = \lambda/d_{\perp}^2$, where $\lambda \approx 10$ in the original MFGS analysis [199]. It was later discovered that the inclusive cross sections are rather insensitive to the precise value of λ in the range $\lambda = 4 - 15$ and that the lower value of $\lambda = 4$ appears to be favored by the J/ψ photoproduction data [201]. In this work, we use $\lambda = 4$. Note also that since the perturbative expression for $\sigma_{q\bar{q}N}$ is valid to the leading order (LO) accuracy, both $g(x', \lambda/d_{\perp}^2)$ and $\alpha_s(\lambda/d_{\perp}^2)$ are taken at the LO accuracy.

The light-cone fraction x' , at which the target gluon density is probed, is larger than Bjorken x . This accounts for the fact that the virtual photon directly couples only to the quarks, which originate through the DGLAP evolution from the gluons with the larger light-cone momenta. In the MFGS model, one uses [199]:

$$x' = x \left(1 + \frac{4m_i^2}{Q^2} \right) \left(1 + 0.75 \frac{\lambda}{Q^2 d_{\perp}^2} \right). \quad (144)$$

It is the dependence of x' on Q^2 that introduces the explicit dependence of the dipole cross section on the virtuality Q^2 , which is rather insignificant. Note also that x' depends on the constituent quark mass m_i .

At fixed small d_{\perp} , as one decreases x the perturbative dipole cross section grows very rapidly as a result of the steeply rising gluon density. If unchecked, this will eventually lead to a contradiction since the perturbative contribution to the dipole cross section is an *inelastic* cross section which should not exceed the typical soft inelastic meson-nucleon cross section at the corresponding energy, which we take to be the inelastic pion-nucleon cross section. Therefore, at given Bjorken x , we apply the perturbative expression for the

dipole cross section up to some critical dipole size, d_{crit} , which is defined by the following equation:

$$\frac{\pi^2}{3} d_{\text{crit}}^2 \alpha_s \left(\frac{\lambda}{d_{\text{crit}}^2} \right) x' g \left(x', \frac{\lambda}{d_{\text{crit}}^2} \right) = \frac{1}{2} \sigma_{\text{tot}}^{\pi N}(W^2), \quad (145)$$

where $W^2 = Q^2/x - Q^2 + m_N^2$. In the right-hand side of Eq. (145), we used the fact that the maximal value of the inelastic pion-nucleon cross section is reached in the black disk limit and is equal to one half of the total cross section. For the latter, we use the Donnachie-Landshoff parameterization [131], see Eq. (112).

The effective scale $Q_{\text{eff}}^2 = \lambda/d_{\perp}^2$ in Eqs. (143) and (145) cannot be too small to guarantee that the perturbative description is applicable. Therefore, $Q_{\text{eff}}^2 \geq Q_0^2$, where Q_0^2 is the initial evolution scale. Using the CTEQ5L parameterization of the gluon density with $Q_0^2 = 1 \text{ GeV}^2$ [160] that was used in the original analysis of Ref. [199] and more recent parameterization, e.g., MSTW 2008 with $Q_0^2 = 1 \text{ GeV}^2$ [202] and GJR 2008 with $Q_0^2 = 0.3 \text{ GeV}^2$ [203], we obtain the following range of small dipole sizes for which the perturbative description of the dipole cross section can be applied:

$$d_{\perp} \leq d_{Q_0} = \sqrt{\frac{\lambda}{Q_0^2}} = \begin{cases} 0.39 \text{ fm}, & \text{CTEQ5L, MSTW2008,} \\ 0.72 \text{ fm}, & \text{GJR2008.} \end{cases} \quad (146)$$

It turns out that the considered parameterizations lead to the similar $\sigma_{q\bar{q}N}$ cross section. Therefore, for definiteness, in our numerical analysis below, we shall use the GJR 2008 parameterization with $Q_0^2 = 0.3 \text{ GeV}^2$ [203]. This choice of Q_0^2 allows one to generate a smooth extrapolation to the non-perturbative region. Note that since the initial evolution scale is very low such that $d_{Q_0} > d_{\pi}$, we shall apply the perturbative description of the dipole cross section only for $d_{\perp} \leq d_{\text{crit}}$.

In the intermediate region, $d_{\text{crit}} \leq d_{\perp} \leq d_{\pi}$, we model the dipole cross section in a simple form that smoothly interpolates between the small- d_{\perp} and large- d_{\perp} pieces of the dipole cross section. The interpolating function is arbitrary, see the discussion in [199]. In this work, we use the following smooth parameterization:

$$H(d_{\perp}) = \frac{e}{e-1} [1 - \exp(-H_1(d_{\perp}))], \quad (147)$$

where

$$H_1(d_{\perp}) = \frac{d_{\perp} - d_{\text{crit}}}{d_{\pi} - d_{\text{crit}}}. \quad (148)$$

Finally, for very large dipole sizes, $d_{\perp} > d_{\pi}$, we impose a residual slow growth with increasing d_{\perp} , see the last line of Eq. (143).

Figure 56 presents the $q\bar{q}$ dipole cross section in the MFGS dipole model with the GJR 2008 parameterization of the gluon density [203] as a function of the dipole size d_{\perp} . All curves correspond to the light quark cross sections ($m_i = 300$ MeV) and $Q^2 = 4$ GeV² (note that the dependence on Q^2 is weak).

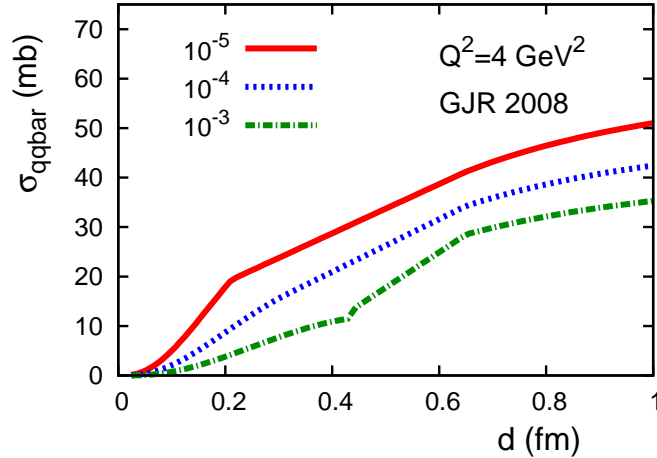


Fig. 56. The dipole cross section, $\sigma_{q\bar{q}}(x, Q^2, d_{\perp}, m_i)$, in the MFGS dipole model with the GJR 2008 parameterization of the gluon density [203] as a function of the dipole size d_{\perp} . All curves correspond to $m_i = 300$ MeV and $Q^2 = 4$ GeV².

5.14.3 Predictions for nuclear structure functions $F_{2A}(x, Q^2)$ and $F_L^A(x, Q^2)$ in the dipole model eikonal approximation

Predictions for nuclear shadowing in the nuclear structure functions $F_{2A}(x, Q^2)$ and $F_L^A(x, Q^2)$ are presented in Figs. 57 and 58 and Figs. 59 and 60, respectively. In Fig. 57, we give the ratio of the nuclear to nucleon structure functions $F_{2A}(x, Q^2)/[AF_{2N}(x, Q^2)]$ as a function of Bjorken x . The results of the calculation using the dipole model eikonal approximation, see Eqs. (138) and (141), are presented by the curves. Different curves correspond to three different values of Q^2 , $Q^2 = 4, 10, \text{ and } 100$ GeV². For comparison, we also give the corresponding predictions of the leading twist theory of nuclear shadowing taken from Figs. 33 and 34, which are given by the shaded bands (the upper boundaries of the bands correspond to model FGS10_L; the lower boundaries correspond to model FGS10_H).

Note that we apply the dipole model eikonal approximation only for $x \leq 0.01$. For $x > 0.01$, the dipole model eikonal approximation is not applicable since the $q\bar{q}$ fluctuations of the virtual photon are no longer coherent at the distance scale $\sim R_A$. In addition to the effect of the finite l_c , the naive application of Eqs. (138) and (140) for $x > 0.01$ is

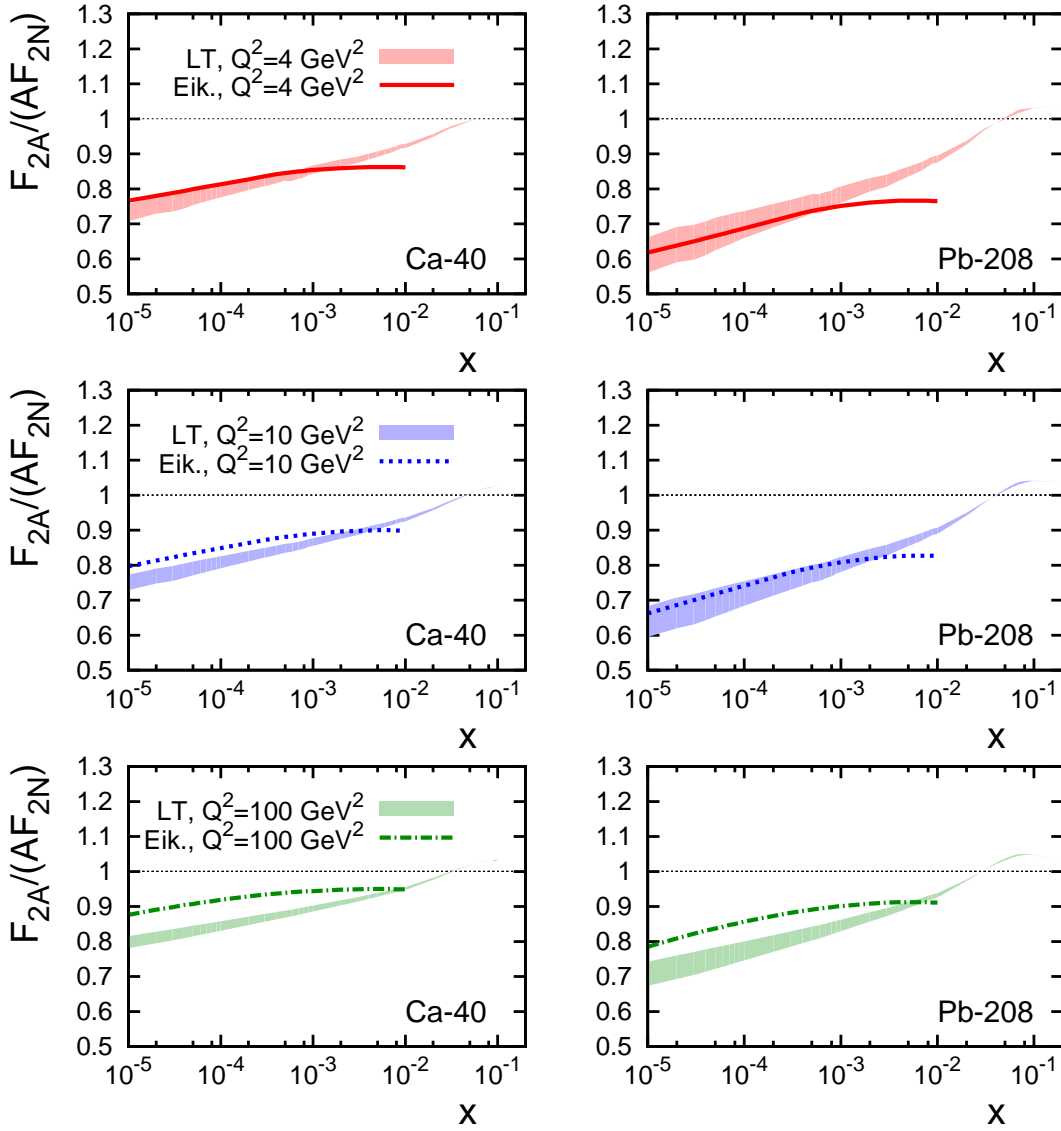


Fig. 57. The ratio of the nuclear to nucleon structure functions $F_{2A}(x, Q^2)/[AF_{2N}(x, Q^2)]$ as a function of Bjorken x . The results of the calculation using the dipole model eikonal approximation, see Eqs. (138) and (141), are given by the curves. The shaded bands represent the corresponding predictions of the leading twist theory of nuclear shadowing taken from Figs. 33 and 34.

bound to significantly overestimate the amount of nuclear shadowing since the effects of antishadowing and QCD evolution are not included in the eikonal approximation.

As one can see from Fig. 57, the amount of nuclear shadowing is rather similar in the dipole model eikonal approximation and the FGS10_L version of the leading twist theory of nuclear shadowing at $Q^2 = 4$ and 10 GeV^2 and for a wide range of x ; model FGS10_H predicts noticeably larger nuclear shadowing for $x < 5 \times 10^{-3}$. As one increases Q^2 , e.g., $Q^2 \geq 10 \text{ GeV}^2$, nuclear shadowing decreases much faster in the dipole model eikonal

approximation than in our leading twist approach (both in FGS10.L and FGS10.H). This trend agrees with our earlier analysis [75] and can be explained as follows. While the Q^2 behavior of $F_{2A}(x, Q^2)/[AF_{2N}(x, Q^2)]$ within the leading twist approach is governed by the QCD DGLAP evolution equation, and is therefore logarithmic, $F_{2A}(x, Q^2)/[AF_{2N}(x, Q^2)]$ in the eikonal approximation decreases with increasing Q^2 (much) faster, which is dictated largely by the Q^2 dependence of the virtual photon light-cone wavefunction. (We discuss the difference between the two approaches in more detail in Sec. 5.14.4.)

Note that in the dipole eikonal approximation, the main contribution to nuclear shadowing for $F_{2A}(x, Q^2)$ originates from large $q\bar{q}$ dipoles, i.e., from the contribution for which the virtual photon wave function is non-perturbative and the description in terms of the $q\bar{q}$ dipoles is at best effective. Hence, it is a recast of the aligned jet contribution.

To illustrate the different Q^2 behavior of nuclear shadowing in the leading twist theory and eikonal approximation, in Fig. 58 we present the shadowing correction, $1 - F_{2A}(x, Q^2)/[AF_{2N}(x, Q^2)]$, as a function of Q^2 for two fixed values of $x = 10^{-4}$ and $x = 10^{-3}$. The curves correspond to the eikonal approximation; the shaded bands are the results of the leading twist theory of nuclear shadowing. As one can see from Fig. 58, with an increase of Q^2 , nuclear shadowing decreases noticeably faster in the eikonal approximation than in our leading twist approach.

In Fig. 59, we present our results for nuclear shadowing for the ratio of the longitudinal structure functions, $F_L^A(x, Q^2)/[AF_L^N(x, Q^2)]$. The labeling of the curves is the same as in Fig. 57. One can see from Fig. 59 that the eikonal approximation predicts significantly smaller nuclear shadowing than the leading twist theory. This can be qualitatively explained by the observation that the small-size configurations of the virtual photon wave function—which are only weakly shadowed—give a more important contribution to $F_L^A(x, Q^2)$ than to $F_{2A}(x, Q^2)$ in the dipole formalism. This leads to the nuclear shadowing in $F_L^A(x, Q^2)$ that is both small and decreases rapidly with increasing Q^2 , i.e., in the eikonal approximation nuclear shadowing in $F_L^A(x, Q^2)$ is essentially a higher-twist effect. At the same time, in our leading twist approach, both small-size and large-size fluctuations of the virtual photon contribute to nuclear shadowing in $F_L^A(x, Q^2)$ and make it a sizable effect at all Q^2 .

To illustrate our discussion of the different Q^2 behavior of nuclear shadowing in the longitudinal structure function $F_L^A(x, Q^2)$ in the leading twist theory and eikonal approximation, in Fig. 60 we present the shadowing correction, $1 - F_L^A(x, Q^2)/[AF_L^A(x, Q^2)]$, as a function of Q^2 for two fixed values of $x = 10^{-4}$ and $x = 10^{-3}$. The curves correspond to the eikonal approximation; the shaded bands are the results of the leading twist theory of nuclear shadowing. As one can see from Fig. 60, with an increase of Q^2 , nuclear shadowing decreases noticeably faster in the eikonal approximation than in our leading twist approach; the absolute value of the shadowing correction is also significantly smaller in the eikonal approximation than in our leading twist approach.

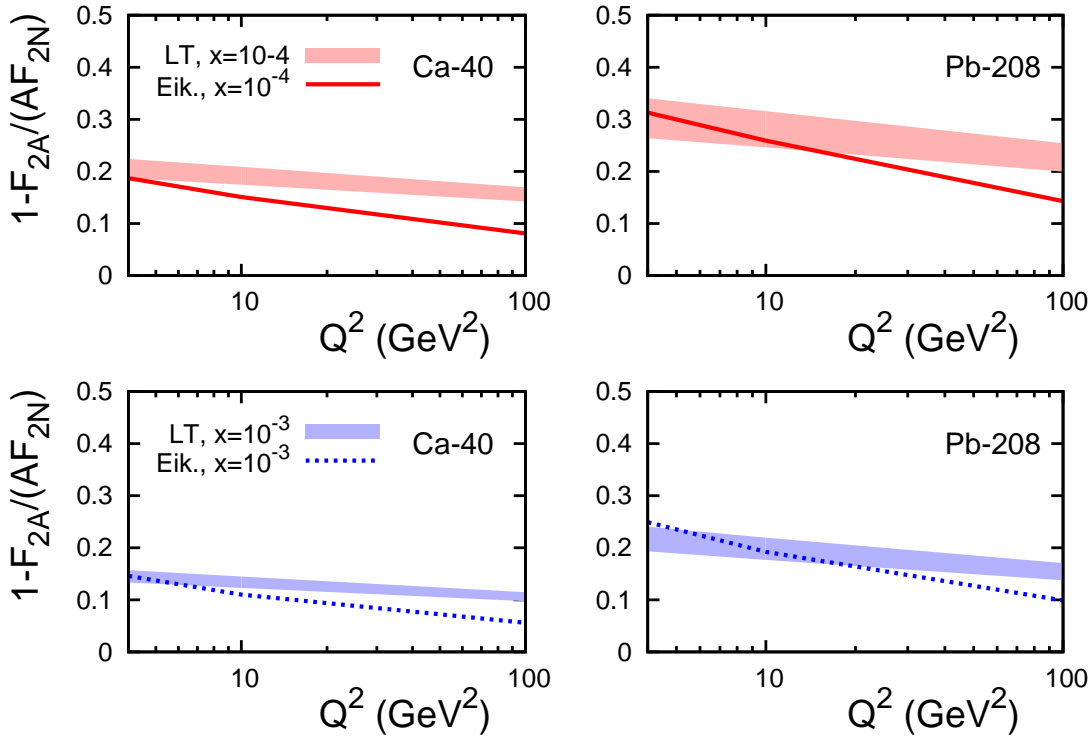


Fig. 58. The shadowing correction to the nuclear structure function $F_{2A}(x, Q^2)$, $1 - F_{2A}(x, Q^2)/[AF_{2N}(x, Q^2)]$, as a function of Q^2 for $x = 10^{-4}$ and $x = 10^{-3}$. The curves correspond to the dipole model eikonal approximation; the shaded bands are the results of the leading twist theory of nuclear shadowing.

5.14.4 Conceptual differences between the leading twist and dipole model eikonal approaches to nuclear shadowing

In this subsection, we discuss conceptual differences between the leading twist and dipole model eikonal approaches to nuclear shadowing in DIS on nuclei. The two key differences that make the two approaches so distinct are related. They are:

- (i) Different space-time evolution of the scattering process. The eikonal model approach strongly violates energy-momentum conservation; the color fluctuation approximation has no such a defect.
- (ii) The neglect of the $|q\bar{q}g\rangle$ component (and higher Fock states) of the virtual photon wave function in the dipole model eikonal approximation and the neglect of the proper QCD evolution (see the discussion in Sec. 5.13). In addition, the Sudakov form factor which arises in QCD calculations because of the gluon radiation (which leads to approximate Bjorken scaling) is neglected within the eikonal approximation.

Strictly speaking, the eikonal approximation has been derived only in the framework of non-relativistic quantum mechanics, where the number of interacting particles is conserved during collisions and the collisions are elastic. In this case, the approximation that the

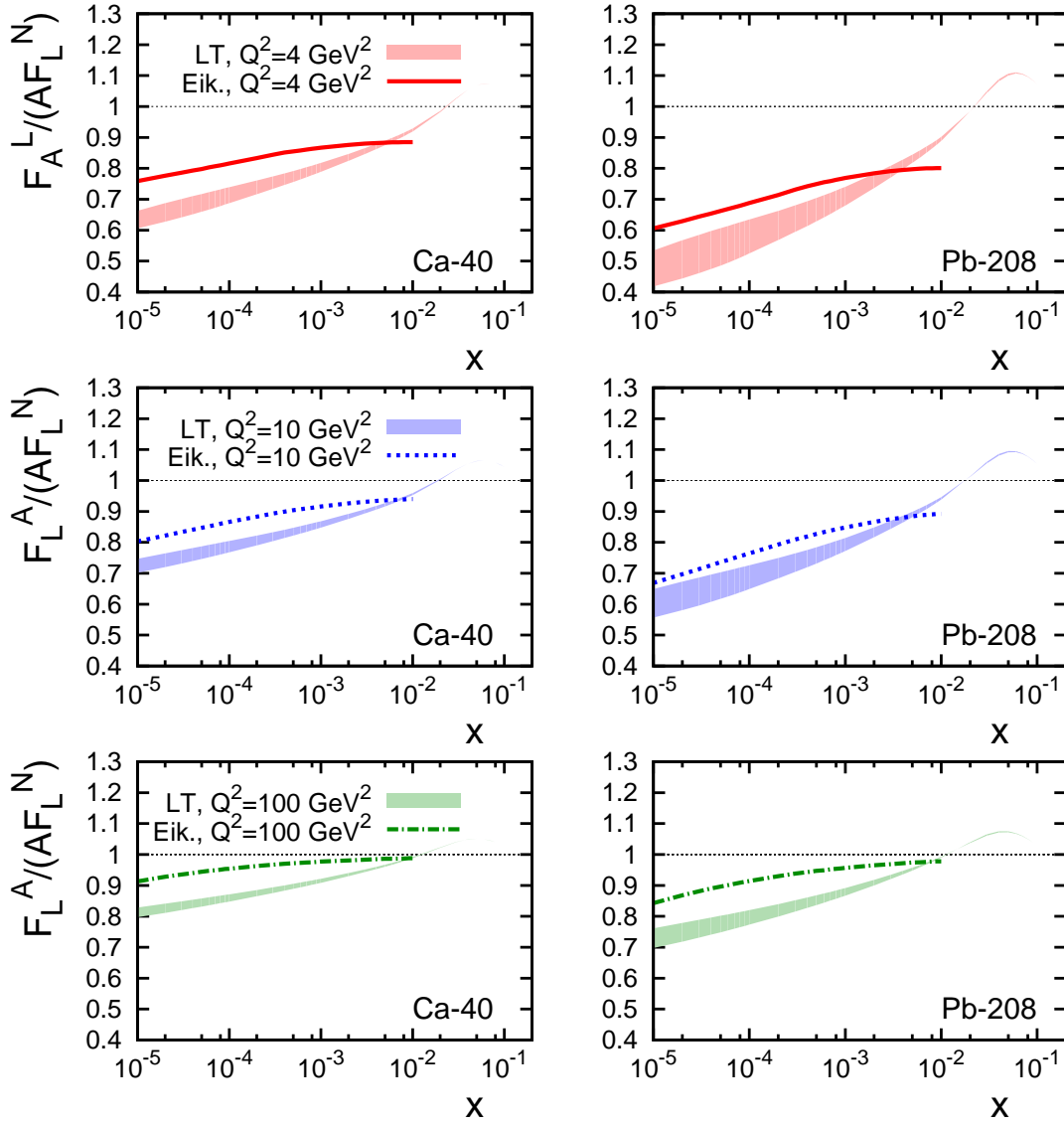


Fig. 59. The ratio of the nuclear to the nucleon longitudinal structure functions, $F_L^A(x, Q^2)/[AF_L^N(x, Q^2)]$, as a function of Bjorken x . The curves represent the results of the dipole model eikonal approximation; the shaded bands correspond to the leading twist theory of nuclear shadowing.

Fock states of the incoming high-energy virtual photon can be considered frozen would be justified, and the procedure of eikonalization can be unambiguously justified.

In contrast, in a quantum field theory such as QCD, the number of bare particles is not conserved. In other words, the number of effective degrees of freedom, or relevant Fock states, in the photon wave function depends on x and Q^2 . For example, the interacting $|q\bar{q}\rangle$ Fock state radiates gluons, thus creating and mixing with $|q\bar{q}g\rangle$, $|q\bar{q}g\dots g\rangle$ states. This mixing is properly taken into account by the QCD evolution in the leading twist approximation.

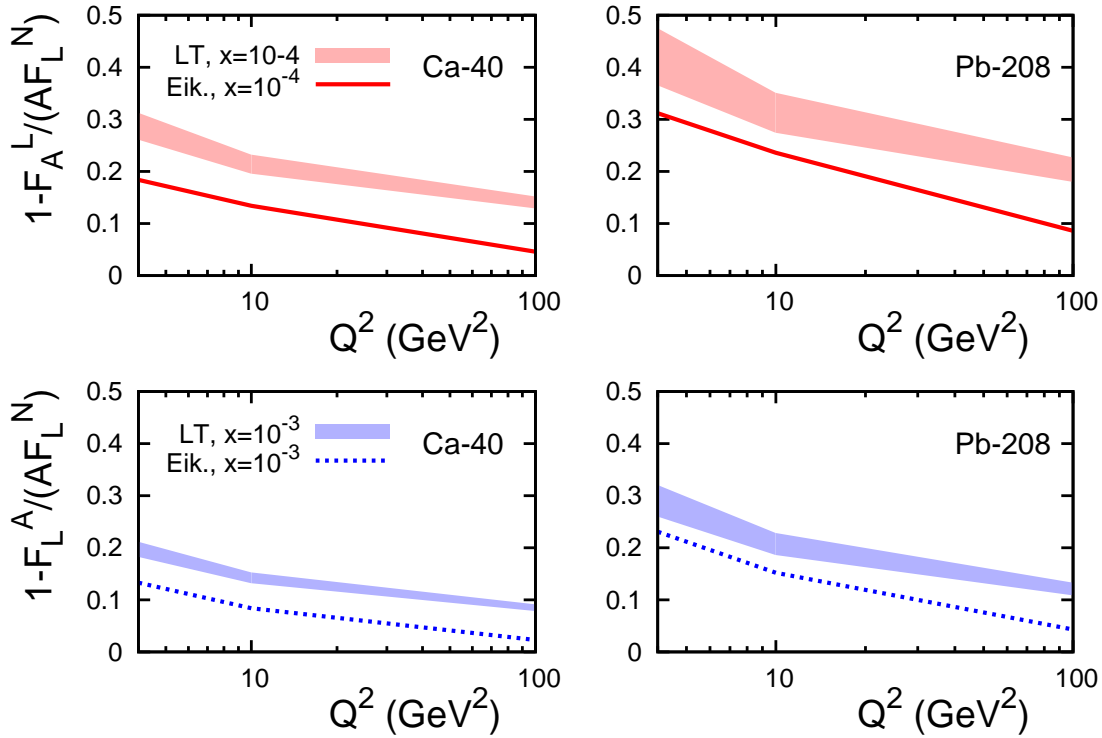


Fig. 60. The shadowing correction to the nuclear longitudinal structure function $F_L^A(x, Q^2)$, $1 - F_L^A(x, Q^2)/[AF_L^N(x, Q^2)]$, as a function of Q^2 for $x = 10^{-4}$ and $x = 10^{-3}$. The curves correspond to the dipole model eikonal approximation; the shaded bands are the results of the leading twist theory of nuclear shadowing.

One immediate consequence of the contrasting pictures of the space-time evolution in the leading twist and dipole model eikonal approaches is the Q^2 dependence of nuclear shadowing. As Q^2 increases, the Fock components of the virtual photon with an increasing number of gluons, $|q\bar{q}g \dots g\rangle$, become important for nuclear shadowing. This follows straightforwardly from the connection between nuclear shadowing and gluon-dominated diffraction, as found in ZEUS and H1 experiments at HERA. As a result, using the factorization theorem, the Q^2 dependence of nuclear shadowing is governed by the DGLAP evolution equation within the leading twist approach.

The dipole model eikonal approximation underestimates nuclear shadowing at large Q^2 —this can be seen in Figs. 57 and 58. (As we mentioned above, this manifests even stronger in the case of the longitudinal structure function $F_L^A(x, Q^2)$, see Figs. 59 and 60.) This happens because the dipole model eikonal approximation includes only the $q\bar{q}$ -component of the virtual photon wave function and neglects diffractively produced inelastic states, such as $q\bar{q}g$, $q\bar{q}gg$, etc. To reproduce the correct Q^2 behavior of nuclear shadowing, which is governed by the DGLAP evolution equation, one should include the complete set of Fock states, i.e., a Q^2 -dependent number of constituents, as well as the QCD evolution trajectories starting at large $x \geq 0.1$, where the nuclear PDFs are not screened in the leading twist approach. (For the discussion of QCD trajectories, see Sec. 5.15.)

It is also worth mentioning that the lack of separation over twists in the dipole eikonal model precludes a simple connection between the nuclear effects in DIS and other hard processes, such as the production of jets in $\gamma^*T \rightarrow jet_1 + jet_2 + X$ and in $pA \rightarrow jet_1 + jet_2 + X$, etc.

Also, there are several technical problems with the implementation of the eikonal approximation. Firstly, in the kinematics where the elastic and inelastic $q\bar{q}$ -nucleon cross sections are compatible, the use of the inelastic $\sigma_{q\bar{q}N}$ cross section alone would significantly underestimate nuclear shadowing.

Secondly, to reproduce nuclear shadowing at the higher end of the shadowing region, $0.01 \leq x \leq 0.1$, one needs to take into account the non-zero longitudinal momentum transfer to the nucleus through the factor $\exp(i2xm_N(z_1 - z_2))$. In order to arrive at this factor in the eikonal approximation, one needs to make a bold assumption that all essential Fock states of the virtual photon have the same invariant mass of the order of Q .

Thirdly, in the target infinite momentum frame, the main source of the disappearance of nuclear shadowing with an increase of Q^2 at fixed x is the mixing between the small- x and large- x contributions, which occurs due to the DGLAP evolution. This effect is absent in the dipole eikonal approximation.

5.15 QCD evolution trajectories

The Q^2 evolution of nuclear PDFs is governed by the DGLAP evolution equations, see Eq. (117). The general trend of the DGLAP Q^2 evolution is well known. As Q^2 increases, the parton densities shift toward lower values of x because of the emission of softer partons. Therefore, the evolution proceeds along a trajectory in the $x - Q^2$ plane, which extends from low Q^2 and high x toward large Q^2 and small x . The detailed knowledge of this trajectory is very important. It enables, for example, to estimate the influence of the input PDFs at the initial evolution scale Q_0^2 on the result of the QCD evolution to higher scales Q^2 and to judge as to what region of x at Q_0^2 contributes to the PDFs after the evolution. Also, an understanding of the QCD evolution trajectory is relevant for the studies of the applicability of the leading twist QCD evolution.

To numerically study the trajectory in the $x - Q^2$ plane along which the DGLAP evolution proceeds, we adopt the following algorithm [74]. At the input scale, $Q_0^2 = 4 \text{ GeV}^2$, we pick an arbitrary value of x_0 , which will serve as the starting point of the evolution trajectory, (x_0, Q_0^2) . For any $Q'^2 > Q_0^2$, we find x' , $x' < x_0$, by requiring that half of $f_{j/A}(x', Q'^2)$ comes from the DGLAP evolution equations where the lower limit of integration is x_0

instead of x' [compare to Eq. (117)]:

$$\frac{1}{2}f_{j/A}(x', Q'^2) = f_{j/A}(x', Q'^2)|_{x_0}, \quad (149)$$

where

$$\begin{aligned} \frac{d f_{j/A}^{ns}(x', Q'^2)|_{x_0}}{d \log Q'^2} &= \frac{\alpha_s(Q'^2)}{2\pi} \int_{x_0}^1 \frac{dy}{y} P_{qq} \left(\frac{x'}{y} \right) f_{j/A}^{ns}(y, Q'^2)|_{x_0}, \\ \frac{d}{d \log Q'^2} \begin{pmatrix} f_A^s(x', Q'^2) \\ f_{g/A}(x', Q'^2) \end{pmatrix} \Big|_{x_0} &= \frac{\alpha_s(Q'^2)}{2\pi} \int_{x_0}^1 \frac{dy}{y} \begin{pmatrix} P_{qq} \left(\frac{x'}{y} \right) & P_{qg} \left(\frac{x'}{y} \right) \\ P_{gq} \left(\frac{x'}{y} \right) & P_{gg} \left(\frac{x'}{y} \right) \end{pmatrix} \begin{pmatrix} f_A^s(y, Q'^2) \\ f_{g/A}(y, Q'^2) \end{pmatrix} \Big|_{x_0} \end{aligned} \quad (150)$$

This procedure allows us to determine point (x', Q'^2) on the curve starting at (x_0, Q_0^2) . By scanning the desired range of values of Q'^2 , we obtain the entire QCD evolution trajectory. Our prescription for the determination of the evolution trajectory provides the quantitative measure of the essential integration region in x which contribute to the parton density for $Q^2 > Q_0^2$ within the DGLAP approximation.

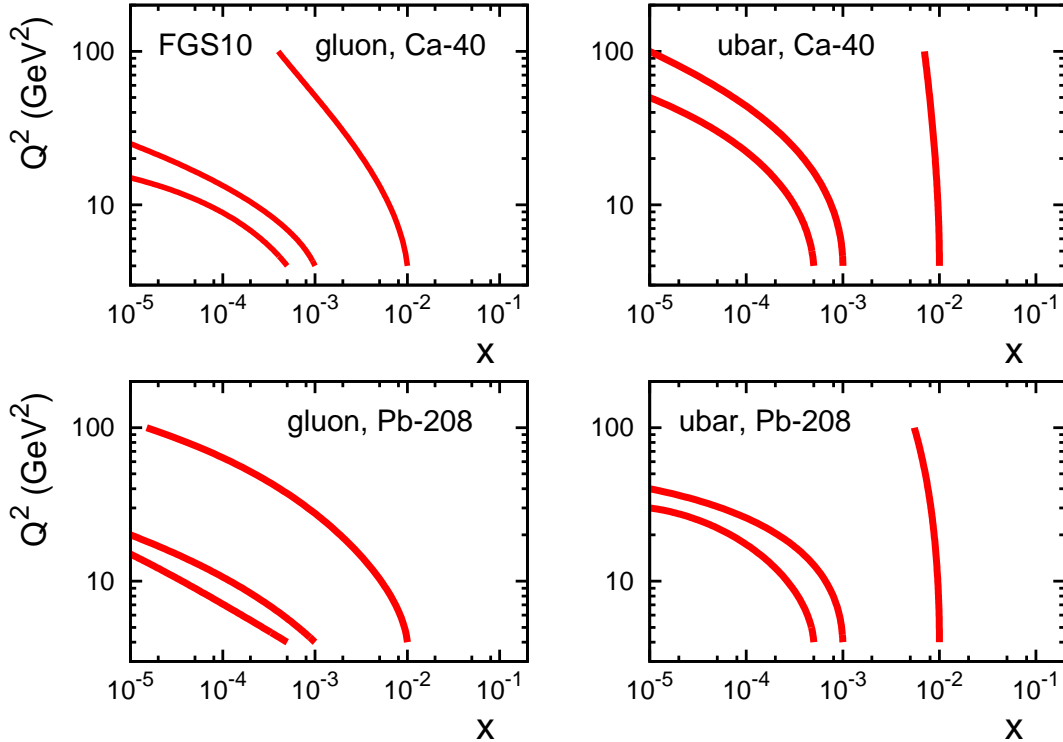


Fig. 61. The QCD evolution trajectories determined by Eqs. (149) and (150) and discussed in the text. The curves for models FGS10_H and FGS10_L are indistinguishable.

The resulting QCD evolution trajectories for three different values of the initial x_0 , $x_0 =$

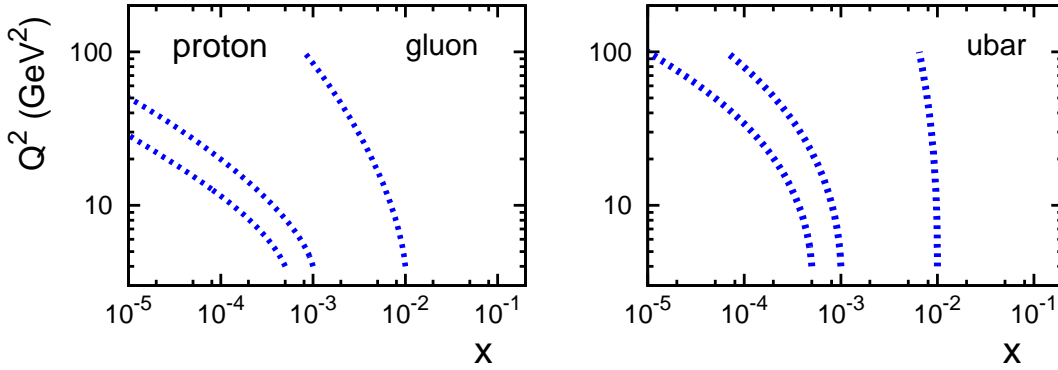


Fig. 62. The QCD evolution trajectories for the free proton.

0.01, 10^{-3} , and 5×10^{-4} , are presented in Fig. 61 (^{40}Ca and ^{208}Pb) and Fig. 62 (free proton). (In Fig. 61, the trajectories for models FGS10_H and FGS10_L are indistinguishable.) As one can see from the figures, the trajectories for the gluon and quark channels are different. Also, the trajectories starting at $x_0 < 0.01$ for the nuclei and free proton are different, too. These features are related and we address them below.

As we progressively decrease the starting point x_0 , we increase the right hand side of Eq. (150) and, hence, $f_{j/A}(x', Q^2)|_{x_0}$. Therefore, the solution of Eq. (149) at fixed given Q^2 can be found at progressively smaller values of x' . Since the gluon parton densities are larger than the quark ones, the found values of x' in the gluon channel are smaller than those in the quark channel, i.e., the trajectories in the gluon channel bend toward smaller x stronger than those in the quark channel. This is true both for nuclei and free proton (see Figs. 61 and 62).

Turning to the comparison between the nuclear and free nucleon cases, we notice that at the starting point $x_0 < 0.01$, where the nuclear modifications of parton distributions are small, the trajectories for ^{40}Ca , ^{208}Pb , and proton are very similar. (The only exception is the gluon channel for ^{208}Pb .) As we decrease x_0 and x' , we move deeper in the shadowing region. This means that at the same small x_0 , the solution of Eq. (149) in the nuclear case can be found at smaller x' than in the free proton case in order to compensate for the suppression of $f_{j/A}(x', Q^2)$ due to nuclear shadowing. As a result, the trajectories in the nuclear case bend toward smaller x stronger than those in the free proton case.

It is also instructive to compare $\ln(Q^2/Q_0^2)$ and $\ln(x/x_0)$ for different trajectories. One can see from Figs. 61 and 62 that for a large range of $x_0 > 10^{-3}$, these logarithms are comparable. This indicates that for this range of x_0 , the double-log approximation should work well. At the same time, $\ln(x/x_0)$ becomes more important than $\ln(Q^2/Q_0^2)$ for gluons in nuclei for $x_0 < 10^{-3}$. However, even in this case, $\alpha_s \ln(x/x_0) \ll 1$ so that corrections to the NLO DGLAP should remain modest.

We will discuss in Sec. 8 that for sufficiently small x and moderate Q_0^2 , the DGLAP approximation may break down due to proximity to the black disk regime. The inspection

of Fig. 61 shows that for very small x , the increase of Q^2 leads to the dominance of the trajectories that avoid the black disk region, so that with an increase of Q^2 (for fixed x) one would reach the kinematics where predictions based on the DGLAP approximation are valid.

5.16 Comparison of predictions of the leading twist theory of nuclear shadowing with fixed-target data

Predictions of the leading twist theory of nuclear shadowing can be compared to the available measurements of $F_{2A}(x, Q^2)$ in nuclear DIS with fixed targets [1–21]; an example of such a comparison is presented in Figs. 63 and 64.

In Fig. 63, the NMC data for $F_{2A}(x, Q^2)/[AF_{2N}(x, Q^2)]$ for ^{40}Ca [17] is compared to the predictions of the leading twist theory of nuclear shadowing given by the solid band spanning the predictions of models FGS10_H and FGS10_L (see Sec. 5.1). As we explained in the Introduction, the low- x fixed-target nuclear DIS data points correspond to the low values of Q^2 that are (significantly) lower than our input scale $Q_0^2 = 4 \text{ GeV}^2$ and the alternative possible input scale $Q_0^2 = 2.5 \text{ GeV}^2$ (see Fig. 47 in Sec. 5.9). Therefore, we cannot directly compare our predictions to the data in this kinematics. Hence, in Fig. 63, for the first four data points with $Q^2 < 2.5 \text{ GeV}^2$ [the average values of Q^2 for these points are $\langle Q^2 \rangle = (0.60, 0.94, 1.4, 1.9) \text{ GeV}^2$, respectively], our predictions are evaluated at fixed $Q^2 = 2.5 \text{ GeV}^2$.

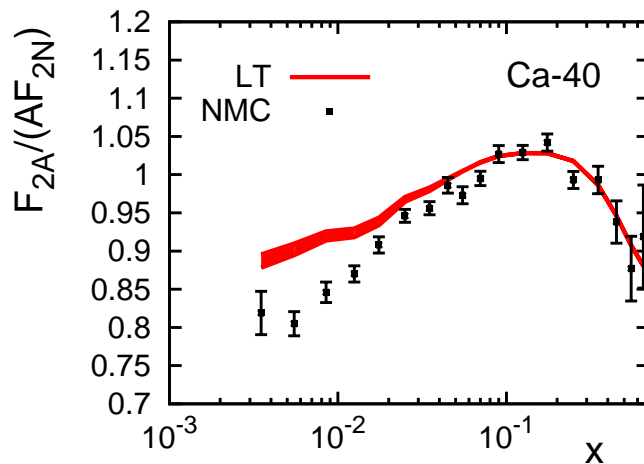


Fig. 63. The ratio of the nuclear (^{40}Ca) to nucleon structure functions $F_{2A}(x, Q^2)/[AF_{2N}(x, Q^2)]$ as a function of x . The data points are the NMC data [17]. The solid band is the prediction of the leading twist theory of nuclear shadowing.

Figure 64 presents the $12F_{2A}(x, Q^2)/[AF_{2C}(x, Q^2)]$ ratio as a function of the atomic number A . Our leading twist predictions are given by the solid band spanning the predictions

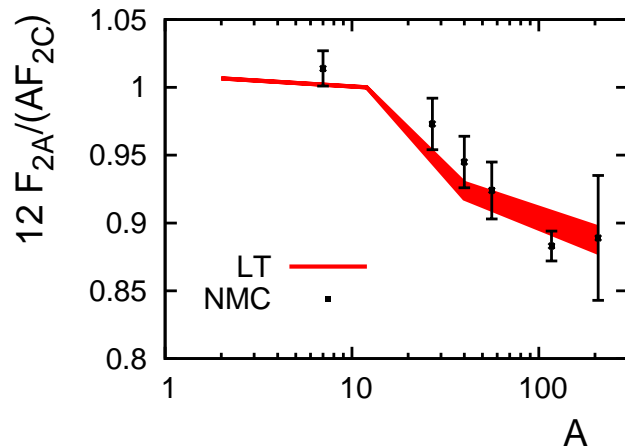


Fig. 64. The $12F_{2A}(x, Q^2)/[AF_{2C}(x, Q^2)]$ ratio as a function of the atomic number A . The data points are the NMC data [20]. The solid band is the prediction of the leading twist theory of nuclear shadowing. All data points correspond to $x = 0.0125$ and $Q^2 = 3.4 \text{ GeV}^2$.

of models FGS10_H (lower boundary) and FGS10_L (upper boundary). Our predictions are evaluated at $x = 0.0125$ and $Q^2 = 3.4 \text{ GeV}^2$ of the NMC data points [20] used for comparison in the figure. As one can see from the figure, the leading twist theory of nuclear shadowing reproduces the A dependence of nuclear shadowing rather well.

It is important to emphasize that one should clearly separate two issues: (i) the validity of the Gribov-Glauber theory of nuclear shadowing for the NMC data, and (ii) the applicability of the leading twist approximation to the NMC fixed-target data. While the Gribov-Glauber theory has been shown to work with high precision in the NMC kinematics, the straightforward application of the leading twist theory of nuclear shadowing to the NMC fixed-target data fails, see Fig. 63. Below we elaborate on these issues.

A fairly good description of the low- x and low- Q^2 NMC data on the nuclear structure function $F_{2A}(x, Q^2)$ was achieved within the Gribov-Glauber theory of nuclear shadowing [97,98]. (A recent analysis [99] in the framework of the Gribov-Glauber theory provided a good description of the NMC data with $Q^2 > 2 \text{ GeV}^2$.) As an input for these calculations, phenomenological parameterizations that fit well the inclusive and diffractive structure functions of the nucleon were used. In contrast to our strictly leading twist analysis, the phenomenological parameterizations used in [97–99] effectively included higher twist contributions, see the discussion in Sec. 5.13.

The Gribov-Glauber theory of nuclear shadowing combined with phenomenological fits to inclusive diffraction in photon-nucleon scattering (the accurate data on the real photon diffraction for the relevant energies is available, see Ref. [204]) provides a good description of nuclear shadowing in real photon-nucleus scattering [100–102].

The fact that the A dependence of nuclear shadowing is reproduced well by the leading

twist theory of nuclear shadowing, see Fig. 64, also indicates that the Gribov-Glauber theory works for the NMC data.

All these arguments put together indicate that it is very natural to have rather significant higher twist effects at small Q^2 since, for this kinematics, the contribution of small diffractive masses M_X becomes important. Production of small diffractive masses M_X is dominated by the production of vector mesons, which is definitely a higher twist phenomenon.

To model the role of the higher twist contribution to nuclear shadowing, we explicitly calculate the contribution of the ρ , ϕ and ω vector mesons to nuclear shadowing using the vector meson dominance (VMD) model. The resulting $F_{2A}^{\text{VMD}}(x, Q^2)/[AF_{2N}(x, Q^2)]$ reads [76,88]:

$$\begin{aligned} \frac{F_{2A}^{\text{VMD}}(x, Q^2)}{AF_{2N}(x, Q^2)} = & 1 - \frac{A-1}{2} \frac{Q^2(1-x)}{\pi F_{2N}(x, Q^2)} \sum_{V=\rho,\phi,\omega} \frac{\sigma_V^2}{f_V^2} \left(\frac{m_V^2}{Q^2 + m_V^2} \right)^2 H(Q^2) \\ & \times \int d^2b \int_{-\infty}^{\infty} dz_1 \int_{z_1}^{\infty} dz_2 \rho_A(b, z_1) \rho_A(b, z_2) \cos(\Delta_V(z_2 - z_1)) e^{-(A/2)\sigma_V \int_{z_1}^{z_2} dz \rho_A(b, z)}, \quad (151) \end{aligned}$$

where m_V is the vector meson mass; g_V is the $V \rightarrow e^+e^-$ coupling constant; σ_V is the vector meson-nucleon total scattering cross section; $\Delta_V = x m_V(1 + m_V^2/Q^2)$; $H(Q^2) = 1/(1+Q^2/Q_0^2)$ is an additional damping factor suppressing the overlap between the virtual photon and vector meson wave functions at large Q^2 . The VMD parameters g_V and σ_V have their usual values, see, e.g., [88]: $\sigma_\rho = \sigma_\omega = 25$ mb, $\sigma_\phi = 10$ mb, $f_\rho^2/(4\pi) = 2$, $f_\omega^2/(4\pi) = 23$, and $f_\phi^2/(4\pi) = 13$. For the nucleon structure function $F_{2N}(x, Q^2)$ for low Q^2 and x , we used the NMC parameterization [19] for $x > 0.006$ and the ALLM97 fit [205] for $x < 0.006$ (the original ALLM fit [206]) gives similar results).

The inclusion of the VMD contribution significantly increases the nuclear shadowing correction. Adding together our leading twist and the VMD contributions, we obtain the predictions given by the lower solid band in Fig. 65. (Like in the case of Fig. 63, the band corresponds to the theoretical uncertainty of our leading twist theory predictions.) As one can see from the figure, while the lower band somewhat overestimates the amount of nuclear shadowing, the description of the data is still fairly good (except for the lowest x point).

Since one does not have an unambiguous way to add the LT and VMD contributions, as an illustration, we consider the scenario when the VMD contribution is added with the coefficient 1/2. This coefficient accounts for the duality between the continuum and VMD contributions to diffraction, see also the discussion in Ref. [194]. The corresponding prediction is given by the upper band in Fig. 65. As one can see from the figure, the "LT+0.5 VMD" prescription provides a good description of the NMC data.

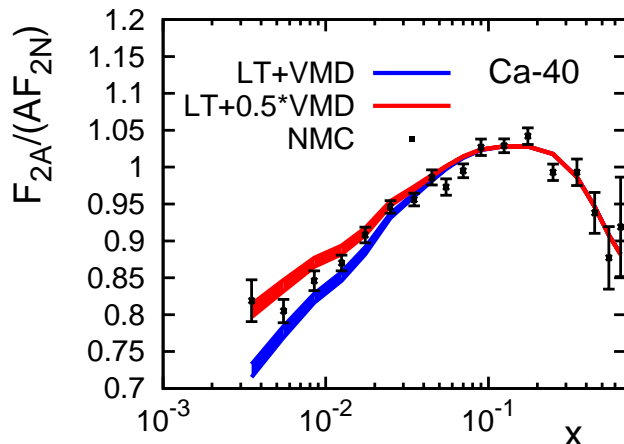


Fig. 65. Comparison of the $F_{2A}(x, Q^2)/[AF_{2N}(x, Q^2)]$ ratio for ^{40}Ca [17] to our predictions corresponding to the sum of the leading twist and VMD contributions. The lower band corresponds to LT+VMD; the upper band corresponds to LT+0.5VMD (see the text).

Figures 63 and 65 illustrate the important qualitative phenomenon that the higher twist effects play an important role in nuclear shadowing in the considered kinematics. This conclusion is in a broad agreement with the phenomenological approaches to nuclear shadowing which include both the scaling (leading twist) and lowest mass (ρ , ω and ϕ) vector meson (higher twist) contributions [85–92,94,95].

One should also mention a very different approach to nuclear shadowing, where nuclear shadowing is a purely higher twist effect [207]. The analysis of [207] confirms our observation that the higher twist effects in the fixed-target kinematics are large. So far the connection of the approach of [207] to the Gribov theory is not clear. In particular, the diagrams that correspond to the vector meson production (which dominates the higher twist small- x contribution in the Gribov theory) seem to be neglected in [207] as a very high twist effect. It would be interesting to compare predictions for the double scattering contribution to $F_{2A}(x, Q^2)$ made using the approach of Ref. [207] and the Gribov relation between shadowing and diffraction [see Eq. (43)], which, in this limit, is a consequence of unitarity, see the discussion in Sec. 3.

5.17 The EMC effect for heavy nuclei and the Lorentz dilation of the nuclear Coulomb field

This subsection is based on Ref. [208]. In QCD one usually treats the parton wave function of a nucleus A as built of quarks and gluons. As a result, it satisfies the following

momentum sum rule:

$$\int_0^1 [x_A V_A(x_A, Q^2) + x_A S_A(x_A, Q^2) + x_A G_A(x_A, Q^2)] dx_A = 1, \quad (152)$$

where the summation over the quark flavors is assumed; (V_A, S_A, G_A) refer to the (valence quark, sea quark, gluon) distributions in the target; $x_A = Q^2/(2q_0 M_A)$ where q_0 is the virtual photon energy and M_A is the nucleus mass. In this approximation, one neglects electromagnetic effects both in the hadron wave function at the initial scale of the evolution, Q_0^2 , and in the DGLAP QCD evolution.

In the case of a fast particle, its Coulomb field is transformed into the field of equivalent photons. As a result, the photons become dynamical degrees of freedom. To take them into account requires the modification of the QCD evolution equations by including the momentum distribution of the photons, P_A , in addition to the standard contributions of quarks and gluons. Thus, the presence of the photon component in the nuclear light-cone wave function leads to the following modification of the momentum sum rule:

$$\int_0^1 [x_A V_A(x_A, Q^2) + x_A S_A(x_A, Q^2) + x_A G_A(x_A, Q^2) + x_A P_A(x_A, Q^2)] dx_A = 1. \quad (153)$$

To remove the kinematic effects, it is convenient to rescale the variables by introducing the light-cone fraction x defined as

$$x = Ax_A, \quad (154)$$

where A is the atomic mass number of the nucleus A . It satisfies the inequality $0 < x < A$ and differs from the Bjorken x for the scattering off a proton, $x_p = Q^2/(2q_0 m_p)$, due to the nuclear binding energy. In terms of x , Eq. (153) reads:

$$\int_0^A [(1/A)(xV_A(x, Q^2) + xS_A(x, Q^2) + xG_A(x, Q^2)) + xP_A(x, Q^2)] dx = 1. \quad (155)$$

In this review we are interested in the A dependence of nuclear PDFs, and, hence, the electromagnetic effects at the level of the proton and neutron is of no relevance for our analysis since they are canceled out in the ratio of the nucleus and nucleon PDFs. As a result, the main effect is the presence of the Coulomb coherent field of the nucleus and not the Coulomb fields of individual nucleons.

It is possible to calculate the contribution of the coherent field using Fermi-Weizsacker-Williams approximation for the wave function of a rapid projectile with nonzero electric

charge [209]; this is the only contribution which is proportional to Z^2 . Subtracting the contribution of the individual nucleons which is proportional to Z , one finds for the photon field of a rapid nucleus [208]:

$$\Delta x P_A(x, Q^2) = \frac{\alpha_{\text{em}}}{\pi} \frac{Z(Z-1)}{A} \int dk_t^2 k_t^2 \frac{F_A^2(k_t^2 + x^2 m_N^2)}{(k_t^2 + x^2 m_N^2)^2}, \quad (156)$$

where F_A is the nuclear electric form factor; k_t is the transverse momentum of the active nucleon in the nucleus.

The explicit evaluation of Eq. (156) shows that a rather significant fraction of the nucleus light-cone momentum is carried by the additional photons in the medium and heavy nuclei. Defining λ_γ as

$$\lambda_\gamma = (1/A) \int_0^A \Delta x P_A(x, Q^2) dx, \quad (157)$$

one finds

$$\begin{aligned} \lambda_\gamma(^4\text{He}) &= 0.03\%, & \lambda_\gamma(^{12}\text{C}) &= 0.11\%, \\ \lambda_\gamma(^{27}\text{Al}) &= 0.21\%, & \lambda_\gamma(^{56}\text{Fe}) &= 0.35\%, \\ \lambda_\gamma(^{197}\text{Au}) &= 0.65\%. \end{aligned} \quad (158)$$

In the discussed approximation, the eA cross section could be written as a convolution of the ep cross section and the nucleon density in the nucleus. Performing the Taylor series expansion in powers of k^2/m_N^2 (k is the nucleon momentum in the nucleus), one finds that the bulk effect of the additional photon component is that individual nucleons carry only the $(1 - \lambda_\gamma(A))$ fraction of the nucleus light-cone momentum (we neglect here the effect of possible modification of the bound nucleon wave function). This effect can be accounted for by the following rescaling:

$$\begin{aligned} x q_A(x, Q^2) &= A x' q_N(x', Q^2), \\ x g_A(x, Q^2) &= A x' g_N(x', Q^2), \end{aligned} \quad (159)$$

where

$$x' = x / (1 - \lambda_\gamma(A)). \quad (160)$$

Equation (159) leads to the modification of the nuclear structure functions. In particular, for the ratio $R_A^{\text{EMC}}(x_p, Q^2) = (2/A) F_{2A}(x_p, Q^2) / F_{2D}(x_p, Q^2)$ also known as the EMC ratio,

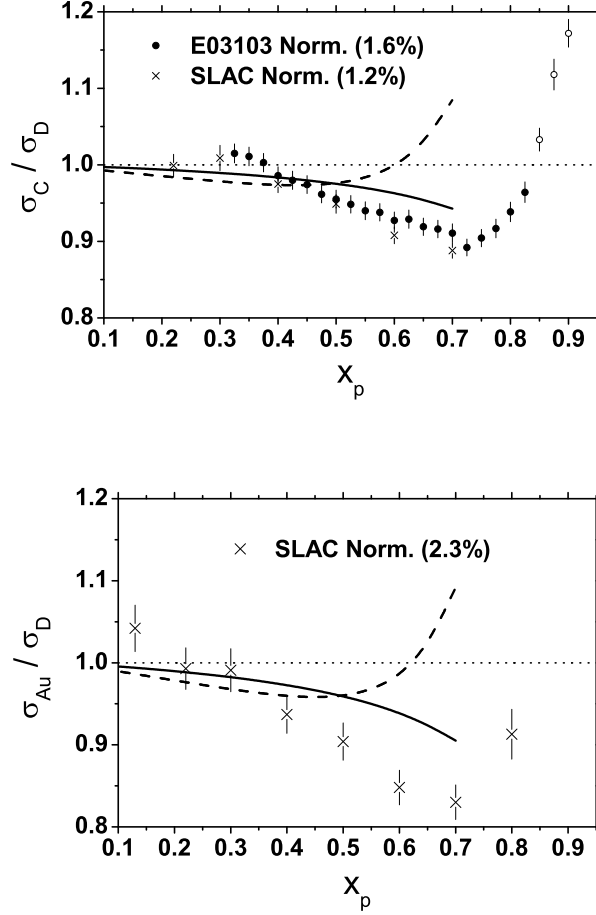


Fig. 66. The EMC ratio as a function of x_p . The solid curve is the result that takes into account the effect of the nuclear Coulomb field resulting in the proper definition of x calculated using Eq. (159); it is applicable for $x \leq 0.7$ only. The dashed curve includes also the Fermi motion effect. The data are from [16,210]; the open circles correspond to $W < 2$ GeV.

it leads to the effect that explains a half of the effect observed in the data for $x \leq 0.55$ where the Fermi motion effects are small, see Fig. 66. Note here that for light nuclei, the main effect is due to the proper definition of the light-cone fraction x [Eq. (154)], which enters in the convolution formula, and a small correction from the Coulomb effect. For heavy nuclei, a comparable contribution comes also from the Coulomb effect. Overall, our observation that the hadronic EMC effect exceeds few percent only for $x \geq 0.55$, where the structure functions are very small and an important role is played by short-range nucleon-nucleon correlations, confirms our starting approximation to treat nuclei as many-nucleon systems with relativistic corrections treated within the light-cone many-nucleon approximation.

One can see from Eq. (159) that the discussed correction is on the scale of a fraction of percent for the region of $x \leq 0.1$, which is the focus of the present review, since the parton distributions $xq(x, Q^2)$ and $xg(x, Q^2)$ are changing in this x -range rather slowly as $x^{-\lambda(Q^2)}$, with $\lambda(Q^2)$ varying between 0.2 and 0.4. The only other potentially significant effect is the change of the fraction of the momentum of the nucleus carried by the gluons. It is usually determined based on the application of Eq. (155) and is close to ~ 0.5 . An account of the photons results in its reduction by $-2\lambda_\gamma(A)$, i.e., by about 1.4% for heavy nuclei. Only half of this reduction is accounted for by the rescaling in Eq. (159). The rest may somewhat reduce the enhancement of the gluon ratio at $x \sim 0.1$ (antishadowing) which follows from the application of the momentum sum rule. However, as we pointed out in Sec. 5.1.4, our estimates of the modification of the gluon PDF for these x have rather large uncertainties.

6 Final states in DIS with nuclei at small x

In Sec. 5 we demonstrated that the existence of leading twist diffraction in DIS leads to the significant suppression of the nuclear PDFs at small x . In this section, we explore consequences of the leading twist shadowing phenomenon for the final states produced in the small x processes induced by hard probes. In particular, we consider the following three characteristics of the final states: diffraction, spectra of leading particles, and fluctuations of multiplicity at central rapidities.

6.1 Nuclear diffractive structure functions and diffractive parton distribution functions

6.1.1 Coherent diffraction

Let us consider diffractive DIS with nuclei, $\gamma^*A \rightarrow XA'$, which is characterized by the presence of a rapidity gap between the products of the photon dissociation, X , and the final nuclear state A' . We first address the case of the coherent scattering when the nucleus remains intact, $A' = A$, see Fig. 67. Coherent scattering is readily amenable to the theoretical methods which were successful in the case of inclusive eA scattering and is also easier to detect experimentally in collider experiments (see the discussion in the end of this subsection).

Squaring the $eA \rightarrow e'XA$ amplitude, one obtains the $eA \rightarrow e'XA$ cross section expressed in terms of the nuclear diffractive structure function $F_{2A}^{D(4)}$ [compare to Eq. (83)]:

$$\frac{d^4\sigma_{eA}^D}{dx_{\mathbb{P}} dt dx dQ^2} = \frac{2\pi\alpha^2}{xQ^4} \left(1 + (1 - y)^2\right) F_{2A}^{D(4)}(x, Q^2, x_{\mathbb{P}}, t). \quad (161)$$

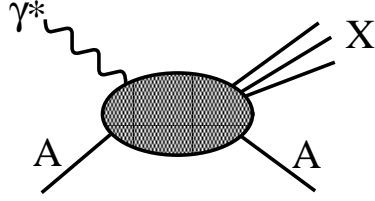


Fig. 67. Coherent diffractive DIS with nuclei.

In Eq. (161), we ignored the contribution of the longitudinal diffractive structure function $F_{L,A}^{D(4)}$ —its contribution is small in the considered kinematics.

From the practical point of view, it is not feasible to detect the recoil nucleus at the small values of t characteristic for coherent scattering. Therefore, in the following discussion we concentrate on the diffractive cross section integrated over the momentum transfer t which is expressed in terms of the nuclear diffractive structure function $F_{2A}^{D(3)}$ [compare to Eq. (86)]:

$$F_{2A}^{D(3)}(x, Q^2, x_{\mathcal{P}}) = \int_{-1 \text{ GeV}^2}^{t_{\min}} dt F_{2A}^{D(4)}(x, Q^2, x_{\mathcal{P}}, t). \quad (162)$$

It follows from the QCD factorization theorem for diffraction in DIS that one can introduce the nuclear diffractive parton distributions $f_{j/A}^{D(3)}(\beta, Q^2, x_{\mathcal{P}})$ and express $F_{2A}^{D(3)}$ in terms of $f_{j/A}^{D(3)}(\beta, Q^2, x_{\mathcal{P}})$ [compare to Eq. (85)]:

$$F_{2A}^{D(3)}(x, Q^2, x_{\mathcal{P}}) = \beta \sum_{j=q,\bar{q},g} \int_{\beta}^1 \frac{dy}{y} C_j\left(\frac{\beta}{y}, Q^2\right) f_{j/A}^{D(3)}(y, Q^2, x_{\mathcal{P}}), \quad (163)$$

where $\beta = x/x_{\mathcal{P}}$.

The derivation of the modification of the nuclear diffractive structure function and nuclear diffractive PDFs by nuclear shadowing proceeds very similarly to the derivation of nuclear shadowing in the usual nuclear PDFs presented in Sec. 3. At small x , the virtual photon interacts with many nucleons of the target, and the $\gamma^*A \rightarrow XA$ scattering amplitude is given by the sum of the multiple scattering contributions presented in Fig. 68 (compare to Fig. 9). Graphs *a*, *b*, *c* correspond to the interaction with one, two, and three nucleons of the nuclear target, respectively. Graph *a* is the impulse approximation; graphs *b* and *c* contribute to the shadowing correction. Note that the interactions with four and more nucleons (at the amplitude level) are not shown, but they are implied.

With help of the graphical representation for the $\gamma^*A \rightarrow XA$ amplitude in Fig. 68 and working along the lines of the derivation of nuclear shadowing presented in Sec. 3, the

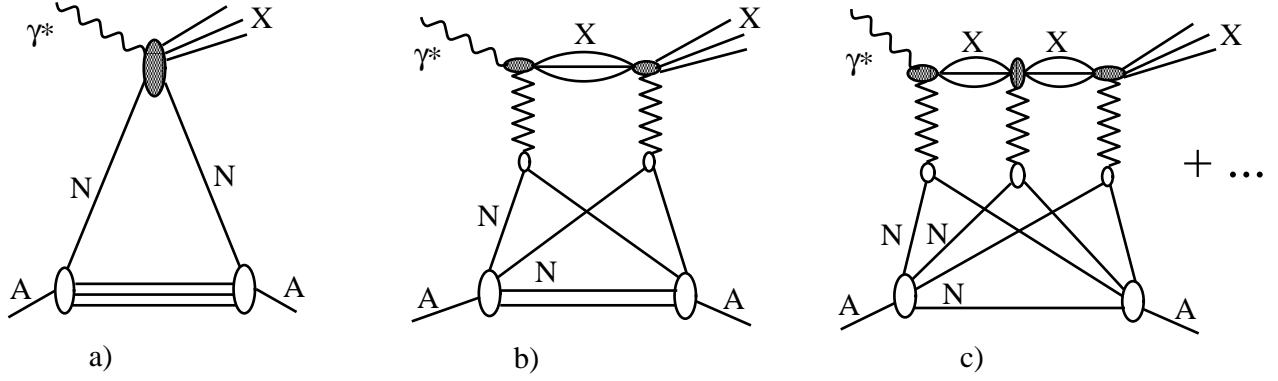


Fig. 68. The multiple scattering series for the $\gamma^* A \rightarrow X A$ scattering amplitude. Graphs *a*, *b*, *c* correspond to the interaction with one, two, and three nucleons of the nuclear target, respectively. Graph *a* is the impulse approximation; graphs *b* and *c* contribute to the shadowing correction.

expression for $f_{j/A}^{D(3)}(\beta, Q^2, x_P)$ can be obtained in a rather straightforward way. Using the color fluctuation formalism which takes into account inelastic intermediate states and the non-zero longitudinal momentum transfer, we obtain for the $\gamma^* A \rightarrow X A$ scattering amplitude in the impact parameter space:

$$\Gamma_{\gamma^* A \rightarrow X A}(b) = \langle A | \sum_i \Gamma_{\gamma^* X}(\vec{b} - \vec{r}_{i\perp}) e^{iz_i \Delta_{\gamma^* X}} \prod_{j \neq i} (1 - \Theta(z_j - z_i) \Gamma_X(\vec{b} - \vec{r}_{j\perp})) | A \rangle, \quad (164)$$

where the brackets $\langle A | \dots | A \rangle$ denote the matrix element between the nuclear ground state; $\Gamma_{\gamma^* X}$ is the $\gamma^* N \rightarrow X N$ scattering amplitude in the impact parameter space (37); Γ_X is the diffractive state X -nucleon scattering amplitude; as in Sec. 3, $\Delta_{\gamma^* X} = (M_X^2 + Q^2)/(2q_0)$ is the longitudinal momentum transfer to the nucleons. These scattering amplitudes are proportional to the $\sigma_{\gamma^* N \rightarrow X N}$ and σ_{soft}^j cross sections, respectively (see the discussion in Sec. 3). Assuming that the nuclear wave function squared is given by the product of independent, one-nucleon densities, ρ_A [see Eq. (39)], and neglecting the t dependence of the $\gamma^* N \rightarrow X N$ diffractive amplitude compared to the nuclear form factor [see Eq. (37)], the integration over the positions of the nucleons in Eq. (164) can be carried out analytically with the following result:

$$\begin{aligned} & \Gamma_{\gamma^* A \rightarrow X A}(b) \\ &= A \frac{1 - i\eta}{2} \sqrt{\frac{16\pi \frac{d\sigma_{\gamma^* N \rightarrow X N}(t_{\min})}{dt}}{1 + \eta^2}} \int dz \rho_A(b, z) e^{iz \Delta_{\gamma^* X}} \\ & \times \left(1 - \frac{1 - i\eta}{2} \sigma_{\text{soft}}^j(x, Q^2) \int_z^\infty dz' \rho_A(b, z') \right)^{A-1} \\ &= A \frac{1 - i\eta}{2} \sqrt{\frac{16\pi \frac{d\sigma_{\gamma^* N \rightarrow X N}(t_{\min})}{dt}}{1 + \eta^2}} \int dz \rho_A(b, z) e^{iz \Delta_{\gamma^* X}} e^{-\frac{A}{2}(1-i\eta)\sigma_{\text{soft}}^j(x, Q^2) \int_z^\infty dz' \rho_A(b, z')} \end{aligned} \quad (165)$$

The $\gamma^*A \rightarrow XA$ cross section is expressed in terms of the corresponding amplitude as

$$\sigma_{\gamma^*A \rightarrow XA} = \int dt \frac{d\sigma_{\gamma^*A \rightarrow XA}}{dt} = \int d^2b |\Gamma_{\gamma^*A \rightarrow XA}(b)|^2. \quad (166)$$

Substituting Eq. (165) in Eq. (166), we obtain

$$\begin{aligned} \sigma_{\gamma^*A \rightarrow XA} &= 4\pi A^2 \frac{d\sigma_{\gamma^*N \rightarrow XN}}{dt}(t_{\min}) \int d^2b \\ &\times \left| \int_{-\infty}^{\infty} dz e^{iz\Delta_{\gamma^*X}} e^{-\frac{A}{2}(1-i\eta)\sigma_{\text{soft}}^j(x, Q^2)} \int_z^{\infty} dz' \rho_A(b, z') \rho_A(b, z) \right|^2. \end{aligned} \quad (167)$$

The nuclear and nucleon diffractive cross sections in Eq. (167) can be expressed in terms of the corresponding diffractive structure functions. Therefore, Eq. (167) leads to the following expression for the nuclear diffractive structure function $F_{2A}^{D(3)}$:

$$\begin{aligned} F_{2A}^{D(3)}(\beta, Q^2, x_P) &= 4\pi A^2 F_{2N}^{D(4)}(\beta, Q^2, x_P, t_{\min}) \int d^2b \\ &\times \left| \int_{-\infty}^{\infty} dz e^{ix_P m_N z} e^{-\frac{A}{2}(1-i\eta)\sigma_{\text{soft}}^j(x, Q^2)} \int_z^{\infty} dz' \rho_A(b, z') \rho_A(b, z) \right|^2. \end{aligned} \quad (168)$$

Note that we expressed the longitudinal momentum transfer Δ_{γ^*X} in terms of x_P , $\Delta_{\gamma^*X} = x_P m_N$. Using the QCD factorization theorem for diffraction (163) in the right-hand and left-hand sides of Eq. (168), we obtain the expression for the nuclear diffractive PDFs $f_{j/A}^{D(3)}$:

$$\begin{aligned} \beta f_{j/A}^{D(3)}(\beta, Q^2, x_P) &= 4\pi A^2 \beta f_{j/N}^{D(4)}(\beta, Q^2, x_P, t_{\min}) \int d^2b \\ &\times \left| \int_{-\infty}^{\infty} dz e^{ix_P m_N z} e^{-\frac{A}{2}(1-i\eta)\sigma_{\text{soft}}^j(x, Q^2)} \int_z^{\infty} dz' \rho_A(b, z') \rho_A(b, z) \right|^2. \end{aligned} \quad (169)$$

Finally, assuming the exponential t dependence of $f_{j/N}^{D(4)}$, i.e., using Eq. (59), we obtain our final expression for the nuclear diffraction parton distribution $\beta f_{j/A}^{D(3)}$ [26,211]:

$$\begin{aligned} \beta f_{j/A}^{D(3)}(\beta, Q^2, x_P) &= 4\pi A^2 B_{\text{diff}} \beta f_{j/N}^{D(3)}(\beta, Q^2, x_P) \int d^2b \\ &\times \left| \int_{-\infty}^{\infty} dz e^{ix_P m_N z} e^{-\frac{A}{2}(1-i\eta)\sigma_{\text{soft}}^j(x, Q^2)} \int_z^{\infty} dz' \rho_A(b, z') \rho_A(b, z) \right|^2. \end{aligned} \quad (170)$$

The structure of the answer resembles the case of the diffractive productions of vector mesons (after the generic diffractive state X is replaced by a single vector meson), see e.g., Ref. [80].

Equation (170) should be compared to Eq. (64): the both equations are derived in the color fluctuation approximation characterized by the cross section $\sigma_{\text{soft}}^j(x, Q^2)$ that determines the strength of the multiple rescatterings. Note also that the nuclear shadowing correction to $\beta f_{j/A}^{D(3)}$ given by Eq. (170) corresponds to the diffractive unitary cut in the language of the AGK cutting rules, see Eq. (24) and graph a in Fig. 8.

The physics interpretation of Eq. (170) is rather straightforward: the diffractive scattering takes place on any of A nucleons of the target at point (\vec{b}, z) ; the produced diffractive state gets absorbed on the way out with the probability amplitude $e^{-\frac{A}{2}(1-i\eta)\sigma_{\text{soft}}^j(x, Q^2) \int_z^\infty dz' \rho_A(b, z')}$.

In the limit of very small $x_{\mathcal{P}}$, the effect of the finite coherent length, i.e., the $e^{ix_{\mathcal{P}}m_N z}$ factor, can be neglected and Eq. (170) can be presented in the following simplified form:

$$\beta f_{j/A}^{D(3)}(\beta, Q^2, x_{\mathcal{P}}) \approx 16\pi B_{\text{diff}} \beta f_{j/N}^{D(3)}(\beta, Q^2, x_{\mathcal{P}}) \int d^2\vec{b} \left| \frac{1 - e^{-\frac{A}{2}(1-i\eta)\sigma_{\text{soft}}^j(x, Q^2)T_A(b)}}{(1-i\eta)\sigma_{\text{soft}}^j(x, Q^2)} \right|^2. \quad (171)$$

In Eq. (170), we neglected the possible dependence of $\sigma_{\text{soft}}^j(x, Q^2)$ on β (the dependence on the diffractive mass M_X). Since the total probability of diffraction changes rather weakly as one varies the rescattering cross section, see e.g., Ref. [34], this seems to be a reasonable first approximation. At the same time, in the region of small β and small x that corresponds to the triple Pomeron kinematics for the soft inelastic diffraction, one expects a suppression of diffraction as compared to the color fluctuation approximation used in Eq. (170). Indeed, Eq. (170) evaluated at $Q^2 = Q_0^2 = 4 \text{ GeV}^2$ essentially corresponds to treating diffraction as a superposition of elastic scattering of different components of the virtual photon wave function. This is a reasonable approximation for the configurations with the masses comparable to Q^2 . In the $\beta \ll 1$ limit (which corresponds to $M_X^2 \gg Q^2$), one approaches the limit analogous to the soft triple Pomeron limit, in which case diffraction off nuclei is strongly suppressed compared to elastic scattering, see, e.g., Refs. [212,213]. Hence, we somewhat overestimate diffraction for small β and relatively small Q_0^2 scales. At larger Q^2 , diffraction at small β is dominated by the QCD evolution from $\beta \geq 0.1$ at Q_0^2 and, hence, the accuracy of our approximation improves. Thus, in our numerical studies, we neglect the effect of the potential small- β suppression that we just discussed.

One can immediately see from Eq. (170) that the Regge factorization, i.e., the factorization of $f_{j/A}^{D(3)}(\beta, Q^2, x_{\mathcal{P}})$ into the product of the Pomeron flux factor $f_{\mathcal{P}}(x_{\mathcal{P}})$ and the PDFs of the Pomeron $f_j(\beta, Q^2)$, see Eq. (88), is not valid for the nuclear diffractive parton distributions, even if it approximately holds for the nucleon case. At fixed $x_{\mathcal{P}}$, the right-

hand side of Eq. (170) depends not only on β , but also on Bjorken x since the screening factor is given by the exponential factor containing $\sigma_{\text{soft}}^j(x, Q^2)$ which is a function of x . In addition, the right-hand side of Eq. (170) depends on the atomic mass number A since the effect of nuclear shadowing increases with increasing A . The breakdown of the Regge factorization approximation is a result of the increase of nuclear shadowing both with the increase of the incident energy (decrease of x) and the atomic number A . This precludes the possibility of the scenario offered in Ref. [214], where coherent diffraction in DIS on the nucleon and nuclear targets is provided by the same universal diffractive PDFs—a "universal Pomeron".

We demonstrated in Sec. 5 that the interaction with $N \geq 3$ nucleons of the nuclear target provides a very small correction to nuclear shadowing for $x \geq 10^{-2}$. Hence, a comparison of the diffractive cross section and the shadowing correction to the inclusive cross section in this kinematics would provide a very stringent test of the theory by testing the relation:

$$-\delta F_{2A}(x, Q^2) = -F_{2A}^{(b)}(x, Q^2) = \frac{1 - \eta^2}{1 + \eta^2} \int dx_{\mathbb{P}} F_{2A}^{D(3)}(x, Q^2, x_{\mathbb{P}}). \quad (172)$$

where $F_{2A}^{(b)}(x, Q^2)$ is the contribution of graph b in Fig. 9 to the shadowing correction to $F_{2A}(x, Q^2)$. Note here that the recoil effects, which are important for such x , do not affect this relation.

In the collider mode, it is rather straightforward to measure coherent diffraction by selecting events with the rapidity gap and requiring that no neutrons are produced in the zero angle calorimeter (ZDC). Practically all events satisfying these requirements would correspond to coherent diffraction. However, measurements of the t dependence would require the use of Roman pots at unrealistically small distances from the beam. The only exception is exclusive channels where one can measure the total transverse momentum of the produced system. In this case, coherent scattering can be selected using the distinctly sharp t dependence in the forward direction (forward diffractive peak), which originates from the square of the nuclear form factor $F_A(t)$.

6.1.2 Incoherent diffraction

The coherent diffractive scattering dominates the $\gamma A \rightarrow XA'$ diffraction at small momentum transfers t close to $t_{\min} \approx -x^2 m_N^2 (1 + M_X^2/Q^2)$. For $|t| > |t_{\min}|$, the probability for the nucleus to stay intact rapidly decreases and the diffraction is dominated by the incoherent final states $A' \neq A$. The case important for practical applications is when one sums over all products of the nuclear disintegration and uses the completeness of the final states $|A'\rangle$. The corresponding cross section reads, see, e.g., [80]:

$$\begin{aligned}
\sigma_{\gamma^*A \rightarrow XA'} &= \int d^2\vec{b} \sum_{A' \neq A} \langle A | \Gamma_{\gamma^*A \rightarrow XA}^\dagger(b, r_i) | A' \rangle \langle A' | \Gamma_{\gamma^*A \rightarrow XA}(b, r_i) | A \rangle \\
&= \int d^2\vec{b} \left[\langle A | |\Gamma_{\gamma^*A \rightarrow XA}(b, r_i)|^2 | A \rangle - |\langle A | \Gamma_{\gamma^*A \rightarrow XA}(b, r_i) | A \rangle|^2 \right], \quad (173)
\end{aligned}$$

where $\Gamma_{\gamma^*A \rightarrow XA}(b, r_i)$ is the $\gamma^*A \rightarrow XA$ scattering amplitude in the impact parameter space which also depends on the positions of the involved nucleons,

$$\Gamma_{\gamma^*A \rightarrow XA}(b, r_i) = \sum_i \Gamma_{\gamma^*X}(\vec{b} - \vec{r}_{i\perp}) e^{iz_i \Delta_{\gamma^*X}} \prod_{j \neq i} \left(1 - \Theta(z_j - z_i) \Gamma_X(\vec{b} - \vec{r}_{j\perp}) \right). \quad (174)$$

The integration over the positions of the nucleons with the weight given by the wave function squared of the nuclear ground state is denoted by $\langle A | \dots | A \rangle$ in Eq. (173).

Using Eq. (174), we obtain for $|\Gamma_{\gamma^*A \rightarrow XA}(b, r_i)|^2$:

$$\begin{aligned}
|\Gamma_{\gamma^*A \rightarrow XA}(b, r_i)|^2 &= \sum_i |\Gamma_{\gamma^*X}(\vec{b} - \vec{r}_{i\perp})|^2 \prod_{j \neq i} \left| \left(1 - \Theta(z_j - z_i) \Gamma_X(\vec{b} - \vec{r}_{j\perp}) \right) \right|^2 \\
&+ \sum_{i \neq i'} \Gamma_{\gamma^*X}^*(\vec{b} - \vec{r}_{i'\perp}) \Gamma_{\gamma^*X}(\vec{b} - \vec{r}_{i\perp}) e^{i\Delta_{\gamma^*X}(z_i - z_{i'})} \\
&\times \prod_{j' \neq i'} \left(1 - \Theta(z_{j'} - z_{i'}) \Gamma_X^*(\vec{b} - \vec{r}_{j'\perp}) \right) \prod_{j \neq i} \left(1 - \Theta(z_j - z_i) \Gamma_X(\vec{b} - \vec{r}_{j\perp}) \right). \quad (175)
\end{aligned}$$

The first term in Eq. (175), which we shall denote $|\Gamma_{\gamma^*A \rightarrow XA}^{(1)}(b, r_i)|^2$ for brevity, corresponds to the incoherent contribution, which scales as A and arises from the interaction of the probe with the same nucleon of the target. The second term in Eq. (175), which we shall refer to as $|\Gamma_{\gamma^*A \rightarrow XA}^{(2)}(b, r_i)|^2$, is similar to the coherent contribution since it scales as the number of the nucleon pairs, $A(A-1)$, and arises from the interference diagrams when the external electromagnetic probe couples to different nucleons.

Let us evaluate the contribution of the first term in Eq. (175). In this calculation, from the outset, one cannot neglect the slope of the $\gamma^*N \rightarrow XN$ amplitude, B_{diff} . Therefore, instead of approximate Eq. (37), we shall use the exact expression:

$$\Gamma_{\gamma^*X}(\vec{b} - \vec{r}_{i\perp}) = \frac{(1 - i\eta)}{4\pi B_{\text{diff}}} \sqrt{\frac{16\pi \frac{d\sigma_{\gamma^*N \rightarrow XN}}{dt}(t_{\min})}{1 + \eta^2}} e^{-(\vec{b} - \vec{r}_{i\perp})^2 / (2B_{\text{diff}})}. \quad (176)$$

Equation (176) is a standard expression for the scattering amplitude (profile function) in the Glauber formalism. Integrating with the nuclear density, we obtain:

$$\int d^2\vec{r}_{i\perp} \rho_A(\vec{r}_{i\perp}, z_i) |\Gamma_{\gamma^*X}(\vec{b} - \vec{r}_{i\perp})|^2$$

$$\begin{aligned}
&= \frac{1}{\pi B_{\text{diff}}^2} \frac{d\sigma_{\gamma^* N \rightarrow XN}}{dt}(t_{\min}) \int d^2 \vec{r}_{i\perp} \rho_A(\vec{r}_{i\perp}, z_i) e^{-(\vec{b}-\vec{r}_{i\perp})^2/B_{\text{diff}}} \\
&\approx \frac{1}{B_{\text{diff}}} \frac{d\sigma_{\gamma^* N \rightarrow XN}}{dt}(t_{\min}) \rho_A(b, z_i) = \sigma_{\gamma^* N \rightarrow XN} \rho_A(b, z_i). \tag{177}
\end{aligned}$$

For the profile function (scattering amplitude) corresponding to the rescattering of state X on the remaining $A - 1$ nucleons of the target, we use the form similar to Eq. (176):

$$\Gamma_X(\vec{b} - \vec{r}_{j\perp}) = \frac{\sigma_{XN \rightarrow XN}(1 - i\eta)}{4\pi B_X} e^{-(\vec{b}-\vec{r}_{j\perp})^2/(2B_X)}, \tag{178}$$

where $\sigma_{XN \rightarrow XN}$ is the elastic XN cross section and B_X is its slope. Their numerical values will be defined later on. Working along the lines of the derivation in Eq. (177), we obtain

$$\int d^2 \vec{r}_{j\perp} dz_j \rho_A(\vec{r}_{j\perp}, z_j) \left| \left(1 - \Theta(z_j - z_i) \Gamma_X(\vec{b} - \vec{r}_{j\perp}) \right) \right|^2 = 1 - \int_{z_i}^{\infty} dz_j \rho_A(b, z_j) \sigma_X^{\text{inel}}, \tag{179}$$

where σ_X^{inel} is the XN inelastic cross section,

$$\sigma_X^{\text{inel}} = \sigma_X - \frac{\sigma_X^2(1 + \eta^2)}{16\pi B_X}. \tag{180}$$

Using Eqs. (177)-(180) and integrating over z_i and the impact parameter b , we obtain the following compact expression for the contribution of $|\Gamma_{\gamma^* A \rightarrow XA}^{(1)}(b, r_i)|^2$ to $\sigma_{\gamma^* A \rightarrow XA}$:

$$\begin{aligned}
&\int d^2 \vec{b} \langle A | \sum_i |\Gamma_{\gamma^* X}(\vec{b} - \vec{r}_{i\perp})|^2 \prod_{j \neq i} \left| \left(1 - \Theta(z_j - z_i) \Gamma_X(\vec{b} - \vec{r}_{j\perp}) \right) \right|^2 | A \rangle \\
&= A \sigma_{\gamma^* N \rightarrow XN} \int d^2 b dz \rho_A(b, z) e^{-A\sigma_X^{\text{inel}} \int_z^{\infty} dz' \rho_A(b, z')}. \tag{181}
\end{aligned}$$

Now we turn to the evaluation of the second term in Eq. (175), $|\Gamma_{\gamma^* A \rightarrow XA}^{(2)}(b, r_i)|^2$. Assuming that the nucleons in the nuclear target are independent, it can be written in the following explicit form:

$$\begin{aligned}
&|\Gamma_{\gamma^* A \rightarrow XA}^{(2)}(b, r_i)|^2 \equiv \sum_{i \neq i'} \Gamma_{\gamma^* X}^*(\vec{b} - \vec{r}_{i'\perp}) \Gamma_{\gamma^* X}(\vec{b} - \vec{r}_{i\perp}) e^{i\Delta_{\gamma^* X}(z_i - z_{i'})} \\
&\times \prod_{j' \neq i'} \left(1 - \Theta(z_{j'} - z_{i'}) \Gamma_X^*(\vec{b} - \vec{r}_{j'\perp}) \right) \prod_{j \neq i} \left(1 - \Theta(z_j - z_i) \Gamma_X(\vec{b} - \vec{r}_{j\perp}) \right) \\
&= A(A - 1) \Gamma_{\gamma^* X}^*(\vec{b} - \vec{r}_{2\perp}) \Gamma_{\gamma^* X}(\vec{b} - \vec{r}_{1\perp}) e^{i\Delta_{\gamma^* X}(z_1 - z_2)}
\end{aligned}$$

$$\begin{aligned}
& \times (1 - \Theta(z_2 - z_1)\Gamma_X(b - \vec{r}_{2\perp}) - \Theta(z_1 - z_2)\Gamma_X^*(b - \vec{r}_{1\perp})) \\
& \times \prod_{j \neq 1,2} (1 - \Theta(z_j - z_1)\Gamma_X(b - \vec{r}_{j\perp}) - \Theta(z_j - z_2)\Gamma_X^*(b - \vec{r}_{j\perp})) . \tag{182}
\end{aligned}$$

The integration over the transverse positions of the nucleons weighted with the nuclear density can be carried out using the explicit expressions for Γ_{γ^*X} and Γ_X :

$$\begin{aligned}
& \prod_{i=1}^A \int d^2\vec{r}_{i\perp} \rho_A(\vec{r}_{i\perp}, z_i) |\Gamma_{\gamma^*A \rightarrow XA}^{(2)}(b, r_i)|^2 = A(A-1)4\pi \frac{d\sigma_{\gamma^*N \rightarrow XN}}{dt}(t_{\min}) \rho_A(b, z_1) \rho_A(b, z_2) \\
& \times e^{i\Delta_{\gamma^*X}(z_1 - z_2)} \left(1 - \Theta(z_2 - z_1) \frac{\sigma_X(1 - i\eta)}{8\pi B_X} - \Theta(z_1 - z_2) \frac{\sigma_X(1 + i\eta)}{8\pi B_X} \right) \\
& \times \prod_{j \neq 1,2} \left(\int d^2\vec{r}_{j\perp} \rho_A(\vec{r}_{j\perp}, z_j) - \Theta(z_j - z_1) \frac{\sigma_X(1 - i\eta)}{2} \rho_A(b, z_j) \right. \\
& \left. - \Theta(z_j - z_2) \frac{\sigma_X(1 + i\eta)}{2} \rho_A(b, z_j) \right) . \tag{183}
\end{aligned}$$

The expression in Eq. (183) can be significantly simplified by neglecting the contribution of the real part of the $XN \rightarrow XN$ amplitude in the second line of Eq. (183):

$$\Theta(z_2 - z_1) \frac{\sigma_X(1 - i\eta)}{8\pi B_X} + \Theta(z_1 - z_2) \frac{\sigma_X(1 + i\eta)}{8\pi B_X} \approx \frac{\sigma_X}{8\pi B_X} . \tag{184}$$

Integrating over the longitudinal coordinates of all interacting nucleons and the impact parameter b , we obtain

$$\begin{aligned}
& \int d^2\vec{b} \langle A | |\Gamma_{\gamma^*A \rightarrow XA}^{(2)}(b, r_i)|^2 | A \rangle = 4\pi A(A-1) \frac{d\sigma_{\gamma^*N \rightarrow XN}}{dt}(t_{\min}) \left(1 - \frac{\sigma_X}{8\pi B_X} \right) \\
& \times \int d^2\vec{b} \left| \int dz \rho_A(b, z) e^{i\Delta_{\gamma^*X}z} e^{-\frac{A}{2}(1-i\eta)\sigma_X} \int_z^\infty dz' \rho_A(b, z') \right|^2 . \tag{185}
\end{aligned}$$

This completes the calculation of the first term, $\langle A | |\Gamma_{\gamma^*A \rightarrow XA}(b, r_i)|^2 | A \rangle$, in Eq. (173). The second term in Eq. (173), $|\langle A | \Gamma_{\gamma^*A \rightarrow XA}(b, r_i) | A \rangle|^2$, corresponds to the purely coherent diffraction and was already calculated in Sec. 6.1.1:

$$\begin{aligned}
& \int d^2\vec{b} |\langle A | \Gamma_{\gamma^*A \rightarrow XA}(b, r_i) | A \rangle|^2 = 4\pi A^2 \frac{d\sigma_{\gamma^*N \rightarrow XN}}{dt}(t_{\min}) \\
& \times \int d^2\vec{b} \left| \int dz \rho_A(b, z) e^{i\Delta_{\gamma^*X}z} e^{-\frac{A}{2}(1-i\eta)\sigma_X} \int_z^\infty dz' \rho_A(b, z') \right|^2 . \tag{186}
\end{aligned}$$

Therefore, the $\int d^2\vec{b} \langle A | |\Gamma_{\gamma^*A \rightarrow XA}^{(2)}(b, r_i)|^2 | A \rangle$ and $\int d^2\vec{b} |\langle A | \Gamma_{\gamma^*A \rightarrow XA}(b, r_i) | A \rangle|^2$ terms partially cancel each other. Adding together Eqs. (181), (185), and (186), we obtain our final expression for the cross section of incoherent diffraction $\sigma_{\gamma^*A \rightarrow XA'}$:

$$\begin{aligned}
\sigma_{\gamma^* A \rightarrow XA'} &= A\sigma_{\gamma^* N \rightarrow XN} \int d^2b dz \rho_A(b, z) e^{-A\sigma_X^{\text{inel}} \int_z^\infty dz' \rho_A(b, z')} \\
&\quad - 4\pi A \left[A \frac{\sigma_X}{8\pi B_X} + \left(1 - \frac{\sigma_X}{8\pi B_X} \right) \right] \frac{d\sigma_{\gamma^* N \rightarrow XN}}{dt}(t_{\min}) \\
&\quad \times \int d^2\vec{b} \left| \int dz \rho_A(b, z) e^{i\Delta_{\gamma^* X} z} e^{-\frac{A}{2}(1-i\eta)\sigma_X \int_z^\infty dz' \rho_A(b, z')} \right|^2. \tag{187}
\end{aligned}$$

Expressing the diffractive cross sections in Eq. (187) in terms of the corresponding diffractive structure functions, see Eqs. (161) and (162), we obtain the expression for the *incoherent* nuclear diffractive structure function $F_{2A, \text{incoh}}^{D(3)}$:

$$\begin{aligned}
F_{2A, \text{incoh}}^{D(3)}(\beta, Q^2, x_P) &= AF_{2N}^{D(3)}(\beta, Q^2, x_P) \int d^2b dz \rho_A(b, z) e^{-A\sigma_X^{\text{inel}} \int_z^\infty dz' \rho_A(b, z')} \\
&\quad - 4\pi A \left[A \frac{\sigma_X}{8\pi B_X} + \left(1 - \frac{\sigma_X}{8\pi B_X} \right) \right] B_{\text{diff}} F_{2N}^{D(3)}(\beta, Q^2, x_P) \\
&\quad \times \int d^2\vec{b} \left| \int dz \rho_A(b, z) e^{ix_P m_N z} e^{-\frac{A}{2}(1-i\eta)\sigma_X \int_z^\infty dz' \rho_A(b, z')} \right|^2. \tag{188}
\end{aligned}$$

At this point, it is appropriate to discuss the parameters σ_X and B_X . As follows from our derivation, the rescattering cross section σ_X has the same meaning as the cross section σ_{soft}^j that we introduced and discussed in Sec. 5.1.2. Therefore, in our numerical analysis, we use $\sigma_X = \sigma_{\text{soft}}^q$, where σ_{soft}^q corresponds to the \bar{u} -quarks. For the slope parameter B_X , we used $B_X = 7 \text{ GeV}^{-2}$, which is consistent with the value of the diffractive slope $B_{\text{diff}} = 6 - 7 \text{ GeV}^2$ [62,72]; like B_{diff} , B_X is known with a significant uncertainty (of the order of 15%). As a result, we observe that $\sigma_X/(8\pi B_X)$ is not a small parameter, $\sigma_X/(8\pi B_X) \sim \mathcal{O}(1)$, and also that $\sigma_X^{\text{inel}} \sim \mathcal{O}(\sigma_X)$.

One should note that in our calculation of incoherent diffraction, we considered the absorption due to the inelastic piece of the diffractive state X -nucleon interaction. However, other inelastic transitions—such as, e.g., $Xp \rightarrow X'p$, where $X' \neq X$ —can also in principle lead to rapidity gap events. While these transitions are very small at $t = 0$ since they are mostly spin-flip, they will still decrease the effective absorption cross section σ_X and will lead to an increase of $F_{2A, \text{incoh}}^{D(3)}$. We expect that the overall effect will be numerically small; it will be smaller than the theoretical uncertainty of our predictions associated with the uncertainty of the value of B_X .

A direct application of the AGK cutting rules connects the shadowing (screening) correction to the total cross section with the corresponding contributions to the diffractive final states, which involve both the final states where the nucleus remains intact (coherent diffraction) and where it breaks up and several nucleons are produced (incoherent diffraction). Since the incoherent contribution constitutes $15 \div 25\%$ for ^{40}Ca and $3 \div 5\%$ for ^{208}Pb of the coherent contribution for a wide range of σ_X (these values refer to the studied kinematics of $Q^2 = 4 \text{ GeV}^2$ and $x_P = 10^{-3}$ and $x_P = 10^{-2}$, see Sec. 6.1.4 and

Table 5), one can correct for these effects. One can also test the importance of the incoherent contribution by studying the multiplicity of neutron production in the nuclear break-up, see e.g., Ref. [215].

It is worth noting that we calculated the incoherent cross section for the final state where the nucleus decays into a collection of nuclear fragments without hadron production. On the other hand, HERA experimental data indicate that in DIS, the ratio of the double diffraction dissociation $e + p \rightarrow e + X + Y$ to the single diffraction $e + p \rightarrow e + X + p$, r_{double} , is rather large: r_{double} is of the order ~ 0.4 . To arrive at this estimate, one uses the factorization approximation for $t = 0$, which corresponds to $r_{\text{double}}(t = 0) \sim 0.2$, and the fact that the ratio of the t -slopes of the double and single diffraction dissociation is of the order of two. Hence, one expects that r_{double} for nuclei will be of the same magnitude. It would be a challenge to separate the incoherent contribution with and without hadron production since the hadrons will be produced predominantly at the rapidities close to the nucleus rapidity.

6.1.3 Numerical predictions for coherent diffraction

One way to quantify the effect of nuclear shadowing on the nuclear diffractive parton distributions is to introduce the probability of diffraction for a given parton flavor j , P_{diff}^j [26,211]:

$$P_{\text{diff}}^j = \frac{\int_x^{0.1} dx_{\mathcal{P}} \beta f_j^{D(3)}(\beta, Q^2, x_{\mathcal{P}})}{x f_j(x, Q^2)}. \quad (189)$$

For hard process with a specific trigger, the probability of diffraction may be close to R_{diff}^q (for the measurement of the diffractive structure function $F_{2N}^{D(3)}$) or to R_{diff}^g (b -quark production). Also, the probability of diffraction can have an intermediate value between R_{diff}^q and R_{diff}^g , for instance, for the s -quark production.

Figure 69 presents P_{diff}^j of Eq. (189) as a function of Bjorken x at $Q^2 = 4 \text{ GeV}^2$, where the nuclear diffractive PDF $f_{j/A}^{D(3)}(\beta, Q^2, x_{\mathcal{P}})$ is calculated using Eq. (170). The two sets of curves correspond to models FGS10_H and FGS10_L. Also, for comparison, we present P_{diff}^j for the proton by the dot-dashed curves. The two left panels correspond to the \bar{u} -quark channel; the two right panels correspond to the gluon channel. The upper row of panels is for ^{40}Ca ; the lower row is for ^{208}Pb .

The results presented in Fig. 69 merit a discussion. First, the probability of diffraction in the gluon channel is larger (by approximately a factor of two) than that in the quark channel. This is a direct consequence of the very large gluon diffractive PDF of the nucleon. Second, the probability of diffraction for nuclei is smaller than that for the free proton for FGS10_L and compatible with the free proton for FGS10_H. This is a consequence

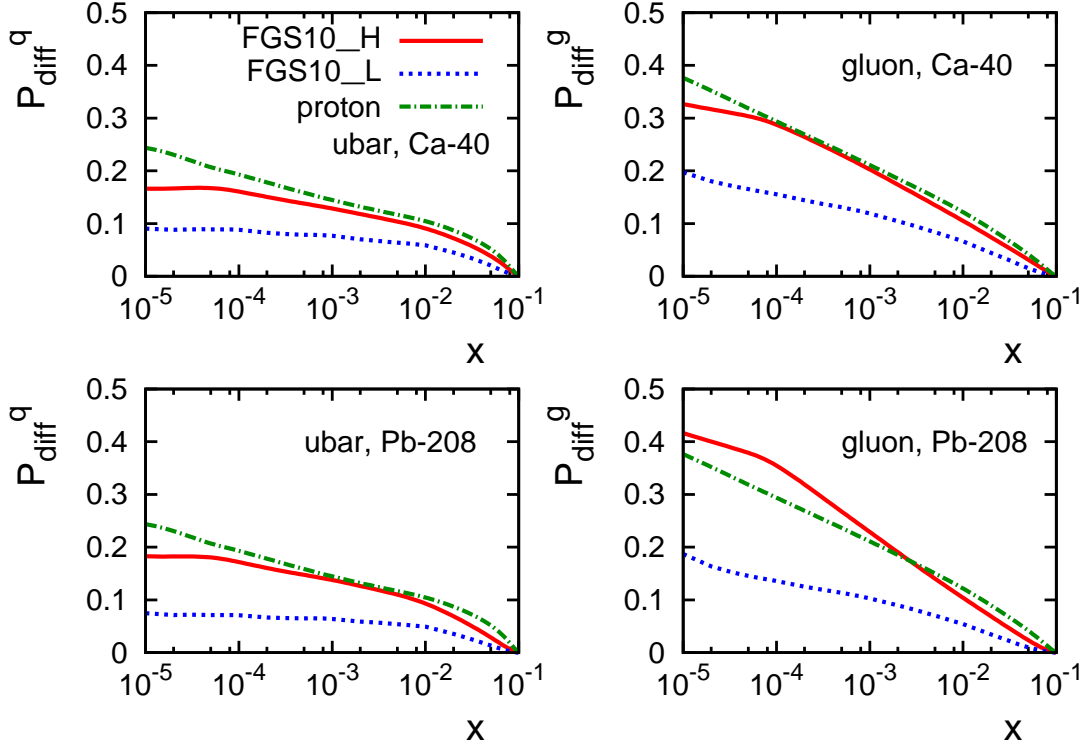


Fig. 69. The probability of diffraction, P_{diff}^j of Eq. (189), as a function of Bjorken x at $Q^2 = 4$ GeV^2 . The solid and dotted curves correspond to models FGS10_H and FGS10_L, respectively. For comparison, P_{diff}^j for the proton is given by the dot-dashed curves. The left panels correspond to the \bar{u} -quark channel; the right panels correspond to the gluon channel. The upper row of panels is for ^{40}Ca ; the lower row is for ^{208}Pb .

of the different values of the cross section $\sigma_{\text{soft}}^j(x, Q^2)$ in models FGS10_L and FGS10_H, which determines the magnitude of the multiple interactions in our treatment of coherent diffraction in DIS with nuclei in the color fluctuation approximation. Since $\sigma_{\text{soft}}^j(x, Q^2)$ is smaller in model FGS10_H than in model FGS10_L, the survival probability of the diffractive state X [the numerator of P_{diff}^j in Eq. (189)] is larger in the FGS10_H case. In addition, the smaller $\sigma_{\text{soft}}^j(x, Q^2)$ in model FGS10_H leads to the smaller nuclear PDFs (larger nuclear shadowing), which further increases P_{diff}^j in model FGS10_H compared to the FGS10_L case. As a result, P_{diff}^j is significantly larger in model FGS10_H than in model FGS10_L.

Figure 70 presents our predictions for the probability of diffraction P_{diff}^j as a function of x for different values of Q^2 : $Q^2 = 4, 10, \text{ and } 100$ GeV^2 . One can see from the figure that the Q^2 dependence of P_{diff}^j is faster in the gluon channel than in the quark one. This trend can be understood by recalling that usual nuclear PDFs enter the denominator of Eq. (189) and noticing that the Q^2 evolution increases usual nuclear PDFs faster in the gluon channel than in the quark one.

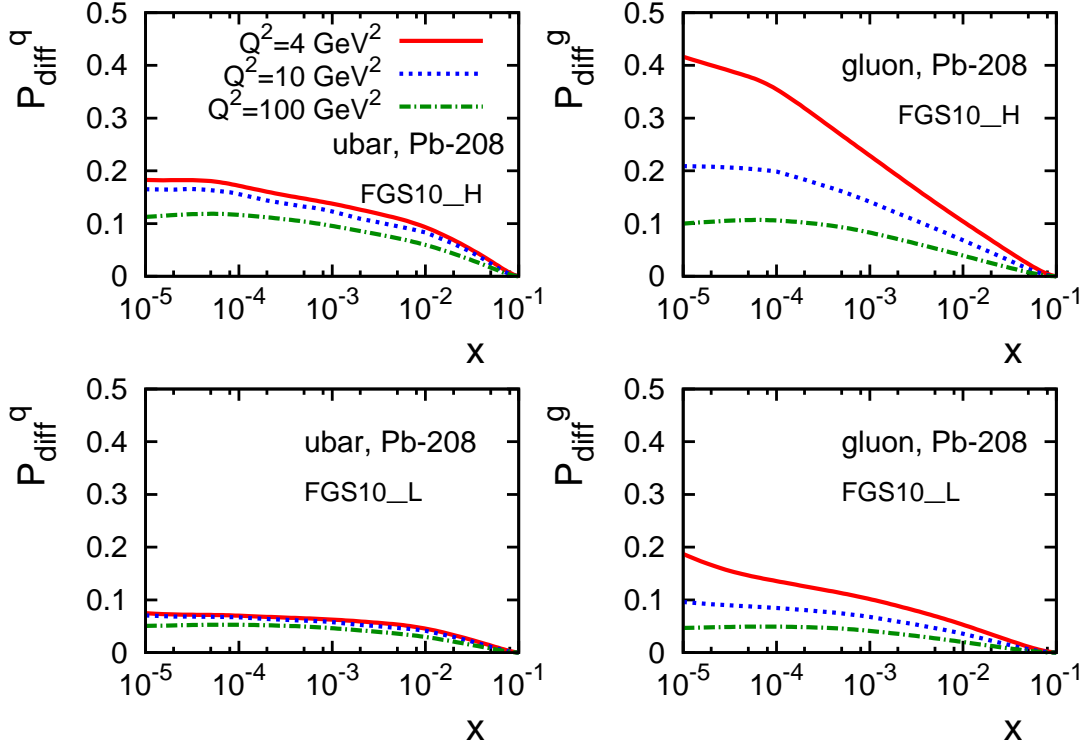


Fig. 70. The probability of diffraction, P_{diff}^j of Eq. (189), as a function of Bjorken x for different values of Q^2 . All curves correspond to ^{208}Pb .

While the color fluctuation approximation is our main approach to the treatment of the multiple interactions, one can also evaluate P_{diff}^j in the quasi-eikonal approximation. The latter is done by replacing $\sigma_{\text{soft}}^j(x, Q^2)$ in Eq. (170) by $\sigma_2^j(x, Q^2)$, see Eq. (52) and also Fig. 29. Since $\sigma_2^j(x, Q^2) < \sigma_{\text{soft}}^j(x, Q^2)$, the absorption of the diffractive state X is not as large as in the color fluctuation approximation and, as a result, the probability of diffraction should be significantly larger.

The trend of the A dependence of the probability of diffraction P_{diff}^j is rather non-trivial since it comes from different A dependences of the numerator and denominator in Eq. (189). To disentangle the two and also to better understand the role of nuclear shadowing in nuclear diffractive PDFs, it is useful to study the A dependence of the numerator of Eq. (189). An example of this is presented in Fig. 71, where we plot $\int_x^{0.1} dx_{\mathbb{P}} \beta f_j^{D(3)}(\beta, Q^2, x_{\mathbb{P}})/A$ as a function of A at $Q^2 = Q_0^2 = 4 \text{ GeV}^2$. In the figure, the points (squares for $x = 10^{-4}$ and open circles for $x = 10^{-3}$) are the results of our explicit calculations for ^{12}C , ^{40}Ca , ^{110}Pd , and ^{208}Pb ; the smooth curves is a two-parameter fit to the $A \geq 40$ points in the following form:

$$\frac{1}{A} \int_x^{0.1} dx_{\mathbb{P}} \beta f_j^{D(3)}(\beta, Q^2, x_{\mathbb{P}}) = a_1 A^{1/3(1-a_2)}, \quad (190)$$

where a_1 and a_2 are the free parameters of the fit. The resulting values of a_1 and a_2 are summarized in Table 4.

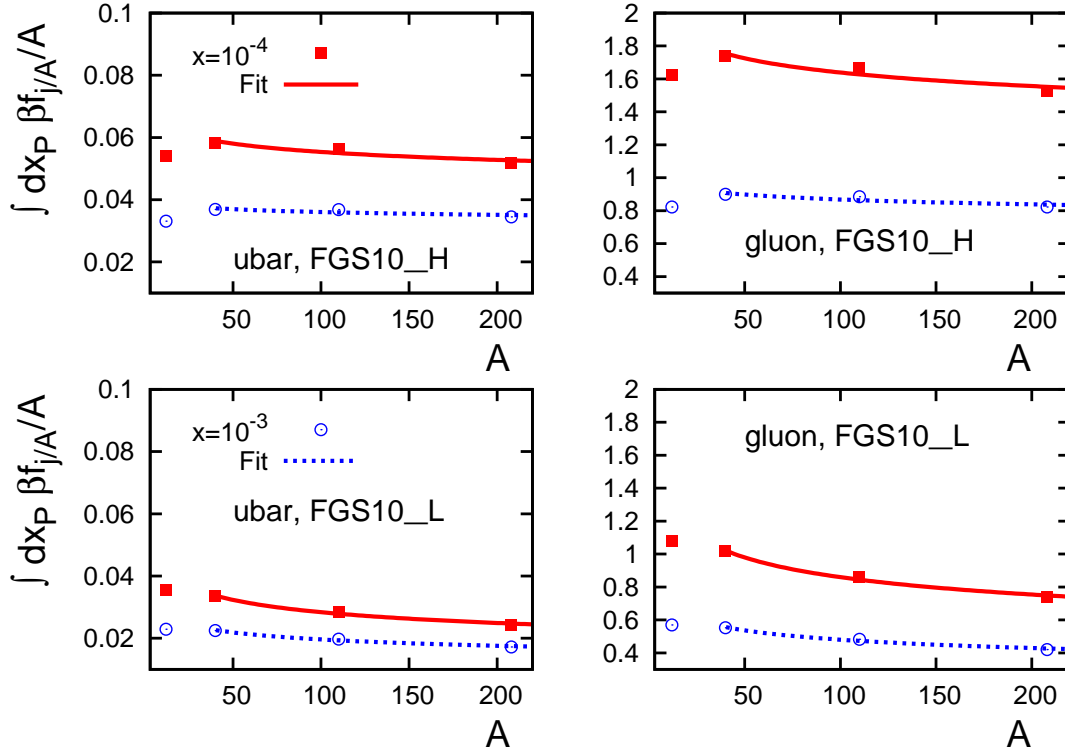


Fig. 71. The A dependence of nuclear diffractive PDFs. The points (squares and open circles) are the results of our calculations of $\int_x^{0.1} dx_P \beta f_j^{D(3)}(\beta, Q^2, x_P)/A$ for ^{12}C , ^{40}Ca , ^{110}Pd , and ^{208}Pb ; the smooth curves is a two-parameter fit of Eq. (190).

	$a_{1,\text{ubar}}$	$a_{2,\text{ubar}}$	$a_{1,\text{gluon}}$	$a_{2,\text{gluon}}$
10^{-4}				
FGS10_H	0.0758	1.205	2.307	1.223
FGS10_L	0.0675	1.565	2.048	1.566
10^{-3}				
FGS10_H	0.0426	1.109	1.090	1.149
FGS10_L	0.0404	1.471	1.008	1.484

Table 4

The parameters a_1 and a_2 of the fit of Eq. (190).

The parameterization in Eq. (190) interpolates between the two limiting regimes: $\int_x^{0.1} dx_P \beta f_j^{D(3)}/A \propto A^{1/3}$ corresponding to the (unshadowed) impulse approximation and $\int_x^{0.1} dx_P \beta f_j^{D(3)}/A \propto A^{-1/3}$ corresponding to full-fledged nuclear shadowing. As one can see from Table 4 and also from Fig. 71, $\int_x^{0.1} dx_P \beta f_j^{D(3)}(\beta, Q^2, x_P)/A$ decreases as A is increased. This is consistent with the expectation of the onset of the full-fledged nuclear

shadowing that reduces the A dependence of the t -integrated diffractive parton distributions (structure functions, cross sections) from $A^{4/3}$ (impulse approximation) to $A^{2/3}$.

Note that apparently ^{12}C is too light for this trend to present; we did not include the $A = 12$ point in the fit of Eq. (190).

Having addressed the A dependence of the nuclear diffractive PDFs, we can now better understand the A dependence and the absolute value of the probability of diffraction P_{diff}^j . Since both $\int_x^{0.1} dx_{\mathcal{P}} \beta f_j^{D(3)}(\beta, Q^2, x_{\mathcal{P}})/A$ and $f_{j/A}(x, Q^2)/A$ are rather flat functions of A , see Eqs. (128) and (190), P_{diff}^j very weakly depends on A for $A \geq 40$ (see Fig. 69). As to the absolute value of P_{diff}^j , nuclei do not seem to enhance the probability of diffraction compared to the free proton case. This is a result of the strong leading twist nuclear shadowing that significantly suppresses nuclear diffractive PDFs and slows down the onset of the black disk limit, where P_{diff}^j is supposed to approach $1/2$.

Next we present our predictions for the nuclear diffractive PDFs $f_{j/A}^{D(3)}$. To this end, it is convenient to present our results in terms of the ratio of the nuclear to free proton diffractive PDFs $f_{j/A}^{D(3)}/(Af_{j/N}^{D(3)})$. Figures 72 and 73 show the $f_{j/A}^{D(3)}/(Af_{j/N}^{D(3)})$ ratio for ^{40}Ca and ^{208}Pb at $Q^2 = 4 \text{ GeV}^2$ as a function of the light-cone fraction β at fixed $x_{\mathcal{P}} = 2 \times 10^{-4}$ (four upper panels of Fig. 72), $x_{\mathcal{P}} = 10^{-3}$ (four lower panels of Fig. 72), $x_{\mathcal{P}} = 10^{-2}$ (four upper panels of Fig. 73), and $x_{\mathcal{P}} = 0.05$ (four lower panels of Fig. 73). The solid and dotted curves correspond to models FGS10_H and FGS10_L, respectively (see the text). The left columns of the panels correspond to the \bar{u} -quark; the right columns of the panels correspond to the gluons.

Several features of Figs. 72 and 73 deserve a discussion.

- (i) At small fixed $x_{\mathcal{P}}$, the dependence of $f_{j/A}^{D(3)}/(Af_{j/N}^{D(3)})$ on β is rather weak since it enters only through the rescattering cross section $\sigma_{\text{soft}}^j(x = x_{\mathcal{P}}\beta, Q_0^2)$, see Eq. (170).
- (ii) By the same token, the dependence of $f_{j/A}^{D(3)}/(Af_{j/N}^{D(3)})$ on $x_{\mathcal{P}}$ at fixed β is also very weak (compare the upper panels with the respective lower panels). See also Fig. 74.
- (iii) Since $\sigma_{\text{soft}}^{j(\text{H})}$ is smaller than $\sigma_{\text{soft}}^{j(\text{L})}$, the nuclear diffractive PDFs are larger in model FGS10_H (the solid curves lie above the dotted ones). Note also that $f_{j/A}^{D(3)}/(Af_{j/N}^{D(3)})$ is flavor-independent in model FGS10_L (dotted curves) since the corresponding $\sigma_{\text{soft}}^{j(\text{L})}$ is taken to be the same for all parton flavors.
- (iv) The nuclear dependence of $f_{j/A}^{D(3)}/(Af_{j/N}^{D(3)})$ is rather weak, too. See also Fig. 71 and our discussion above.
- (v) Our analysis shows that the Q^2 dependence of $f_{j/A}^{D(3)}/(Af_{j/N}^{D(3)})$, which results from the separate DGLAP evolution of $f_{j/A}^{D(3)}$ and $f_{j/N}^{D(3)}$, is also very insignificant. See Fig. 75.

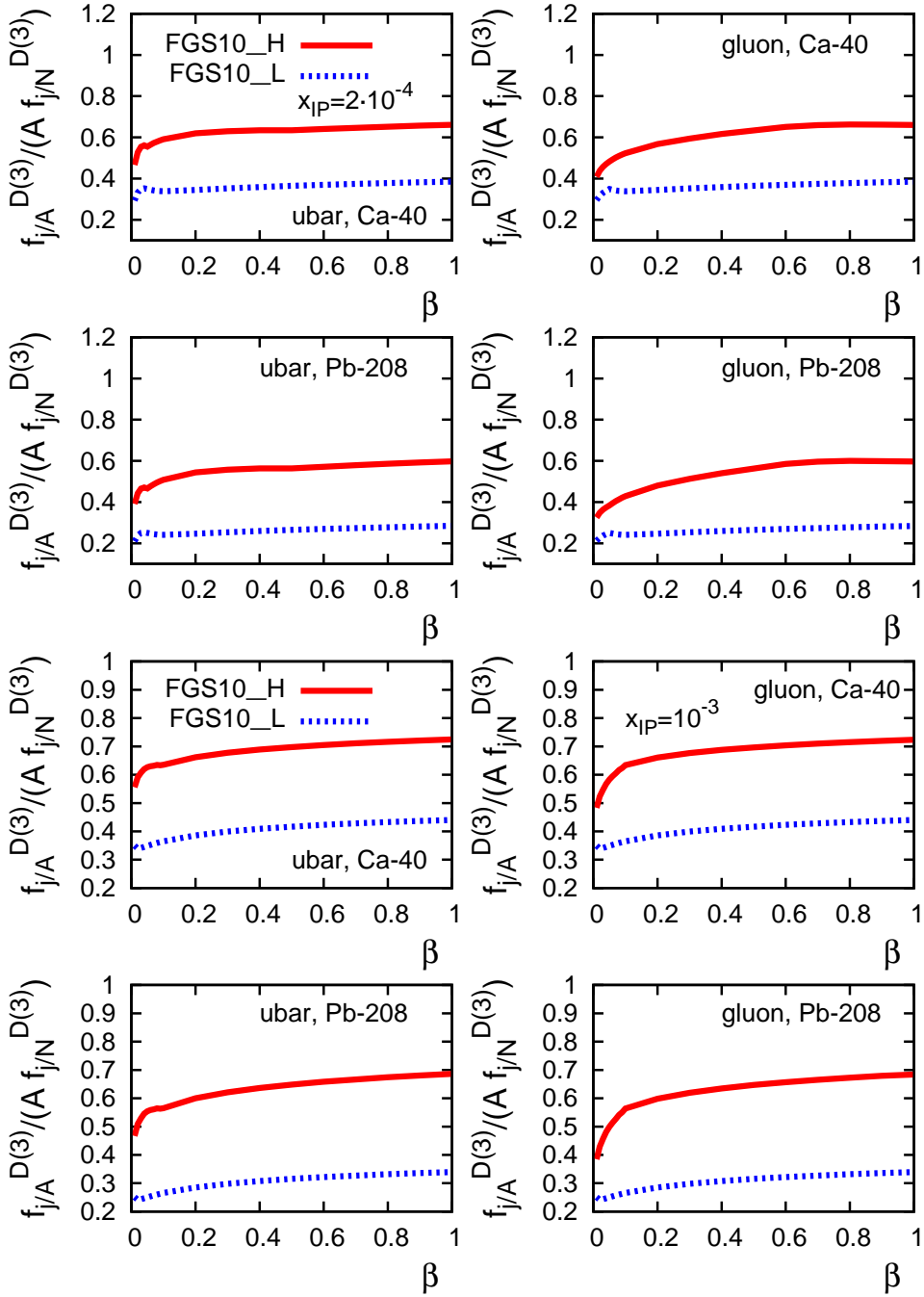


Fig. 72. The $f_{j/A}^{D(3)}(\beta, Q^2, x_P) / [A f_{j/N}^{D(3)}(\beta, Q^2, x_P)]$ ratio as a function of β at $x_P = 2 \times 10^{-4}$ (four upper panels) and $x_P = 10^{-3}$ (four lower panels) at $Q^2 = 4 \text{ GeV}^2$ and for ^{40}Ca and ^{208}Pb . The left column of panels corresponds to the \bar{u} -quark density; the right column corresponds to the gluon density. The solid and dashed curves correspond to models FGS10_H and FGS10_L, respectively.

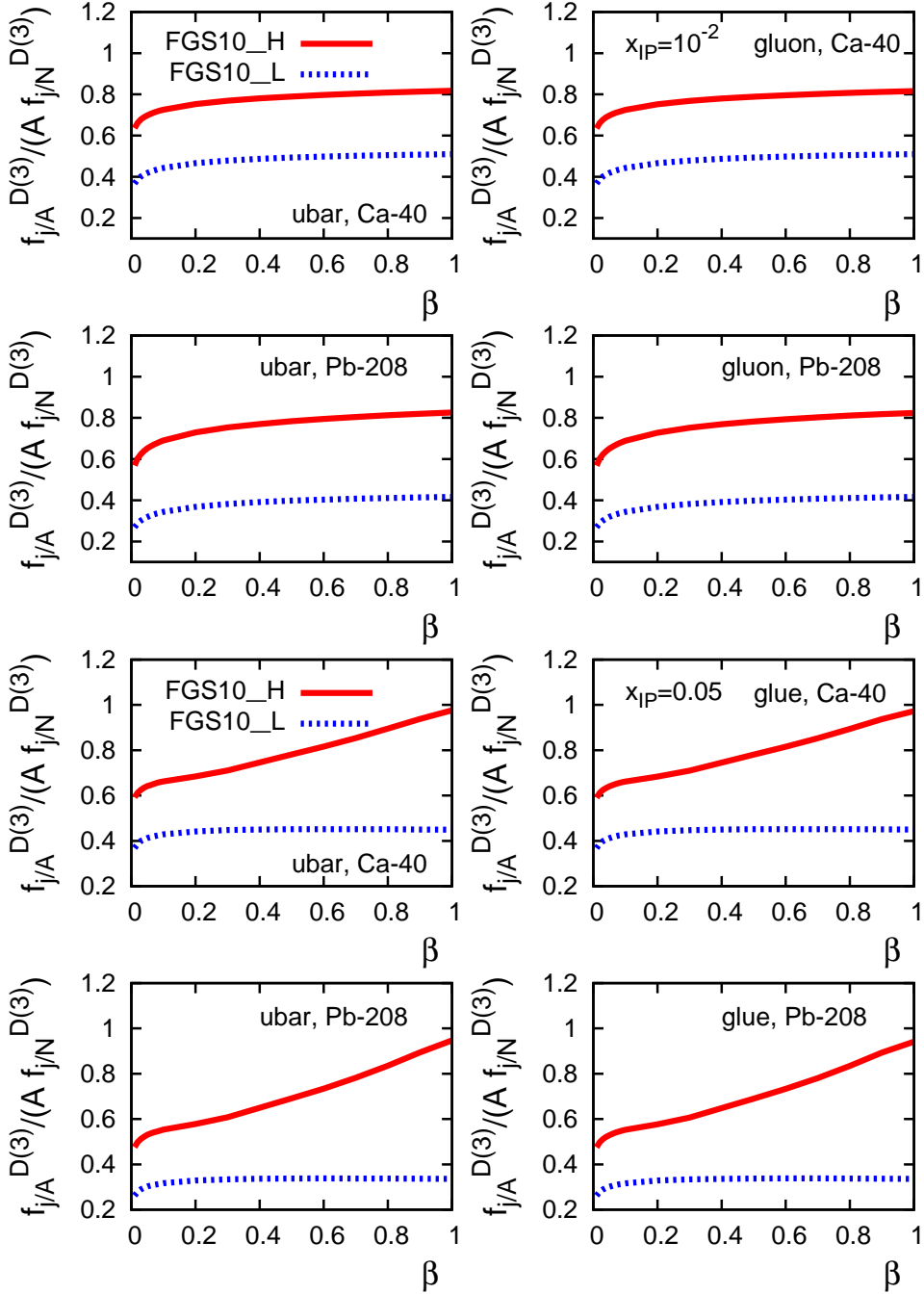


Fig. 73. The $f_{j/A}^{D(3)}(\beta, Q^2, x_P) / [A f_{j/N}^{D(3)}(\beta, Q^2, x_P)]$ ratio as a function of β at $x_P = 10^{-2}$ (four upper panels) and $x_P = 0.05$ (four lower panels) at $Q^2 = 4 \text{ GeV}^2$ and for ^{40}Ca and ^{208}Pb . For the rest of the legend, see Fig. 72.

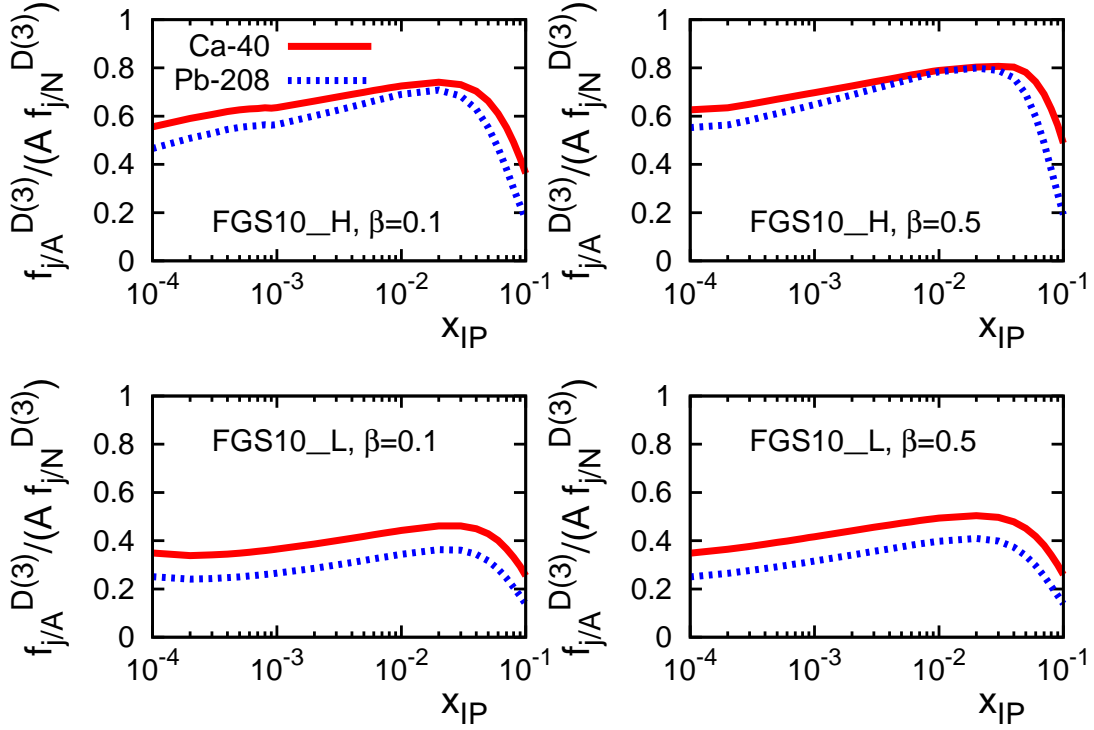


Fig. 74. The $f_{j/A}^{D(3)}(\beta, Q^2, x_P)/[A f_{j/N}^{D(3)}(\beta, Q^2, x_P)]$ ratio as a function of x_P at fixed $\beta = 0.1$ and $\beta = 0.5$ and at $Q^2 = 4 \text{ GeV}^2$. All curves correspond to the \bar{u} -quark parton distribution.

As an illustration of the x_P dependence, in Fig. 74, we present $f_{j/A}^{D(3)}/(A f_{j/N}^{D(3)})$ as a function of x_P at fixed $\beta = 0.1$ and $\beta = 0.5$ and $Q^2 = 4 \text{ GeV}^2$. All curves correspond to the \bar{u} -quark parton distribution. [The flavor dependence of $f_{j/A}^{D(3)}/(A f_{j/N}^{D(3)})$ is weak.] At small x_P , $x_P \leq 0.05$, $f_{j/A}^{D(3)}/(A f_{j/N}^{D(3)})$ very weakly depends on x_P ; the values of $f_{j/A}^{D(3)}/(A f_{j/N}^{D(3)})$ are naturally the same as in Figs. 72 and 73. As one increases x_P , $f_{j/A}^{D(3)}/(A f_{j/N}^{D(3)})$ initially increases because $\sigma_{\text{soft}}^j(x, Q^2)$ decreases, which leads to a smaller suppression of the diffractively produced state X by the multiple interactions with the target nucleons. However, as x_P becomes larger than approximately 0.02, the coherence of the nucleus is destroyed by the $e^{ix_P m_N z}$ exponent in Eq. (170) and nuclear coherent diffraction rapidly vanishes.

Next we present our predictions for the Q^2 dependence of $f_{j/A}^{D(3)}/(A f_{j/N}^{D(3)})$. Figure 75 shows $f_{j/A}^{D(3)}/(A f_{j/N}^{D(3)})$ as a function of β at small fixed value of $x_P = 10^{-3}$ for ^{208}Pb for three different values of Q^2 : $Q^2 = 4, 10$ and 100 GeV^2 . As one can see from the figure, the Q^2 dependence almost completely cancels in the ratio of the nuclear and nucleon diffractive PDFs.

A few words of explanation about our procedure is in order here. At fixed x_P , we calculated $f_{j/A}^{D(3)}(\beta, Q^2, x_P)$ as a function of β at fixed $Q_0^2 = 4 \text{ GeV}^2$ using Eq. (170). The result was used as an input for the DGLAP evolution equations (117) to higher Q^2 scales, $Q^2 = 10$

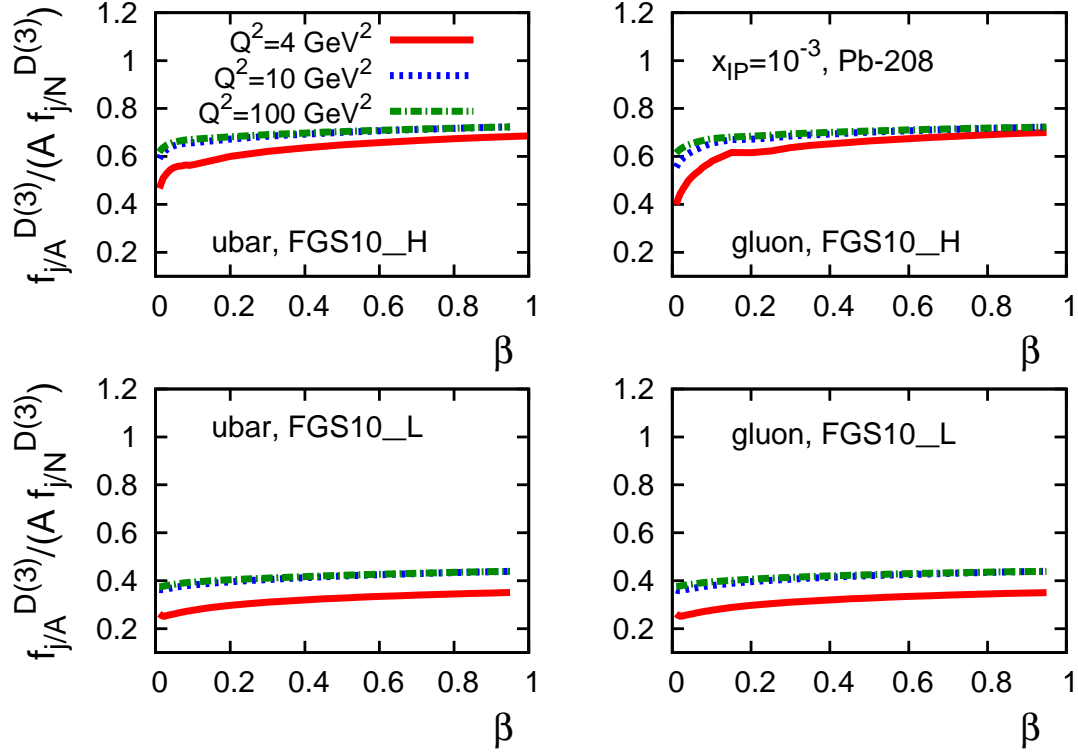


Fig. 75. The Q^2 dependence of the $f_{j/A}^{D(3)}(\beta, Q^2, x_P)/[A f_{j/N}^{D(3)}(\beta, Q^2, x_P)]$ ratio as a function of β at fixed $x_P = 10^{-3}$ for ^{208}Pb .

and 100 GeV^2 . The Q^2 evolution of the free proton diffractive PDFs, $f_j^{D(3)}(\beta, Q^2, x_P)$, was performed separately. Having the nuclear and nucleon diffractive PDFs at desired values of Q^2 , we formed the $f_{j/A}^{D(3)}/(A f_{j/N}^{D(3)})$ ratio presented in Fig. 75.

Our predictions for $f_{j/A}^{D(3)}/(A f_{j/N}^{D(3)})$ in Figs. 72, 73, and 74 are very weakly flavor-dependent. Nevertheless, $f_{j/A}^{D(3)}/(A f_{j/N}^{D(3)})$ is not exactly equal to the ratio of the nuclear to nucleon diffractive structure functions, $F_{2A}^{D(3)}/(A F_{2N}^{D(3)})$. Therefore, we separately show our predictions for the NLO nuclear and nucleon diffractive structure functions and present an example of the resulting $F_{2A}^{D(3)}/(A F_{2N}^{D(3)})$ ratio in Fig. 76. As one can see in the figure, the predicted $F_{2A}^{D(3)}/(A F_{2N}^{D(3)})$ are very similar to $f_{j/A}^{D(3)}/(A f_{j/N}^{D(3)})$ from Figs. 72 and 74.

Our predictions for $F_{2A}^{D(3)}/(A F_{2N}^{D(3)})$ can be directly compared to the predictions for $F_{2A}^{D(3)}/(A F_{2N}^{D(3)})$ made in the framework of the color dipole model [27]. We begin with the β dependence and compare the two upper panels of Fig. 76 to Fig. 7 of Ref. [27]. We observe that the predicted shape of $F_{2A}^{D(3)}/(A F_{2N}^{D(3)})$ as a function of β is similar in the two approaches, especially for ^{40}Ca . Moreover, for model FGS10_H and ^{40}Ca , our predictions are also close in the absolute value to those of Ref. [27]. At the same time, for ^{208}Pb , our prediction for $F_{2A}^{D(3)}/(A F_{2N}^{D(3)})$ is that it mildly increases with increasing β and takes on the values in the interval $0.6 \leq F_{2A}^{D(3)}/(A F_{2N}^{D(3)}) \leq 0.7$ (FGS10_H) and $0.25 \leq F_{2A}^{D(3)}/(A F_{2N}^{D(3)}) \leq 0.35$

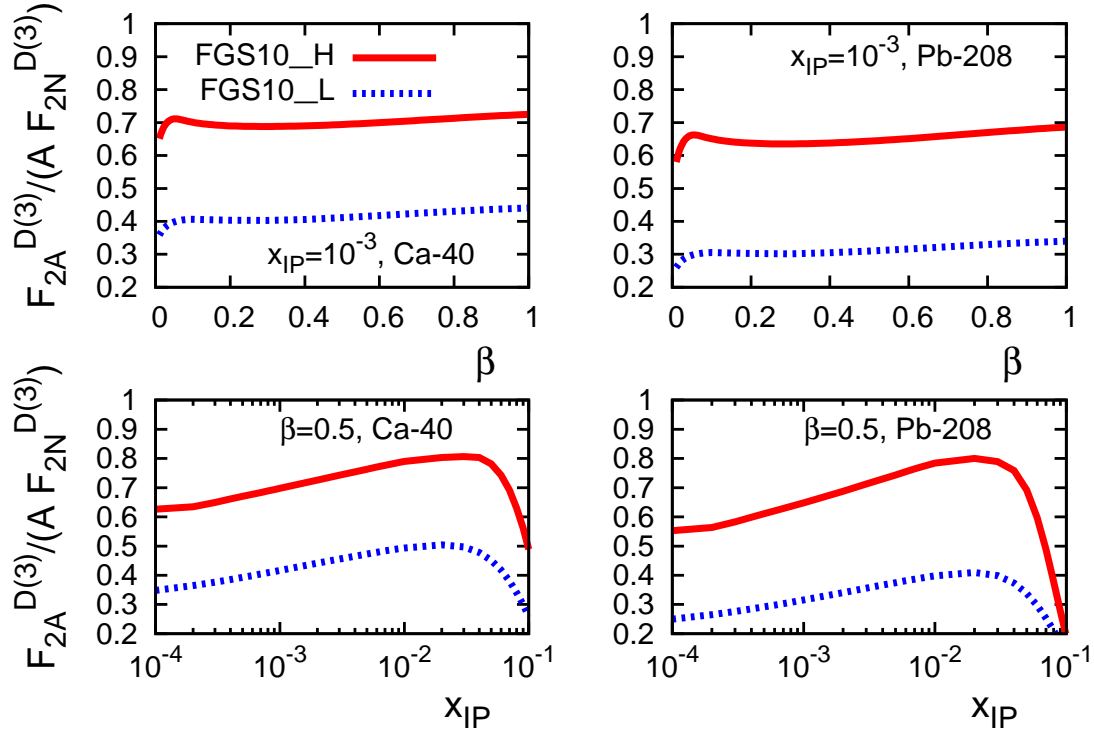


Fig. 76. Predictions for the ratio of the nuclear to nucleon diffractive structure functions, $F_{2A}^{D(3)}/(AF_{2N}^{D(3)})$, at $Q_0^2 = 4 \text{ GeV}^2$.

(FGS10_L), while the prediction of [27] is that $F_{2A}^{D(3)}/(AF_{2N}^{D(3)})$ rather rapidly changes from 0.6 to 1.2 between $\beta = 0$ and $\beta = 0.3$ and further grows and becomes approximately 1.4 as β approaches unity.

Turning to the x_P dependence of $F_{2A}^{D(3)}/(AF_{2N}^{D(3)})$, the two lower panels of Fig. 76 are to be compared to Fig. 11 of Ref. [27]. For $x_P \leq 0.01$, the two approaches predict the similar shape of $F_{2A}^{D(3)}/(AF_{2N}^{D(3)})$ as a function of x_P . For ^{40}Ca and model FGS_L, the predictions of the two approaches are also close in the absolute values. At the same time, the trend of the A dependence is opposite: our leading twist approach predicts that $F_{2A}^{D(3)}/(AF_{2N}^{D(3)})$ for ^{40}Ca is slightly larger than that for ^{208}Pb , while $F_{2A}^{D(3)}/(AF_{2N}^{D(3)})$ for ^{208}Pb is noticeably larger than that for ^{40}Ca in Ref. [27]. Also, we predict smaller values of $F_{2A}^{D(3)}/(AF_{2N}^{D(3)})$ for ^{208}Pb compared to the curves in Fig. 11 of Ref. [27]. While the $x_P > 0.01$ region is not shown in Ref. [27], we predict a dramatic decrease of $F_{2A}^{D(3)}/(AF_{2N}^{D(3)})$ for $x_P > 0.01$ as a consequence of the decrease of the coherence length in this region (see the discussion above).

One should also mention that one expects the different Q^2 dependences of $F_{2A}^{D(3)}/(AF_{2N}^{D(3)})$ in the leading twist approach and color dipole model: while the Q^2 dependences of $F_{2A}^{D(3)}/(AF_{2N}^{D(3)})$ is very slow (logarithmic) in the leading twist theory (see, e.g., Fig. 75), it is faster in the color dipole model due to the eventual dominance of small-size configu-

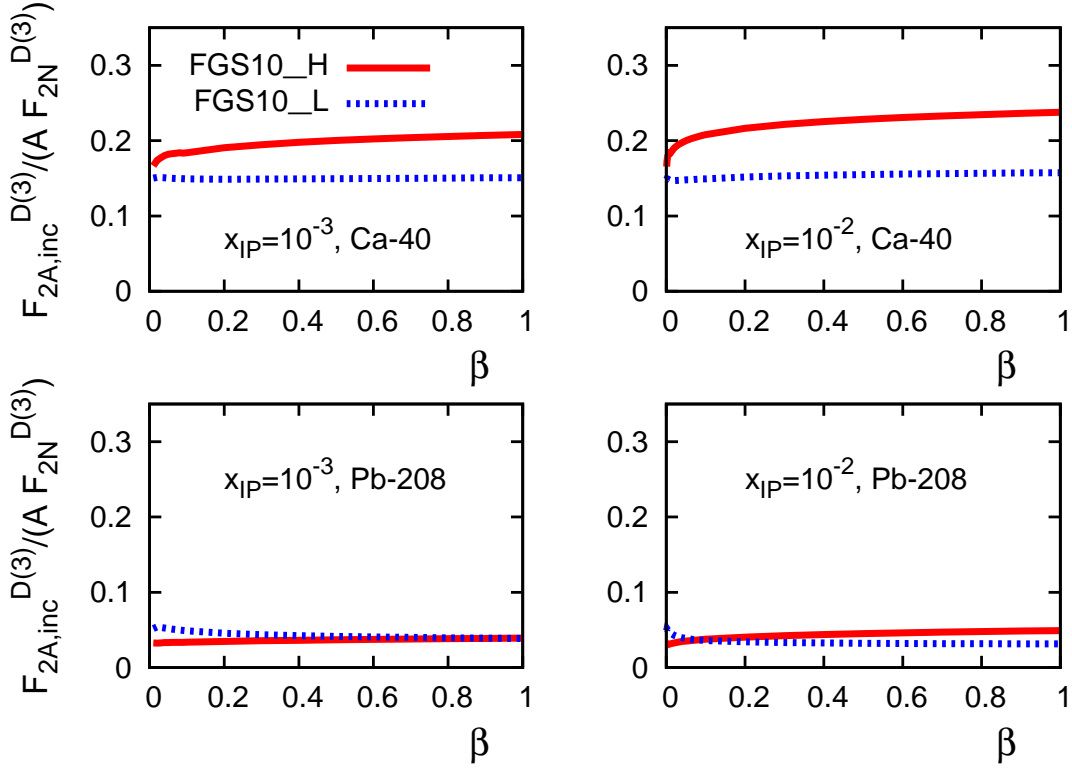


Fig. 77. The ratio of the incoherent nuclear and free nucleon diffractive structure functions, $F_{2A,inc}^{D(3)}/(A F_{2N}^{D(3)})$, as a function of β at fixed $x_{IP} = 10^{-3}$ and 10^{-2} and $Q^2 = 4 \text{ GeV}^2$.

rations in the virtual photon wave function at large Q^2 .

Also, unlike the leading twist theory of nuclear shadowing that allows one to predict nuclear diffractive PDFs of separate flavors, the dipole model does not have a consistent way to predict, e.g., the gluon nuclear diffractive PDF. (The same is also true for the usual nuclear PDFs, see the discussion in Sec. 5.)

6.1.4 Numerical predictions for incoherent diffraction

In this subsection, we present our numerical predictions for hard incoherent diffraction in eA DIS. The corresponding incoherent structure function, $F_{2A,inc}^{D(3)}$, is given by Eq. (188). The essential input for this equation is the rescattering cross section σ_X and the corresponding slope B_X . As we discussed above, we take $\sigma_X = \sigma_{soft}^{q(H)}(x, Q_0^2)$ [$\sigma_{soft}^{q(H)}(x, Q_0^2)$ corresponds to the \bar{u} quark and model FGS10_H, see Eq. (106) and Fig. 29] and $B_X = 7 \text{ GeV}^{-2}$.

As an illustration of the resulting incoherent diffractive structure function, in Fig. 77 we show the $F_{2A,inc}^{D(3)}/(A F_{2N}^{D(3)})$ ratio as a function of β at fixed $x_{IP} = 10^{-3}$ and 10^{-2} and $Q^2 = 4 \text{ GeV}^2$. The two upper panels correspond to ^{40}Ca ; the two lower panels are for ^{208}Pb .

Our predictions for $F_{2A,\text{incoh}}^{D(3)}/(AF_{2N}^{D(3)})$ can be compared to the coherent case presented in Fig. 76 (two upper panels). While the shapes of the β dependence of $F_{2A,\text{incoh}}^{D(3)}/(AF_{2N}^{D(3)})$ and $F_{2A}^{D(3)}/(AF_{2N}^{D(3)})$ are very similar, the incoherent diffractive structure functions are smaller than the coherent ones: incoherent diffraction constitutes approximately 15-25% for ^{40}Ca and 3-5% for ^{208}Pb of the coherent diffraction (depending on the choice of model FGS10_H or FGS10_L). The $F_{2A,\text{incoh}}^{D(3)}/F_{2A}^{D(3)}$ ratio at $\beta = 0.5$, $Q_0^2 = 4 \text{ GeV}^2$, and $x_P = 10^{-3}$ and 10^{-2} (the β -dependence is weak) is summarized in Table 5.

A/model	$F_{2A,\text{incoh}}^{D(3)}/F_{2A}^{D(3)}, x_P = 10^{-3}$	$F_{2A,\text{incoh}}^{D(3)}/F_{2A}^{D(3)}, x_P = 10^{-2}$
^{40}Ca , FGS10_H	0.20	0.23
^{40}Ca , FGS10_L	0.15	0.16
^{208}Pb , FGS10_H	0.037	0.045
^{208}Pb , FGS10_L	0.041	0.032

Table 5

The $F_{2A,\text{incoh}}^{D(3)}/F_{2A}^{D(3)}$ ratio at $\beta = 0.5$, $Q_0^2 = 4 \text{ GeV}^2$, and $x_P = 10^{-3}$ and 10^{-2} . The ratio is weakly β -dependent.

When comparing our results for incoherent diffraction to those of Ref. [27], one has to keep in mind that the break-up channel in Ref. [27] corresponds to the sum of the coherent and incoherent channels in this work (one needs to add the corresponding curves in Figs. 77 and 76). The conclusion that can be drawn is similar to the one we already presented and discussed above: our leading twist approach and the color dipole formalism of Ref. [27] predict a very similar shape of the β dependence of the $(F_{2A}^{D(3)} + F_{2A,\text{incoh}}^{D(3)})/(AF_{2N}^{D(3)})$ ratio. Moreover, for ^{40}Ca and model FGS10_H, the predictions of the both approaches are also close in the absolute values. For model FGS10_L and ^{40}Ca and for the both models (FGS10_H and FGS10_L) and ^{208}Pb , our predictions for $(F_{2A}^{D(3)} + F_{2A,\text{incoh}}^{D(3)})/(AF_{2N}^{D(3)})$ are smaller than the corresponding $F_{2A}^{D(3)}/(AF_{2N}^{D(3)})$ in the break-up channel in Ref. [27].

6.2 Exclusive diffraction at small x

In this subsection, we consider hard coherent exclusive production of real photons (deeply virtual Compton scattering, DVCS) and vector mesons (J/ψ , ρ , ...) off nuclei:

$$\gamma^* + A \rightarrow \gamma(J/\psi, \rho, \dots) + A. \quad (191)$$

The QCD factorization theorems proved for the exclusive meson production by longitudinally polarized virtual photons [216,217] and for the photon production initiated by transversely polarized virtual photon (DVCS) [218] allow one to express the amplitudes

of the processes in Eq. (191) as the convolution of the hard interaction block, the meson $q\bar{q}$ wave function (in the case of meson production), and the generalized parton distributions (GPDs) of the target. The proofs of the QCD factorization for these processes were based on the dominance in the considered processes of the contribution of the point-like component of the wave function of highly virtual longitudinally polarized photon. Derived formulas have demonstrated that the GPDs enter the description of a wide range of hard exclusive processes in an universal way.

In the case of the hard exclusive processes initiated by transversely polarized photons, the QCD factorization theorem is also applicable, although for larger Q^2 than in the case of longitudinally polarized photons. This is because the contribution of non-perturbative QCD (the aligned jet model) is suppressed by the Sudakov form factor only. This form factor is not compensated by processes with gluon radiation since the amplitudes for such processes are suppressed by the overlapping integral with the wave function of the vector meson which is mostly non-perturbative. The HERA data indicate that the ratio of the transverse and longitudinal cross sections of ρ meson production does not change with W or with t indicating that the squeezing of the $q\bar{q}$ dipole is similar in the two cases. This suggests that the Sudakov radiation in these processes starts as early as at $k_t \sim \Lambda_{QCD}$.

Evolution equations for bilocal operators, whose matrix elements are now referred to as GPDs, were first studied in [219]. GPDs were used in [220] to parameterize the matrix elements of bilocal operators between hadronic states with non-equal momenta (non-forward matrix elements), which appear in the QCD description of hard exclusive processes (DVCS, productions of mesons by longitudinally polarized photons, etc.) Over the last ten years, the subject of GPDs has been one of the most active fields in hadronic physics, see [221–224] for the reviews.

GPDs generalize usual PDFs and, in general, depend on two-light cone fractions x_1 and x_2 of the partons emitted/absorbed by the target, the invariant momentum transfer $t = (P' - P)^2$ with P' and P the final and initial momenta of the target, respectively, and the resolution scale Q^2 , see Fig. 78. The direct calculation of the amplitudes of the hard

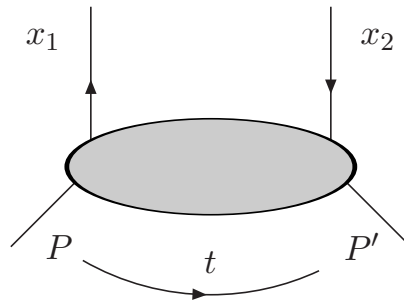


Fig. 78. The kinematic dependence of generalized parton distributions.

exclusive processes in question shows that

$$x_1 = \frac{Q^2 + M^2}{\nu}, \quad x_2 = \frac{M^2 - M_V^2}{\nu}, \quad (192)$$

where M^2 is the invariant mass squared in the quark loop in the transition $\gamma^* \rightarrow V$ (we consider here the case of small x where the amplitude is predominantly imaginary); $\nu = W^2 + Q^2 - m_T^2$.

In the following we will use the variables $x_{\pm} = (x_1 \pm x_2)/2$. In the Bjorken limit of fixed $x_B = Q^2/\nu$ and $Q^2 \rightarrow \infty$, the light-cone fraction x_- is fixed by the external kinematics:

$$x_- = \frac{Q^2 + M_V^2}{\nu} \rightarrow x_B/2. \quad (193)$$

Moreover, for the leading contribution to the imaginary part, the light-cone fraction x_+ is also constrained:

$$x_+ \rightarrow x_B/2. \quad (194)$$

In the literature, the symmetric variables of Ji [221] are often used. They are related to x_{\pm} as

$$x = \frac{x_+}{1 - x_-}, \quad \xi = \frac{x_-}{1 - x_-} = \frac{x_B}{2 - x_B}. \quad (195)$$

In this review, we will refer to the Bjorken variable x_B simply as x where it does not cause confusion.

Note that in the limit $x \rightarrow 0$ and $Q^2 = \text{const} \gg \Lambda_{QCD}^2$, the relation between x_+ and x is qualitatively different from Eq. (194). Indeed, an increase of the transverse momenta of the partons in the overlapping integral for the process $\gamma^* + T \rightarrow \gamma + T$ with an increase of energy [225] leads to $M^2 \gg Q^2$ and, hence, results in the following relations:

$$x_1 \rightarrow x_2, \quad x_+ \rightarrow \frac{M^2}{\nu}, \quad x \ll x_+. \quad (196)$$

6.2.1 Nuclear GPDs at small x and impact parameter dependent nuclear PDFs

The number of GPDs depend on the spin of the target: for the spinless target, one has one twist-two chirally-even GPD H^j (we follow here the notations of [223]).

In Ref. [182], the leading twist theory of nuclear shadowing was generalized to the non-forward kinematics and the expression for the nuclear GPD H at small x was derived. In the $x_- = 0$ limit, the nuclear diagonal GPD reads:

$$\begin{aligned}
H_A^j(x, x_- = 0, t, Q_0^2) &= AF_A(t)H_N^j(x, x_- = 0, t, Q_0^2) \\
&- \frac{A(A-1)}{2} 16\pi B_{\text{diff}} \Re e \left\{ \frac{(1-i\eta)^2}{1+\eta^2} \int d^2\vec{b} e^{i\vec{\Delta}_\perp \cdot \vec{b}} \int_{-\infty}^{\infty} dz_1 \int_{z_1}^{\infty} dz_2 \int_x^{0.1} dx_{\mathcal{P}} \right. \\
&\times \rho_A(b, z_1) \rho_A(b, z_2) e^{im_N x_{\mathcal{P}}(z_1 - z_2)} e^{-\frac{A}{2}(1-i\eta)\sigma_{\text{soft}}^j(x, Q_0^2) \int_{z_1}^{z_2} dz' \rho_A(\vec{b}, z')} \\
&\times \left. \frac{1}{x_{\mathcal{P}}} f_j^{D(3)}(\beta, Q_0^2, x_{\mathcal{P}}) \right\}, \tag{197}
\end{aligned}$$

where H_N^j is the GPD of the free nucleon. As in the case of the calculation of the nuclear PDFs, H_A^j in Eq. (197) is evaluated at $Q^2 = Q_0^2$. The t dependence of the rescattering contribution (shadowing correction) originates mostly from the overlap of the nuclear wave functions, with an additional small correction due to the t dependence of the elementary amplitudes which enter with $t_{\text{eff}} \sim t/N^2$ for the interaction with N nucleons. This is a rather small effect that can effectively be taken into account with a good accuracy by using in Eq. (197) the nuclear matter density rather than the distribution of the point-like nucleons. This is because the t dependence of the elementary GPDs in the case of sea quark distribution is close to that of the proton e.m. form factor. In the gluon channel, the t dependence of the elementary GPD is given by the two-gluon form factor.

A more accurate treatment would require taking into account the $x-b$ correlations in the nucleon GPDs. One should also note that the effects of the t dependence of the elementary GPDs are more important for the lightest nuclei like ^2H and ^4He . A generalization for this case is straightforward since the t dependence of the two dominant terms (impulse approximation and double scattering) can be determined in a model-independent way.

Figure 79 presents our predictions for the ratio $H_A^j(x, x_- = 0, t)/[AF_A(t)H_N^j(x, x_- = 0, t)]$ as a function of x for different values of t . The two left panels correspond to the \bar{u} -quark distributions; the two right panels correspond to the gluon distributions. All curves correspond to $Q^2 = Q_0^2 = 4 \text{ GeV}^2$ and model FGS10_H. Since the t dependence of the shadowing correction to $H_A^j(x, x_- = 0, t)$ [the second term in Eq. (197)] is significantly slower than that of the impulse approximation [the first term in Eq. (197)], the effect of nuclear shadowing expectedly increases as $|t|$ is increased. Note also that for the t dependence of the forward limit of the nucleon GPDs $H_N^j(x, x_- = 0, t)$, we use the exponential parameterization with the slope $B_{\text{DVCS}} = 5.45 \pm 0.19 \pm 0.34 \text{ GeV}^{-2}$ [141]:

$$H_N^j(x, x_- = 0, t, Q^2) = e^{-\frac{1}{2}B_{\text{DVCS}}|t|} H_N^j(x, x_- = 0, t = 0, Q^2) = e^{-\frac{1}{2}B_{\text{DVCS}}|t|} f_{j/N}(x, Q^2). \tag{198}$$

We also neglect a small difference in the t dependence of the gluon and quark GPDs.

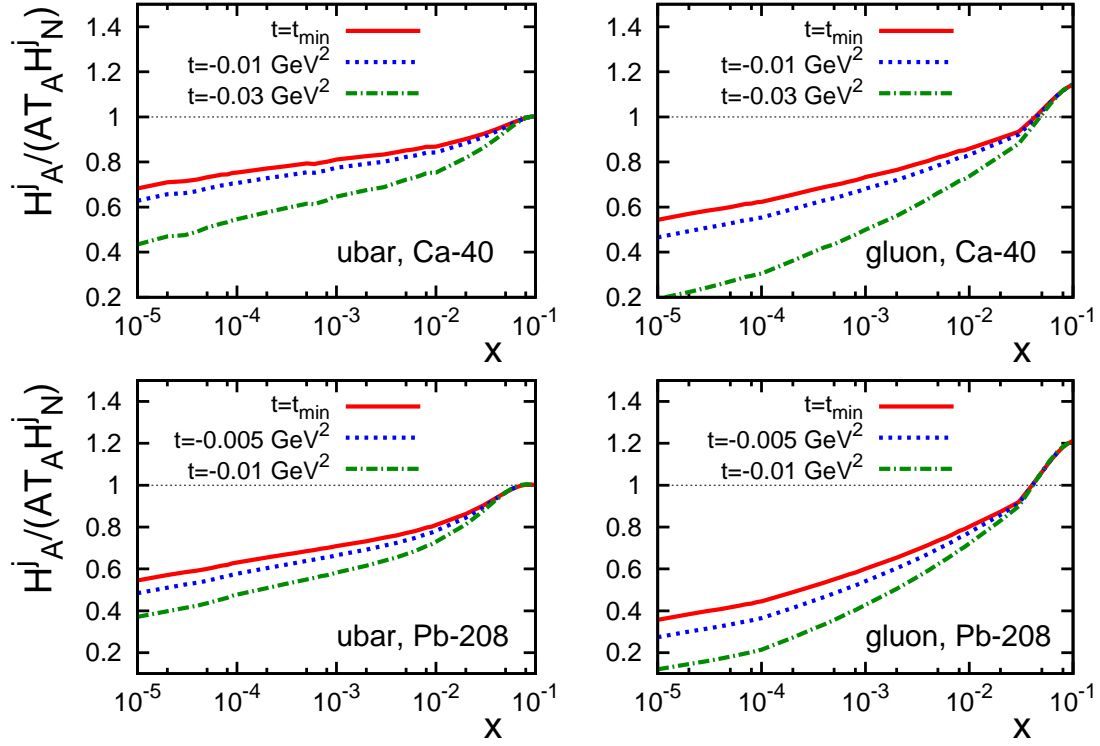


Fig. 79. The ratio $H_A^j(x, x_- = 0, t) / [A F_A(t) H_N^j(x, x_-, t)]$ as a function of x for different values of t . All curves correspond to $Q^2 = Q_0^2 = 4 \text{ GeV}^2$ and model FGS10_H.

In quantum mechanics and quantum field theory, it is convenient to consider high energy scattering amplitudes in the impact parameter representation by making the Fourier transform from the momentum representation to the coordinate representation. Since the amplitudes of hard exclusive process depend on t only through the GPDs, it is natural to consider the GPDs in the impact parameter space. In the $x_- = 0$ limit, the momentum transfer t is purely transverse, $t = -\Delta_\perp^2$, and one obtains the nuclear GPD in the mixed momentum-impact parameter representation (see also [226]):

$$H_A^j(x, x_- = 0, b, Q^2) = \int \frac{d^2 \vec{\Delta}_\perp}{(2\pi)^2} e^{-i \vec{\Delta}_\perp \cdot \vec{b}} H_A^j(x, x_- = 0, t = -\Delta_\perp^2, Q^2). \quad (199)$$

Substituting Eq. (199) in Eq. (197), one obtains the expression for the $x_- = 0$ limit of the nuclear GPD H_A^j at small x in the impact parameter space:

$$\begin{aligned}
H_A^j(x, x_- = 0, b, Q_0^2) &= AT_A(b) f_{j/N}(x, Q_0^2) \\
&- \frac{A(A-1)}{2} 16\pi B_{\text{diff}} \Re \left\{ \frac{(1-i\eta)^2}{1+\eta^2} \int_{-\infty}^{\infty} dz_1 \int_{z_1}^{\infty} dz_2 \int_x^{0.1} dx_{\mathcal{P}} \right. \\
&\times \rho_A(b, z_1) \rho_A(b, z_2) e^{im_N x_{\mathcal{P}}(z_1 - z_2)} e^{-\frac{A}{2}(1-i\eta)\sigma_{\text{soft}}^j(x, Q_0^2)} \int_{z_1}^{z_2} dz' \rho_A(\vec{b}, z') \\
&\times \left. \frac{1}{x_{\mathcal{P}}} f_j^{D(3)}(\beta, Q_0^2, x_{\mathcal{P}}) \right\}. \tag{200}
\end{aligned}$$

Note that in the first line of Eq. (200), we neglected the weak t dependence of the free nucleon GPD compared to the steep t dependence of the nuclear form factor (see the discussion above) and used the fact that $H_N^j(x, 0, 0, Q^2) = f_{j/N}(x, Q^2)$. A comparison of Eq. (200) to Eq. (130) shows that, indeed, $f_{j/A}(x, Q^2, b) = H_A^j(x, \xi = 0, b, Q^2)$ which demonstrates consistency of our treatment of nuclear shadowing for H_A^j and for nuclear PDFs.

In general, GPDs do not lend themselves to the probabilistic interpretation. However, in the $x_- = 0$ limit, they do: $H_A^j(x, x_- = 0, b, Q^2)$ is the probability to find the parton of flavor j with the light-cone fraction x and the transverse distance b from the transverse center of momentum of the nucleus [109,226]. In fact, one can formally prove that the diagonal GPDs in the b -space are positive-definite [227]. The equivalence of the impact parameter dependent nuclear PDFs and the $x_- = 0$ limit of nuclear GPDs in the impact parameter space implies that the spacial image of the nuclear GPDs in this limit is the same as for nuclear PDFs and is given by Fig. 40.

6.2.2 Modeling nuclear GPDs and the role of skewness

Equation (197) defines our expression for the nuclear GPD $H_A^j(x_+, x_-, t, Q^2)$ in the $x_- = 0$ limit at the initial evolution scale Q_0^2 . However, in general, experimental observables measured in hard exclusive processes (191) probe a much more complicated function, namely, the integration of perturbatively calculable coefficient functions (scattering kernels) with the GPD $H_A^j(x_+, x_-, t, Q^2)$ over the entire region of the light-cone variable x , $0 \leq x \leq 1$. At the same time, at high energies (small x_B), the situation simplifies because the high-energy scattering amplitudes are predominantly imaginary; the imaginary part of the $\gamma^* + A \rightarrow \gamma(J/\psi, \rho, \dots) + A$ scattering amplitudes can be approximated in terms of the diagonal GPDs.

Several theoretical ideas were suggested which help to evaluate non-diagonal GPDs at small x_B . It was observed in [181] that GPDs at small x and sufficiently large Q^2 are calculable through diagonal GPDs. The reason is that $x_1 - x_2 \approx 2\xi$ is conserved in the kernel of the QCD evolution equations for the GPDs. At the same time, x_+ evolves similarly to the case of the QCD evolution equations for usual PDFs. An analysis of the trajectories for the QCD evolution shows that for sufficiently large Q^2 , dominant

trajectories correspond to x_+ at Q_0^2 that are much larger than x_- (see the discussion in Sec. 5.15). Hence, GPD at small x and large Q^2 can be calculated through the diagonal GPDs at the initial Q_0^2 . Note, however, that there is a substantial Q^2 interval where there is significant sensitivity to the boundary condition.

There are also additional considerations applicable for moderate Q^2 . Let us first consider the case of DVCS $\gamma^* + N \rightarrow \gamma + N$. We argued before that the dominant configurations in the photon wave function, which dominate the interaction with the nucleon for $Q^2 \sim \text{few GeV}^2$, are aligned jet configurations. If we neglect contributions of other configurations, we can write explicitly the integral over the momenta in the quark loop and notice that this part of the interaction is not sensitive to the skewness. As a result, the main difference between the diagonal $\gamma^* + N \rightarrow \gamma^* + N$ amplitude at $t = 0$ (which is expressed through the total cross section of the $\gamma^* N$ scattering) and the corresponding DVCS amplitude is due to different energy denominators, which are equal to $1/(Q^2 + M_{q\bar{q}}^2)$ for the $\gamma^* \rightarrow q\bar{q}$ transition and $1/M_{q\bar{q}}^2$ for the $\gamma \rightarrow q\bar{q}$ transition ($M_{q\bar{q}}^2$ is the invariant mass squared of the $q\bar{q}$ system). Therefore, one finds that

$$R = \frac{\Im m T(\gamma^* p \rightarrow \gamma p)|_{t=0}}{\Im m T(\gamma^* p \rightarrow \gamma^* p)|_{t=0}} \approx 2. \quad (201)$$

On the other hand, at the leading order accuracy, R is equal to the ratio of the GPDs at the cross-over point $x_+ = x_-$ and the usual PDFs:

$$R = \frac{\sum_q e_q^2 [H^q(x_-, x_-, t=0, Q^2) + H^{\bar{q}}(x_-, x_-, t=0, Q^2)]}{\sum_q e_q^2 [q(2x_-, Q^2) + \bar{q}(2x_-, Q^2)]}, \quad (202)$$

where $\sum_q e_q^2$ is the sum over all active quark flavors (quarks and antiquarks) with the weight given by the quark charge squared e_q^2 ; the denominator is evaluated at Bjorken $2x_- \approx 2\xi \approx x$. Therefore, R directly constrains the GPDs at the cross-over line $x_+ = x_-$ ($x_2 = 0$) and is very sensitive to the $x_- \rightarrow 0$ behavior of the GPDs, see the discussion in [228]. The QCD evolution leads to a slow increase of R with Q^2 . R has been measured in the free proton case at HERA [141,229]; it agrees well with the predictions of [230,231].

A useful, though rough, approximation for the gluon GPD, which is relevant for the exclusive vector meson production, is to use the symmetry of the $\gamma^* + T \rightarrow V + T$ amplitude with respect to the transposition $x_1\nu \rightarrow x_2\nu$ [216]. Odd powers of x_- do not contribute and one obtains:

$$H^g(x_1, x_2, \dots) = H^g((x_+ + x_-)/2, (x_+ + x_-)/2, \dots) + \frac{x_-^2}{2} \frac{\partial^2}{\partial^2 x_-} H^g(x_+ + x_-, x_+ - x_-)|_{x_-=0}. \quad (203)$$

Taking $H^g(x_1, x_2) \propto 1/(x_1 x_2)^{n/2}$, where $H^g(x, x) \propto 1/x^n$ and $n \sim 0.2 \div 0.3$, we can estimate

$$H^g(x_1, x_2) \approx H^g(x_+, x_- = 0) \left(1 + \frac{x_-^2}{x_+^2}\right)^{n/2}. \quad (204)$$

Hence, we see that for a wide range of skewness, one can estimate the non-diagonal gluon GPD as the diagonal gluon GPD at the average point $x = x_+$. For example, for $x_2 = 0$ which enters the description of the exclusive vector meson production at large Q^2 ,

$$H^g(x_1, x_2 = 0) \approx H^g(x_1/2, x_1/2)(1 + n/2). \quad (205)$$

In summary, at high energies (small ξ) and in the leading logarithmic approximation (LLA), generalized parton distributions at an input scale Q_0^2 can be approximated well by the usual parton distributions [181]:

$$\begin{aligned} H_A^q(x_+, x_-, t = 0, Q_0^2) &= q_A(x, Q_0^2), \\ H_A^g(x_+, x_-, t = 0, Q_0^2) &= g_A(x, Q_0^2), \end{aligned} \quad (206)$$

where $x = x_+$. Note that we do not introduce the additional factor of x in the second line of Eq. (206) as was done, e.g., in Refs. [223] and [181]; this factor is essentially a matter of convention. The form of Eq. (206) allows us to use the diagonal approximation reproducing the boundary condition for $R \approx 2$ (see Eq. (201)) (though this condition is expected to be violated for very small x , see the discussion above).

In Eq. (206) we did not consider the t dependence. However, it can be straightforwardly restored since it does not conflict with the LLA. Therefore, we have the following final relation between the small- ξ GPDs and the impact parameter dependent PDFs:

$$\begin{aligned} H_A^j(x_+, x_-, t, Q_0^2) &= H_A^j(x, x_- = 0, t, Q_0^2) = \int d^2\vec{b} e^{i\vec{\Delta}_\perp \cdot \vec{b}} H_A^j(x, x_- = 0, b, Q_0^2) \\ &= \int d^2\vec{b} e^{i\vec{\Delta}_\perp \cdot \vec{b}} f_{j/A}(x, Q_0^2, b). \end{aligned} \quad (207)$$

Note that the right-hand side of Eq. (207) is known: it is predicted by the leading twist theory of nuclear shadowing, see Eq. (197) and (200). Note also that as the value of Q^2 is increased, the accuracy of Eq. (207) worsens since the DGLAP evolution for GPDs introduces additional skewness (dependence on ξ). Equation (207) defines the nuclear GPDs that we shall use below to make predictions for various observables in hard exclusive reactions with nuclei.

The skewness ratio R can also be introduced for nuclear targets and separate parton

flavors:

$$R_{j/A} \equiv \frac{H_A^j(x_-, x_-, t=0, Q_0^2)}{f_{j/A}(2x_-, Q_0^2)} = \frac{H_A^j(x_-, x_- = 0, t=0, Q_0^2)}{f_{j/A}(2x_-, Q_0^2)} = \frac{f_{j/A}(x_-, Q_0^2)}{f_{j/A}(2x_-, Q_0^2)}. \quad (208)$$

Here we used Eq. (207) and the fact that in the forward limit ($x_- \rightarrow 0$ and $t \rightarrow 0$), the GPD H reduces to the usual PDFs. Hence, the skewness ratio $R_{j/A}$ is given in terms of the usual nuclear PDFs evaluated at different light-cone fractions.

Figure 80 presents our predictions for $R_{j/A}$ of Eq. (208) as a function of ξ at $Q_0^2 = 4 \text{ GeV}^2$. The solid curves correspond to ^{40}Ca ; the dotted curves correspond to ^{208}Pb ; models FGS10_H and FGS10_L give numerically indistinguishable predictions for $R_{j/A}$. For comparison, we also give the skewness ratio $R_{j/A}$ for the free proton target as dot-dashed curves. In Fig. 80, the left panel corresponds to \bar{u} -quarks; the right panel corresponds to the gluon channel. As one can see from the figure, $R_{j/A}$ depends weakly on the atomic mass number and the parton flavor. Also, $R_{j/A}$ is a weak function of x_- for $10^{-5} \leq x_- \leq 10^{-2}$.

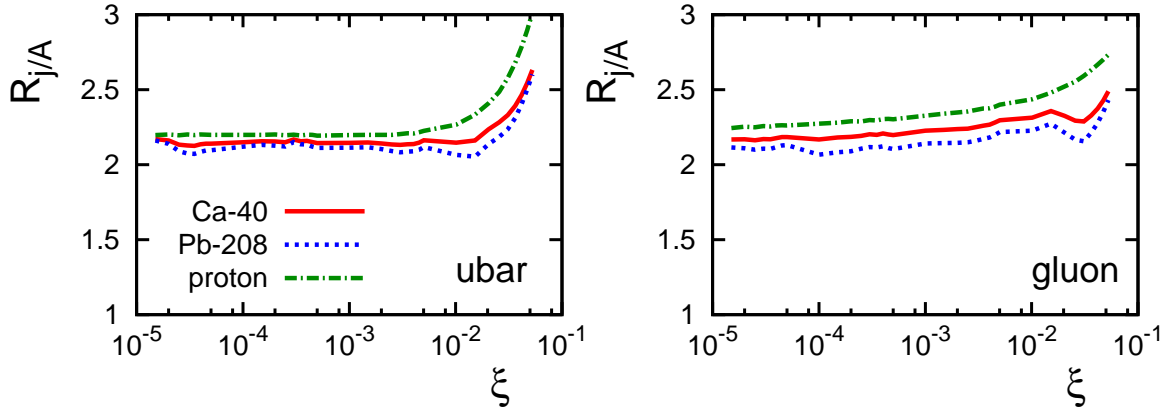


Fig. 80. The skewness ratio $R_{j/A}$ of Eq. (208) as a function of ξ at $Q_0^2 = 4 \text{ GeV}^2$ for ^{40}Ca (solid curves), ^{208}Pb (dotted curves) and free proton (dot-dashed curves). The left panel is for the \bar{u} -quark distribution; the right panel is for the gluon distribution.

The numerical value of $R_{j/A}$ is very important for the phenomenology of GPDs. The fact that $R_{j/A}$ for the proton is of the order of 2 – 2.5 is in agreement with the analysis of the HERA data on the skewness ratio R of Eq. (201) [141,229], the aligned jet type model for the proton GPDs at the input scale [230,231], and the phenomenological parameterization of proton GPDs as the conformal partial wave decomposition [228] (see the discussion in Ref. [228]). The value of $R_{j/A}$ is somewhat smaller for nuclei than for the free nucleon since nuclear shadowing tames the increase of nuclear PDFs with decreasing Bjorken x . Note that the discussed model may overestimate $R(Q_0^2)$. Indeed, as we discussed above, $R \sim 2$ corresponds to the dominance of the AJM contribution with small transverse momenta. Nuclear shadowing reduces this contribution to nuclear PDFs as compared to the contribution of components with large transverse momenta, for which R is closer to unity. Hence, the effect of the reduction of $R_{j/A}$ with an increase of A and a decrease of

x may be somewhat larger than presented in Fig. 80.

6.2.3 Leading twist nuclear shadowing and coherent nuclear DVCS

Having defined and discussed the expression for the nuclear GPDs at small ξ [see Eq. (207)], we can now form predictions for various observables measured in high-energy hard exclusive processes with nuclei (191). (In this review, we consider only *diffractive* hard exclusive processes.) The cleanest ways to access GPDs is via DVCS; below we focus on unpolarized coherent nuclear DVCS, $\gamma^* + A \rightarrow \gamma + A$, see Fig. 81.

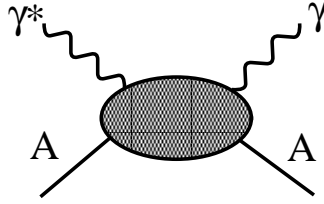


Fig. 81. Coherent deeply virtual Compton scattering (DVCS) with nuclei.

At the photon level, the $\gamma^* + A \rightarrow \gamma + A$ cross section reads, see, e.g., [232]:

$$\frac{d\sigma_{\text{DVCS}}}{dt} = \frac{\pi\alpha_{\text{em}}^2 x^2 (1 - \xi^2)}{Q^4 \sqrt{1 + \epsilon^2}} |\mathcal{A}_{\text{DVCS}}(\xi, t, Q^2)|^2, \quad (209)$$

where α_{em} is the fine-structure constant; $\epsilon^2 = 4x_B^2 m_N^2 / Q^2$; $\mathcal{A}_{\text{DVCS}}$ is the DVCS amplitude (more precisely, it is the so-called Compton form factor). At high energies (small Bjorken x and x_-), $\mathcal{A}_{\text{DVCS}}$ is predominantly imaginary. At the leading order in the strong coupling constant α_s (the handbag approximation), the imaginary part of $\mathcal{A}_{\text{DVCS}}$ is given in terms of the quark nuclear GPDs at the $x_- = x_+ = \xi$ cross-over line,

$$\Im m \mathcal{A}_{\text{DVCS}}(\xi, t, Q^2) = -\pi \sum_q e_q^2 \left[H_A^q(\xi, \xi, t, Q^2) + H_A^{\bar{q}}(\xi, \xi, t, Q^2) \right], \quad (210)$$

where e_q are the quark charges; $H_A^q(\xi, \xi, t, Q^2)$ are given by Eq. (207). Note that Eq. (210) involves the $q + \bar{q}$ singlet combination of the quark GPDs.

The DVCS process interferes and competes with the purely electromagnetic Bethe-Heitler (BH) process, see Fig. 82.

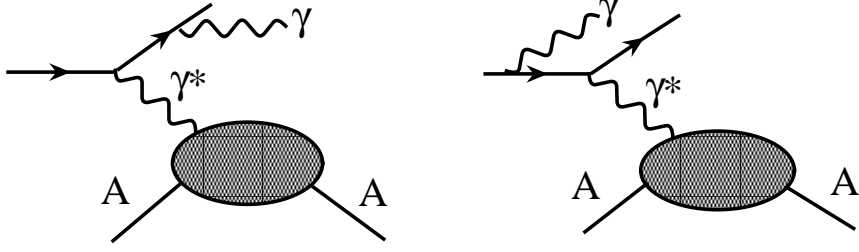


Fig. 82. Coherent Bethe-Heitler (BH) process with nuclei.

The BH cross section at the photon level can be written in the following form [232]:

$$\frac{d\sigma_{\text{BH}}}{dt} = \frac{\pi\alpha_{\text{em}}^2}{4Q^2t(1+\epsilon)^{5/2}(1-y-y^2/2)} \int_0^{2\pi} \frac{d\phi}{2\pi} \frac{1}{\mathcal{P}_1(\phi)\mathcal{P}_2(\phi)} |\mathcal{A}_{\text{BH}}(\xi, t, Q^2, \phi)|^2, \quad (211)$$

where $y = (q \cdot P_A)/(k \cdot P_A) = Q^2/(xs)$ is the fractional energy loss of the incoming lepton with momentum k (q is the momentum of the virtual photon, P_A is the momentum of the incoming nucleus, s is the total invariant energy squared); ϕ is the angle between the lepton and hadron scattering planes; $\mathcal{P}_1(\phi)$ and $\mathcal{P}_2(\phi)$ are proportional to the lepton propagators; $|\mathcal{A}_{\text{BH}}(x, t, Q^2)|^2$ is the BH amplitude squared. The expressions for $\mathcal{P}_{1,2}(\phi)$ and $|\mathcal{A}_{\text{BH}}(x, t, Q^2)|^2$ can be found in Refs. [232,233]. Note that $|\mathcal{A}_{\text{BH}}(x, t, Q^2)|^2$ is proportional to the nuclear electric form factor squared, $|F_A(t)|^2$, and the nucleus charge squared, Z^2 .

Note that at high energies (small Bjorken x), the $\gamma^* + A \rightarrow \gamma + A$ amplitude is predominantly imaginary. The contribution of the interference between the DVCS and BH amplitudes is proportional to the real part of the DVCS amplitude, sizable and concentrated at small t . However, after the integration over ϕ , the interference term essentially disappears and, thus, can be safely neglected.

Integrating the differential cross sections in Eqs. (209) and (211) over t , one obtains the corresponding t -integrated cross sections:

$$\begin{aligned} \sigma_{\text{DVCS}} &= \int_{t_{\text{max}}}^{t_{\text{min}}} dt \frac{d\sigma_{\text{DVCS}}}{dt}, \\ \sigma_{\text{BH}} &= \int_{t_{\text{max}}}^{t_{\text{min}}} dt \frac{d\sigma_{\text{BH}}}{dt}, \end{aligned} \quad (212)$$

where $t_{\text{min}} \approx -x^2 m_N^2$ (the exact expression can be found in [232]); $t_{\text{max}} = -1 \text{ GeV}^2$ (in practice, one can take $|t_{\text{max}}|$ much smaller for heavy nuclei, e.g., $\approx -0.1 \text{ GeV}^2$ for ^{208}Pb .)

Figure 83 presents our calculations for the t -integrated DVCS (solid curves) and BH (dotted curves) cross sections as a function of x at fixed $Q^2 = Q_0^2 = 4 \text{ GeV}^2$. The left panel

corresponds to ^{40}Ca ; the right panel corresponds to ^{208}Pb . Note that at the given large scale along the y -axis, models FGS10_H and FGS10_L give indistinguishable predictions.

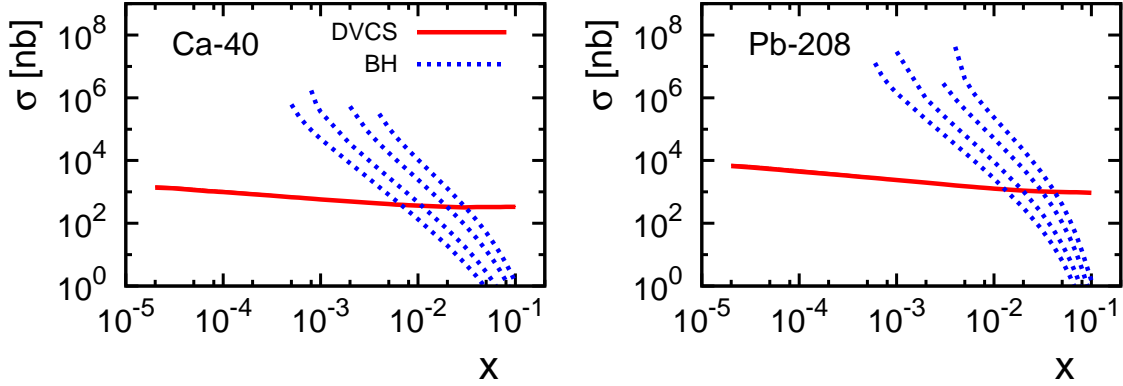


Fig. 83. The DVCS (solid curves) and Bethe-Heitler (dotted curves) cross sections (212) as functions of Bjorken x at $Q_0^2 = 4 \text{ GeV}^2$. The left panel corresponds to ^{40}Ca ; the right panel corresponds to ^{208}Pb . Four curves for the BH cross section correspond to the four values of \sqrt{s} in Table 6 (the rightmost dotted curve corresponds to the lowest \sqrt{s} ; the leftmost dotted curve corresponds to the largest \sqrt{s}).

The BH cross section explicitly depends on the energy of the process through the variable y . In Fig. 83, the four values of the BH cross section correspond to the values of y , $y = Q^2/(xs)$, that correspond to the energy settings presented in Table 6. These energies of the lepton and hadron beam are the discussed energy settings of a future Electron-Ion Collider. The rightmost dotted curve corresponds to the lowest \sqrt{s} ; the leftmost dotted curve corresponds to the largest \sqrt{s} . The dotted curves extend from large x down to the smallest possible x defined by the condition that $y \geq 0.95$.

E_l (GeV)	E_N (GeV) in ^{208}Pb	\sqrt{s} (GeV)	E_N (GeV) in ^{40}Ca	\sqrt{s} (GeV)	E_N (GeV) free nucleon	\sqrt{s} (GeV)
11	24	32	30	36	60	51
11	100	66	125	74	250	105
5	100	44	125	50	250	71
20	100	90	125	100	250	141

Table 6

The lepton and hadron beam energies and the corresponding \sqrt{s} that correspond to the BH cross section presented in Figs. 83 and 84.

For comparison with the nuclear case, we also present the free proton DVCS and BH cross sections as functions of x at $Q_0^2 = 4 \text{ GeV}^2$ in Fig. 84. The dot-dashed curve corresponds to the DVCS cross section; the four dotted curves correspond to the BH cross section evaluated at the four values of \sqrt{s} presented in Table 6 (the rightmost dotted curve corresponds to the lowest \sqrt{s} ; the leftmost dotted curve corresponds to the largest \sqrt{s}).

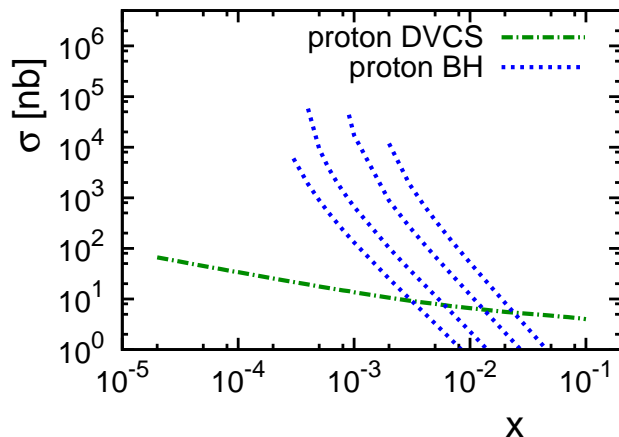


Fig. 84. The free proton DVCS (dot-dashed curve) and Bethe-Heitler (dotted curves) cross sections as functions of Bjorken x at $Q_0^2 = 4 \text{ GeV}^2$. Four curves for the BH cross section correspond to the four values of \sqrt{s} in Table 6 (the rightmost dotted curve corresponds to the lowest \sqrt{s} ; the leftmost dotted curve corresponds to the largest \sqrt{s}).

In our calculations, we used the standard expressions for the DVCS and BH cross sections [232]. For the free proton GPDs, we used Eq. (198) along with the leading order CTEQ5L parameterization for $f_{j/N}(x, Q_0^2)$ [160].

As one can see from Fig. 83, in the considered kinematics (note that we considered the kinematics of a future EIC) and for the considered medium-heavy (^{40}Ca) and heavy (^{208}Pb) nuclei, the BH cross section is much larger than the DVCS cross section for small x . One of the main reasons for this is the dramatic enhancement of the BH cross section at small $t \approx t_{\min}$ by the factor $1/t$, see Eq. (211). Therefore, in order to extract a small DVCS signal on the background of the dominant BH contribution, one needs to consider the observable differential in t and generally stay away from $t \approx t_{\min}$.

Figure 85 presents our predictions for the differential DVCS cross section (solid curves) and BH cross section (dotted curves), see Eqs. (209) and (211), as functions of the momentum transfer $|t|$ at fixed $Q_0^2 = 4 \text{ GeV}^2$ and $x = 10^{-3}$ and $x = 5 \times 10^{-3}$. The two upper panels correspond to ^{40}Ca ; the two bottom panels corresponds to ^{208}Pb . For $x = 10^{-3}$ (two left panels), the BH contribution is evaluated assuming a high-energy EIC setting with $E_l = 20 \text{ GeV}$ and $E_N = 125 \text{ GeV}$ (for ^{40}Ca) and $E_N = 100 \text{ GeV}$ (for ^{208}Pb). For $x = 5 \times 10^{-3}$ (two right panels), the BH contribution is calculated using a low-energy EIC setting with $E_l = 11 \text{ GeV}$ and $E_N = 30 \text{ GeV}$ (for ^{40}Ca) and $E_N = 24 \text{ GeV}$ (for ^{208}Pb).

As one can see from Fig. 85, the t dependence of the DVCS and BH differential cross sections has the characteristic shape of the nuclear form factor squared, with distinct minima and maxima. However, the minima of the DVCS cross section are shifted toward smaller t : this is the effect of the leading twist nuclear shadowing in quark nuclear GPDs. The shift of the minima toward smaller t can be interpreted as an increase of the transverse

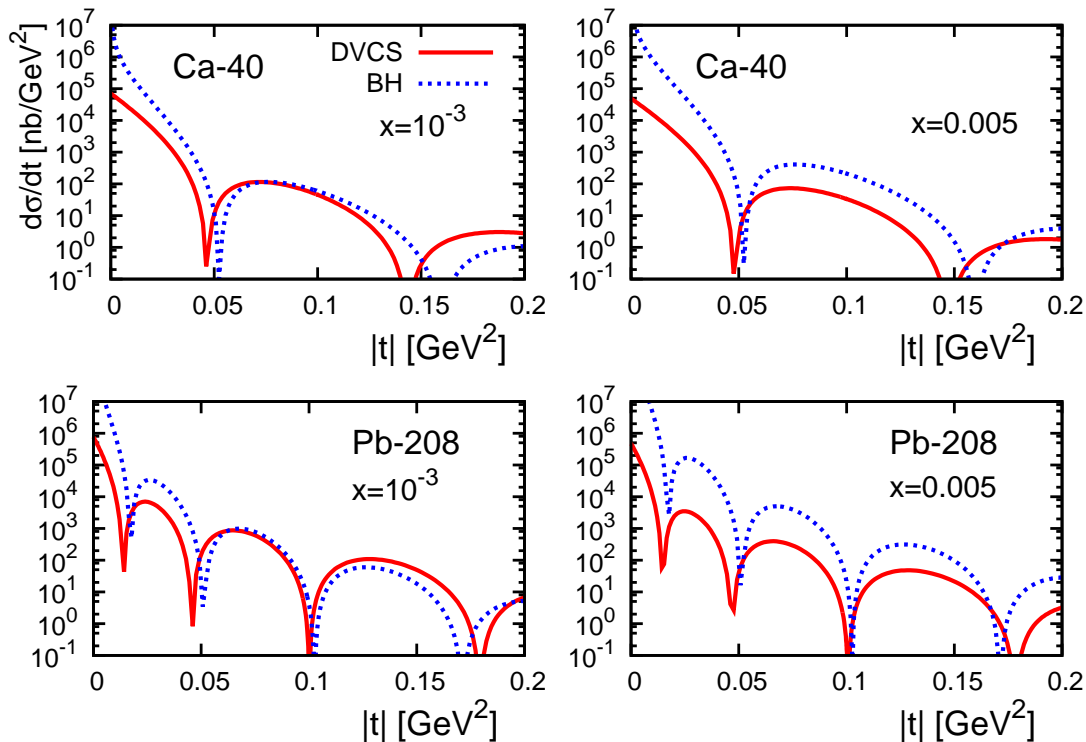


Fig. 85. The DVCS (solid curves) and Bethe-Heitler (dotted curves) cross sections, see Eqs. (209) and (211), as functions of $|t|$ at $Q_0^2 = 4 \text{ GeV}^2$ and $x = 10^{-3}$ and $x = 5 \times 10^{-3}$. The upper panels corresponds to ^{40}Ca ; the lower panels corresponds to ^{208}Pb .

size of the distributions of quarks in nuclei—this is exactly the phenomenon that we discussed and quantified in Sec. 5.6.

One has to note that the shift of the position of the minima in Fig. 85 is very small. One way to enhance the effect is to use lighter nuclei, such as, e.g., ^4He and ^{12}C (see Fig. 87 and discussion below). Also, the shift of the minima presented in Fig. 85 is smaller than that predicted in Ref. [182] where a different model for nuclear shadowing in quark nuclear GPDs was used (the larger shadowing in Ref. [182] leads to the larger shift of the minima).

While an access to the effect of nuclear shadowing in nuclear GPDs through the measurement of the DVCS cross section seems to be problematic (the shifts of the minima are probably too challenging to measure experimentally), an interesting possibility is offered by the measurement of DVCS cross section asymmetries [182]. These asymmetries are proportional to the interference between the DVCS and BH amplitudes and, thus, use the large and well known BH amplitude to amplify the generally smaller DVCS amplitude.

One example is the beam-spin asymmetry, A_{LU} , measured with the longitudinally polarized lepton beam and unpolarized nuclear target. In the leading twist approximation, A_{LU}

for a spinless nuclear target reads [182]:

$$A_{\text{LU}}(\phi) = -\frac{8K(2-y)ZF_A(t)\Im m\mathcal{A}_{\text{DVCS}}(\xi, t, Q^2)}{\frac{1}{x}|\mathcal{A}_{\text{BH}}|^2 + \frac{xt\mathcal{P}_1(\phi)\mathcal{P}_2(\phi)}{Q^2}4(1-y+y^2/2)|\Im m\mathcal{A}_{\text{DVCS}}|^2} \sin \phi, \quad (213)$$

where $K \propto \sqrt{t_{\text{min}} - t}$ is the kinematic factor [232]; Z is the nuclear charge; $F_A(t)$ is the nuclear electric form factor; $\Im m\mathcal{A}_{\text{DVCS}}$ is given by Eq. (210); ϕ is the angle between the lepton and hadron scattering planes. The overall minus sign corresponds to the negatively charged lepton beam. To consistently work to the leading twist accuracy, one should use only the leading twist contributions to $\mathcal{P}_1(\phi)$, $\mathcal{P}_2(\phi)$ and $|\mathcal{A}_{\text{BH}}|^2$. However, in the considered kinematics, $Q^2 = 4 \text{ GeV}^2$, $x = 10^{-3}$ and small t , the higher twist effects are either absent (at $\phi = 90^\circ$) or numerically insignificant. Therefore, in the evaluation of A_{LU} , we use the standard expressions for $\mathcal{P}_1(\phi)$, $\mathcal{P}_2(\phi)$ and $|\mathcal{A}_{\text{BH}}|^2$ [232,233].

Figure 86 presents our predictions for $A_{\text{LU}}(\phi = 90^\circ)$ as a function of $|t|$ at fixed $Q_0^2 = 4 \text{ GeV}^2$ and $x = 10^{-3}$. The solid curves correspond to ^{40}Ca (left panel) and ^{208}Pb . For comparison, $A_{\text{LU}}(\phi = 90^\circ)$ for the free proton is given by the dot-dashed curve. As in Fig. 85, the BH contribution to $A_{\text{LU}}(\phi = 90^\circ)$ is evaluated assuming a high energy EIC setting with $E_l = 20 \text{ GeV}$ and $E_N = 125 \text{ GeV}$ (for ^{40}Ca) and $E_N = 100 \text{ GeV}$ (for ^{208}Pb).

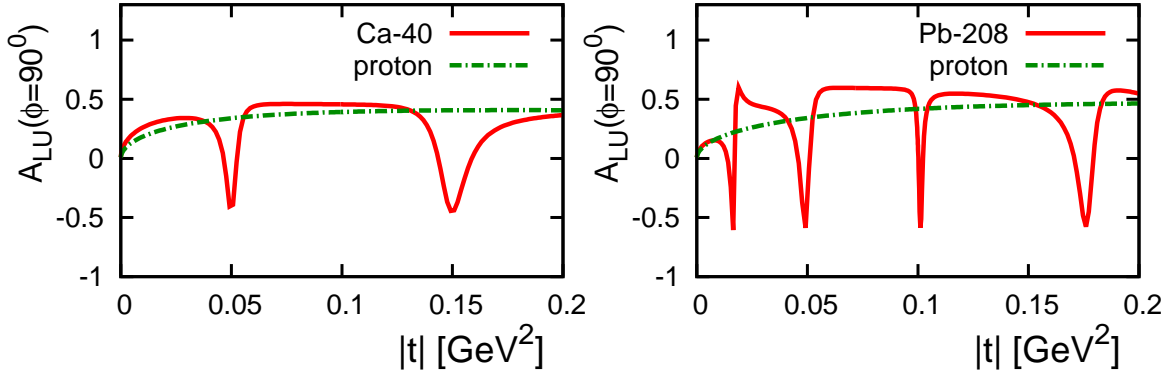


Fig. 86. The DVCS beam-spin asymmetry at $\phi = 90^\circ$, $A_{\text{LU}}(\phi = 90^\circ)$, as a function of $|t|$ at fixed $Q_0^2 = 4 \text{ GeV}^2$ and $x = 10^{-3}$. The solid curves in the left and right panels correspond to ^{40}Ca and ^{208}Pb , respectively. For comparison, $A_{\text{LU}}(\phi = 90^\circ)$ for the free proton is given by the dot-dashed curve.

Our predictions for $A_{\text{LU}}(\phi = 90^\circ)$ for nuclei are rather remarkable. The sole reason for the dramatic oscillations of $A_{\text{LU}}(\phi = 90^\circ)$ as a function of $|t|$ is nuclear shadowing that shifts the t behavior of the DVCS amplitude relative to the BH one. Loosely speaking, $A_{\text{LU}}(\phi = 90^\circ)$ is given by the ratio of the imaginary part of the DVCS amplitude and the BH amplitude, i.e., by the ratio of the solid and dotted curves from Fig. 85.

In more detail, the trend of the t behavior of A_{LU} in Fig. 85 can be explained as follows. At small t , $t \approx t_{\text{min}}$, A_{LU} is vanishingly small due to the kinematic factor K . As $|t|$ is increased,

the kinematic factors rapidly increase A_{LU} . At the same time, nuclear shadowing works in the opposite direction and decreases $\Im m\mathcal{A}_{\text{DVCS}}$, see Fig. 79. Near the position of the first minimum of the nuclear form factor, $|t| \approx 0.05 \text{ GeV}^2$ for ^{40}Ca and $|t| \approx 0.01 \text{ GeV}^2$ for ^{208}Pb , $\Im m\mathcal{A}_{\text{DVCS}}$ changes sign and A_{LU} goes through zero and eventually reverses its sign. (Note that at these values of $|t|$, the nuclear electric form factor $F_A(t)$ is still positive.) As $|t|$ is further increased, $|\Im m\mathcal{A}_{\text{DVCS}}|$ increases, which increases $|A_{\text{LU}}|$. As $|t|$ is increased even further, the nuclear form factor $F_A(t)$ changes sign and makes A_{LU} again positive. The asymmetry stays positive until $\Im m\mathcal{A}_{\text{DVCS}}$ changes the sign near the second minimum of the nuclear form factor. Then, the mechanism of the oscillations just described repeats itself. In summary, the dramatic oscillations of A_{LU} as a function of $|t|$ is a result of the leading twist nuclear shadowing that causes the t dependence of the shadowing correction to $\Im m\mathcal{A}_{\text{DVCS}}$ to be different from that of the impulse approximation to $\Im m\mathcal{A}_{\text{DVCS}}$. (If the effect of shadowing is neglected, the t dependence of the DVCS and BH amplitudes is the same and A_{LU} behaves as in the free proton case, see the dot-dashed curve in Fig. 79.)

As we remarked earlier, in order to enhance the effect of the relative shift of the position of the minima of the differential DVCS and BH cross sections, one can consider light nuclei, such as, e.g., ^4He and ^{12}C . Figure 87 presents an example of such a study for ^{12}C . In the left panel of the figure, the DVCS (solid curve) and BH (dotted curve) cross sections are plotted as a function $|t|$ at fixed $Q^2 = 4 \text{ GeV}^2$ and $x = 10^{-3}$. As one can see from the panel, the relative shift of the position of the first minimum of the differential DVCS and BH cross sections for ^{12}C is significantly larger than that for ^{40}Ca and ^{208}Pb . In the right panel of Fig. 87, the beam-spin asymmetry at the angle $\phi = 90^\circ$, $A_{\text{LU}}(\phi = 90^\circ)$, is plotted as a function of $|t|$ at $Q^2 = 4 \text{ GeV}^2$ and $x = 10^{-3}$. The asymmetry reveals the dramatic pattern of oscillations, similarly to the case of the heavier nuclei presented in Fig. 86 and already discussed.

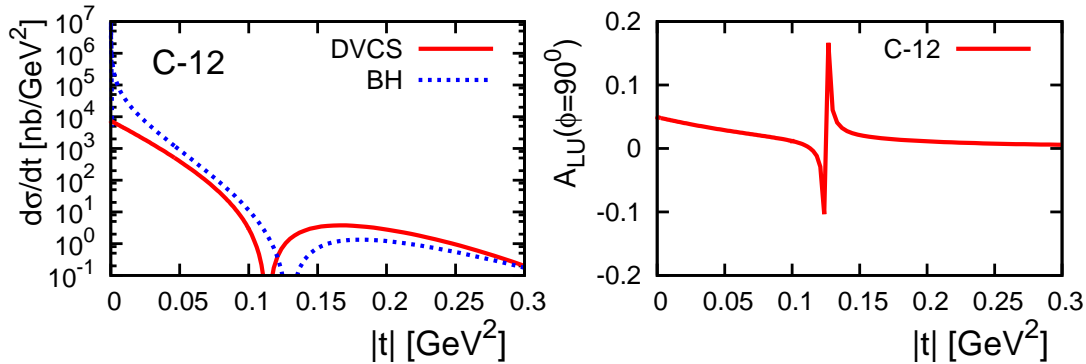


Fig. 87. Left panel: The DVCS and BH cross sections for ^{12}C as functions of $|t|$ at $Q^2 = 4 \text{ GeV}^2$ and $x = 10^{-3}$. Right panel: The DVCS beam-spin asymmetry for ^{12}C , $A_{\text{LU}}(\phi = 90^\circ)$, as a function of $|t|$ at $Q^2 = 4 \text{ GeV}^2$ and $x = 10^{-3}$.

The DVCS beam-spin asymmetry enhances and accesses the imaginary part of the DVCS amplitude. Its real part can be probed by considering the DVCS asymmetry measured with the lepton beams of opposite signs (the beam-charge asymmetry) or by studying

the ϕ -angle modulation of the unpolarized cross section. While the imaginary part of the DVCS amplitude accesses GPDs at the $x = \xi$ cross-over line, see Eq. (210), the real part involves the GPDs in the entire region of x , and, hence, is sensitive to the whole host of nuclear effects (shadowing, antishadowing, EMC-type suppression, etc.). The pattern of nuclear modifications of the real part of the nuclear DVCS amplitude is quite different from the one for the imaginary part; it was presented and discussed in Refs. [29,30].

Comment. The differential measurements of coherent nuclear DVCS for small t appear very challenging since the final nucleus is emitted at very small angles. At the same time, it is possible to suppress the inelastic contribution (at least for the heavy nuclei) in the collider kinematics since the break-up of the nucleus is accompanied by the emission of neutrons which are easily detected by a zero-degree calorimeter.

6.2.4 Predictions for the ratio of vector meson (J/ψ , Υ) production

In the leading twist approach to hard exclusive processes, exclusive electroproduction of heavy vector mesons (J/ψ , Υ) with nuclear targets probes the nuclear gluon GPD. Similarly to the case of DVCS discussed above, at high energies, the theoretical description can be simplified and the answer is expressed in terms of the usual nuclear gluon PDF. In particular, in the leading logarithmic approximation, the cross section for coherent production of longitudinally polarized vector mesons in the $t = 0$ limit reads [194]:

$$\frac{d\sigma_{\gamma_L^* A \rightarrow VA}}{dt} \Big|_{t=0} = \frac{4\pi^3 \Gamma_V M_V}{3\alpha_{\text{em}} Q^6} \eta_V^2 T(Q^2) |1 + i\beta|^2 \alpha_s(Q^2) [xg_A(x, Q^2)]^2, \quad (214)$$

where Γ_V is the $V \rightarrow e^+e^-$ decay width; M_V is the vector meson mass; β is the ratio of real to imaginary parts of the $\gamma^* A \rightarrow VA$ scattering amplitude; the factor $T(Q^2)$ accounts for pre-asymptotic effects, i.e., $T(Q^2 \rightarrow \infty) = 1$. The parameter η_V is defined in terms of the $q\bar{q}$ component of the vector meson light-cone wave function, $\Phi_V^{q\bar{q}}$,

$$\eta_V = \frac{1}{2} \frac{\int \frac{dz d^2 k_t}{z(1-z)} \Phi_V^{q\bar{q}}(z, k_k)}{\int dz d^2 k_t \Phi_V^{q\bar{q}}(z, k_k)}. \quad (215)$$

In the ratio of the vector meson production on the nucleus and the free proton, all fine details of Eq. (214) to a good accuracy cancel and one obtains:

$$R_{\text{VM}} \equiv \frac{d\sigma_{\gamma_L^* A \rightarrow VA}/dt(t=0)}{A^2 d\sigma_{\gamma_L^* N \rightarrow VN}/dt(t=0)} = \left(\frac{g_A(x, Q^2)}{A g_N(x, Q^2)} \right)^2. \quad (216)$$

Therefore, the ratio R_{VM} is a sensitive direct measure of the effects of nuclear shadowing and antishadowing in the nuclear gluon distribution. We neglected here the effect of

skewness which can be accounted for by substituting x in Eq. (216) by x_+ . The ratio $r = x_+/x$ depends on Q^2 and the mass of the produced vector meson. For example, for the photoproduction of J/ψ , $r \approx 1$ and it slowly decreases with Q^2 to $r \approx 1/2$, while for the Υ case, $r \sim 1/2$ already for $Q^2 = 0$ [234].

Figure 88 presents our predictions for the ratio $R_{\text{VM}} = [g_A(x, Q^2)/(A g_N(x, Q^2))]^2$ as a function of x for $Q^2 = 4$ and 10 GeV^2 . The shaded bands reflect the theoretical uncertainty of our predictions: the lower boundaries of the bands correspond to model FGS10.H; the upper boundaries correspond to model FGS10.L. As one can see from Fig. 88, the suppression of R_{VM} for small x due to nuclear shadowing and the enhancement around $x \approx 0.1$ due to antishadowing are very significant.

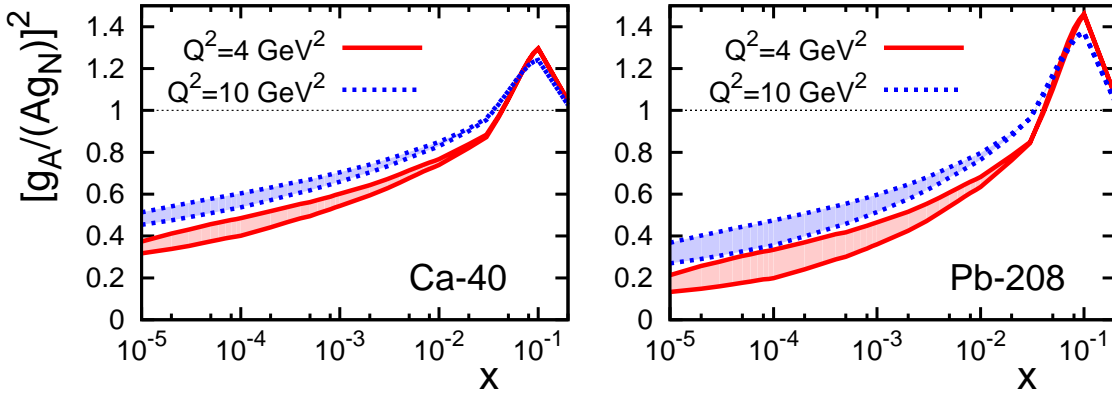


Fig. 88. The ratio $R_{\text{VM}} = (g_A(x, Q^2)/[A g_N(x, Q^2)])^2$ as a function of x at $Q^2 = 4 \text{ GeV}^2$ (solid curves) and $Q = 10 \text{ GeV}^2$ (dotted curves). The shaded bands reflect the theoretical uncertainty of our predictions.

Since the t dependence of the nuclear gluon distribution is known, one can also study the t dependence of hard exclusive heavy vector meson production. Again, it is convenient to present the results in terms of the ratio of the production on the nucleus and on the nucleon, $R_{\text{VM}}(t)$:

$$R_{\text{VM}}(t) \equiv \frac{d\sigma_{\gamma_L^* A \rightarrow VA}/dt}{A^2 d\sigma_{\gamma_L^* N \rightarrow VN}/dt} \approx \frac{d\sigma_{\gamma_L^* A \rightarrow VA}/dt}{A^2 d\sigma_{\gamma_L^* N \rightarrow VN}/dt(t=0)} = \left(\frac{g_A(x, Q^2, t)}{A g_N(x, Q^2)} \right)^2, \quad (217)$$

where $g_A(x, Q^2, t) = H_A^g(x, \xi = 0, t, Q^2)$ given by Eq. (197). Note that in Eq. (217), we neglected the weak t dependence of the nucleon gluon GPD compared to that of the nucleus one and assumed that the entire t dependence comes from the gluon nuclear GPD. The latter is a good approximation for heavy nuclei.

Figure 89 presents our predictions for the ratio $R_{\text{VM}}(t)$ of Eq. (217) for ^{208}Pb as a function of $|t|$ at $Q^2 = 4$ and 10 GeV^2 and $x = 10^{-3}$ and $x = 5 \times 10^{-3}$. The shaded bands (barely distinguishable at the given scale along the y -axis) span the predictions for the gluon nuclear shadowing made using models FGS10.H and FGS10.L. One can see from Fig. 89

that the Q^2 and x dependence of $R_{VM}(t)$ is rather weak. Also, the t behavior of $R_{VM}(t)$ is very similar to that of $d\sigma_{DVCS}/dt$ in Fig. 85; the difference is that $R_{VM}(t)$ probes the gluon nuclear GPD, while $d\sigma_{DVCS}/dt$ probes the quark nuclear GPDs. Since the effect of shadowing is larger in the gluon channel, the shift of the positions of the minima toward smaller t of $d\sigma_{\gamma_L^*A\rightarrow VA}/dt$ with respect to the impulse approximation is larger than the shift between the coherent nuclear DVCS and BH cross sections presented in Fig. 85.

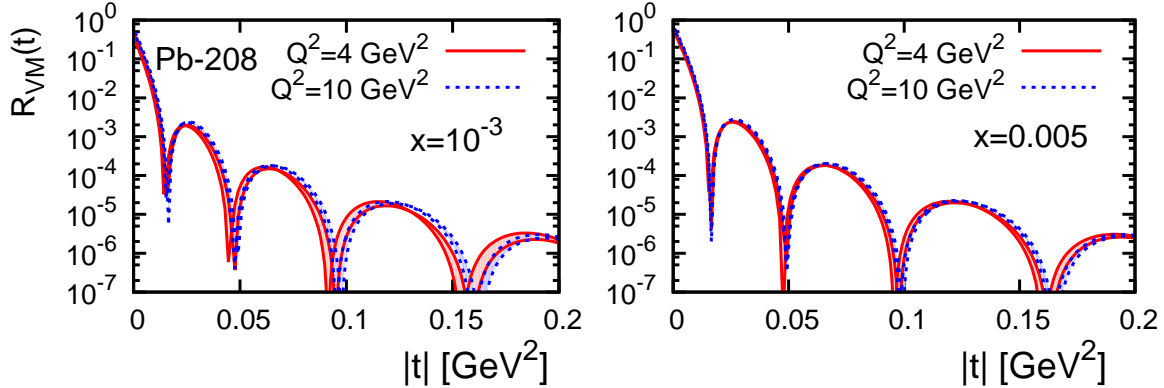


Fig. 89. The ratio $R_{VM}(t) = (g_A(x, Q^2, t)/[Ag_N(x, Q^2)])^2$ of Eq. (217) as a function of $|t|$ at $Q^2 = 4$ and 10 GeV^2 and $x = 10^{-3}$ and $x = 5 \times 10^{-3}$. The shaded bands reflect the theoretical uncertainty of our predictions.

Photoproduction of J/ψ on nucleons and nuclei in the dipole formalism was discussed in [235]. It was suggested that high precision measurement of the transverse momenta of J/ψ would allow one to determine the t dependence of the $\gamma+A \rightarrow J/\psi+A$ amplitude and, hence, determine the transverse distribution of gluons in nuclei using a Fourier transform of the amplitude. Unfortunately the processes $\gamma+A \rightarrow J/\psi+A^*$, where A^* denotes excited nuclear states which decay into the ground state and a photon (photons), dominate the cross section beyond the first minimum making it very difficult to observe the coherent channel beyond the first minimum [236]. At the same time, if the precision measurements of the t dependence at $t \sim 0$ are feasible, it would be possible to check the change of the t slope as compared to the impulse approximation, which we find to be of the order of $10 - 15\%$ depending on x , see the discussion of $\langle b^2 \rangle$ in Sec. 5.6.

Comment. In this section, we estimated the ratio of the vector meson production on the nucleus and the free proton, R_{VM} , using next-to-leading order (NLO) nuclear and proton gluon distributions, where the latter was given by the CTEQ5M fit. Our estimate is subject to several theoretical uncertainties including (i) the implementation of the effect of skewness, and (ii) the uncertainty in the choice of a parameterization of the gluon distribution in the free proton. Our initial analysis shows that the latter uncertainty dominates. Moreover, while the relevant formulas were derived in the leading-order (LO) approximation, we assumed that the form of the expression for R_{VM} is the same in the NLO approximation. Hence, we used the NLO CTEQ5M parameterization for the gluon density which corresponds to the energy-dependence of the cross section of electroproduction

of vector mesons on a nucleon which is close to the experimentally observed one.

6.3 Nuclear effects in inclusive leading hadron spectra in eA collisions

Numerous data on hadron-nucleus scattering at fixed-target energies indicate that the multiplicities of leading hadrons, $N_A(z)$,

$$N_A(z) \equiv \frac{1}{\sigma_{\text{inel}}(aA)} \frac{d\sigma(z)^{a+A \rightarrow h+X}}{dz}, \quad (218)$$

strongly decrease with an increase of A . In definition (218), z is the light-cone fraction of the projectile “ a ” momentum carried by hadron “ h ”. On the contrary, for inclusive hadron production in DIS, the QCD factorization theorem implies that no such dependence should be present in the kinematics where the leading twist contribution dominates. This indicates that there should be an interesting transition from the soft physics dominating the interactions of real photons with nuclei to the hard physics in the inclusive hadron production in the DIS kinematics. (At sufficiently high energies, the transition to the leading twist regime will be delayed by the presence of a significant Q^2 range, where the interaction is close to the black disk limit—see the discussion in Sec. 8.) The transition between the soft and hard regimes should be manifested in the disappearance of the A dependence of the leading spectra at large z :

$$N_A(z, Q^2) = N_N(z, Q^2), \text{ for } z \geq 0.2, Q^2 \geq \text{few GeV}^2. \quad (219)$$

At small x , a new interesting phenomenon should emerge in DIS within the LT approximation because of the presence of diffraction and nuclear shadowing for smaller z . Indeed, diffraction originates from the presence of partons with relatively small virtualities in the γ^* wave function, which screen the color of the leading parton(s) with large virtualities and can rescatter elastically from the target (several target nucleons in the case of a nuclear target). Inelastic interactions of these soft partons with several nucleons should lead to a plenty of new revealing phenomena in small- x eA DIS, which resemble hadron-nucleus scattering, but with a shift in the rapidity from y_{max} (current). (It is important that far from the BDR, the pQCD part is not shadowed.) This shift can be expressed through the average masses of the hadron states produced in the diffraction:

$$y_{\text{soft partons}} \sim y_{\text{max}} - \ln \left(\langle M_X^2 \rangle / \mu^2 \right), \quad (220)$$

where $\mu \sim 1$ GeV is the typical soft QCD scale. In the notation used for diffraction in DIS, one has $\langle M_X^2 \rangle = Q^2 \langle (1/\beta - 1) \rangle$, where β is the light-cone fraction of the interacting parton with respect to the Pomeron exchange, see Eq. (84). Using the information on the

β distributions measured at HERA (2006 H1 fit B [61]), one concludes that for moderate Q^2 , $\langle M_X^2 \rangle \sim 3 Q^2$. Note also that the values of $\langle M_X^2 \rangle$ are different for the quark and gluon channels: $\langle M_X^2 \rangle \sim 2 Q^2$ for the quarks and $\langle M_X^2 \rangle \sim 6 Q^2$ for the gluons.

The partons with the rapidities given by Eq. (220) interact in multiple collisions and lose their energy, which leads to a dip in the ratio $\eta_A(y) \equiv N_A(y)/N_p(y)$. At the same time, these multiple interactions should generate larger multiplicities at smaller rapidities. The application of the Abramovsky-Gribov-Kancheli (AGK) rules [119] indicates that for $y \leq y_{\text{soft partons}} - \Delta$, where $\Delta = 2 - 3$, the hadron multiplicity in the case of DIS off nuclei will be enhanced by the factor $\eta_A(y)$:

$$\eta_A(y) = \frac{AF_{2N}(x, Q^2)}{F_{2A}(x, Q^2)} \equiv \frac{A}{A_{\text{eff}}}. \quad (221)$$

One should note that this estimate neglects the effects of the energy conservation and the increase of multiplicities at central rapidities with an increase of W . In the case of deuteron-gold collisions, the observed increase of multiplicity is smaller than that given by the AGK rules by a factor of 0.7, cf. the discussion in Ref. [237], which is in line with the account of energy-momentum conservation.

At the rapidities close to the nuclear rapidities, a further increase of $\eta_A(y)$ is possible because of the formation of hadrons inside the nucleus. A sketch of the expected rapidity dependence of $\eta_A(y)$ is presented in Fig. 90.

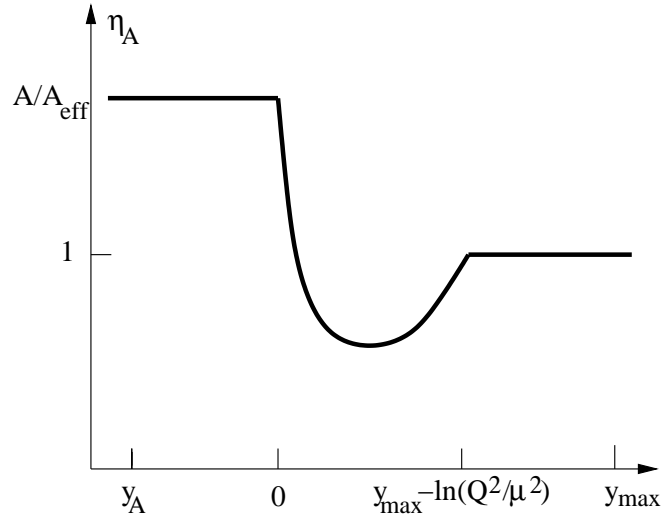


Fig. 90. A sketch of the ratio of the nuclear to free proton hadron multiplicities, $\eta_A(y) = N_A(y)/N_p(y)$ as a function of the hadron rapidity.

The discussed phenomenon should be more pronounced for collisions at central impact parameters leading to a correlation between the number of particles produced in the nucleus fragmentation region and the depletion at the rapidities given by Eq. (220).

With an increase of Q^2 at fixed x , an increasingly larger fraction of collisions occurs due to the scattering off the partons that had large enough x at the initial Q^2 scale where nuclear shadowing is absent. For these events, multiple interactions are absent and do not contribute significantly to the processes where several nucleons of the nucleus are wounded. Hence, though the fraction of the events with long-range correlations described above should drop with Q^2 similarly to the decrease of the overall shadowing effect, the strength of the correlations in the events, where several nucleons are wounded, would remain strong.

6.4 Hadron production at central rapidities

We discussed in Sec. 2.4 that the application of the AGK cutting rules allows one to write the inelastic (non-diffractive) cross section as a sum of the positive cross sections with exactly j nucleons involved in the inelastic interactions, σ_j , see Eq. (28). In the approximation when the fluctuations of the effective rescattering cross section σ_X are neglected, the probability of the interaction with j nucleons is [120] [see Eq. (28)]:

$$p_j \equiv \frac{\sigma_j}{\sigma_{\text{summed}}^{hA,\text{inel}}} = \frac{\frac{A!}{(A-j)!j!} \int d^2b [x(b)]^j [1-x(b)]^{A-j}}{\int d^2b [1-(1-x(b))^A]}, \quad (222)$$

where $x(b) = \sigma_X^{\text{inel}} T_A(b)$; σ_X^{inel} is the non-diffractive component of σ_X , which is given by Eq. (180); $T_A(b)$ is the nuclear optical density. To account for the fluctuations of σ_X^{inel} , one would have to add the integral over σ_X^{inel} with the measure $P(\sigma_X^{\text{inel}})$ both in the numerator and denominator of Eq. (222). This would obviously lead to a broader distribution over the number of "wounded" nucleons (see below).

The average number of the "wounded" nucleons, $\nu = \sum_{n=1}^A j p_j$, satisfies the relation which is an example of the so-called AGK cancellation [120],

$$\nu \equiv \sum_{n=1}^A j p_j = \frac{A \sigma_X^{\text{inel}}}{\int d^2b [1-(1-x(b))^A]}, \quad (223)$$

where the denominator has the meaning of the inelastic cross section for the interaction of the diffractive configuration, $\sigma_{\text{summed}}^{hA,\text{inel}}$. Since the fraction of diffractive events (which also include the processes with the break-up of the nucleus) in eA scattering is larger than in eN scattering, the number of wounded nucleons ν is somewhat larger than the $A \sigma_{\text{tot}}^{\gamma^* N} / \sigma_{\text{tot}}^{\gamma^* A}$ ratio.

In addition, one also expects a number of phenomena resulting from the existence of the long-range correlations in rapidity. These include:

(a) Local fluctuations of the multiplicity in the central rapidity region, e.g., the observation of a broader distribution of the number of particles per unit of rapidity due to the fluctuations of the number of wounded nucleons [212]. These fluctuations should be larger for the hard processes induced by gluons, for example, for the direct photon production of two high p_t dijets.

(b) The correlation of the central multiplicity with the multiplicity of neutrons in the forward neutron detector.

To illustrate the effect of the broadening of the distribution over multiplicities, we calculate the A dependence of the multiplicity distribution for a fixed rapidity range. We use the H1 analysis of charged particle multiplicities in DIS at HERA in the pseudorapidity range $1 \leq \eta^* \leq 2$ for events without rapidity gaps [238]. The multiplicity distribution is characterized by the probabilities to produce n particles, P_n , which can be described by the negative binomial distribution:

$$P_n(k, \langle n \rangle) = \frac{k(k+1) \dots (k+n-1)}{n!} \left(\frac{\langle n \rangle}{\langle n \rangle + k} \right)^n \left(\frac{k}{\langle n \rangle + k} \right)^k. \quad (224)$$

In Eq. (224), $\langle n \rangle$ is the average multiplicity; the parameter k characterizes the dispersion of the distribution over P_n . Both $\langle n \rangle$ and k are found from fitting to the data. In particular, for the H1 data [238] and for $1 \leq \eta^* \leq 2$ and $80 \leq W \leq 115$ GeV, $\langle n \rangle = 2.52 \pm 0.10$ and $1/k = 0.285 \pm 0.080$.

The probabilities P_n can also be described using the generating function $G(z)$,

$$G(z) = [1 + r(1-z)]^{-k} \equiv \sum_{n=0}^{\infty} P_n(k, \langle n \rangle) z^n, \quad (225)$$

where $r = \langle n \rangle / k$.

To estimate the probabilities P_n for nuclear targets, one notices that the generating function for the production of particles in the interaction with m nucleons, $G_m(z)$, is simply given by

$$G_m(z) = [G(z)]^m. \quad (226)$$

Therefore, the probability to produce n particles in lepton-nucleus DIS, P_n^A , can be introduced by the following relation,

$$G_m(z) = [1 + r(1-z)]^{-km} \equiv \sum_{n=0}^{\infty} P_n^A(k', \langle n' \rangle) z^n, \quad (227)$$

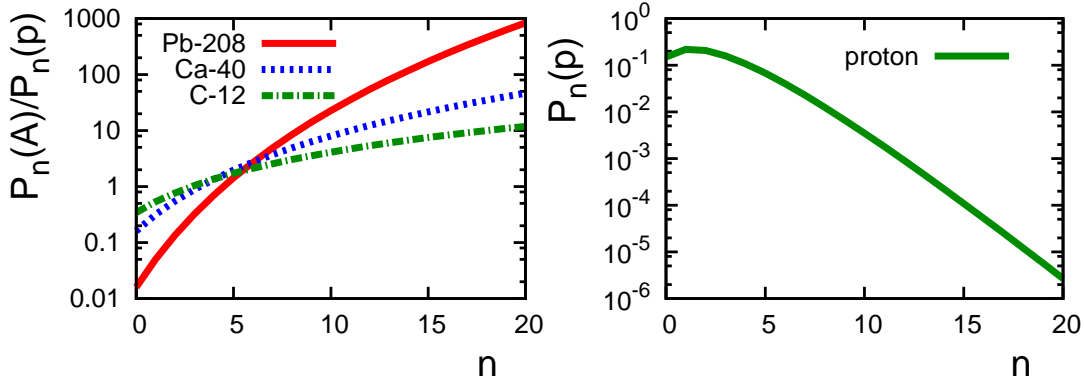


Fig. 91. The multiplicity distributions of Eqs. (222)-(227) as a function of the number of produced particles n . Left panel: The ratio of the nucleus to proton probabilities P_n^A/P_n as a function of n . Right panel: The absolute value of the free proton P_n as a function of n . The curves correspond to the fixed pseudorapidity interval $1 \leq \eta^* \leq 2$, $Q^2 = 4 \text{ GeV}^2$ and $x \sim 10^{-3}$.

where $k' = mk$ and $\langle n' \rangle = m\langle n \rangle$. As follows from Eq. (227), the explicit expression for P_n^A is given by Eq. (224) after the replacement $k \rightarrow mk$ and $\langle n \rangle \rightarrow m\langle n \rangle$.

In our numerical analysis, we neglected the fluctuations in the number of the nucleons participating in the particle production and used $m = \nu$, where ν is the average number of the wounded nucleons given by Eq. (223). To evaluate ν , we used $\sigma_X^{\text{inel}} = 24 \text{ mb}$ [see Eq. (180)], which corresponds to $\sigma_{\text{soft}}^{q(\text{H})} = 29 \text{ mb}$ (the effective rescattering cross section in the sea-quark channel, model FGS10_H) at $Q^2 = 4 \text{ GeV}^2$ and $x \sim 10^{-3}$. This value of Bjorken x approximately corresponds to the kinematics of the H1 analysis of P_n in the ep case discussed above [238].

The results of the calculation of the multiplicity distributions for events without rapidity gaps using Eqs. (222)-(227) are presented in Fig. 91. In the left panel of the figure, we examine the A dependence and plot the ratio of the nucleus to proton probabilities P_n^A/P_n as a function of n . One can see from Fig. 91 that a much broader distribution over multiplicity is predicted for heavy nuclei. Measurements of such distributions would serve as a complementary (to the measurement of the diffractive cross sections) probe of the dynamics of nuclear shadowing. While the nuclear enhancement of P_n^A/P_n for large n is very large, the absolute value of the probabilities is tiny. It is illustrated in the right panel of Fig. 91 where we plot the free proton P_n as a function of n .

With an increase of Q^2 , the pattern of fluctuations in the number of collisions will become more involved since the fluctuations of σ_X^{inel} should increase because of the mixing of the unshadowed and shadowed contributions. This will effectively correspond to the presence of the fluctuations with both small and large cross sections, $\sigma_X^{\text{inel}} \sim 0$ and $\sigma_X^{\text{inel}} \sim \sigma_{\text{inel}}^X(Q_0^2)$, respectively.

The results of the calculation of the fraction of events with enhanced central multiplicities that we just discussed should be considered as an estimate only. The eikonal formulas do

not properly take into account the energy-momentum conservation. In particular, quark-gluon configurations of the projectile propagating through the nucleus are counted n -times in the n -"Pomeron" cuts. Since the multiplicity in the central region depends on energy, accounting for this effect would lead to some suppression of events with double, triple and higher multiplicity.

Another effect neglected in our analysis is the gluon radiation by a quark propagating through the nuclear medium. It is a relatively small effect in the leading twist approximation, for a review, see Ref. [239]. However, with the onset of the black disk regime, the pattern changes quite strongly, see the discussion in Sec. 8.

7 Leading twist nuclear shadowing and suppression of hard coherent diffraction in proton-nucleus scattering

In the last two decades intensive studies of hard processes with rapidity gaps were performed at $p\bar{p}$ colliders at CERN and FNAL, for a review, see Ref. [240]. These processes are usually referred to as hard diffractive processes. Examples of such types of processes studied at the Tevatron include the production of two jets, Z , and W bosons in the reaction

$$p + \bar{p} \rightarrow 2 \text{jets} (Z, W, \dots) + X + \text{gap} + p. \quad (228)$$

The probability of the presence of rapidity gaps in the events with hard subprocess, P_{gap} , is rather small. At the Tevatron, applying a cut on Feynman x of the recoiled proton, $x_F(p) \geq 0.93$, one finds that $P_{\text{gap}} \approx 0.01$ [240,241]. (The cross section of each hard diffractive channel constitutes approximately 1% of the contribution of the corresponding channel to the inclusive $p\bar{p}$ cross section.) In such processes, multiple soft and hard interactions are not suppressed and the QCD factorization theorem, which is valid for hard diffraction in DIS [59], is not applicable. Hence, one expects a strong suppression of P_{gap} compared to the naive application of the QCD factorization theorem with the diffractive PDFs measured at HERA. Qualitatively, the breakdown of factorization is due to the dominance of small impact parameters in the diffractive PDFs and nearly 100% absorption in pp scattering at such impact parameters. The magnitude of the suppression—a factor of $5 \div 10$ —is in agreement with such expectations, see e.g., the discussion in Ref. [242]. The factorization breaking can also be explained by the absorptive effects associated with multi-Pomeron exchanges that make the gap survival very unlikely in the case of hadronic collisions [243].

Since we developed the theory of nuclear diffractive PDFs (see Sec. 6), we can make predictions for the rates of the pA reaction analogous to the elementary reaction in Eq. (228):

$$p + A \rightarrow 2 \text{jets} (Z, W, \dots) + X + \text{gap} + A. \quad (229)$$

This involves the combination of the effects of soft absorption in pA scattering and the model of the diffractive PDFs as well as the use of the leading twist theory of nuclear shadowing. Using hard coherent production of two jets in proton-nucleus scattering as an example, we demonstrate that soft multiple rescatterings lead to the factorization breaking of hard diffraction in proton-nucleus scattering which is larger than that in hadron-nucleon scattering. We also compare the hard diffractive and electromagnetic (ultraperipheral) mechanisms of the reaction (229) in the RHIC and LHC kinematics and make quantitative estimates of the feasibility to study the high-energy real photon-proton scattering at RHIC and the LHC. Numerical results presented in this section update the results of our earlier work on this subject [211].

7.1 *Soft coherent diffraction off nuclei*

Before proceeding to calculate the gap survival probability, we need to briefly review main elements of the theory of inelastic coherent diffraction off nuclei. The Gribov formalism does not make specific predictions for this process as it requires a more detailed information about the hadron-multi-Pomeron vertices.

To address this problem one can use the concept of color fluctuations which we already discussed in the context of multiple rescatterings in the calculation of nuclear PDFs, see Sec. 5. One introduces a distribution over the strength of interactions in the projectile h , $P_h(\sigma)$. The probability $P_h(\sigma)$ is constrained by the following relations:

$$\begin{aligned} \int d\sigma P_h(\sigma) &= 1, \\ \int d\sigma \sigma P_h(\sigma) &= \sigma_{\text{tot}}, \\ \omega_\sigma &\equiv \frac{\int d\sigma \sigma^2 P_h(\sigma)}{[\int d\sigma \sigma P_h(\sigma)]^2} - 1 = \frac{d\sigma(h+p \rightarrow M_X + p)/dt}{d\sigma(h+p \rightarrow h+p)/dt}(t=0). \end{aligned} \quad (230)$$

In Eq. (230), the first line is the probability conservation sum rule; the second line is the relation to the total cross section; the third line is the relation between the parameter ω_σ that characterizes the dispersion of the distribution $P_h(\sigma)$ and the ratio of the differential and elastic cross sections. In addition, pQCD constrains the $\sigma \rightarrow 0$ behavior of $P(\sigma)$. This information and Eq. (230) in combination with the information on coherent inelastic diffraction in hadron-deuteron scattering allows one to reconstruct $P_h(\sigma)$ for hadron-proton interactions.

Using the color fluctuation formalism it is possible to derive the expression for the cross

section of inelastic coherent diffraction off nuclei (diffractive dissociation) [74,133,134,244]:

$$\sigma_{DD}^{hA} = \int d^2 b \left(\int d\sigma P_h(\sigma) |\Gamma_A(b, \sigma)|^2 - \left| \int d\sigma P_h(\sigma) \Gamma_A(b, \sigma) \right|^2 \right). \quad (231)$$

In Eq. (231), b is the impact parameter; $\Gamma_A(b, \sigma)$ is the amplitude of interaction of the projectile in the configuration with the cross section σ with the nucleus at the impact parameter b , cf. [245]:

$$\Gamma_A(b, \sigma) = 1 - \exp\left(-\frac{A}{2} \sigma T_A(b)\right), \quad (232)$$

where $T_A(b) = \int dz \rho_A(b, z)$ and ρ_A is the nuclear density normalized to unity. The energy-dependence of σ_{DD}^{hA} is determined by the energy-dependence of $P_h(\sigma)$, which is modeled based on the available experimental information and extrapolations to the LHC energies [134]. Note that in Eq. (232), we neglected the slope of the elementary hadron-nucleon scattering amplitude compared to the slope of the nuclear form factor and assumed that the elementary scattering amplitude is purely imaginary, which is a good approximation at high energies. Calculations based on Eq. (232) describe well the data on the coherent diffraction at the fixed-target energies, which are unfortunately rather limited, see Ref. [75] for a review.

The notion of $P_h(\sigma)$ provides a compact phenomenological description of soft coherent diffraction in hadron-nucleon and hadron-nucleus scattering. The function $P_h(\sigma)$ describes the probability that the incoming hadron interacts with target nucleons with a given cross section σ . In other words, $P_h(\sigma)$ describes cross section fluctuations in the energetic projectile. As follows from Eq. (231), ignoring cross section fluctuation, i.e., setting $P_h(\sigma) \propto \delta(\sigma - \sigma_{\text{tot}})$, would result in the unphysical result $\sigma_{DD}^{hA} = 0$ that once again illustrates that diffraction is not possible without fluctuations of the strength of the interaction.

The formalism of cross section fluctuations is rather general and is based on the space-time picture of the strong interaction that we discussed in Sec. 2.1. In this picture, the incoming hadron is represented by a coherent superposition of eigenstates of the scattering operator. Since different eigenstates correspond to different σ , the scattered state is in general different from the incoming state, but it has the same quantum numbers. This corresponds to the process of diffractive dissociation. We also used the formalism of cross section fluctuations in our analysis of nuclear shadowing in eA DIS in Sec. 3 and 5.

One should note that the formalism of cross section fluctuations implicitly uses the assumption of the completeness of the scattering eigenstates and, hence, it is applicable only at $t \approx 0$. At $t \neq 0$, the diffractive final state can be produced as a result of the elastic scattering of a constituent of the projectile off the target even if there are no fluctuations

of the strength of the projectile-target interaction. A simple example is scattering of the deuteron off the proton target in the impulse approximation. For $t = 0$, the cross section of the process ${}^2H p \rightarrow pnp$ is equal to zero due to orthogonality of the 2H and continuum wave functions, while for finite t , the cross section is $\propto 1 - F_D^2(t)$, where $F_D(t)$ is the deuteron form factor.

The function $P_h(\sigma)$ is different for different projectiles: protons, pions, photons. (The pion case was considered in Sec. 5.1.2.) In the case of the proton projectiles (especially at the collider energies), $P_h(\sigma)$ has a narrow dispersion around $\langle\sigma\rangle = \sigma_{\text{tot}}$, where σ_{tot} is the total proton-nucleon cross section. Hence, a good approximation to Eq. (231) can be given in the following form:

$$\sigma_{DD}^{hA} \approx \frac{\omega_\sigma \sigma_{\text{tot}}^2 A^2}{4} \int d^2b T_A^2(b) e^{-A\langle\sigma\rangle T(b)}. \quad (233)$$

Equation (233) can be interpreted as follows. Since the fluctuations are small, we need to take them into account only in the interaction with one of the nucleons at a given impact parameter b . The corresponding scattering amplitude squared (in the impact parameter space) is proportional to $A^2 \omega_\sigma \sigma_{\text{tot}}^2 T_A^2(b)$. On the way through the nucleus, the fluctuation is partially absorbed (suppressed) with the $\langle\sigma\rangle = \sigma_{\text{tot}}$ characteristic cross section. The corresponding soft suppression factor can be read off directly from Eq. (233):

$$T_{\text{soft}}^{pA} = \exp(-A\sigma_{\text{tot}} T_A(b)). \quad (234)$$

One can see from Eq. (231) that only scattering off the periphery of the nucleus contributes to the cross section of diffraction. Numerical results indicate a strong drop of soft diffraction with an increase of energy as a result of the decrease of cross section fluctuations (dispersion ω_σ). For instance, ω_σ decreases from $\omega_\sigma = 0.15$ at the Tevatron energies ($\sqrt{s} = 546$ and 1800 GeV) to $\omega_\sigma = 0.1$ at pA scattering energies at the LHC ($\sqrt{s} \approx 9$ TeV) and further down to $\omega_\sigma = 0.065$ at pp scattering energies at the LHC ($\sqrt{s} = 14$ TeV) [134].

7.2 Hard coherent diffraction in pA scattering

In the case of hard coherent pA diffraction, we need to take into account two effects: the reduction of the soft diffraction due to the suppression of the fluctuations in a wide range of impact parameters and the reduction of the nuclear diffractive PDFs due to the shadowing effects which we discussed in Sec. 6. The soft suppression factor, T_{soft}^{pA} , should be compared to the factor that suppresses hard coherent diffraction in γ^*A DIS. Let us recall Eq. (171) that expresses the nuclear diffractive PDF $f_{j/A}^{D(3)}$ in the very high-energy limit, which allows one to neglect the effect of the finite coherence length. Equation (171) can

be interpreted as follows. The incoming virtual photon fluctuates into its hard diffractive component long time before the photon interacts with the target. The hard diffractive component elastically rescatters on the target nucleus, which gives the suppression factor $[1 - \exp(-\frac{A}{2}\sigma_{\text{soft}}^j(x, Q^2) T_A(b))]^2$, and emerges as the final hard diffractive state. (Remember that $\sigma_{\text{soft}}^j(x, Q^2)$ describes the strength of the interaction of the configurations which are involved in the hard diffraction in DIS.) Note that we set $\eta = 0$ in Eq. (171) to be consistent with our discussion of soft diffraction.

It is important to note that the expression for $f_{j/A}^{D(3)}$ in Eq. (171) corresponds to diffractive dissociation of the virtual photon [the corresponding expression for the hadron-nucleus case is given by Eq. (233)] since the elastic contribution to DIS is absent (suppressed by the smallness of $\alpha_{\text{e.m.}}$). Therefore, the analogy between Eqs. (233) and (171) enables us to introduce the attenuation factor characterizing the suppression of hard coherent diffraction in DIS on nuclear targets due to the effect of nuclear shadowing (multiple interactions with the target nucleons),

$$T_{\text{hard}}^{\gamma^*j/A} = \exp\left(-A\sigma_{\text{soft}}^j(x, Q) T_A(b)\right). \quad (235)$$

As we discussed in Sec. 3.1, in general, the calculation of $T_{\text{hard}}^{\gamma^*j/A}$ is model-independent only for the interaction with two nucleons. For the interaction with $N \geq 3$ nucleons, we implicitly used the color fluctuation approximation in Eq. (235). This approximation is equivalent to the observation of the small dispersion of $P_h(\sigma)$ used in the derivation of Eq. (233), see details in Sec. 3.1, and takes into account the presence of the point-like configurations in the interaction of a hard probe with the nucleon which contribute to the total cross section but not to the diffractive cross section.

7.3 *Suppression factor for hard proton-nucleus coherent diffraction*

As an example of the hard coherent diffractive process on heavy nuclear targets, we consider the hard coherent diffractive production of two jets in the reaction $p + A \rightarrow 2\text{jets} + X + A$. In this process, A denotes the nucleus; X denotes the soft diffractive component; the invariant mass of the jets provides the hard scale.

The $p + A \rightarrow 2\text{jets} + X + A$ cross section can be readily obtained by generalizing the well-known expression for the dijet inclusive cross section in hadron-hadron scattering [246] and by introducing the new quantity, the screened nuclear diffractive PDFs $\tilde{f}_{j/A}^{D(3)}$:

$$\frac{d^3\sigma^{p+A\rightarrow 2\text{jets}+X+A}}{dx_1 dp_T^2 dx_P} \propto \sum_{i,j,k,l=q,\bar{q},g} f_{i/p}(x_1, Q_{\text{eff}}^2) \tilde{f}_{j/A}^{D(3)}(x_2, Q_{\text{eff}}^2, x_P) \overline{\sum} |\mathcal{M}(ij \rightarrow kl)|^2 \frac{1}{1 + \delta_{kl}}, \quad (236)$$

where $f_{i/p}$ are the usual proton PDFs; $\overline{\sum} |\mathcal{M}(ij \rightarrow kl)|^2$ are the invariant matrix elements for two-to-two parton scattering given in Table 7.1 of [246]; x_1 and x_2 are the light-cone momentum fractions of the active quarks of the proton and the nucleus, respectively; p_T is the transverse momentum of each of the jets in the final state; Q_{eff}^2 is the effective hard scale of the process. For the simplification of our analysis, we consider only the case of the 90° hard parton scattering in the center of mass frame, which constrains x_1 (as a function of $x_2 = \beta x_P$) and Q_{eff}^2 :

$$x_1 = \frac{4p_T^2}{\beta x_P s}, \quad Q_{\text{eff}}^2 = 4p_T^2, \quad (237)$$

where \sqrt{s} is the proton-nucleon invariant mass. The term "screened PDF" means that this parton distribution contains certain soft suppression effects, i.e., the screened PDF is suppressed compared to the analogous PDF extracted from hard processes.

The derivation of the expression for the screened nuclear diffractive PDFs, $\tilde{f}_{j/A}^{D(3)}$, is carried out similarly to the derivation of Eq. (233), see also Fig. 92. The final expression reads:

$$\begin{aligned} \tilde{f}_{j/A}^{D(3)}(x, Q^2, x_P) &= 4\pi A^2 \tilde{f}_{j/N}^{D(4)}(x, Q^2, x_P, t_{\min}) \int d^2b T_A^2(b) e^{-A(\sigma_{\text{tot}}(s) + \sigma_{\text{soft}}^j(x, Q^2))T_A(b)} \\ &= 4\pi A^2 B_{\text{diff}} \tilde{f}_{j/N}^{D(3)}(x, Q^2, x_P) \int d^2b T_A^2(b) e^{-A(\sigma_{\text{tot}}(s) + \sigma_{\text{soft}}^j(x, Q^2))T_A(b)}, \end{aligned} \quad (238)$$

where $\tilde{f}_{j/N}^{D(4)}$ is the screened diffractive PDF of the nucleon, which enters the QCD description of the $p + p \rightarrow 2\text{jets} + X + p$ reaction [see Eqs. (239) and (241) and their discussion below]; $\sigma_{\text{tot}}(s)$ is the total proton-nucleon cross section. In Eq. (238), we neglected the slope and the real part of the elementary $p + N \rightarrow 2\text{jets} + X + N$ scattering amplitude and a small longitudinal momentum transfer in the $p + N \rightarrow 2\text{jets} + X + N$ vertex. In the second line of Eq. (238), we assumed that the t dependence of the screened diffractive PDFs is the same as that of the usual ones, see Eq. (92) and used the following relation:

$$\tilde{f}_{j/N}^{D(4)}(x, Q^2, x_P, t_{\min}) = B_{\text{diff}} \tilde{f}_{j/N}^{D(3)}(x, Q^2, x_P). \quad (239)$$

For comparison with the nuclear case [see Eq. (236)], we also present the cross section of the hard coherent diffractive dijet production in proton-proton scattering:

$$\begin{aligned}
& \frac{d^3 \sigma^{p+p \rightarrow 2 \text{jets} + X+p}}{dx_1 dp_T^2 dx_{\mathcal{P}}} \\
& \propto \sum_{i,j,k,l=q,\bar{q},g} f_{i/p}(x_1, Q_{\text{eff}}^2) \tilde{f}_{j/N}^{D(3)}(\beta, Q_{\text{eff}}^2, x_{\mathcal{P}}) \overline{\sum} |\mathcal{M}(ij \rightarrow kl)|^2 \frac{1}{1 + \delta_{kl}} \\
& \equiv r_h \sum_{i,j,k,l=q,\bar{q},g} f_{i/p}(x_1, Q_{\text{eff}}^2) f_{j/N}^{D(3)}(\beta, Q_{\text{eff}}^2, x_{\mathcal{P}}) \overline{\sum} |\mathcal{M}(ij \rightarrow kl)|^2 \frac{1}{1 + \delta_{kl}}. \quad (240)
\end{aligned}$$

The screened diffractive PDF of the nucleon, $\tilde{f}_{j/N}^{D(3)}$, is introduced through the suppression factor r_h and the usual diffractive PDF of the nucleon $f_{j/N}^{D(3)}$:

$$\tilde{f}_{j/N}^{D(3)} \equiv r_h f_{j/N}^{D(3)}. \quad (241)$$

The suppression factor r_h takes into account the significant factorization breaking in hard hadron-hadron diffraction (see the discussion in the beginning of this section). In our numerical analysis, we used the following model for r_h :

$$r_h = \frac{0.75}{N(s)} = 0.75 \left(\int_{1.5/s}^{0.1} dx_{\mathcal{P}} \int_{-\infty}^0 dt f_{\mathcal{P}/p}(x_{\mathcal{P}}, t) \right)^{-1}. \quad (242)$$

This expression is based on the phenomenological model of [241], which describes the suppression of diffraction at the Tevatron ($\sqrt{s} = 546$ and 1800 GeV) by rescaling the Pomeron flux, $f_{\mathcal{P}/p}(x_{\mathcal{P}}, t)$, by the factor $N(s)$. In Eq. (242), the Pomeron flux is given by the standard expression:

$$f_{\mathcal{P}/p}(x_{\mathcal{P}}, t) = \frac{1}{x_{\mathcal{P}}^{1+2\epsilon+2\alpha't}} \frac{\beta_{\mathcal{P}pp}^2(t)}{16\pi}, \quad (243)$$

where $\epsilon = 0.1$; $\alpha' = 0.25 \text{ GeV}^{-2}$; $\beta_{\mathcal{P}pp}(t)$ is the $\mathcal{P}pp$ form factor [241].

We also introduced the additional factor of 0.75 in Eq. (242) in order to phenomenologically take into account the observation that the effects of factorization breaking should be larger in the elementary diffractive PDFs at $t = 0$ [see Eq. (238)] than in the t integrated diffractive PDFs [see Eq. (242)].

The application of Eq. (242) at the RHIC and LHC energies gives:

$$\begin{aligned}
r_h &= \frac{1}{4.2}, & \text{RHIC,} \\
r_h &= \frac{1}{16.0}, & \text{LHC.}
\end{aligned} \quad (244)$$

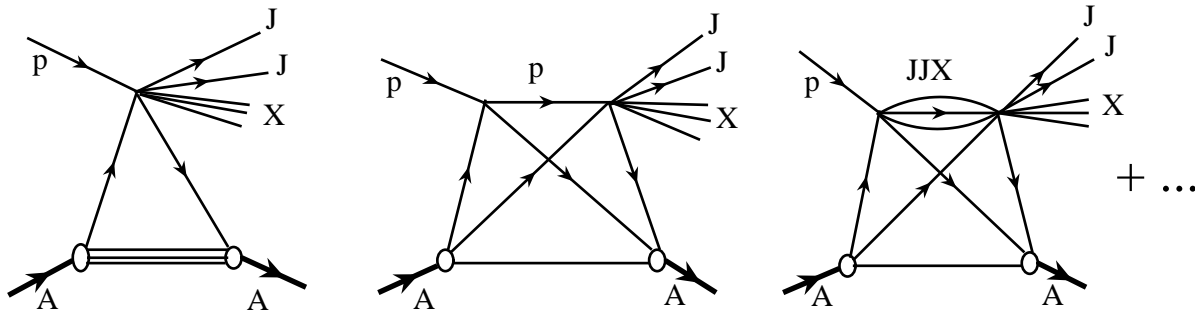


Fig. 92. Graphs representing first terms of the multiple scattering series for the $p + A \rightarrow 2 \text{jets} + X + A$ scattering amplitude.

Note that in the simple model that we use here, the amount of the suppression does not depend on the light-cone fraction β . However, the recent NLO QCD analysis [247] found that r_h in the $p\bar{p}$ scattering decreases with an increase of β for large β . This effect would further suppress the hard diffraction mechanism as compared to the electromagnetic one (see discussion below).

Returning to the case of hadron-nucleus scattering and the discussion of Eq. (238), it is important to emphasize that in the case of hard coherent proton-nucleus diffraction, the nuclear suppression factor, T_{hard}^{pA} , is the product of the soft and hard suppression factors introduced previously,

$$T_{\text{hard}}^{pA} = T_{\text{soft}}^{pA} T_{\text{hard}}^{\gamma^*A}. \quad (245)$$

This can be understood from Fig. 92, which represents first terms of the multiple scattering series for the $p + A \rightarrow 2 \text{jets} + X + A$ scattering amplitude. The rescattering cross section in the middle graph is $\sigma_{\text{tot}}(s)$; the rescattering cross section in the right graph is $\sigma_{\text{soft}}^j(x, Q^2)$ (in the color fluctuation approximation). Therefore, the resulting nuclear attenuation, which results from the sum of the middle and right graphs, is driven by the $\sigma_{\text{tot}}(s) + \sigma_{\text{soft}}^j(x, Q^2)$ effective cross section. After the eikonalization (summing all graphs corresponding to the interaction with all nucleons of the target), one obtains Eq. (245).

Equation (238) can be interpreted in two complimentary ways. On the one hand, one can start from soft diffractive dissociation of protons on heavy nuclei, see Eq. (233). Since we are interested in the hard diffractive component of the diffractive dissociation cross section, one has to take into account the additional suppression of the nuclear diffractive PDFs given by the $T_{\text{hard}}^{\gamma^*A}$ factor. As a result, one arrives at Eq. (245). On the other hand, one can start from the expression for inclusive diffraction of protons on nuclei, which is proportional to the nuclear diffractive PDFs (171). Since the final diffractive state contains a soft component, which is partially absorbed by the nucleus, one should take into account this suppression by introducing the T_{soft}^{pA} factor, which represents the probability of the absence of soft inelastic interactions at a given impact parameter b .

The comparison of the nuclear screened diffractive PDFs $\tilde{f}_{j/A}^{D(3)}$ to the nucleon screened diffractive PDFs $\tilde{f}_{j/N}^{D(3)}$, i.e., the comparison of the diffractive production of two jets in the pA and pp cases, can be quantified by introducing the factor λ^j ,

$$\lambda^j(x, Q^2) \equiv \frac{\tilde{f}_{j/A}^{D(3)}(x, Q^2, x_{\mathcal{P}})}{\tilde{f}_{j/N}^{D(3)}(x, Q^2, x_{\mathcal{P}})} = 4\pi A^2 B_{\text{diff}} \int d^2b T_A^2(b) e^{-A(\sigma_{\text{tot}}(s) + \sigma_{\text{soft}}^j(x, Q^2))T_A(b)}. \quad (246)$$

In Eq. (246), $\sigma_{\text{soft}}^j(x, Q^2)$ is the effective cross section introduced and discussed in Sec. 5.1.2, see Fig. 29. For the proton-nucleon cross section, $\sigma_{\text{tot}}(s)$, we use the Donnachie-Landshoff parameterization [131]:

$$\sigma_{\text{tot}}(s) = 21.7 s^{0.0808} + 56.08 s^{-0.4525} \text{ mb}. \quad (247)$$

Certain features of Eq. (246) deserve a discussion. First, while the diffractive PDFs depend separately on β and $x_{\mathcal{P}}$, the factor λ^j depends only on their product $x = \beta x_{\mathcal{P}}$ in our approach [compare to the $f_{j/A}^{D(3)}/(Af_{j/N}^{D(3)})$ ratio that also depends only on Bjorken x in our approach]. Second, λ^j is weakly flavor-independent because $\sigma_{\text{tot}}(s) \gg |\sigma_{\text{soft}}^g - \sigma_{\text{soft}}^q|$ (again, it should be compared to the $f_{j/A}^{D(3)}/(Af_{j/N}^{D(3)})$ ratio which is also weakly flavor-independent). In addition, since the slope B_{diff} is independent on the hard scale Q^2 in our approach, λ^j has a very weak dependence on Q^2 .

Figures 93 and 94 present the results for the ratio of the nuclear to proton screened diffractive PDFs, $\lambda^j = \tilde{f}_{j/A}^{D(3)}/\tilde{f}_{j/N}^{D(3)}$, see Eq. (246), in the RHIC and LHC kinematics. The RHIC kinematics corresponds to $\sqrt{s} = 200$ GeV; the LHC kinematics corresponds to $\sqrt{s} \approx 9.9$ TeV per nucleon for proton- ^{40}Ca collisions and $\sqrt{s} \approx 8.8$ TeV per nucleon for proton- ^{208}Pb collisions, see Table 7 and Ref. [248].

Figure 93 shows λ^j as a function of Bjorken x at $Q^2 = 4$ GeV 2 for ^{40}Ca and ^{208}Pb . The solid curves correspond to model FGS10_H and the dotted curves correspond to model FGS10_L. All curves are for the \bar{u} -quark flavor; the predictions for the gluon channel differ from the presented ones insignificantly. Despite the fact that λ^j is of the order of unity, the corresponding suppression of hard diffraction is very large because in the absence of the suppression, nuclear diffractive PDFs would have been enhanced compared to the nucleon diffractive PDFs by the very large factor $f_{j/A}^{D(3)}/f_{j/N}^{D(3)} \propto A^{4/3}$.

Figure 94 presents the A dependence of λ^j at fixed $x = 10^{-3}$ and $Q_0^2 = 4$ GeV 2 , i.e., at fixed $\sigma_{\text{soft}}^j(x, Q_0^2)$. As seen from Fig. 94, the A dependence of λ^j is rather slow. A simple fit gives that $\lambda \propto A^{0.28}$ at both the RHIC and LHC.

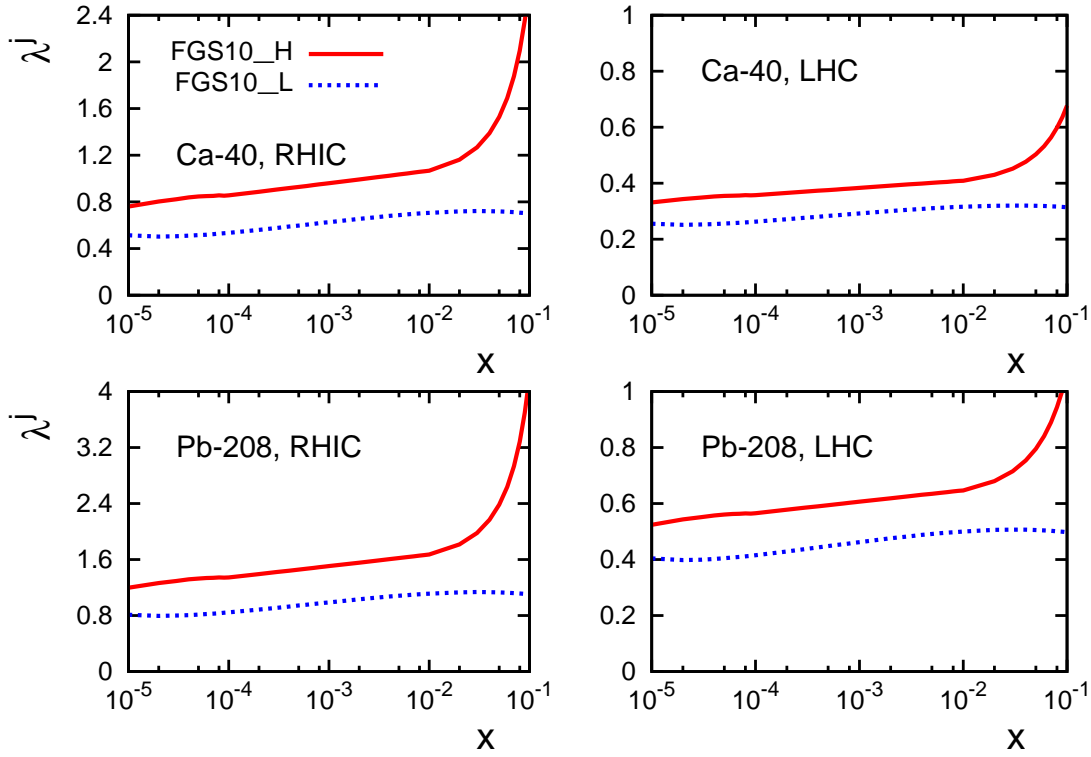


Fig. 93. The ratio of the nuclear to proton screened diffractive PDFs, $\lambda^j = \tilde{f}_{j/A}^{D(3)}/\tilde{f}_{j/N}^{D(3)}$, see Eq. (246), as a function of Bjorken x at $Q^2 = 4 \text{ GeV}^2$ in the RHIC and LHC kinematics. The solid curves correspond to model FGS10_H; the dotted curves correspond to model FGS10_L.

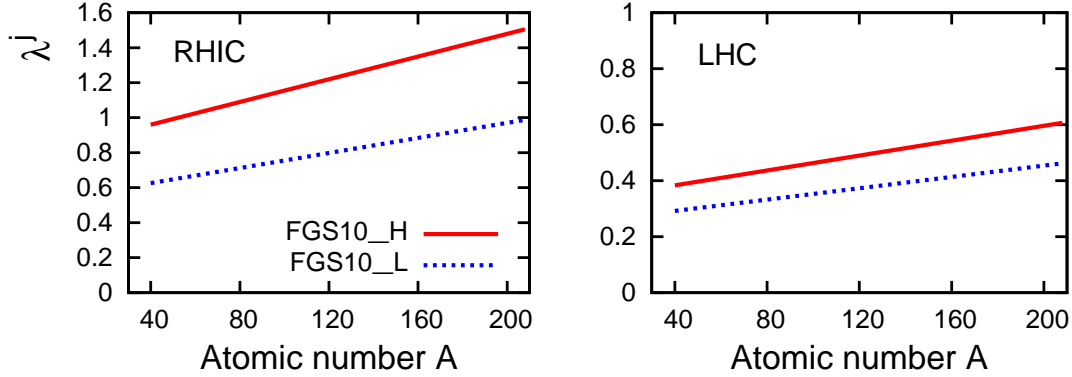


Fig. 94. The ratio of the nuclear to proton screened diffractive PDFs, $\lambda^j = \tilde{f}_{j/A}^{D(3)}/\tilde{f}_{j/N}^{D(3)}$, as a function of the atomic number A at $x = 10^{-3}$ and $Q^2 = 4 \text{ GeV}^2$ in the RHIC and LHC kinematics. The solid curves correspond to model FGS10_H; the dotted curves correspond to model FGS10_L.

7.4 Hard diffraction and ultraperipheral proton-nucleus collisions

In proton-heavy-nucleus collisions (for example, ^{208}Pb), most of the diffractive events ($\sim 80\%$) will be generated by the scattering of the proton off the coherent nuclear Coulomb

field at large impact parameters, $p + A \rightarrow p + \gamma + A \rightarrow X + A$ [134], see Fig. 95. These

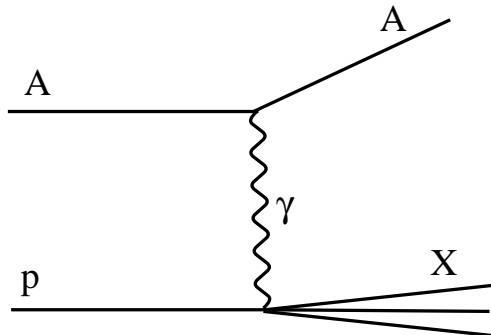


Fig. 95. The ultraperipheral $p + A \rightarrow X + A$ scattering.

ultraperipheral proton-nucleus collisions open a possibility for studies of hard photon-proton interactions at extremely high energies and allow one to probe the gluon density in the proton at the values of Bjorken x , which are a factor of ten smaller (for the same virtuality) than those probed at HERA [249–251].

In Sec. 7.3, we studied jet production in hard coherent proton–heavy-nucleus diffraction, $p + A \rightarrow 2 \text{ jets} + X + A$; in this section, we compare it to the production of hard jets by the photon-proton interaction, where the photon is coherently produced by the elastically recoiled nucleus, $p + A \rightarrow p + \gamma + A \rightarrow 2 \text{ jets} + X + A$. This corresponds to the situation when the generic final state X in Fig. 95 contains a hard two-jet component and a soft remaining part X .

Qualitatively, we expect that the rate of the hard dijet production through the hard diffractive mechanism will be significantly smaller than that due to the ultraperipheral mechanism because of the following two suppression effects. First, hard diffractive dijet production is suppressed by the λ^j factor discussed in Sec. 7.3, see Figs. 93 and 94. Second, the shapes of the parton distributions in the photon and screened nuclear diffractive PDFs are rather different. In the photon case, the dominant contribution to the photon PDFs comes from the $\beta \sim 1$ region corresponding to the kinematics where a pair of jets is at the rapidities close to the gap. In the screened nuclear diffractive PDFs at large virtualities, which are relevant for the measurements at the LHC, the main contribution comes from small β , see Fig. 3 of Ref. [26].

As we just mentioned, hard coherent dijet production in proton-nucleus scattering can proceed via the e.m. mechanism, when the nucleus coherently emits a quasi-real photon which interacts with the proton and diffractively produces two hard jets, $p + A \rightarrow p + \gamma + A \rightarrow 2 \text{ jets} + X + A$, see Fig. 95. The corresponding cross section can be written as a sum of the resolved and direct photon contributions (the separation into the resolved and direct components is only meaningful in the leading-order calculation):

$$\frac{d^3\sigma_{\text{em}}^{p+A \rightarrow 2\text{jets}+X+A}}{dx_1 dp_T^2 dx_{\mathcal{P}}} \propto r_{\text{em}} \sum_{i,j,k,l=q,\bar{q},g} f_{i/p}(x_1, Q_{\text{eff}}^2) \frac{dN_{\gamma}(x_{\mathcal{P}})}{dx_{\mathcal{P}}} f_{j/\gamma}(\beta, Q_{\text{eff}}^2) \overline{\sum} |\mathcal{M}(ij \rightarrow kl)|^2 \frac{1}{1 + \delta_{kl}} + \sum_{i,j,k,l=q,\bar{q},g} f_{i/p}(x_1, Q_{\text{eff}}^2) \frac{dN_{\gamma}(x_{\mathcal{P}})}{dx_{\mathcal{P}}} \delta(\beta - 1) \overline{\sum} |\mathcal{M}(i\gamma \rightarrow kl)|^2 \frac{1}{1 + \delta_{kl}}, \quad (248)$$

where $dN_{\gamma}(x_{\mathcal{P}})/dx_{\mathcal{P}}$ is the flux of equivalent photons [249] expressed in terms of $x_{\mathcal{P}}$ instead of the photon energy ω ($\omega = x_{\mathcal{P}}p_{\text{lab}}$, where p_{lab} is the momentum of the nucleus in the laboratory frame); $f_{j/\gamma}$ is the PDF of the real photon; $\overline{\sum} |\mathcal{M}(i\gamma \rightarrow kl)|^2$ are the invariant matrix elements for the direct photon-parton scattering, see Table 7.9 in [246]; r_{em} is a phenomenological factor describing the factorization breaking for the resolved (hadron-like) component of the real photon. The exact value of r_{em} is uncertain: It ranges from $r_{\text{em}} = 0.34$ [252] to $r_{\text{em}} \approx 1$ with large errors [253]. Since our analysis is a simple leading-order estimate, we conservatively take $r_{\text{em}} = 0.5$.

The flux of equivalent photons approximately equals [254]:

$$\begin{aligned} \frac{dN_{\gamma}(x_{\mathcal{P}})}{dx_{\mathcal{P}}} &= \frac{Z^2 \alpha_{\text{em}} \omega}{\pi^2 \gamma^2} \int_{|b| \geq R_A} d^2b \left[K_1^2 \left(\frac{\omega|b|}{\gamma} \right) + \frac{1}{\gamma^2} K_1^2 \left(\frac{\omega|b|}{\gamma} \right) \right] \Big|_{\omega=x_{\mathcal{P}}p_{\text{lab}}} \\ &= \frac{2Z^2 \alpha_{\text{em}}}{\pi x_{\mathcal{P}}} \left[x K_0(x) K_1(x) + \frac{x^2}{2} (K_0^2(x) - K_1^2(x)) \right], \end{aligned} \quad (249)$$

where Z is the nuclear charge; γ is the Lorentz factor of the fast moving nucleus; R_A is the effective nuclear radius, $R_A = 1.145 A^{1/3}$; p_{lab} is the momentum of the nucleus in the laboratory frame. Table 7 summarizes the values of p_{lab} and γ that we used in our analysis, see also [35]. In the table, $\sqrt{s_{NN}}$ is the invariant energy of the pA collision per nucleon; $\gamma = \sqrt{s_{NN}}/(2m_N)$; the proton beam energy is 250 GeV for RHIC and 7 TeV for the LHC (we assume the maximal energy for the latter).

Nucleus	p_{lab} , RHIC	$\sqrt{s_{NN}}$, RHIC	γ , RHIC	p_{lab} , LHC	$\sqrt{s_{NN}}$, LHC	γ , LHC
^{40}Ca	125 GeV	354 GeV	187	3.5 TeV	9.9 TeV	5280
^{208}Pb	100 GeV	316 GeV	169	2.76 TeV	8.8 TeV	4690

Table 7

The values of the momentum of the nucleus in the laboratory frame, p_{lab} , the invariant energy of the pA collision per nucleon, $\sqrt{s_{NN}}$, and the Lorentz factor of the fast moving nucleus, γ , in the RHIC and LHC kinematics used in our analysis. Note that we use that the proton beam energy is 250 GeV for RHIC and 7 TeV for the LHC.

To quantify the comparison between the hard and e.m. mechanisms of the $p + A \rightarrow$

2 jets + X + A process, we introduce the ratio R :

$$R(\beta, x_P, p_T) = \frac{d^3 \sigma_{\text{hard}}^{p+A \rightarrow 2 \text{jets} + X + A}}{dx_1 dp_T^2 dx_P} \bigg/ \frac{d^3 \sigma_{\text{em}}^{p+A \rightarrow 2 \text{jets} + X + A}}{dx_1 dp_T^2 dx_P}, \quad (250)$$

where the numerator and denominator are given by Eqs. (236) and (248), respectively (we introduced the subscript "hard" for the cross section in Eq. (236)), with the equal coefficients of proportionality. In the simplified kinematics that we use, at given p_T and x_P , the ratio R depends only on β .

In our analysis, we considered two cases: The dijet production summed over gluon and quark jets and the production of two heavy-quark jets (c and b quarks). The resulting ratios R at $p_T = 5$ GeV and $x_P = 10^{-4}$, 10^{-3} and 10^{-2} as functions of β are presented in Fig. 96. The left column of panels correspond to model FGS10_H; the right column of panels correspond to FGS10_L. The four upper panels are for ^{40}Ca ; the four lower panels are for ^{208}Pb . All curves correspond to the LHC kinematics, see Table 7.

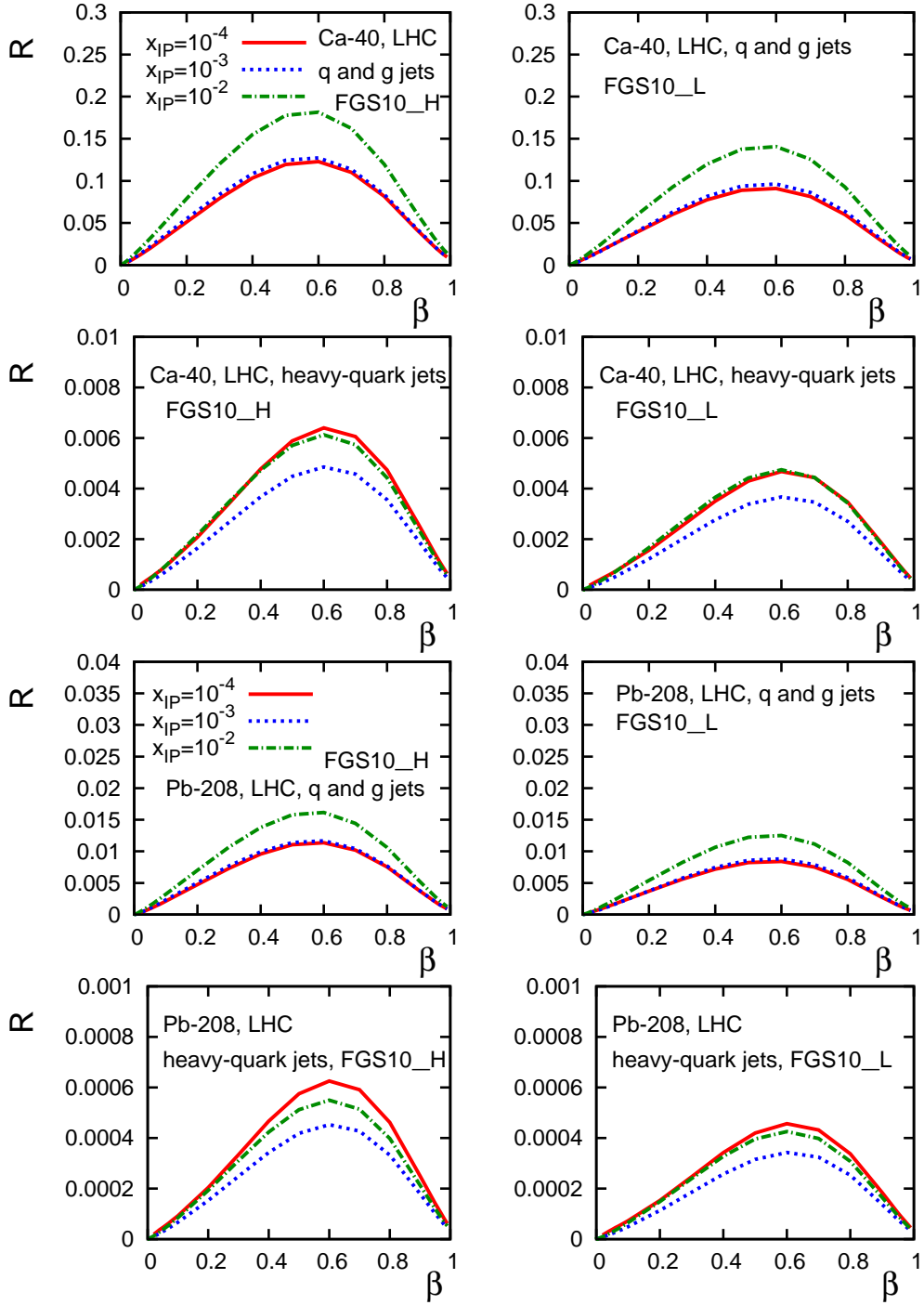


Fig. 96. The suppression of hard diffractive dijet (quark and gluon jets and heavy-quark jets) production compared to e.m. coherent dijet production in proton-nucleus scattering at the LHC. The suppression factor R of Eq. (250) at $p_T = 5$ GeV and $x_P = 10^{-4}$, 10^{-3} and 10^{-2} as a function of β .

The results presented in Fig. 96 deserve a detailed discussion. The dependence of the ratio R for the quark and gluon jets on $x_{\mathcal{P}}$ can be explained as follows. The main contribution to the $x_{\mathcal{P}}$ dependence of R at fixed β comes from the changing of x_1 . As $x_{\mathcal{P}}$ is decreased, x_1 is increased, see Eq. (237), which diminishes the role played by the gluons in the projectile. As explained in the following, it is the gluon contribution that affects R most significantly. Hence, R decreases with decreasing $x_{\mathcal{P}}$. Note that the dependence of the diffractive PDFs on $x_{\mathcal{P}}$, $f_{j/N}^{D(3)}(\beta, x_{\mathcal{P}}, Q_{\text{eff}}^2) \propto 1/x_{\mathcal{P}}^{1+2\epsilon}$, see Eq. (243), is similar to the $1/x_{\mathcal{P}} \ln(1/x_{\mathcal{P}})$ -behavior of the e.m. cross section. Therefore, these two factors weakly affect the $x_{\mathcal{P}}$ dependence of R .

The dependence of R on β is rather fast and reflects different shapes of the proton diffractive PDFs and the PDFs of the real photon. While the proton diffractive PDFs times β are flat in the $\beta \rightarrow 0$ limit, the photon PDFs times β grow. This explains why R approaches zero when β is small. In the opposite limit, $\beta \rightarrow 1$, diffractive PDFs are small and the e.m. contribution wins over due to the non-vanishing direct photon contribution, i.e., $R \rightarrow 0$ as $\beta \rightarrow 1$.

In Fig. 96, the ratio R at its peak is much larger for the production of quark and gluon jets than for the production of heavy-quark jets. An examination shows that this effect is due to the large gluon diffractive PDF, which in tandem with the large $gg \rightarrow gg$ hard parton invariant matrix element [246], works to increase R in the presence of the gluon jets.

One should also note that the ratio R is much larger for ^{40}Ca than for ^{208}Pb . This is because the ^{40}Ca flux of the equivalent photons, which is proportional to Z^2 [see Eq. (249)], is 16 times smaller than that for ^{208}Pb .

We used the following input in our numerical analysis of the ratio R . We used the LO parameterization of the real photon PDFs from Ref. [255]. We have also checked that the use of a different parameterization [256] leads to rather similar predictions.

The suppression factor λ^j (246), which implicitly enters Eq. (250) at the scale $Q^2 = Q_{\text{eff}}^2 = 4p_T^2 = 100 \text{ GeV}^2$, very weakly depends on Q^2 . Therefore, for λ^j , we used the results of our calculation at $Q^2 = 4 \text{ GeV}^2$ presented in Fig. 93.

The δ -function for the direct photon contribution was numerically modeled in the following simple form:

$$\delta(\beta - 1) = \frac{1}{\pi} \frac{\epsilon}{(\beta - 1)^2 + \epsilon^2}, \quad \text{with } \epsilon = 0.01. \quad (251)$$

Besides the LHC, RHIC also has the potential to measure hard diffraction in proton-nucleus scattering. We consider a typical example of the corresponding RHIC kinematics with 250 GeV protons scattering on the beams of ^{40}Ca and ^{208}Pb , see Table 7. Producing

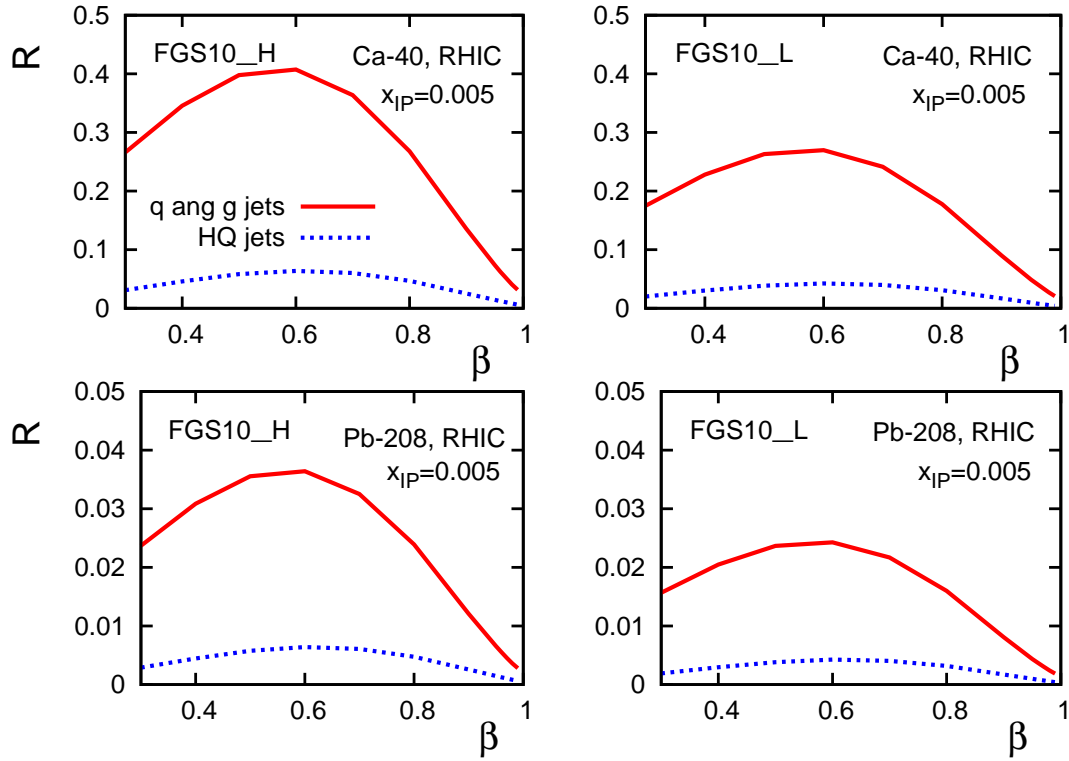


Fig. 97. The suppression factor R of Eq. (250) in the RHIC kinematics and at $p_T = 5$ GeV and $x_P = 5 \times 10^{-3}$ as a function of β . The solid curves correspond to quark and gluon jets; the dotted curves correspond to heavy-quark jets. The left panels correspond to FGS10_H model; the right panels correspond to FGS10_L model.

sufficiently high diffractive masses, e.g., $M_X^2 = 500$ GeV², one accesses the typical kinematics of hard diffraction, $x_P = 5 \times 10^{-3}$ and $\beta > 0.3$. Note also that the suppression of hard diffraction at RHIC is approximately four times smaller than at the LHC, see Eq. (244).

We calculated the suppression factor R of Eq. (250) in the considered RHIC kinematics at $p_T = 5$ GeV. The resulting values of R as a function of β are presented in Fig. 97. The solid curves correspond to quark and gluon jets; the dotted curves correspond to heavy-quark jets. The left panels correspond to FGS10_H model; the right panels correspond to FGS10_L model. As seen from Fig. 97, the factor R at RHIC is larger than that at the LHC. This is mostly a consequence of the decrease of the flux of equivalent photons when going from the LHC to RHIC kinematics.

Our results presented in this subsection can be summarized as follows. For proton-²⁰⁸Pb scattering at the LHC, hard diffraction is suppressed compared to the e.m. contribution, especially at $x_P = 10^{-4}$ and large β , e.g., for $\beta > 0.8$, see Fig. 96. The suppression is very strong for the production of heavy-quark jets. The physical reason for the suppression is the strong coherent Coulomb field of ²⁰⁸Pb, which enhances the e.m. mechanism of hard diffraction.

Replacing ^{208}Pb by ^{40}Ca , the hard diffractive mechanism becomes almost compatible to the e.m. one in the case of the production of quark and gluons jets. However, like in the case of ^{208}Pb , the production of heavy-quark jets is dominated by the e.m. mechanism.

As a result of the smaller Lorentz dilation factor γ at RHIC, the factor R at the RHIC kinematics is larger than at the LHC.

Our results suggest the following experimental strategies. First, the use of heavy nuclei in pA scattering at the LHC will provide a clean method to study hard real photon-proton scattering at the energies exceeding the HERA energies by the factor of ten. Second, taking lighter nuclei and choosing the appropriate kinematics, where the e.m. contribution can be controlled, one can effectively study the factorization breaking in nuclear diffractive PDFs. Third, in the same kinematics, a comparison of the dijet diffractive production to the heavy-quark-jet diffractive production will measure the nuclear screened diffractive gluon PDF. It can be compared to the nuclear diffractive PDFs, which will be measured in nucleus-nucleus ultraperipheral collisions at the LHC and which could also be measured in eA coherent diffraction in DIS at an Electron-Ion Collider.

8 The black disk regime

8.1 Introduction

The aim of this section is to quantify the kinematical domain of small x and large Q^2 where the onset of a new QCD regime of the strong interaction with a small coupling constant—black disk regime (BDR)—occurs and its role in the nuclear shadowing phenomenon in DIS. We outline properties of this new QCD regime which are strikingly different from those of the pQCD regime and soft QCD regime, compare theoretical expectations with experimental data obtained at HERA, RHIC, and Tevatron and make predictions for the LHC.

The approximation of the low parton densities is applicable in the kinematical domain where the nuclear shadowing effect in the interaction of a hadron projectile with a two-nucleon system represents a correction to the total cross section. (In the case of a heavy nucleus, nuclear shadowing is larger due to the larger number of nucleons at the same impact parameter.) In this kinematics and in the target rest frame, a tiny ($\approx 4k_{t,\text{soft}}^2/Q^2$) fraction of the phase volume kinematically allowed for the light-cone wave function of the virtual photon is occupied by its non-perturbative component which dominates nuclear shadowing effects ($k_{t,\text{soft}}$ is a typical soft momentum of the parton constituents of the virtual photon). Its dependence on Q^2 and x is properly taken into account by QCD evolution equations, see the discussion in the preceding sections. At the same time, the interaction of the most of configurations of the virtual photon wave function, whose phase

volume is $1 - 4k_{t,\text{soft}}^2/Q^2$, is not shadowed — the color transparency phenomenon. The color transparency phenomenon has been observed in fixed-target experiments at FNAL and TJNAF, for overview and references, see, e.g., [257,258]. However, the color transparency phenomenon for the interaction with a target of the quark-gluon configurations with a small but fixed transverse size in the photon wave function along with the regime of small parton densities disappear at sufficiently small x as a consequence of specific properties of pQCD.

Perturbative QCD predicts a rapid increase of the structure functions and parton distributions with an increase of energy, which was observed at FNAL and HERA, see Sec. 8.4. At sufficiently high energies, this increase comes in conflict with the probability conservation. It follows from the probability conservation that the cross section for the scattering of a wave packet of quarks and gluons off a nucleon (nucleus) at a given impact parameter b cannot increase with an increasing energy forever since it is bound from above. The physical meaning of this boundary is that the absorption cannot exceed 100%, see Sec. 8.3. Indeed, the probability for a wave packet of quarks and gluons to interact inelastically with the target cannot exceed unity, or, equivalently, the probability not to interact at a given b is positive. This regime is referred to as the black disk regime (BDR) because it has the features of scattering (diffraction) of light on a completely absorbing disk in the classical wave optics. Within the BDR, at sufficiently small x the most part of the virtual photon wave function participates in the nuclear shadowing phenomenon.

In the BDR, the structure function of a hadron target at a given impact parameter b is given by the convolution of the virtual photon light-cone wave function with the cross section of interaction of the produced quark and gluon wave packet with the target. For a transversally polarized virtual photon, $F_T(x, Q^2, b) \leq cQ^2 \ln(x_0/x)$, i.e., $F_T(x, Q^2, b)$ is allowed to only slowly (logarithmically) increase with increasing energy. Note that such a behavior is realized in pQCD assuming the k_t factorization in the DGLAP approximation of pQCD as well as in the resummation models (the term is explained in Sec. 8.4) [259–262]. In this case, transverse momenta of partons in the photon wave function increase with energy [225]; this phenomenon is a precursor of the change of the pQCD regime at sufficiently small x . The origin of this increase is the same as for the running coupling constant in QED and QCD — the singular behavior of the light-cone wave function of the virtual photon in coordinate space (the polarization operator of the photon at large Q^2 is $\Pi_{\text{em}}(Q^2) \propto Q^2 \ln(Q^2/Q_0^2)$). This property reveals qualitative and quantitative difference of the BDR regime in QCD from the popular hypothesis of saturation, i.e., the energy independence of parton densities at extremely small x , for a recent discussion, see e.g., [263]. The theoretical boundary on the behavior of the structure functions integrated over all impact parameters is weaker, e.g., $F_T(x, Q^2) \leq cQ^2 \ln^3(x_0/x)$ [264].

In addition to the probability conservation, the energy-momentum conservation plays also an important role in the onset of the BDR. The account of the latter effect significantly reduces the number of gluons (gluon showers) in the multi-Regge kinematics as compared

to leading $\log(x)$ approximations and resummation models, see the discussion in Sec. 8.10. In particular, the energy-momentum conservation is relevant for the applicability of the DGLAP approximation in the HERA kinematics where the masses $M^2 \approx Q^2$ dominate in the cross section of diffraction in DIS. This should be contrasted with the onset of the triple Pomeron limit where $M^2 \gg Q^2$. As a result, the DGLAP approximation, which accounts for the conservation of the longitudinal energy-momentum, is better suited to evaluate the probability conservation, the radius of convergence of pQCD series, etc. Note however that numerical studies show that puzzles with violation of probability conservation within pQCD calculations occur at comparatively moderate x where the DGLAP approximation is formally justified, see Sec. 8.10.

At sufficiently high energies, the interaction of hadronic configurations of the virtual photon will eventually reach its geometric limit (BDR), but this will take place at different collision energies for different fluctuations. For instance, according to pQCD calculations, the BDR should initially be achieved for the interaction of colorless two-gluon ($q\bar{q}g$) dipoles and later, for significantly larger energies, also for the interaction of $q\bar{q}$ colorless dipoles.

The complete absorption of the projectile wave function in the BDR means the violation of the leading twist approximation and an onset of a new QCD regime with a different continuous symmetry, see Sec. 8.11. Within the BDR, nuclear shadowing in the total cross section of DIS achieves its maximal value allowed by probability conservation for the collisions at central impact parameters and does not depend on the nuclear thickness; diffractive processes become a shadow of inelastic ones. Significant pre-selection "energy losses" can be considered as a precursor of the onset of BDR, see Sec. 8.7.

The BDR is well known in hadron-hadron and hadron-nucleus interactions. For example, it takes place in the scattering of protons off heavy nuclei and in elastic pp collision at collider energies at the zero impact parameter, for a review and references, see [265]. A new distinctive feature of high energy QCD is that the BDR is expected for the interaction of small-size colorless quark-gluon wave packets (e.g., bound quarkonium states like J/ψ) which interact rather weakly at medium energies.

The distinctive property of the BDR that the interaction of small-size dipoles remains strong leads to a number of features of the onset of the BDR that can be used as experimental signals. By comparing the properties of the BDR with the available data, one finds evidence that an onset of the BDR for hard processes has been observed indirectly in diffraction in DIS (i.e., for the $q\bar{q}g$ colorless dipole scattering off nucleons) [237] and directly in dA collisions at RHIC, see the discussion in Sec. 8.9.

8.2 BDR vs. weak density limit

For the accurate calculation of nuclear shadowing in the weak density limit, it was sufficient to evaluate the interaction of the projectile with 2-3 nucleons. On the contrary, the calculations of shadowing in the vicinity of the BDR requires evaluation and summing of the whole series of multiple collisions. (We draw attention to the fact that the concept of series over multiple collisions becomes ill-defined in the kinematics close to the BDR since each term in this series becomes large and not under control.)

To visualize the challenging theoretical phenomena, we consider the dipole scattering off a nuclear target within the optical model with the potential $V = \sigma \rho_A$ and ignore temporarily its fundamental flaws. Here σ is the dipole-nucleon cross section (rapidly increasing with energy) and ρ_A is the nuclear density. At sufficiently high energies, the dipole-nucleus inelastic cross section becomes equal $\pi R_A^2 +$ terms $\propto R_N R_A \ln^2(x_0/x)$, where R_A (R_N) is the nuclear (nucleon) radius, since the optical potential V increases with an increase of energy, i.e., the cross section becomes independent of the optical potential V . Naturally, this answer is strongly different from what one would obtain in the weak density limit. One can use this model as the guide to pQCD. In the kinematics, where the effective parameter characterizing the perturbative QCD series, η ,

$$\eta = \alpha_s(Q_0^2)(N_c/2\pi) \ln(Q^2/Q_0^2) \ln(x_0/x) \geq 1, \quad (252)$$

the pQCD series loses the advantage of an asymptotic series, which was ensured at moderate x by the smallness of the running coupling constant, and becomes a series with the finite radius of convergence. Thus, the theoretical challenge is how to define the series properly or to find a more effective theoretical framework because at very large energies (in the kinematics of the BDR), cross sections will become independent of the coupling constant and all traces of the weak coupling regime will disappear.

8.3 Formal definition of BDR

To formulate the condition of probability conservation, it is instructive to consider the amplitude $A(s, t)$ of elastic scattering of a projectile (e.g., a heavy $q\bar{q}$ pair) off a hadron (nucleus) target in the impact parameter representation:

$$A(s, b) = \frac{1}{2s} \int \frac{d^2 q_t}{(2\pi)^2} e^{i\vec{q}_t \cdot \vec{b}} A(s, t), \quad (253)$$

where the momentum transfer is transverse, and $q_t^2 = -t$. Since the angular momentum is conserved in the scattering process, the impact parameter b is conserved as well for

$s \gg m_i^2$ (m_i denote the masses of the involved particles) and the scale of the interaction. The inclusion of the spins of the colliding particles leads to trivial modifications of the above formula and to the appearance of the spin-flip amplitudes.

In the case of scattering of a heavy quarkonium, the exact S-matrix unitarity condition reads, see e.g., Ref. [266]:

$$\Im m A(s, b) = \frac{1}{2} |A(s, b)|^2 + \text{positive terms}. \quad (254)$$

The rather stringent unitarity condition emerges in the case of high energies, where the interactions are driven by the inelastic interactions, and the scattering amplitudes are predominantly imaginary. Indeed, defining the profile function as

$$\Gamma(s, b) = -iA(s, b), \quad (255)$$

one can express the total, elastic and inelastic cross sections in terms of the profile function $\Gamma(s, b)$ as:

$$\left. \begin{array}{l} \sigma_{\text{tot}}(s) \\ \sigma_{\text{el}}(s) \\ \sigma_{\text{inel}}(s) \end{array} \right\} = \int d^2b \times \left\{ \begin{array}{l} 2 \Re \Gamma(s, b) \\ |\Gamma(s, b)|^2 \\ 1 - |1 - \Gamma(s, b)|^2. \end{array} \right. \quad (256)$$

Since the high energy dynamics is driven by the inelastic processes, $\sigma_{\text{el}} \leq \sigma_{\text{inel}}$. Also, at high energies $\Re A(s, b)/\Im m A(s, b) \ll 1$. Under these conditions, Eq. (256) leads to the restriction:

$$\Im m A(s, b) \leq 1. \quad (257)$$

In the case of the inelastic cross section, the integrand $\Gamma^{\text{inel}}(s, b) \equiv [1 - |1 - \Gamma(s, b)|^2]$ corresponds to the *probability of the inelastic interaction* for a given impact parameter b . Since the strength of the inelastic interaction increases with energy, at high enough energies, the wave packet will interact inelastically with the target with the probability close to unity and, hence,

$$\Gamma(s, b) = 1. \quad (258)$$

This equation provides the formal definition of the BDR. The generalization of this condition to the interaction of a wave packet of quarks and gluons gives:

$$\Gamma(s, b^2, d_{\perp}^2) = 1, \quad (259)$$

where d_{\perp} is the transverse size of the projectile wave packet.

Exploring the conservation of probability, we will often use a colorless dipole as a projectile. The concept of the dipole wave function is well-defined in QCD in the following two important cases. First, within the validity of the concept of the LT approximation, explicitly taking into account different components of the projectile (virtual photon, etc.) wave function or including them instead into the interaction produces the same results. Second, it is the case of the strong interaction of a projectile with a target. It has been understood long ago that the sum over the contributions of different components of the virtual photon wave function squared and integrated over the allowed phase volume gives the polarization operator of the photon with bare and highly virtual quarks. Hence, in the case when the interaction becomes strong, the use of the concept of a dipole is justified. The conservation of probability for the interaction of such a dipole has approximately the same form as the unitarity of the S-matrix in the s -channel and all restrictions valid for the scattering of heavy quarkonium states should be close to the ones for the scattering of such a wave packet.

It is worth emphasizing that although formally the expression for σ_{el} in Eq. (256) is dominated by the contribution of small b , it should be understood in the sense of the Babinet's principle for the wave diffraction in the classical electrodynamics: the scattering from the complementary screens (an opaque absorbing disk vs. a hole of the same geometry) are identical. It is the surrounding wave that generates the elastic scattering in the proximity of the BDR. To check this interpretation of the expression for σ_{el} , one can consider the propagation of a deuteron through a heavy nucleus at $b \sim 0$. Selecting a typical event where, e.g., a proton interacts inelastically with several nucleons, one can calculate the probability for the neutron to pass through the nucleus without inelastic interactions. The answer is obviously zero, while a naive application of Eq. (256) would give a number of the order of unity.

The contribution of small b to σ_{inel} is determined by the value of $1 - |\Gamma(s, b)|^2$. As one can see from Eq. (256), the BDR corresponds to the regime when $\sigma_{\text{el}} = \sigma_{\text{inel}}$. The interpretation of $\sigma_{\text{el}} = \sigma_{\text{inel}}$ in the language of the Babinet's principle of complimentary screens is that the amount of the absorbed light (inelastic cross section) is equal to the amount of light that passed around the target without interactions (elastic cross section). The latter is equal to the amount of light that passes through a hole in the shape of the target.

8.4 Observations of an onset of the BDR

Theoretical methods for the evaluation of nuclear shadowing in DIS at moderately small x are based on the leading twist approximation, which is justified by the difference in scales characterizing soft and hard interactions, and resulting QCD factorization theorems. As we have already mentioned, with an increase of the collision energy (decrease

of x), the interaction at a fixed resolution scale Q^2 becomes stronger and the hierarchy over the powers of $1/Q^2$ disappears. This is a reflection of the fact that in all currently used approximations to pQCD—DGLAP and resummation models (see below)—the total inelastic cross section of the interactions of a small color dipole with a hadronic target is proportional to the gluon density of the target [Eq. (143)], which increases with a decrease of x approximately as a power of $1/x$.

A note on terminology is in order here. It has recently been understood that the accurate account of the double logarithmic terms is important for the improvement of the calculations of small x behavior of DIS, see, e.g., Refs. [259–262]. Therefore, in this review, we refer to all such approaches as *resummation models*.

As a result of the fast increase of the gluon density at small x , all the approximations just mentioned should break down at sufficiently high energies since they lead to the probability of the inelastic interactions at a fixed impact parameter b exceeding unity. An important role in the evaluation is played by the fact that the gluon distribution is more narrow in the impact parameter space than that given by e.m. radius of a nucleon [267]. This conclusion is based on the analysis of the gluon core of the target probed in hard exclusive processes and the QCD factorization theorem for hard exclusive processes [216,217], which allows one to fit the two-gluon form factor, $F_{2g}(t)$, in the following simple form, $F_{2g}(t) = 1/(1 - t/m_g^2)^2$ where $m_{2g} \approx 1$ GeV. The knowledge of the two-gluon form factor allows one to evaluate the probability of hard processes at a given impact parameter.

Analyses of special processes observed at HERA, RHIC and Tevatron (FNAL) data indicate that an onset of the violation of the LT approximation occurs in the kinematical domain achieved at the existing generation of accelerators. The signals of an onset of the BDR include:

- (i) The gluon distribution which is large and rapidly increases with energy, see, e.g., Ref. [160], corresponds to the probability of the interaction of the color singlet gluon dipole at the zero impact parameter which is $\approx 1/2$, see, e.g., Ref. [268].
- (ii) The significant diffractive gluon density [61,62] corresponds to $\sigma_{\text{el}}/\sigma_{\text{tot}} \approx 1/2$ for the interaction of the color singlet gluon dipole at central impact parameters, where σ_{el} and σ_{tot} refer to the respective integrands in Eq. (256).
- (iii) In the elastic pp collisions at Tevatron, the partial waves for zero impact parameters are close to unity. However, at present it is unclear whether this is the BDR for hard or soft QCD interactions. If hard QCD interactions dominate, one expects an increase of the hadron transverse momenta as a function of the centrality of a collision.
- (iv) Significant "fractional energy losses" in the fragmentation region have recently been discovered at RHIC in the hard processes $d + A \rightarrow \pi(2\pi) + X$, for the discussion and references, see Sec. 8.8 and 8.9.

All these observations taken together indicate that the onset of a new QCD regime—we refer to it as the black disk regime (BDR)—occurs for the scattering of colorless gluon

dipole off a proton (at zero impact parameters) on the verge of the kinematics of HERA and, in the certain kinematics of small x , also at the LHC. We stress that in the HERA kinematics, as well as in the kinematics of the future Electron-Ion Collider (EIC), the full-fledged BDR has not been and will not be realized. Instead, only an onset (approach) to the full BDR may take place. The kinematics achieved at the LHC in pp and pA collisions for $x \leq 10^{-5}$ and in the ultraperipheral processes in heavy ion collisions as well as dimuon pair production for $x < 10^{-5}$ will allow for an onset of the BDR.

8.5 *The onset of BDR in the dipole model: inclusive scattering*

8.5.1 *The dipole model with the impact parameter dependence*

The dipole model for γ_T^* -nucleon (nucleus) scattering in the impact parameter representation allows for a quantitative analysis of the restrictions on the region of applicability of pQCD due to probability conservation since it gives a smooth interpolation between the calculable pQCD regime, model-dependent soft QCD regime and the BDR hard regime. Our interest is in the kinematics of the large $Q^2 = \text{const}$ and sufficiently small x .

The dipole approximation assumes that the γ^* wave function is given by the superposition of $q\bar{q}$ dipoles of transverse diameters d_\perp and that higher order components are included in the interaction². Note that such a procedure breaks down in the vicinity of the BDR where the number of constituents is regulated by the target. However, in the BDR, another approximation is useful. In particular, one can sum over the contributions of different components of the photon wave function, account for the lack of nondiagonal transitions [270], and use the completeness of QCD states. The resulting cross section is expressed in terms of the $q\bar{q}$ component of the photon wave function where both q and \bar{q} are strongly virtual — a result reminiscent of the dipole model.

As we repeatedly discussed in this review, in the target rest frame, the incoming photon interacts with the target via its partonic fluctuations. Since the interaction time is much shorter than the lifetime of the fluctuations at small x , the DIS amplitude can be factorized in three factors: one describing the formation of the fluctuation, another – the hard interaction with the target, and the final factor describing the formation of the hadronic final state.

² In the case of a dipole of the small transverse size, the dipole model of the inelastic DIS cross section is equivalent to the leading order DGLAP and BFKL [269] approximations and resummation models for this cross section in the target rest frame. To prove this, one can evaluate the dominant Feynman diagrams by taking the residues over the energies carried by the quark-antiquark pair in the photon fragmentation region. Note also that the infinite momentum frame structure function arises when the residues are taken over the fractions of the photon momentum carried by any parton in the direction of the target momentum.

Within this high-energy factorization framework, the *inelastic* contribution to the transverse and longitudinal structure functions, F_T and F_L , respectively, at a given impact parameter b can be written in the following factorized form:

$$F_{T,L}^{\text{inel}}(x, Q^2, b) = \frac{Q^2}{4\pi^2\alpha_{\text{em}}} 2 \int dz d^2d_{\perp} \sum_i |\Psi_{T,L}(z, Q^2, d_{\perp}^2, m_i^2)|^2 \Gamma^{\text{inel}}(s, d_{\perp}, x, b), \quad (260)$$

where $\Psi_{T,L}(z, Q^2, d_{\perp}^2, m_i^2)$ are the $q\bar{q}$ components of light-cone wave functions of the transversely and longitudinally polarized virtual photon, respectively, see Eq. (139); z is the photon momentum fraction carried by one of the dipole constituents; s is the invariant energy of the dipole-target system [$s = (P+q)^2$ for the $q\bar{q}$ dipole]. The dependence of Γ^{inel} on z is rather weak and will be neglected in our analysis below. (Note that $\Psi_{T,L}$ are usually called the light-cone wave functions, although Ψ_L arises as the result of cancellation between the time and longitudinal components of the electromagnetic current.)

The *inelastic* contribution to the structure functions of a target is obtained by the integration over the impact parameter b :

$$F_{T,L}^{\text{inel}}(x, Q^2) = \int d^2b F_{T,L}^{\text{inel}}(x, Q^2, b). \quad (261)$$

In the LT approximation, the inelastic impact factor (profile function) is given by the following expression, see e.g., [194,199,216]:

$$2\Gamma^{\text{inel}}(x, b, d_{\perp})_{\text{pQCD}} = \frac{\pi^2 F^2}{4} d_{\perp}^2 \alpha_s(Q_{\text{eff}}^2) x' g_T(x', Q_{\text{eff}}^2, b), \quad (262)$$

where F^2 is the Casimir operator of the color group, $F^2(\text{triplet}) = 4/3$ and $F^2(\text{octet}) = 3$; $g_T(x, Q_{\text{eff}}^2, b)$ is the generalized gluon distribution of a given target T (in the $\xi = 0$ limit) that was introduced and discussed in Sec. 5.5. When the target is a nucleus, $g_T(x, Q_{\text{eff}}^2, b)$ is the impact parameter dependent nuclear PDF (nuclear GPD), see Eq. (200) and Fig. 40. In the case of the scattering from the nucleon, $g_T(x, Q_{\text{eff}}^2, b)$ is given by the product of the structure function and the two-dimensional Fourier transform of the two-gluon form factor [268,271] (see the discussion below). The integration of $2\Gamma^{\text{inel}}(x, b, d_{\perp})_{\text{pQCD}}$ over the impact parameter gives the perturbative (small- d_{\perp}) part of the dipole cross section used in Sec. 5.14, see Eq. (143):

$$2 \int d^2b \Gamma^{\text{inel}}(x, b, d_{\perp})_{\text{pQCD}} = \frac{\pi^2}{3} d_{\perp}^2 \alpha_s(Q_{\text{eff}}^2) x' g_T(x', Q_{\text{eff}}^2). \quad (263)$$

The unitarity relation (256) provides the relation between $\Gamma^{\text{inel}}(b)$ and $\Gamma(b)$ that can be employed [in combination with Eq. (263)] to calculate $\Gamma(b)$.

In the limit of small dipoles, where $\Gamma^{\text{inel}}(x, b, d_{\perp})_{\text{pQCD}}$ is small and far away from the BDR, $\Gamma(x, b, d_{\perp})_{\text{pQCD}} \approx \Gamma^{\text{inel}}(x, b, d_{\perp})_{\text{pQCD}}$ and $\sigma_{\text{tot}}(s) \approx \sigma_{\text{inel}}(s)$. As the size of the dipole increases, the non-perturbative dynamics starts to play a role and one has to model $\Gamma(x, b, d_{\perp})$. One effect is an increase of the number of constituents. We take this effect into account phenomenologically by requiring the effective interaction to match the understood properties of the interaction. In particular, we use the interpolation formula in the impact parameter representation that coincides with the pQCD formula in the small- d_{\perp} limit and smoothly matches the non-perturbative soft QCD physics for large d_{\perp} (cf. Sec. 5.14):

$$2\Gamma(x, b, d_{\perp}) = \sigma_{q\bar{q}N}(x, Q^2, d_{\perp}, m_i) f(x, d, b), \quad (264)$$

where $\sigma_{q\bar{q}N}(x, Q^2, d_{\perp}, m_i)$ is the dipole cross section of Eq. (143); $f(x, d, b)$ is the Fourier transform of the form factor $f(x, d_{\perp}, t)$ introduced in Ref. [268] ($f(x, d_{\perp}, t)$ is a generalization of the two-gluon form factor discussed in Ref. [271]) and measured in the hard diffractive processes at HERA:

$$f(x, d_{\perp}, b) = \int \frac{d^2 q_{\perp}}{(2\pi)^2} e^{iq_{\perp} b} f(x, d_{\perp}, t = -q_{\perp}^2). \quad (265)$$

The form factor $f(x, d_{\perp}, t)$ satisfies the condition $f(x, d_{\perp}, t = 0) = 1$, which leads to $\int d^2 b f(x, d_{\perp}, b) = 1$ and automatically ensures that Eq. (264) is consistent with Eq. (256). The form factor $f(x, d_{\perp}, t)$ is modeled as the product of three functions describing the contributions to the overall t dependence coming from the target, projectile and Gribov diffusion [268]:

$$f(x, d_{\perp}, t) = \frac{1}{[1 - t/M^2(d_{\perp}^2)]^2} \frac{1}{1 - t/m_2^2 d_{\perp}^2/d_{\pi}^2} e^{\alpha' t d_{\perp}^2/d_{\pi}^2 \log(x_0/x)}, \quad (266)$$

where the effective mass squared $M^2(d_{\perp}^2)$ is defined as:

$$M^2(d_{\perp}^2) = \begin{cases} m_1^2 - (m_1^2 - m_0^2) \frac{d_{\perp}^2}{d_{\pi}^2}, & d_{\perp} \leq d_{\pi}, \\ m_0^2, & \text{otherwise.} \end{cases} \quad (267)$$

The parameters in Eqs. (266) and (267) are $m_0^2 = 0.7 \text{ GeV}^2$ (from the fits to the nucleon form factor), $m_1^2 = 1.1 \text{ GeV}^2$ (from the fits to diffractive ρ , ω and J/ψ electroproduction), $m_2^2 = 0.6 \text{ GeV}^2$, $d_{\pi} = 0.65 \text{ fm}$, $\alpha' = 0.25 \text{ GeV}^{-2}$, and $x_0 = 0.01$. The last factor in Eq. (266) is set to unity for $x > x_0$.

Figure 98 presents the results of the calculation of the impact factor for the nucleon of Eq. (264), $\Gamma(x, b, d_{\perp})$, as a function of the impact parameter b for four fixed dipole sizes, $d_{\perp} = 0.2, 0.4, 0.6$, and 0.8 fm . All curves correspond to $Q^2 = 4 \text{ GeV}^2$.

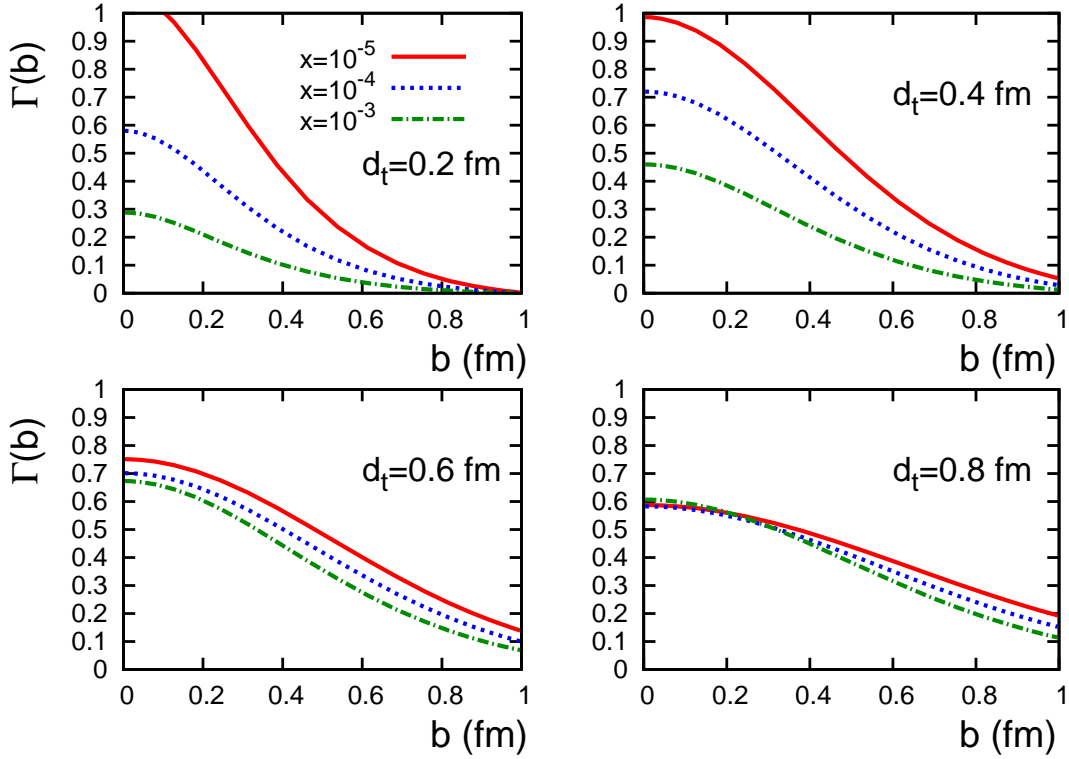


Fig. 98. The impact factor for the nucleon of Eq. (264) as a function of the impact parameter b for several fixed dipole sizes d_{\perp} .

In the case of nuclei, the impact factor can be calculated adopting the procedure of Ref. [268]. For small dipoles, $d_{\perp} \leq d_0 = 0.2$ fm, according to the QCD factorization theorem, the dipole cross section and the resulting impact factors are obtained by replacing the gluon distribution in the proton in Eq. (262) by that in the nucleus:

$$2\Gamma_A(x, b, d_{\perp})_{\text{pQCD}} = \frac{\pi^2 F^2}{4} d_{\perp}^2 \alpha_s(Q_{\text{eff}}^2) x' g_A(x', Q_{\text{eff}}^2, b). \quad (268)$$

The impact parameter dependent gluon distribution in nuclei entering Eq. (268) is given by Eq. (130) and is illustrated in Figs. 40, 41, and 42.

As we explained in detail in Sec. 5.14, as one increases the transverse dipole size, the dynamics of the dipole-target interaction becomes progressively non-perturbative and for sufficiently large dipoles, $d_{\perp} \approx d_{\pi} = 0.65$ fm, it is completely determined by the soft interactions. In particular, it is reliable to assume that at $d_{\perp} = d_{\pi}$ fm, the nuclear impact factor can be evaluated in the Glauber multiple scattering formalism:

$$\Gamma_A(x, b, d_{\perp}) = 1 - e^{-\frac{1}{2} A \sigma_{\pi N}(x) T_A(b)}, \quad (269)$$

where $\sigma_{\pi N}(x)$ is the total pion-nucleon cross section. In the intermediate region, $d_0 =$

$0.2 \text{ fm} \leq d_{\perp} \leq d_{\pi} = 0.65 \text{ fm}$, the nuclear impact factor is modeled by interpolating between the pQCD expression of Eq. (268) and the calculation at $d_{\perp} = 0.65 \text{ fm}$ of Eq. (269):

$$\Gamma_A(x, b, d_{\perp}) = [\Gamma_A(x, b, d_{\pi}) - \Gamma_A(x, b, d_0)] \frac{d_{\perp}^2 - d_0^2}{d_{\pi}^2 - d_0^2} + \Gamma_A(x, b, d_0). \quad (270)$$

Finally, for the dipoles with the size $d > d_{\pi}$, the nuclear impact factor is given by Eq. (269), where the total pion-nucleon cross section is allowed to slowly grow as

$$\sigma_{\pi N}(x, d_{\perp}) = \sigma_{\pi N} \frac{1.5 d_{\perp}^2}{d_{\perp}^2 + d_{\pi}^2/2}. \quad (271)$$

The interpolation is chosen so that for $d_{\perp}^2 = d_{\pi}^2$, the cross section is equal to $\sigma_{\pi N}$. It also takes into account the presence of the fluctuations of the strength of the πN interaction leading to $\sigma > \sigma_{\pi N}$ as indicated by the presence of the inelastic πN diffraction, see the discussion in Sec. 7.1.

The resulting nuclear impact factor is presented in Fig. 99. We plotted $\Gamma_A(x, b, d_{\perp})$ for ^{208}Pb as a function of the impact parameter b for different values of Bjorken x ($x = 10^{-5}$, 10^{-4} , and 10^{-3}) and dipole sizes d_{\perp} ($d_{\perp} = 0.2, 0.4$, and 0.6 fm). All curves correspond to $Q^2 = 4 \text{ GeV}^2$ (the dependence on Q^2 is weak and enters through the definition of x' in the dipole cross section). The solid (red) curves correspond to the nuclear shadowing for the gluon distribution in model FGS10_H; the dotted curves correspond to FGS10_L. For comparison, we also give the dot-dashed curves corresponding to the nuclear gluon distribution that is not shadowed (impulse approximation) and the thin solid (black) curves corresponding to the free proton case (same as in Fig. 98).

The results presented in Fig. 99 deserve a discussion.

(i) Model FGS10_H, which corresponds to larger shadowing than model FGS10_L, naturally leads to the smaller value of $\Gamma_A(x, b, d_{\perp})$. The difference between the two models increases as one decreases x and the amount of nuclear shadowing.

(ii) In both FGS10_H and FGS10_L models, nuclear shadowing at central impact parameters is very large. Therefore, at small b , the solid and dotted curves lie significantly below the dot-dashed curves. When b increases and becomes compatible to the nuclear size, $R_A \approx 7 \text{ fm}$ for ^{208}Pb , nuclear shadowing begins to rapidly disappear and all nuclear curves converge.

(iii) The b dependence of all nuclear curves is flat for $b < 7 \text{ fm}$, which is essentially determined by the nuclear optical density $T_A(b)$ and the nuclear size R_A . At the same time, the b dependence of the free nucleon impact factor is determined by the form factor $f(x, d_{\perp}, b)$ of Eq. (265), whose characteristic scale is the effective radius of the gluon distribution in the nucleon, which is smaller than 1 fm . This effective radius decreases as d_{\perp} is decreased, see Eq. (265), and, hence, the proton $\Gamma(x, b, d_{\perp})$ increases. Therefore, at very small dipole sizes, the proton $\Gamma(x, b, d_{\perp})$ can exceed the nuclear impact factor $\Gamma_A(x, b, d_{\perp})$.

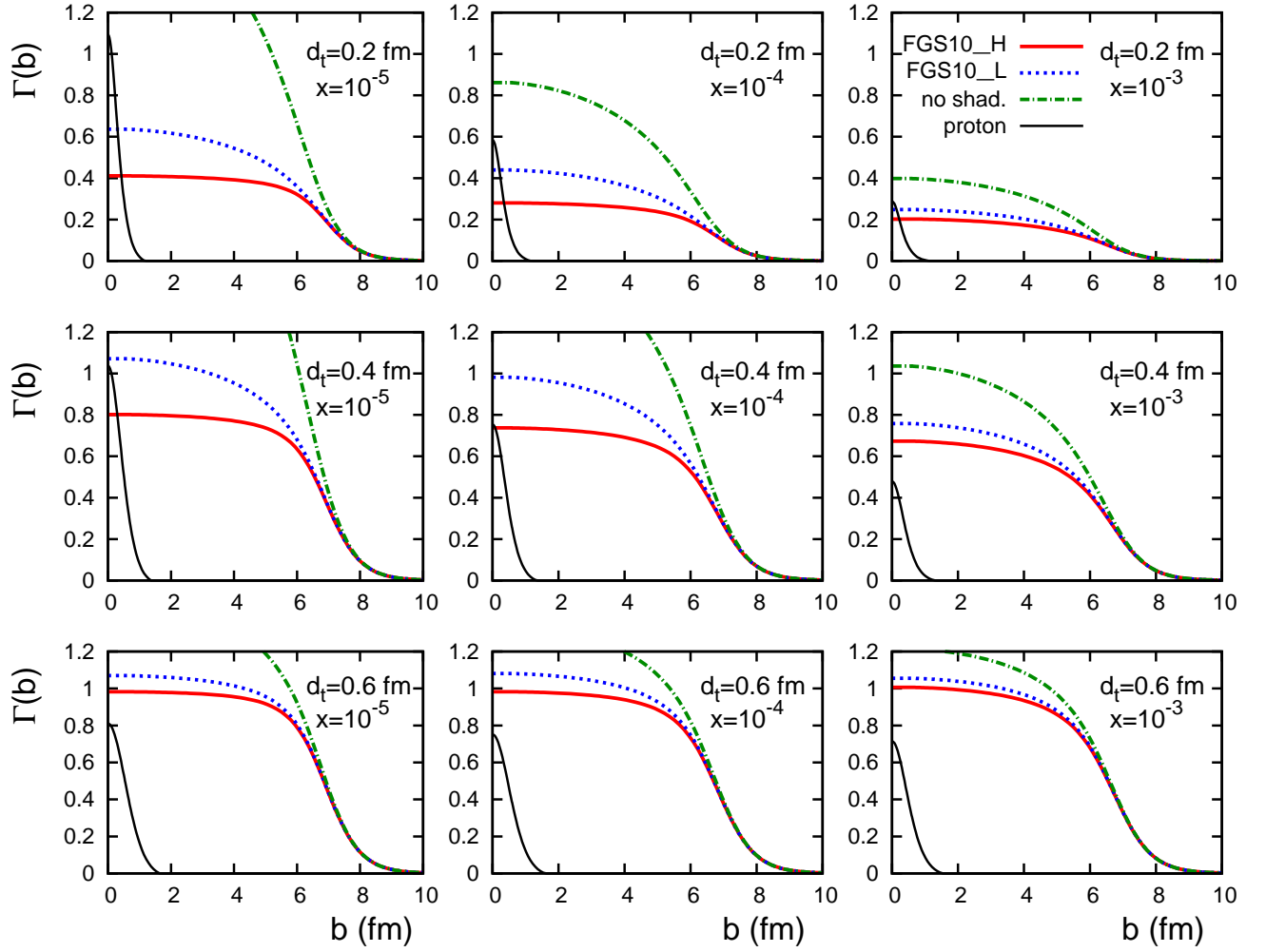


Fig. 99. The impact factor $\Gamma_A(x, b, d_\perp)$ for ^{208}Pb at $Q^2 = 4 \text{ GeV}^2$ as a function of the impact parameter b for different values of x and dipole sizes d_\perp . The solid (red) curves correspond to model FGS10.H; the dotted curves correspond to FGS10.L. For comparison, we also give the impulse approximation predictions for $\Gamma_A(x, b, d_\perp)$ by the dot-dashed curves and the free proton $\Gamma(x, b, d_\perp)$ by the thin solid (black) curves.

As we explained above, unitarity of the scattering matrix places the model-independent constraint of the impact factor: $\Gamma(x, b, d_\perp) \leq 1$. As one can see from Figs. 98 and 99, this unitarity constraint is not always satisfied in the dipole formalism, unless special measures are taken; we will not discuss ways and means to correct the dipole formalism to make it to comply with the unitarity constraint.

It follows from the QCD factorization theorem that the interaction with a target of a colorless two-gluon dipole or a dipole, where a gluon is substituted by a $q\bar{q}$ pair, is larger than that for a $q\bar{q}$ dipole by the factor $F^2(8)/F^2(3) = 9/4$, where F^2 is the Casimir operator of color group $SU(3)_c$. Hence, the interaction of such dipoles with nucleons and nuclei reaches the BDR at significantly lower energies. One example of such processes is

diffraction into large masses ($M^2 \gg Q^2$) in DIS where the dominant role is played by the $q\bar{q}g$ component of the photon light-cone wave function.

8.5.2 Nuclear enhancement of the dipole cross section

Nuclei provide a better arena to study the dynamics of high parton densities than the free nucleon since (i) the number of partons in the transverse slice of a nucleus is enhanced by the number of nucleons and, (ii) the distribution of nuclear matter over impact parameters is almost flat. In the language of the impact factors, the nuclear $\Gamma_A(x, b, d_\perp)$ is enhanced compared to the free proton $\Gamma(x, b, d_\perp)$, but the enhancement is partially masked by nuclear shadowing.

To quantify this enhancement, we introduce the ratio of the nuclear to free proton impact factors, R_Γ :

$$\begin{aligned} R_\Gamma(x, Q^2, b, d_\perp) &\equiv \frac{\Gamma_A(x, b, d_\perp)}{\Gamma(x, b, d_\perp)} \\ &= \frac{g_A(x', Q_{\text{eff}}^2, b)}{f(x, d_\perp, b)g_N(x', Q_{\text{eff}}^2)} = \frac{AT_A(b)r_g(x', Q_{\text{eff}}^2, b)}{f(x, d_\perp, b)}. \end{aligned} \quad (272)$$

The second line is valid only for small dipoles, $d_\perp < 0.2$ fm, when the impact factors can be calculated in pQCD, see Eqs. (262) and (268). In this case, $r_g(x, Q^2, b) \equiv g_A(x, Q^2, b)/(AT_A(b)g_N(x, Q^2))$ is the factor characterizing the impact parameter dependent nuclear shadowing in the gluon channel, see Figs. 40, 41, and 42; $f(x, d_\perp, b)$ is the free nucleon two-gluon form factor, see Eqs. (265) and (266). The R_Γ factor somewhat depends on the used model for the dipole cross that enters through the model-dependent definitions of x' and Q_{eff}^2 . Still, the strongest model-dependence of the R_Γ factor in Eq. (272) comes from modeling of the nucleon two-gluon form factor $f(x, d_\perp, b)$. We also emphasize that R_Γ depends strongly on the impact parameter b through the rapid b dependence of $f(x, d_\perp, b)$, see Fig. 99.

Figure 100 presents our predictions for R_Γ of Eq. (272) for ^{208}Pb at $Q^2 = 4$ GeV² as a function of Bjorken x ; the results are given for two selected dipole sizes, $d_\perp = 0.2$ and 0.4 fm, and two values of the impact parameter b (see explanations below). The solid curves correspond to model FGS10_H; the dotted curves correspond to FGS10_L; the dot-dashed curves correspond to the nuclear gluon PDF in the impulse approximation (no shadowing).

Evidently (cf. Fig. 99), the lower limit on the value of R_Γ is achieved at the impact parameter $b = 0$; this case is presented in the two upper panels of Fig. 100. As one can see from Fig. 100, without the effect of the leading twist nuclear shadowing, $R_\Gamma(b = 0) \approx 2$. The strong nuclear shadowing in the gluon channel at small x reduces the enhancement

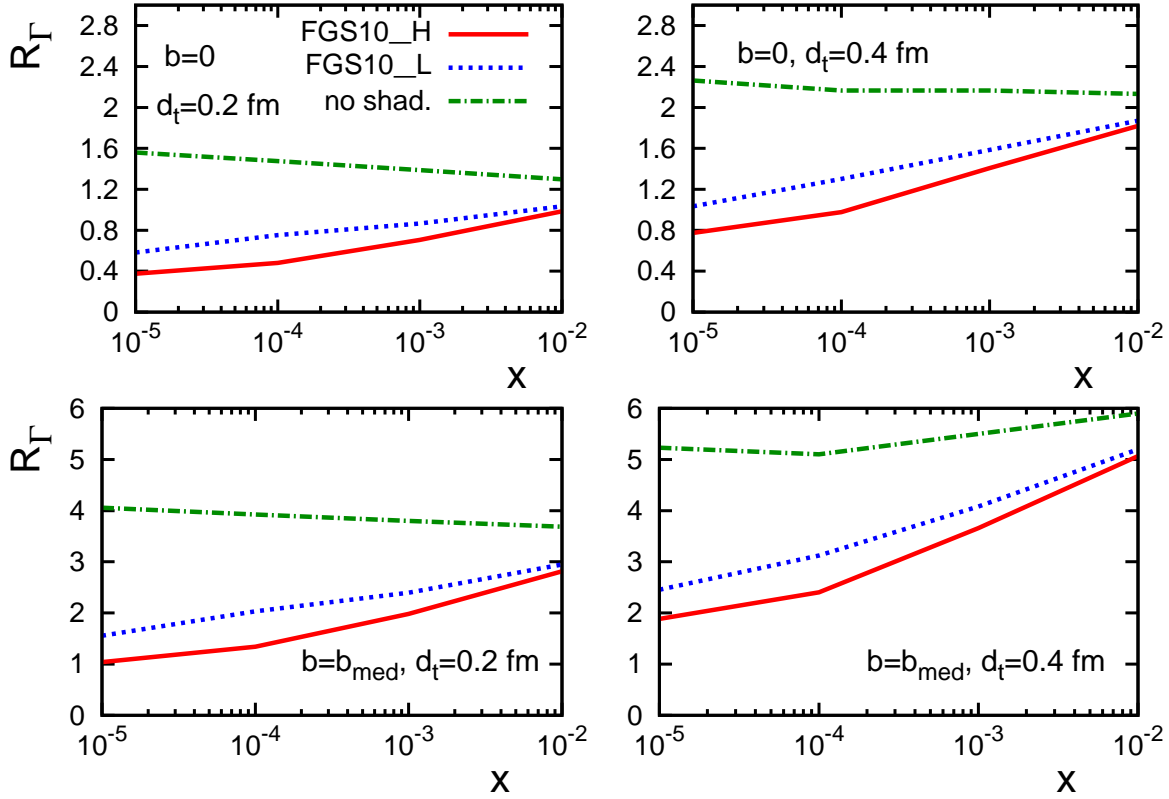


Fig. 100. The R_Γ factor of Eq. (272) for ^{208}Pb at $Q^2 = 4 \text{ GeV}^2$ as a function of Bjorken x for two values of the dipole size, $d_\perp = 0.2$ and 0.4 fm , and two values of the impact parameter b . The upper panels correspond to the central impact parameter $b = 0$; the lower panels correspond to the median impact parameter b_{med} [see Eq. (273)].

factor from $R_\Gamma(b = 0) \approx 2$ down to $R_\Gamma(b = 0) \approx 0.4 - 1.2$ at $x = 10^{-5} - 10^{-4}$. Therefore, for studies of the effects of high parton densities, which are probed when the values of the impact factor are close to unity, heavy nuclei at central impact parameters do not give any advantage over the free nucleon at $b = 0$. The advantage of nuclear targets is that the physics of large parton densities occupies a large volume in the impact parameter space.

The shapes of the b dependence of the nuclear $\Gamma_A(x, b, d_\perp)$ and free nucleon $\Gamma(x, b, d_\perp)$ are very different: while $\Gamma_A(x, b, d_\perp)$ is almost a step-function, the nucleon $\Gamma(x, b, d_\perp)$ is a steep function peaking at $b = 0$. Another possibility to compare the nucleus and nucleon impact factors is to compare them at a certain median value b_{med} that we define by the following relations:

$$\begin{aligned}
2\pi \int_0^{b_{\text{med}}} db b f(x, d_{\perp}, b) &= \frac{1}{2}, \\
2\pi \int_0^{b_{\text{med}}} db b T_A(b) &= \frac{1}{2}.
\end{aligned}
\tag{273}$$

Equation (273) corresponds to the situation when no selection of impact parameters is performed and, hence, it is natural to compare nucleon and nucleus cases for such b_{med} that half of the gluon density is located at $b > b_{\text{med}}$.

The values of b_{med} resulting from solving Eq. (273) are different for the nucleus and free nucleon. For instance, for the nucleon, b_{med} varies between $b_{\text{med}} = 0.41$ fm at $d_{\perp} = 0.2$ fm and $x = 0.01$ and $b_{\text{med}} = 0.73$ fm at $d_{\perp} = 0.6$ fm and $x = 10^{-5}$ (at fixed d_{\perp} , the x dependence of b_{med} is weak). For the nucleus of ^{208}Pb , $b_{\text{med}} = 2.5$ fm. While the nucleon $\Gamma(x, b = b_{\text{med}}, d_{\perp})$ is significantly smaller than $\Gamma(x, b = 0, d_{\perp})$ (by at least a factor of two), the nuclear $\Gamma_A(x, b = b_{\text{med}}, d_{\perp})$ is essentially the same as $\Gamma_A(x, b = 0, d_{\perp})$. Therefore, $R_{\Gamma}(b_{\text{med}})$ should be larger than $R_{\Gamma}(b = 0)$ by at least a factor of two. The enhancement factor R_{Γ} at $b = b_{\text{med}}$ as a function of Bjorken x is presented in the two lower panels of Fig. 100.

While our numerical results for R_{Γ} in the unrealistic scenario when the leading twist nuclear shadowing is neglected (dot-dashed curves in Fig. 100) are in a quantitative agreement with the nuclear enhancement of the saturation scale Q_s^2 discussed in Ref. [272], our principal predictions for R_{Γ} in the framework of the leading twist nuclear shadowing (solid and dotted curves in Fig. 100) correspond to a significantly smaller enhancement than in the model of [272].

8.5.3 Probability conservation as the constraint on the region of applicability of the LT approximation

The application of QCD factorization theorems, LO and NLO approximations leads to the contradiction with the probability conservation due to the non-linear relations between QCD Green functions. Within these approximations, the violation of the probability conservation for the interaction of small dipoles follows from the mismatch between the inelastic cross section increasing with energy $\propto x g_T(x, Q^2)$ and the elastic/diffractive cross section $\propto [x g_T(x, Q^2)]^2$, where $g_T(x, Q^2)$ is the gluon density of the target. The mismatch progressively increases with a decrease of x and ultimately breaks down the condition that $\sigma_{\text{el}} \leq \sigma_{\text{inel}}$. Note that a more accurate treatment would involve generalized parton distributions (GPDs) for the description of diffractive processes. However, the account of the QCD evolution demonstrated that this will not change significantly the x and Q^2 dependencies, but will somewhat increase the absolute value of the diffractive cross section, see, e.g., [74].

The strongest constraint on the kinematical region of applicability of the LT approximation follows from the requirement of probability conservation at small impact parameters. In the derivation, one uses the impact parameter representation of the dipole-target scattering amplitude (253) and determines how close the resulting impact factor $\Gamma(x, b, d_\perp)$ is to unity.

Let us begin our quantitative consideration from the analysis of the interaction of a colorless $q\bar{q}$ dipole with a hadron (nucleus) target. It was explained above that the probability conservation places the model-independent constraint of the impact factor, $\Gamma(x, b, d_\perp) \leq 1$. As one can see from Figs. 98 and 99, this constraint is not satisfied at very small x in the dipole model or, more generally, in pQCD. However, the $q\bar{q}$ dipole-nucleon interaction still remains rather far from the unitarity limit for small dipoles with $d_\perp \leq 0.3$ fm (i.e., for the dipoles of the size comparable to the size of J/ψ or smaller) practically in the whole range of energies available at HERA, except at very small b , which contribute very little to the total cross section. This constraint can be made more explicit by introducing the critical dipole size, d_{BDR} , for which the impact factor Γ is rather close to unity, e.g.:

$$\Gamma(x, b, d_{\text{BDR}}) = \frac{3}{4}. \quad (274)$$

Figure 101 presents d_{BDR} [the solution of Eq. (274)] for ^{208}Pb at $Q^2 = 4 \text{ GeV}^2$ as a function of Bjorken x at the central impact parameter $b = 0$. The thick solid curve corresponds to model FGS10_H; the dotted curve corresponds to FGS10_L; the dot-dashed curve corresponds to the nuclear gluon PDF in the impulse approximation (no shadowing). Also, for comparison, the thin solid curve gives the solution of Eq. (274) for the free proton case.

The results presented in Fig. 101 deserve a discussion.

- (i) The nuclear shadowing in the gluon channel is larger in model FGS10_H than that in model FGS10_L. Therefore, the impact factor in model FGS10_H is smaller than that in model FGS10_L and, hence, the transverse sizes solving Eq. (274), d_{BDR} , are larger for FGS10_H than for FGS10_L.
- (ii) By turning off the leading twist nuclear shadowing, one significantly increases the nuclear impact factor, which can now reach its limiting value for rather small dipole sizes (the dot-dashed curve in Fig. 101). Remarkably, for $x \leq 10^{-4}$, the corresponding $d_{\text{BDR}} < 0.2$ fm, which means that it is determined using the perturbative expression (268), i.e., in a model-independent way. Note that in the limit of large x , $x \geq 0.01$, the effect of nuclear shadowing is small and all nuclear curves in Fig. 101 converge to the regime of small parton density.

An increase of the impact parameter away from $b = 0$ in Eq. (274) and in Fig. 101 will lead to (i) an increase of d_{BDR} (models FGS10_L and FGS10_H), and (ii) the disappearance of the reaching of the BDR regime in the free proton case.

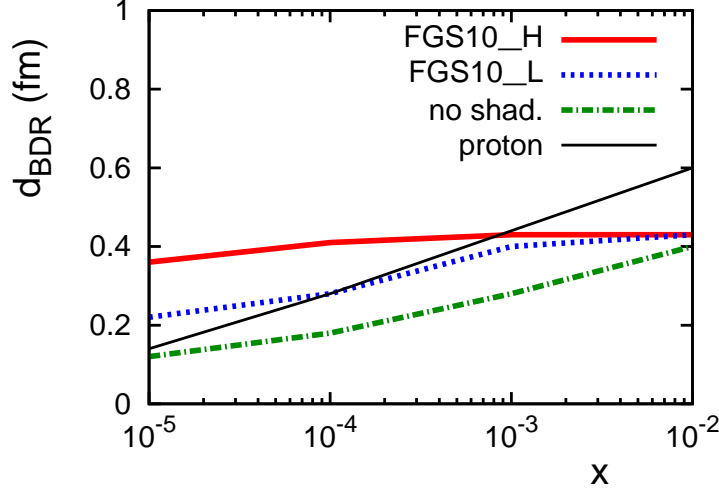


Fig. 101. The critical transverse dipole size d_{BDR} of Eq. (274) for ^{208}Pb at $Q^2 = 4 \text{ GeV}^2$ as a function of Bjorken x at the central impact parameter $b = 0$. The thick solid curve corresponds to model FGS10_H; the dotted curve corresponds to FGS10_L; the dot-dashed curve corresponds to the nuclear gluon PDF in the impulse approximation (no shadowing). For comparison, the thin solid curve gives d_{BDR} for the free proton case.

For $x \leq 10^{-3}$, we approximately parameterize the x (energy) dependence of d_{BDR} in the following simple form:

$$d_{\text{BDR}}(x) = (x/x_0)^n d_{\text{BDR}}(x_0), \quad (275)$$

where $x_0 = 0.001$. By fitting to the points in Fig. 101, we find that $n \approx 0.04$ for model FGS10_H, $n \approx 0.13$ for model FGS10_L, $n \approx 0.18$ for the no-shadowing case, and $n \approx 0.21$ for the free proton case. Note that these values correspond to $Q^2 = 4 \text{ GeV}^2$. As one increases Q^2 , the exponent n in Eq. (275) should also increase. Therefore, after the BDR has been reached for the dipoles of sufficiently small sizes for which the pQCD approach is applicable for moderate x , the further expansion of the BDR to smaller d_{\perp} becomes rather rapid.

The situation with the unitarity constraint is different in the gluon channel since the interaction of a colorless dipole built of color octet constituents is significantly stronger than for the color singlet $q\bar{q}$ dipole. In particular, in the pQCD regime, the inelastic cross section is stronger by the factor of 9/4 and by the factor of 81/16 in the elastic channel. The inelastic impact factor for the colorless dipole with color octet constituents, $\Gamma_{\text{inel}}^{gg}$, can be obtained by the rescaling of the inelastic $q\bar{q}$ dipole impact factor:

$$\Gamma^{gg,\text{inel}}(x, b, d_{\perp}) = \frac{9}{4} \Gamma^{\text{inel}}(x, b, d_{\perp}), \quad (276)$$

in the kinematics where the resulting $\Gamma^{gg,\text{inel}}(x, b, d_{\perp})$ is still smaller than unity.

Equation (276) allows us to quantitatively study the approach to the BDR in the gluon channel when the probability of inelastic interactions is close to unity. For instance, we can define the critical size d'_{BDR} for which $\Gamma_{\text{inel}}^{gg}(x, b, d'_{BDR}) = 3/4$, or equivalently, the total impact factor $\Gamma^{gg}(x, b, d'_{BDR}) = 1/2$, see Eqs. (256) and (268). It follows from Eq. (256) that this value of $\Gamma^{gg}(x, b, d_{\perp})$ is reached for $\Gamma(x, b, d_{\perp}) = 1 - \sqrt{2/3} \approx 0.18$. As one can see from Fig. 98, this value of $\Gamma(x, b, d_{\perp})$ is reached in a rather wide range of b and x at $Q^2 = 4 \text{ GeV}^2$, which is near the edge of the HERA kinematics.

One should also note that the fact that $\Gamma^{gg}(x, b, d_{\perp}) \gg \Gamma(x, b, d_{\perp})$ implies the significantly larger diffraction in the gluon channel compared to the quark one for moderate values of Q^2 , $Q^2 \sim 4 \text{ GeV}^2$, which is indeed indicated by the analysis of the HERA inclusive diffraction data—see the discussion in Sec. 3.5.

To estimate the proximity to the BDR in the gluon channel in the case of scattering off nuclei, one can again use the rescaling of the $q\bar{q}$ -nucleus impact factor, Eq. (276), along with the model for $\Gamma_A(x, b, d_{\perp})$, see the discussion in Sec. 8.5. The onset of the BDR in the gluon channel can be inferred from Fig. 99, in a direct analogy to the case of the $q\bar{q}$ dipole discussed above.

We can also introduce the maximal transverse momentum of the gluon, for which the interaction is close to the BDR:

$$p_{t,\text{BDR}} \equiv \frac{\pi}{2d'_{\text{BDR}}}. \quad (277)$$

For $p_t \leq p_{t,\text{BDR}}$, the interaction is close to the BDR and, hence, the average transverse momenta are also close to $p_{t,\text{BDR}}$. In the opposite limit, the condition for the applicability of the LT approximation is that

$$Q_0^2 \gg 4p_{t,\text{BDR}}^2. \quad (278)$$

Finally, we remark that the restrictions due to the probability conservation are less severe for inclusive structure functions where the region around $b = 0$ gives only a small contribution to the integrated quantity. These restrictions play a more important role in the description of the structure of the final states in the new particle production, especially in multiparton interactions since the dijet production is dominated by the scattering at small impact parameters.

8.5.4 BDR predictions for inclusive structure functions

We demonstrated above that when the BDR is reached, it is reached only for a small fraction of all dipoles. However, if we consider asymptotically large energies, d_{BDR} will

progressively decrease and one will encounter the situation when the dominant contribution to $F_{T,L}^{\text{inel}}(x, Q^2, b)$ comes from the region $d_{\perp} \geq d_{\text{BDR}}$ for which $\Gamma_{\text{inel}}(x, b, d_{\perp}) = 1$. If this limit is reached for all essential impact parameters b , the dipole interacts with the nucleon (nucleus) with the maximal total cross section allowed by the conservation of probability.

In the preceding sections we explained that within the BDR, essential impact parameters increase with an increase of energy. The BDR expression for the dipole-nucleon cross has the following form:

$$\begin{aligned}\sigma_{q\bar{q}N}(x, Q^2, d_{\perp}) &= \Theta(d_{\perp} - d_{\text{BDR}})2\pi R_N^2(1 + c_N \ln^2(x_0/x)) + \Theta(d_{\text{BDR}} - d_{\perp})\sigma_{q\bar{q}N}^{LT} \\ &= \Theta(d_{\perp} - d_{\text{BDR}})2\pi R_{N,\text{eff}}^2 + \Theta(d_{\text{BDR}} - d_{\perp})\sigma_{q\bar{q}N}^{LT},\end{aligned}\quad (279)$$

where c_N is a constant; R_N is the nucleon radius. To simplify formulas we introduced the quantity $R_{N,\text{eff}}^2$. To account for the interaction of the dipoles whose size is sufficiently small, we included the leading twist contribution of $\sigma_{q\bar{q}N}^{LT} = \sigma_{q\bar{q}N}^{\text{inel}}$ (262). This LT contribution follows from the QCD factorization theorem and rapidly increases with energy; it was discussed in the preceding sections dealing with the small parton density limit.

The cross section for the dipole scattering off a nuclear target has the same form as for the nucleon target except for specifics related to the large nuclear radius R_A :

$$\begin{aligned}\sigma_{q\bar{q}A}(x, Q^2, d_{\perp}) &= \Theta(d_{\perp} - d_{\text{BDR}})2\pi[R_A^2 + cR_A R_N \ln^2(x_0/x)] + \Theta(d_{\text{BDR}} - d_{\perp})\sigma_{q\bar{q}A}^{LT} \\ &= \Theta(d_{\perp} - d_{\text{BDR}})2\pi R_{A,\text{eff}}^2 + \Theta(d_{\text{BDR}} - d_{\perp})\sigma_{q\bar{q}A}^{LT},\end{aligned}\quad (280)$$

where R_A is the nucleus radius. In the above formula, we account for the fact that the interaction of the virtual photon at the impact parameters close to the nucleus edge produces the cross section close to that for a nucleon target up to the factor accounting for the number of nucleons within the nuclear edge. To simplify the formula, we introduce $R_{A,\text{eff}}$ — the effective radius of the interaction which increases with energy; c is a constant. The LT contribution $\sigma_{q\bar{q}A}^{LT}$ has been discussed in the review with respect to the weak parton density limit including nuclear shadowing phenomenon.

In the momentum representation, the onset of the BDR for pQCD interactions at extremely small x corresponds to the situation when the average transverse momenta in the quark loop in the photon wave function are (much) larger than the photon virtuality Q , which clearly corresponds to a breakdown of the DGLAP and BFKL approximations. This result follows from the application of the k_t factorization theorem to small x processes. Note that the onset of this regime can already be seen in the DGLAP approximation as the average transverse momenta of quarks in the quark loop attached to the photon gradually increase with a decrease of x [225].

Using Eq. (260) and the discussion following it, the BDR prediction for the inclusive structure functions of heavy nuclei reads:

$$\begin{aligned}
F_{T,L}^A(x, Q^2) &= \frac{Q^2}{4\pi^2\alpha_{\text{em}}} \int_0^1 dz \int_{d_{\text{BDR}}^2}^{d_{\text{soft}}^2} d^2 d_{\perp} \sum_i |\Psi_{T,L}(z, Q^2, d_{\perp}^2, m_i^2)|^2 2\pi R_{A,\text{eff}}^2 \\
&\quad + F_{T,L}^{LT,A}(x, Q_{\text{eff}}^2).
\end{aligned} \tag{281}$$

The BDR is present on the interval $d_{\text{BDR}} \leq d_{\perp} \leq d_{\text{soft}}$, where d_{BDR} is the boundary of the kinematical region where the interaction of the dipole is still black and is calculable in pQCD; d_{soft} is a scale of the order of $1/\Lambda_{\text{QCD}}$, which cuts from above the integral over the dipole sizes. The last term in the above equation is the LT contribution from the dipoles in the wave function of the virtual photon of the transverse sizes $d_{\perp} \leq d_{\text{BDR}}$ whose value and properties follow from the QCD factorization theorem; $Q_{\text{eff}}^2 \geq Q_{\text{BDR}}^2$ and is calculable using the above formulas for the dipole-nucleus interaction. To shorten formulae in the following discussion, we will often omit the LT term whose properties were thoroughly discussed in the review. To obtain a direct correspondence with the Feynman diagrams, it is convenient to work in the momentum representation for the $q\bar{q}$ component of the photon light-cone wave function,

$$\Psi_{T,L}(z, Q^2, k_{\perp}^2, m_i^2) = \int d^2 d_{\perp} e^{-id_{\perp} k_{\perp}} \Psi_{T,L}(z, Q^2, d_{\perp}^2, m_i^2), \tag{282}$$

where we suppressed the indices labeling the photon and quark helicities. The squared light-cone wave functions of the transversely and longitudinally-polarized photon in the momentum space read, see, e.g., [273]:

$$\begin{aligned}
|\Psi_T(z, Q^2, k_{\perp}^2, m_i^2)|^2 &= 6\alpha_{\text{em}} e_i^2 (z^2 + (1-z)^2) \frac{k_{\perp}^2}{(k_{\perp}^2 + Q^2 z(1-z) + m_i^2)^2}, \\
|\Psi_L(z, Q^2, k_{\perp}^2, m_i^2)|^2 &= 24\alpha_{\text{em}} e_i^2 z^2 (1-z)^2 \frac{Q^2}{(k_{\perp}^2 + Q^2 z(1-z) + m_i^2)^2}.
\end{aligned} \tag{283}$$

Equation (281) can be identically rewritten in the momentum representation in the following form:

$$F_{L,T}^A(x, Q^2) = \frac{Q^2}{4\pi^2\alpha_{\text{em}}} \int_0^1 dz \int_0^{k_{i,\text{max}}^2} \frac{d^2 k_{\perp}}{(2\pi)^2} \sum_i |\Psi_{L,T}(z, Q^2, k_{\perp}^2, m_i^2)|^2 2\pi R_{A,\text{eff}}^2, \tag{284}$$

where k_{\perp} has the meaning of the transverse momentum of each quark (orthogonal to the momentum of the virtual photon). Thus, the quark constituent of the $q\bar{q}$ dipole is characterized by the longitudinal momentum fraction z and the transverse momentum k_{\perp} , while the antiquark is characterized by $1-z$ and $-k_{\perp}$. In Eq. (284), we implicitly used the orthogonality of the wave functions of the eigenstates of the QCD Hamiltonian with different energies. As a consequence, the interaction in the BDR is diagonal in z

and k_\perp , c.f. [270]. (Note that Ψ_L results from the cancellation of the components of the polarization vector of a longitudinally polarized photon that separately linearly increase with energy.)

Next, it is convenient to define the mass squared of the $q\bar{q}$ system,

$$M^2 = \frac{k_\perp^2 + m_q^2}{z(1-z)}, \quad (285)$$

and the angle θ between the direction of the momentum of the quark in the center of mass frame and the photon direction (the transverse plane is defined to be perpendicular to this). Neglecting the quark mass m_i^2 compared to M^2 and Q^2 , one obtains:

$$\sin \theta = \frac{2p_t}{\sqrt{M^2}}, \quad z = \frac{1}{2}(1 + \cos \theta). \quad (286)$$

Changing the variables ($|k_\perp|^2, z$) to $(M^2, \cos \theta)$, we readily obtain from Eq. (284) the BDR predictions for the nuclear inclusive structure functions [264]:

$$F_T^A(x, Q^2) = \int_0^{M_{\max}^2} dM^2 \frac{2\pi R_{A,\text{eff}}^2}{12\pi^3} \frac{Q^2 M^2 \rho(M^2)}{(M^2 + Q^2)^2} \int_{-1}^1 d\cos \theta \frac{3}{8} (1 + \cos^2 \theta), \quad (287)$$

$$F_L^A(x, Q^2) = \int_0^{M_{\max}^2} dM^2 \frac{2\pi R_{A,\text{eff}}^2}{12\pi^3} \frac{Q^4 \rho(M^2)}{(M^2 + Q^2)^2} \int_{-1}^1 d\cos \theta \frac{3}{4} \sin^2 \theta, \quad (288)$$

where

$$\rho(M^2) = \sigma^{e^+e^- \rightarrow \text{hadrons}} / \sigma^{e^+e^- \rightarrow \mu^+\mu^-} \approx N_c \sum_i e_i^2. \quad (289)$$

In Eq. (289), $N_c = 3$ is the number of colors; the last equality holds to the leading order in the strong coupling constant α_s . The inclusion of $\rho(M^2)$ in Eqs. (287) and (288) corrects the dipole formulas for higher order corrections (in α_s) contributing at a given M^2 . Moreover, the BDR expressions are insensitive to the number of constituents in the photon wave function. This is due to the theorem—which is well known in QED and QCD—that as a consequence of gauge invariance, the sum over the amplitudes squared for the transitions $\gamma^* \rightarrow q + \bar{q} + g$ gives the polarization operator of the photon with off-shell quarks, i.e., $\rho(M^2)$. We point out again that in the BDR, as a result of the orthogonality of the eigenstates of QCD Hamiltonian with different energies, the non-diagonal transitions between the states with different M^2 in Eqs. (287) and (288) vanish [270].

The integration over θ in Eqs. (287) and (288) can now be performed analytically and one obtains the BDR predictions for the transverse and longitudinal structure functions [264]:

$$F_T^A(x, Q^2) = \frac{2\pi R_{A,\text{eff}}^2}{12\pi^3} Q^2 \rho(M_{\text{max}}^2) \ln(M_{\text{max}}^2/m_0^2) = \frac{2\pi R_{A,\text{eff}}^2}{12\pi^3} Q^2 \rho(M_{\text{max}}^2) \ln(x_0/x), \quad (290)$$

$$F_L^A(x, Q^2) = \frac{2\pi R_{A,\text{eff}}^2}{12\pi^3} Q^2 \rho(M_{\text{max}}^2). \quad (291)$$

When one takes into account only the suppression induced by the square of the nuclear form factor in the rescattering amplitude, then $M_{\text{max}}^2 \leq W^2/(m_N R_A)$, and Eqs. (287) and (288) coincide with the original result of [270], except for the account of the effective nuclear radius $R_{A,\text{eff}}$ increasing with energy. However, in QCD, because of the color transparency, M_{max}^2 is determined by the unitarity constraint and is substantially smaller than $W^2/(m_N R_A)$. Since $M_{\text{max}}^2 \propto Q^2 x^{-n}$ with $n \approx 0.1$, the proportionality of $F_T^A(x, Q^2)$ to $\ln(x_0/x)$ derived by Gribov is retained, but the numerical coefficient is much smaller.

It is important to emphasize that the contribution of small transverse size configurations (which have not reached the BDR) remains significant in a wide range of x and Q^2 . Hence, studies of the total cross sections are a rather ineffective way to search for the onset of the BDR. In particular, it may be rather difficult to distinguish the BDR from the DGLAP approximation with different initial conditions.

Note that the BDR will reveal itself in the interaction of the $q\bar{q}g$ component of the photon wave function with a hadron (nucleus) target at smaller energies compared to the $q\bar{q}$ component. In the leading twist approximation, it will be double counting to consider the $q\bar{q}g$ component since it is included in the interaction; in the BDR, the situation is different.

In what follows we shall demonstrate that studies of DIS final states provide a number of clear signatures of the onset of the BDR, which will be qualitatively different from the leading twist regime. For simplicity, we will assume that the BDR is reached for a significant part of the cross section and, hence, restrict our discussion to DIS on a large nucleus so that edge effects (which are important in the case of scattering off a nucleon) can be neglected.

8.6 Diffractive final states

In Eqs. (287) and (288), the mass M is the mass of the diffractively produced state. Removing the integral over M^2 and noticing that in the BDR diffraction constitutes 50% of all events, we readily obtain predictions for the diffractive structure functions (the

spectrum of the masses of diffractively produced states) from Eqs. (287) and (288):

$$\frac{dF_T^{D(3)}(x, Q^2, M^2)}{dM^2} = \frac{\pi R_{A,\text{eff}}^2 Q^2 M^2 \rho(M^2)}{12\pi^3 (M^2 + Q^2)^2}, \quad (292)$$

$$\frac{dF_L^{D(3)}(x, Q^2, M^2)}{dM^2} = \frac{\pi R_{A,\text{eff}}^2 Q^4 \rho(M^2)}{12\pi^3 (M^2 + Q^2)^2}. \quad (293)$$

Moreover, the spectrum of hadrons in the center of mass of the diffractively produced system should be the same as in e^+e^- annihilation. Hence, the dominant diffractively produced final state will have two jets with a distribution over the center of mass emission angle proportional to $1 + \cos^2 \theta$ for the transverse case and proportional to $\sin^2 \theta$ for the longitudinal case [264]:

$$\frac{dF_T^{D(3)}(x, Q^2, M^2)}{dM^2 d \cos \theta} = \frac{3}{8} (1 + \cos^2 \theta) \frac{\pi R_{A,\text{eff}}^2 Q^2 M^2 \rho(M^2)}{12\pi^3 (M^2 + Q^2)^2}, \quad (294)$$

$$\frac{dF_L^{D(3)}(x, Q^2, M^2)}{dM^2 d \cos \theta} = \frac{3}{4} \sin^2 \theta \frac{\pi R_{A,\text{eff}}^2 Q^4 \rho(M^2)}{12\pi^3 (M^2 + Q^2)^2}. \quad (295)$$

The transverse momentum of the produced jet, $p_t = k_\perp$, and the longitudinal fraction of the photon energy carried by the jet, z , are related to the diffractive mass M and the angle θ by Eq. (286). Hence, in the BDR, diffractive production of high p_t jets is strongly enhanced:

$$\begin{aligned} \langle p_t^2(jet) \rangle_T &= 3M^2/20, \\ \langle p_t^2(jet) \rangle_L &= M^2/5. \end{aligned} \quad (296)$$

This should be compared to the leading twist approximation where $\langle p_t^2(jet) \rangle \propto \ln Q^2$.

The relative rate and distribution of the jet variables for the three jet events (originating from $q\bar{q}g$ configurations) will also be the same as in e^+e^- annihilation and, hence, is given by the standard expressions for the $e^+e^- \rightarrow q\bar{q}g$ subprocess (see e.g., Ref. [274]). The inelastic cross section of the interaction of a color octet dipole is enhanced in pQCD by the factor of 9/4 as compared to the interaction of the triplet $q\bar{q}$ dipole. As a result, the onset of the BDR occurs earlier for processes dominated by the octet configurations, such as the emission of gluons at large angles relative to q and \bar{q} . Consequently, for k_t in the vicinity of the BDR, one expects the enhanced production of the star-like three jet events.

An important advantage of the diffractive BDR signal is that the discussed features of the diffractive final states should hold for $M^2 \leq Q_{\text{BDR}}^2$ (Q_{BDR} is a characteristic scale of

the BDR), even if $Q^2 \geq Q_{\text{BDR}}^2$ because the configurations with the transverse momenta $p_t \leq Q_{\text{BDR}}/2$ still interact in the black disk regime (and correspond to the fluctuations of the transverse size for which the interaction is already black/maximal).

Next we turn to exclusive vector meson production, which in the BDR is in a sense a resurrection of the original vector meson dominance model [275] without off-diagonal transitions. The amplitude of the vector meson-nucleus interaction is proportional to $2\pi R_{A,\text{eff}}^2$ (since each configuration in the virtual photon interacts with the same BDR cross section). This is markedly different from the requirements [137] for matching of generalized vector dominance models (VMD) (see, e.g., [276]) with QCD in the scaling limit. In generalized VMD models, the matrix elements for the non-diagonal transitions between vector mesons are large and lead to strong cancellations mimicking the approximate scaling.

In the BDR, we can factorize out the dipole-nucleus cross section from the overlap integral between the virtual photon and vector meson wave functions and obtain the dominant contribution to the differential cross section of the electroproduction of vector mesons [264]:

$$\begin{aligned} \frac{d\sigma^{\gamma_T^*+A \rightarrow V+A}}{dt} &= \frac{M_V^2}{Q^2} \frac{d\sigma^{\gamma_L^*+A \rightarrow V+A}}{dt} \\ &= \frac{(2\pi R_{A,\text{eff}}^2)^2}{16\pi} \frac{3\Gamma_V M_V^3}{\alpha_{\text{em}}(M_V^2 + Q^2)^2} \frac{4 \left(J_1(\sqrt{|t|} R_{A,\text{eff}}) \right)^2}{|t| R_{A,\text{eff}}^2}, \end{aligned} \quad (297)$$

where Γ_V is the electronic decay width $V \rightarrow e^+e^-$; M_V is the vector meson mass; α_{em} is the fine-structure constant; $J_1(x)$ is the Bessel function. Therefore, the parameter-free BDR prediction that at large Q^2 the vector meson electroproduction initiated by longitudinally-polarized photons behaves as $1/Q^2$ is in a stark contrast with the $1/Q^6$ asymptotic behavior predicted in perturbative QCD [194,216,234]. This makes this reaction very attractive for scanning the transition from the BDR at small Q^2 to the pQCD regime at large Q^2 .

8.7 Post-selection mimicking fractional parton energy losses in inclusive spectra in the vicinity of BDR

In the leading twist approximation, the QCD factorization theorem is valid and leads to the prediction of universal spectra of leading particles (independent of the target) for the scattering off partons of the same flavor. Fundamentally, this can be explained by the fact that, in the Breit frame, the fast parton which is hit by the photon carries practically all of the photon's light-cone momentum ($z \rightarrow 1$). As a result of the QCD evolution, this parton acquires the virtuality $\sim \sqrt{Q^2 Q_0^2}$ and a rather large transverse momentum k_t^2 (which is still $\ll Q^2$). So, in pQCD, quarks and gluons emitted in the process of QCD

evolution and fragmentation of highly virtual partons carry all the photon momentum.

In contrast, in the BDR, the projectile interacts with several nucleons at the same impact parameter. Hence, it follows from the energy-momentum conservation that different subgroups of partons within the wave function of the photon should interact with different nucleons. [These configurations are rather similar to the ones dominating diffractive scattering, see e.g., Eqs. (294) and (295).] The total momentum carried by all subgroups is equal to the photon momentum. As a result, the fraction of the photon momentum carried by any subgroup is less than unity. Thus, the target post-selects different configurations in the projectile depending on the number of nucleons at the same impact parameter and the strength of the interaction. Fragmentation of an individual subgroup into hadrons produces leading hadrons with total energies equal to the energy of the subgroup. Hence, in the BDR case, the spectrum of leading hadrons (in the direction of the virtual photon) is expected to be noticeably more depleted than in the pQCD regime. Although no energy losses occur for the partons propagating through the target, the selection of subgroups of partons effectively looks as significant fractional energy losses.

Neglecting the contribution of $q\bar{q}g$ configurations to the photon wave function, the leading hadron spectrum can be obtained from the θ dependence in Eqs. (294) and (295). For fixed M^2 , the jet distribution over the light-cone fraction z has the following dependence [264]:

$$\begin{aligned}\frac{d\sigma_T}{dz} &\propto 1 + (2z - 1)^2, \\ \frac{d\sigma_L}{dz} &\propto z(1 - z),\end{aligned}\tag{298}$$

where the subscripts denote the transversely and longitudinally polarized photons.

If no special L-T separation procedure is undertaken, at small x one actually measures $\sigma_L + \epsilon\sigma_T$ (ϵ is the photon polarization). In this case, combining Eqs. (294) and (295) we find:

$$\frac{d(\sigma_T + \epsilon\sigma_L)}{dz} \propto \frac{M^2}{8Q^2}(1 + (2z - 1)^2) + \epsilon z(1 - z).\tag{299}$$

In the approximation of Eq. (298), the inclusive spectrum of leading hadrons can be estimated assuming the independent fragmentation of the quark and antiquark with the virtualities $\geq Q^2$ and z and p_t distributions given by Eqs. (294) and (295) (cf. the case of diffractive production of jets discussed above). The independence of fragmentation is justified because large transverse momenta of the quarks dominate in the photon wave function [cf. Eqs. (294) and (295)] and because of the weakness of the final state interaction between q and \bar{q} since α_s is small and the rapidity interval is of the order of unity. Obviously, the independent fragmentation leads to a gross depletion of the leading hadron

spectrum compared to the leading twist approximation where leading hadrons are produced in the fragmentation region of the parton which carries essentially all momentum of the virtual photon. Qualitatively, this pattern is similar to the one expected in the soft regime of the strong interaction since the spectrum of hadrons produced in hadron-nucleus interactions is much softer than that in hadron-nucleon interactions. In addition, taking into account the production of multi-jet states—like $q\bar{q}g$ —will further enhance the departure from the leading twist picture of fragmentation.

Neglecting the gluon emission in the photon wave function, we readily obtain for the total differential multiplicity of leading hadrons in the BDR:

$$\begin{aligned}\frac{dN^{\gamma_T^*/h}}{dz} &= 2 \int_z^1 dy D^{q/h}(z/y, Q^2) \frac{3}{4}(1 + (2y - 1)^2), \\ \frac{dN^{\gamma_L^*/h}}{dz} &= 2 \int_z^1 dy D^{q/h}(z/y, Q^2) 6y(1 - y).\end{aligned}\tag{300}$$

In Eq. (300), $D^{q/h}(z/y, Q^2)$ is the fragmentation function of a quark of flavor q into the hadron h (more accurately, it is the sum of the quark and antiquark fragmentation functions); the factor of two in front of the integrals comes from the fact that we included two quark flavors and assumed that $D^{u/h}(z/y, Q^2) = D^{d/h}(z/y, Q^2)$. The contribution of heavier flavors has been neglected.

An illustration of the results of the calculation of $dN^{\gamma_{T,L}^*/h}/dz$ is presented in Fig. 102. In this figure, we plot the ratio $dN^{\gamma_{T,L}^*/h}/dz/[2D^{u/h}(z, Q^2)]$ as a function of the momentum fraction z . The solid curve corresponds to the transverse photons; the dotted curve corresponds to the longitudinal photons. In the absence of the BDR modifications of the spectrum of the produced particles, this ratio would be unity. For $D^{u/h}(z, Q^2)$, we used the LT up-quark fragmentation function of Ref. [277] at $Q^2 = 2 \text{ GeV}^2$. One can see from the figure that a gross violation of the factorization theorem is expected in the BDR: the spectrum of leading hadrons is much softer for $z > 0.1$. Note also that the use of the leading twist fragmentation functions in the above expression probably underestimates absorption. Hence, the curves in Fig. 102 can be considered as a conservative lower limit on the amount of the suppression due to the BDR dynamics.

With an increase of Q^2 , we expect a further softening of the yield of leading partons related to the change in the partonic structure of the virtual photon wave function: progressively more configurations will contain extra hard gluons, which fragment independently in the BDR, further amplifying deviations from the standard leading twist predictions.

Another important signature of the BDR is the change of p_t distributions with decreasing x (at fixed Q^2). The spectrum of leading hadrons should broaden due to the increased p_t of the fragmenting partons. Hence, the most efficient strategy to look for the onset of

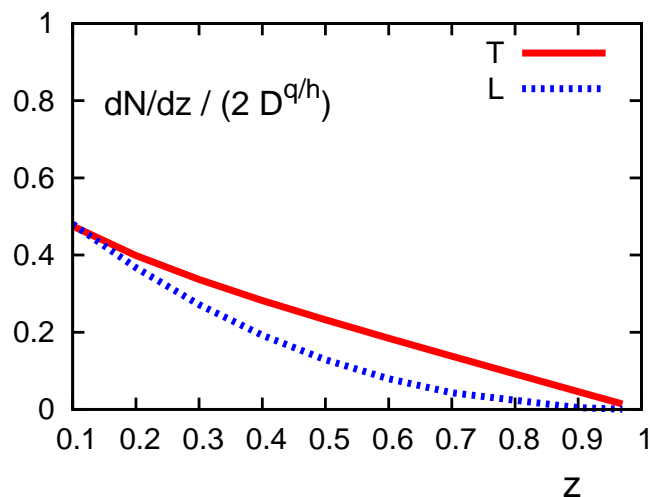


Fig. 102. The ratio $dN^{\gamma_{T,L}^*}/dz/[2D^{u/h}(z, Q^2)]$ as a function of the momentum fraction z . $dN^{\gamma_{T,L}^*}/dz$ is the total differential multiplicity in the BDR calculated using Eq. (300); $D^{u/h}(z, Q^2)$ is the leading twist up-quark fragmentation function of Ref. [277]. The solid curve corresponds to the transverse photons; the dotted curve corresponds to the longitudinal photons. Both curves correspond to $Q^2=2 \text{ GeV}^2$.

the BDR would be to select leading jets in the current fragmentation region and examine the z and p_t dependence of such jets. Qualitatively, the effect of broadening of the p_t distributions is similar to the increase of the p_t distribution in the Color Glass Condensate approach [278], see also Refs. [263,279] for reviews.

An important advantage of inclusive scattering off a nucleus is the possibility to use simple triggers for centrality. For example, one could use the number of nucleons emitted in the nucleus decay (soft nucleons in the nucleus rest frame) to select scattering at the central impact parameters. Such a selection allows for the effective thickness of the nucleus to be increased, as compared to the inclusive situation, by a factor ~ 1.5 and, hence, allows for the BDR to be reached at significantly larger x . The signal for the BDR will be a change of the spectrum with centrality of the collisions, in contrast to the LT case where no such a correlation is expected. Note that the lack of the absorption of leading particles in DIS off nuclei at the fixed-target energies and $Q^2 \geq 2 \text{ GeV}^2$ is well established experimentally, see, e.g. [280].

To summarize, predictions for a number of simple final state observables in the black disk regime (BDR) limit are distinctly different from those made in the leading twist approximation and, hence, will provide model-independent tests of the onset of the BDR.

8.8 Post-selection phenomenon as a precursor of the BDR

It has been explained above that a rapid increase of the amplitudes of hard processes with increasing energy leads at some $x \leq x_{cr}$ (x_{cr} is a certain critical value of Bjorken x) to significant higher twist (HT) terms in the cross sections of the hard processes, i.e., to the violation of the QCD predictions based on factorization theorems. An important physical manifestation of this increase is the suppression of leading jet (high p_t hadron) production as compared to the LT approximation. (The simplest example of this phenomenon is production of the leading hadrons in the BDR for the γ^*A scattering; it was considered in Sec. 8.7.) In this subsection we explain that this phenomenon leads to deviations from the LT approximation in the kinematics, where the effects for inclusive cross section are still small, which serve as a precursor of the BDR.

The evaluation of the suppression of the yield of leading partons (high p_t hadrons) within the classical theory gives the suppression factor at a fixed impact parameter b , $R_{\text{supp}}(b)$:

$$R_{\text{supp}}(b) = e^{-AT_A(b)\sigma_{\text{inel}}}, \quad (301)$$

which should be compared to the impulse approximation expectation of the yield $\propto AT_A(b)$. The suppression is large for central impact parameters where $AT(b) \sim 2 \text{ fm}^{-2}$; even for $\sigma_{\text{inel}} = 10 \text{ mb}$, one obtains $R_{\text{supp}}(b) \approx 1/7$.

At the same time, the eikonal approximation in the form given by the classical or non-relativistic quantum mechanics is inapplicable in a quantum field theory and, in particular, in QCD where all amplitudes are predominantly imaginary and elastic processes are the shadows of inelastic ones. It strongly violates the energy-momentum constraint and should be modified. Indeed, it follows from the combination of the topology of the dominant HT effects and the constraints due to energy-momentum conservation that several valence partons of the projectile should participate in the hard high energy process, which is different from a one-parton situation in the LT approximation where HT effects are absent, see the discussion in Sec. 3.1.4.

It was argued in [264] that in the black disk regime the energy of the projectile splits before the collision—the post-selection phenomenon. The presence of the strong gluon fields in the target selects different manifolds of quark and gluon configurations in the projectile wave function much more strongly than a target with moderate gluon fields. In Sec. 8.7 we considered the simplest example of the inclusive production of the leading hadrons in DIS for $Q \leq 2p_{t,\text{BDR}}$. The interactions with the target are not suppressed up to $p_t \sim p_{t,\text{BDR}}$, leading to the selection of configurations in γ^* where the longitudinal fractions carried by the quark and antiquark are comparable. Thus, the post-selection phenomenon is well suited for the experimental detection of the kinematical region (where x is not far from x_{cr}), where HT effects are significant, i.e., in the kinematics where the strength of the

interaction approaches the BDR strength.

In the case of a parton of a hadron projectile propagating through the nucleus near the BDR, i.e., in the projectile fragmentation region, the effective energy losses were estimated in Ref. [237]. For quarks, they are expected to be of the order of $10\div 15\%$ in the regime of the onset of the BDR and larger deep inside this regime. Also, the effective energy losses are somewhat larger for gluons as the $g \rightarrow gg$ splitting is more symmetric in the light-cone fractions than the qg splitting.

To visualize and evaluate the post-selection phenomenon, we somewhat generalize the technology of the AGK cutting rules [119] to hard processes to account for the nontrivial constraint due to energy-momentum conservation. For the sake of simplicity, we discuss here the simplest case of the exchange by two ladders. The generalization to the general case of exchange by many ladders should be rather straightforward.

(i) As we already discussed in Sec. 3, the contribution of the double ladder exchange diagram to the total cross section σ_2 (the effect of the screening corresponds to $\sigma_2 < 0$, so that $\sigma_{\text{tot}} = \sigma_1 + \sigma_2 < \sigma_1$) can be written as a sum of the contributions of different cuts of the double ladder diagram corresponding to three different final states: diffraction, production of the final states with single multiplicity (the cut of one of the ladders), and production of the states with double multiplicity (the cut of both ladders). Neglecting the real part of the ladder amplitude, we find

$$\begin{aligned}
\sigma_2 &= \sigma_{\text{diff}}^{(2)} + \sigma_{\text{single}}^{(2)} + \sigma_{\text{double}}^{(2)}, \\
\sigma_{\text{diff}}^{(2)} &= -\sigma_2, \\
\sigma_{\text{single}}^{(2)} &= 4\sigma_2, \\
\sigma_{\text{double}}^{(2)} &= -2\sigma_2.
\end{aligned} \tag{302}$$

In this derivation, we ignored the constraint due to the energy-momentum conservation which requires to substitute diffraction by the system of partons taking into account the post-selection phenomenon, see the discussion below.

(ii) The yield of jets (high p_t hadrons) at zero rapidity is not screened since the contributions of σ_{single} and σ_{double} cancel in the inclusive yield as the double cut corresponds to the double multiplicity and $\sigma_{\text{single}} = -2\sigma_{\text{double}}$. Taking into account the energy-momentum conservation does not change this relation which is the application of the AGK combinatorics derived within the "Pomeron Calculus" [114] to hard processes.

(iii) The yield of the leading jets (high p_t hadrons) at large rapidities is screened:

$$\sigma(\text{inclusive}) = (\sigma_1 - |4\sigma_2|)N_{\text{inclusive, single}} + 2|\sigma_2|\kappa N_{\text{inclusive, single}} + |\sigma_2|N_{\text{diff}}, \tag{303}$$

where $N_{\text{inclusive, single}}$ is the multiplicity of the hadrons in the cut of the single ladder; the factor κ accounts for the suppression of the multiplicity for the leading particles in the double ladder cut, which reflects the sharing of the projectile-parton energy between the two ladders. In the kinematics corresponding to the leading particle production, we expect that $\kappa \ll 1$. Therefore, in the case of the central collisions, where diffraction does not contribute, we find the suppression factor close to $1 - 4\sigma_2/\sigma_1$, which is much larger than in the total cross section. Thus, HT effects should reveal themselves at significantly larger x as compared to the BDR. In fact, in the kinematics where the correction to the total cross section due to the higher twist is just 25%, the single multiplicity cross section turns negative [194].

(iv) The smallness of the parameter κ follows from the constraint due to the energy-momentum conservation. To evaluate κ , let us take into account the fundamental property of parton ladders that the leading parton within a ladder carries on average the fraction $1 - \epsilon$ of the initial parton momentum. The double multiplicity hard processes may arise when at least two partons participate in the hard collision. In this case, the system of two leading partons carrying fractions z_1 and z_2 of the projectile momentum is initiated by the parton configuration in the projectile wave function where the partons carry the fraction $z_1(1+\epsilon) + z_2(1+\epsilon)$. This fraction should be compared to $\langle z_1(1+\epsilon) + z_2 \rangle$ in the case of single multiplicity events. An account of $\epsilon \neq 0$ (see below) is important in the fragmentation region as it follows from the light-cone momentum conservation $\sum z_i + (z_1 + z_2)\epsilon = 1$ and $z_i \geq 0$.

(v) The nonzero value of $\epsilon \approx 0.1 \div 0.05$ arises automatically within the LO and NLO DGLAP approximations. ($\epsilon = 0.14$ corresponds to the distance in rapidity between the adjacent partons within the parton ladder equal to $\Delta y = 2$, i.e., in the kinematics achieved at RHIC and HERA; $\epsilon = 0.05$ corresponds to $\Delta y = 3$ which could be achieved in the specific kinematics at the LHC.) The fact that $\epsilon \neq 0$ is ignored within the leading $\alpha_s \log(1/x)$ approximation that assumes the dominance of the multi-Regge kinematics; to some extent, it is accounted for within the resummation models.

(vi) In the case of the interaction with N nucleons, the suppression effect is increasing due to the AGK combinatorics and a small contribution to the cross section from two cut ladders. (The higher order terms $\propto \sigma_3, \sigma_4$ enter the total cross section with alternating signs, which reduces the screening effect as compared to the double scattering approximation. At the same time, these terms enter the expression for the inclusive cross section with a negative sign.) Hence, for central collisions, the actual “post-selection energy loss” should increase with an atomic number $\propto A^{1/3}$.

Let us consider several examples. In the case of a virtual photon projectile, $z_1 \approx z_2 \approx 1/2$ and the production of the leading hadron carrying the fraction $\geq 1 - \epsilon$ is dynamically suppressed. In the limit when the BDR contribution dominates, there are two contributions to the inclusive spectrum: one is due to the diffraction, which is expressed through the virtual photon wave function, and the other one that is due to the wave packet fragmentation. In

the approximation that we considered in this section, they give equal contributions (both suppressed as compared to the LT expectation). The present discussion indicates that the non-diffractive component with $k_t < k_{t,\text{BDR}}$ should be further suppressed as compared to the estimate presented in Sec. 8.7, which originated solely from the structure of the virtual photon wave function. However, the configurations interacting inelastically with nearly the BDR strength will interact with a large probability via several ladders, leading to a further suppression of the forward spectrum.

Our second example is the proton-nucleus scattering. A new feature here is that it is possible to select non-diffractive interactions at different impact parameters. Comparing the yield of leading particles in this case to the impulse approximation expectation, we observe that the contribution of N -ladder interactions leads to the significantly larger "post-selection energy loss" $\approx (N - 1)\epsilon$.

Thus the post-selection phenomenon corresponding to significant effective fractional energy losses is definitely present in QCD. However, to calculate the post-selection phenomenon more accurately, one needs to model LT and HT effects.

8.9 Evidence for post-selection effect in the forward pion production in the deuteron-Gold collisions at RHIC

The leading hadron production for $p_t \sim \text{few GeV}/c$ in hadron-nucleus scattering at high energies can be used as a sensitive test of the onset of the BDR dynamics. In this limit, pQCD provides a good description of the forward single inclusive pion production in pp scattering at the RHIC energies [281]. At the same time, a comparison of the pQCD calculations with the data shows that such calculations grossly overestimate the cross section of the pion production in dAu collisions in the same kinematics. The analysis of [282] has demonstrated that the dominant mechanism of the single pion production in the NN collisions in the kinematics which was studied at RHIC is scattering of the leading quark of the nucleon off the gluons of the target with the median value of x in the range $x_g \sim 0.01 \div 0.03$ depending on the rapidity of the pion. The nuclear gluon density for such x_g is known to be close to the incoherent sum of the gluon fields of the individual nucleons since the coherent length in the interaction is rather modest for such distances (see, e.g., Fig. 34). As a result, the leading twist nuclear shadowing effects can explain only a very small fraction of the observed suppression [282] and one needs a novel dynamical mechanism to suppress the generation of pions in such collisions. In particular, it was pointed out in [282] that the fractional energy losses on the scale of $10 \div 15\%$ give a correct magnitude of the suppression of the inclusive spectrum due to a steep fall of the cross section with x_F , which is consistent with the estimates within the post-selection dynamics.

An important additional information comes from the studies of the correlation of the

leading pion with the pion produced at the central rapidities, $\eta \sim 0$ [283,284], which corresponds to the kinematics which receives the dominant contribution from the scattering off gluons with $x_g \sim 0.01 \div 0.02$. The rate of the correlations for pp scattering is consistent with pQCD expectations. An extensive analysis performed in [237] has demonstrated that the strengths of "hard forward pion" – "hard $\eta \sim 0$ pion" correlations in dAu and pp scattering are similar; a rather small difference in the pedestal originates from the multiple soft collisions. The smallness of the increase of the soft pedestal as compared to pp collisions unambiguously demonstrates that the dominant source of the leading pions is the dAu scattering at large impact parameters. This conclusion is supported by the experimental observation [285] that the associated multiplicity of soft hadrons in events with forward pions is a factor of two smaller than in the minimal bias dAu events. The reduction by a factor of two is consistent with the estimate of [237] based on the analysis of the soft component of $\eta = 0$ production for the forward pion trigger. Overall these data indicate that (i) the dominant source of the forward pion production is $2 \rightarrow 2$ mechanism, (ii) production is dominated by the projectile scattering at large impact parameters, (iii) the proportion of small x_g contribution in the inclusive rate is approximately the same for pp and dAu collisions.

The lack of an additional suppression of the $x_g \sim 0.01$ contribution to the double inclusive spectrum as compared to the suppression of the inclusive spectrum is explained in the post-selection dynamics since the pions with $\eta \sim 0$ are produced in the fragmentation of the gluons with relatively small momenta in the nucleus rest frame, putting these gluons far away from the BDR.

It is difficult to reconcile the enumerated features of the forward pion production data with the $2 \rightarrow 1$ mechanism of Ref. [286] inspired by the Color Glass Condensate model. In the scenario of [286], the incoherent $2 \rightarrow 2$ mechanism is neglected and a strong suppression of the recoil pion production is predicted. Also, it leads to the dominance of the central impact parameters and, hence, to a larger multiplicity for the central hadron production in the events with the forward pion trigger. The observed experimental pattern indicates that the models that neglect the contribution of the $2 \rightarrow 2$ mechanism and consider only $2 \rightarrow 1$ processes, see, e.g., Ref. [287], strongly overestimate the contribution of the $2 \rightarrow 1$ mechanism to the inclusive cross section.

Additional information comes from the recent studies [288,289] of the production of two forward neutral pions in pp and dA scattering. This kinematics strongly enhances the contribution of small x in the target [282]. One leading pion serves as a trigger and the second leading pion has somewhat smaller longitudinal and transverse momenta. The data indicate a strong suppression of the back-to-back production of pions in the central dAu collisions. Also, a large fraction of the double inclusive cross section is isotropic in the azimuthal angle $\Delta\varphi$ between the two pions. In order to understand the origin of the suppression and other features of the data, there has been performed a study [290] which is summarized below.

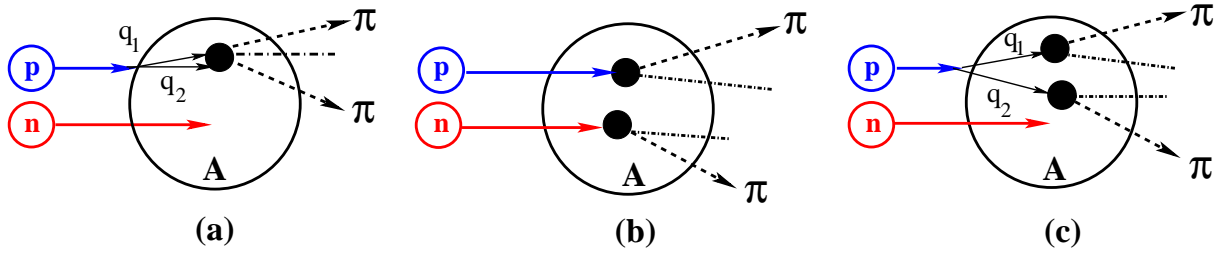


Fig. 103. Three double parton mechanisms of dipion production in dAu collisions.

First, it was demonstrated that for the discussed forward kinematics, the binary hard collisions are dominated by very large $x \sim 0.7 \div 0.8$. As a result, the double scattering mechanism, where two quarks with smaller x scatter off the gluons of the target, gives an important contribution, see Fig. 103 for the case of deuteron-nucleus scattering. The double scattering mechanism leads to the contribution to the cross section which does not depend on $\Delta\varphi$.

In the case of pp scattering, the numerical analysis of [290] indicates that in the RHIC kinematics, the double and single contributions are comparable. This gives a natural explanation to the experimental observation that in pp scattering, the number of events in the pedestal is somewhat larger than in the peak around $\Delta\varphi \sim \pi$, which is dominated by the LT contribution.

In the case of dAu collisions, the double parton interaction contribution for collisions at the central impact parameters is strongly enhanced by the combinatorial factor [in addition to the mechanism analogous to the one for pp scattering shown in Fig.103(a)], it is possible to emit pions in the interactions of quarks of the proton and neutron with two different nucleons of the nucleus [Fig. 103(b)] or in the interactions of quarks of one of the nucleons with two different nucleons of the nucleus [Fig. 103(c)]. In the impulse approximation, the enhancement factor for the multiplicity of the events in the pedestal in dAu collisions as compared to the pp collisions, r_A , is proportional to the nucleus thickness, $T_A(b)$, times the combinatorial factor due to a larger number of quark-quark pairs in two nucleons than in one nucleon. As a result, one finds $r_A \sim 10$ for central dAu collisions with the typical pseudorapidities $\eta_{1,2}$ of two pions probed in the RHIC experiment; r_A increases with an increase of the rapidities of the pions.

Since the single inclusive pion spectrum for $\eta_2 \sim 2 \div 3$ is suppressed by a factor of the order $R_A(b) = 1/3 \div 1/4$, one finds for the ratio of the pedestals in dAu and pp :

$$R_{\text{pedestal}} = r_A R_A(b) \sim 2.5 \div 4, \quad (304)$$

which should be compared with the experimental value of $R_{\text{pedestal}} \sim 3$. Hence, the double scattering mechanism with a strong suppression of pion production at small impact parameters naturally explains the magnitude of the enhancement of the pedestal in central dAu collisions.

If most of the pedestal in the kinematics studied at RHIC is due to the double parton mechanism, the uncertainties in the estimate of the rates due to this mechanism and uncertainties in the strength of the suppression of the single inclusive forward pion spectrum at $b \sim 0$ would make it very difficult to subtract this contribution with a precision necessary to find out whether all pedestal is due to double parton mechanism or there is a room for a small contribution of the $2 \rightarrow 1$ broadening mechanism as assumed in [291].

The suppression of the away peak originating from the LT contribution is due to the following two effects: (i) the gluon shadowing for $x \sim 10^{-3}$, $b \leq 3$ fm and $Q^2 \sim \text{few GeV}^2$ reduces the cross section by a factor of about two (see Fig. 42), (ii) a stronger effect of the effective fractional energy losses due to larger x of the quark in the LT mechanism than in the double parton mechanism leads to the suppression factor of the order of two [290]. Combined together these effects result in a suppression of the order of four as compared to the single pion trigger and overall suppression of the order of ten. This is consistent with the experimentally observed magnitude of the suppression.

Note, however, that for the suppression of such a magnitude, the treatment of the nucleus that neglects fluctuations of the positions of the nucleons in nuclei may be an oversimplification. In particular, it does not take into account a possibility of the "punch through" process in which a quark scatters off one nucleon but does not encounter any extra nucleons at its impact parameter. The probability of such collisions at $b \sim 0$ for interaction with Au nucleus is of the order $5 \div 10\%$ [145]. Thus, these collisions may be responsible for a large fraction of the away peak.

In summary, the RHIC data clearly indicate the break-down of pQCD in the scattering off heavy nuclei at central impact parameters in the kinematics, where pQCD works for the pp scattering. The post-selection effect (effective fractional energy losses) for the propagation of the leading partons is the only proposed mechanism that allows one to explain the suppression of the $2 \rightarrow 2$ mechanism for production of leading pions, which dominates in the pp scattering including such observations as the survival of forward-central correlations, the strength of the pedestal, and the suppression of forward-forward correlations. The processes of the production of two forward pions in pp and dAu scattering due to the double parton mechanism and large suppression of the single pion yield for the scattering at small impact parameters explain the pedestal observed at RHIC and make it difficult to search for the signal of $2 \rightarrow 1$ processes. The magnitude of the away peak is consistent with the expected magnitude of the suppression of the $2 \rightarrow 2$ mechanism due to LT gluon shadowing and fractional energy losses due to the post-selection mechanism.

In the rest frame of the nucleus, the RHIC kinematics corresponds to the interaction of a quark with the energy of the order of 10 TeV and virtuality corresponding to $p_t \sim 1 \div 2$ GeV/c. Such quarks can resolve the gluon fields with $x \sim 3 \times 10^{-4}$. This gives an independent estimate of the kinematics where the BDR sets in for the interaction of quarks. It corresponds to somewhat higher x than the ones we found in the analysis of the impact factors in Sec. 8.5. However, as we mentioned in Sec. 8.7, the single particle

spectrum is more sensitive to non-linear effects than the total cross section since the shadowing effects are amplified in this case.

The observation of the post-selection effects at RHIC in the discussed above kinematics has important implications for AA and pA collisions at the LHC. Indeed, a parton carrying the fraction x_F of the projectile hadron momentum dissociates into N partons long before a collision with a target. So, in the vicinity of the BDR, the energy carried by each of these partons can be estimated as $\approx x'_F/2$ assuming dominance of double inelastic collisions, i.e., $N = 2$. Thus, in this case, a leading parton carries only the fraction $\approx x'_F/2$, which is significantly smaller than the corresponding fraction x'_F expected within the LT approximation. Furthermore, the increase of the collision energy and the atomic number of the target lead to an increase of the effective number of inelastic collisions of a parton, $N(b, x)$. Hence, the fraction of projectile hadron momentum carried by the interacting parton should decrease with an increase of the collision energy tending to $\approx 1/N(b, s)$ — the number of nucleons at a given impact parameter. This picture follows from the generalization of the Gribov-Glauber approximation to inelastic processes at high energies which includes an account of the energy-momentum conservation. This generalization is called the color fluctuation approximation in this review.

Thus, pre-selection effects should be more important at the LHC than at RHIC. To visualize the expected effects, for numerical estimates we use the analysis of the dAu RHIC data described above. Indeed, energies of the partons of 10 TeV and above and $p_t \sim 1 \div 2$ GeV/c (for which the post-selection effect is large) correspond to a wide range of rapidities in the nucleus rest frame for collisions at the LHC energies. For example, for the full LHC energy for proton- ^{208}Pb collisions of $\sqrt{s_{NN}}=8.8$ TeV, the post-selection effect for $p_t \leq 2$ GeV/c should extend to $y_{\max} - y \leq 8$, or $x_F > 3 \times 10^{-4}$, for quarks and to a broader range for gluons.

8.10 Implications of energy-momentum conservation for the onset of BDR

In Sec. 3.1.4, we explained that the eikonal approximation strongly violates the energy-momentum conservation. Here we analyze, albeit briefly, implications of the energy-momentum conservation for the dynamics of an onset of the BDR for hard processes.

The energy-momentum conservation restricts a possible number of gluons radiated within the multi-Regge kinematics. This number can be estimated from the condition that the distance in rapidity between the adjacent gluons in a pQCD ladder should be at least $\geq 2 - 3$ units. This estimate shows that in the whole kinematical region covered by HERA and most of kinematics of hard processes at the LHC (with an exception of a special kinematical region), the number of gluons in the multi-Regge kinematics, N , is small. It is related to the span in the rapidity for a given accelerator, δy , by the following

relation:

$$\delta y = 2 + 3(N + 1) + 2, \quad (305)$$

where the factors of two is an estimate of length in rapidity of each fragmentation region. Let us give illustrative estimates of the production of N gluons in the multi-Regge kinematics at different accelerators:

- (i) $\delta y(\text{HERA}) = \ln(Q/xm_N) \approx 9.2$ for $Q^2 = 4 \text{ GeV}^2$. Therefore, $N \approx 1$.
- (ii) At the LHC for the full energy $\sqrt{s} = (7+7) \text{ TeV}$, the rapidity span is $\delta y = \ln(s/m_N^2) = 18.7$. Then, for instance, if a $q\bar{q}$ dipole in the light-cone wave function of proton carries the proton momentum fraction $z \approx 0.1$ and the partons have the relative momentum $p_t^2 = \text{few GeV}^2$, the number of allowed gluons is $N \approx 3$.
- (iii) In the ultraperipheral collisions at the LHC, $N \approx 2$.

This restriction on N explains the experimental observation of the dominance of large $\beta = Q^2/(Q^2 + M_X^2)$ in the diffraction in DIS, i.e., the contribution of multi-Regge kinematics is a small correction, see the discussion in Sec. 5.1.3. A practical conclusion from this is that production of gluons in the multi-Regge kinematics can be taken into account by calculating only a few Feynman diagrams with the emission of few gluons.

Thus, the energy-momentum conservation ensures the dominance of the double logarithmic approximation of pQCD and the DGLAP saddle point in the inverse Mellin transform of the proton structure functions in a wide kinematical domain, including the kinematics achieved at HERA and most of the kinematics of the LHC. Moreover, as a consequence of the account of the energy-momentum conservation, the multiplicity of gluons in multi-Regge kinematics is significantly smaller than that assumed within the BFKL and Color Glass Condensate (CGC) approaches.

However, at extremely large energies, where the parameter $\alpha_s(Q_0^2)(N_c/2\pi) \ln(x_0/x) \geq 1$, the DGLAP approximation becomes questionable and this kinematics may appear to be a window to the gluon radiation in the multi-Regge kinematics, see also the discussion in Sec. 8.2.

8.11 BDR as new phase transition with the change of continuous symmetry

A direct consequence of the condition of complete absorption, Eq. (259), is the complete disappearance of approximate Bjorken scaling for the $\gamma^* + T \rightarrow X$ DIS cross section: this cross section is independent of Q^2 within the BDR. Such a behavior means the breakdown of the scale invariance characteristic for the parton model and the dynamical two-dimensional conformal invariance characteristic for the DGLAP [292] and BFKL [293]

approximations. Thus, the black disk and pQCD regimes have different continuous symmetries, and the transition from the pQCD regime to the BDR resembles a phase transition with a change of the continuous symmetry.

A hadronic state produced in DIS off a nucleon target within the BDR is a result of fragmentation of three phases of QCD. (These phases depend on the impact parameter of the collision $\vec{b} = \vec{\rho}_1 - \vec{\rho}_2$, where ρ_i are transverse coordinates of the center of mass of the hadrons.) At small impact parameters b , it is the BDR phase without the two-dimensional conformal symmetry; at larger b , it is the pQCD regime with the unbroken chiral and two-dimensional conformal symmetries; and at even larger impact parameters, it is the soft QCD regime with the spontaneously broken chiral symmetry, where the conformal symmetry is probably also spontaneously broken. An important role of transitions with the change of continuous symmetries has important implications for high energy hadron-hadron interactions.

(i) For $b \sim 0$ in the cylinder (in transverse coordinate-rapidity space) centered around $\vec{r} = (\vec{\rho}_1 + \vec{\rho}_2)/2$, the BDR interactions dominate and suppress soft QCD interactions generating the Froissart limit of soft QCD at high energies. The radius of the cylinder grows with an increase of energy, while the BDR scale at given ρ_i grows with the incident energy as well. Note here that the interactions in pp scattering at small impact parameters become practically black for small b , although it is not a priori clear whether pQCD or non-perturbative QCD is responsible for this.

(ii) With an increase of b , the BDR region occupies an almond-shaped transverse area centered around \vec{r} , which is surrounded by the pQCD phase and far out by the non-perturbative phase.

(iii) For $b > 2r_N$, for a wide range of energies most of the interaction region is in the non-perturbative phase with the spontaneously broken chiral symmetry with a small pQCD cylinder around small \vec{r} and practically no BDR region.

8.12 BDR vs. DGLAP approximation regime

An attractive feature of the BDR for a large nucleus is that a new phase of QCD, with a small coupling constant and the continuous symmetry different from that of pQCD, should manifest itself in ep , pA , and AA collisions for a wide range of impact parameters and in a broad range of phenomena.

We have demonstrated in the previous subsections that predictions for many observables in the BDR are qualitatively different from those in the leading twist regime. We summarize here the most striking of these predictions.

- (i) The QCD factorization theorem is violated in the vicinity of the BDR. Therefore, the pQCD and BDR phases have different continuous symmetries, see Sec. 8.11. Also, the independence of the form of leading jets from a target is violated, see Sec. 8.7. In the vicinity of the BDR, a major new effect is the post-selection of projectile configurations which mimics fractional energy losses and leads to the suppression of the leading hadron production for $p_t \leq$ the BDR scale [237], see Sec. 8.8.
- (ii) Compared to the DGLAP approximation, the BDR predicts a more rapid Q^2 dependence and a different—but still rather rapid—increase with energy of structure functions of a nucleon: $F_T^N(x, Q^2) \propto Q^2 R_N^2 \ln(x_0/x)(1 + c_N \ln^2(x_0/x))$ (the coefficient of proportionality is given in Eq. (290)].
- (iii) The structure function of a heavy nucleus should increase with increasing energy more slowly than the nucleon one: $F_T^A(x, Q^2) = Q^2 \ln(x_0/x)(R_A^2 + c R_A R_N \ln^2(x_0/x))$ as a consequence of the large nucleus radius (see the discussion in Sec. 8.5.4). Thus, the ratio of the nuclear to nucleon structure functions decreases with increasing (x_0/x) :

$$F_{2A}/(A^{2/3} F_{2N}) \propto 1/(1 + c_N \ln^2(x_0/x)) + c A^{-1/3}. \quad (306)$$

It would be a difficult problem to distinguish experimentally such a behavior from the leading twist nuclear shadowing phenomenon.

- (iv) The cross section of diffraction should reach nearly half of the total cross section.
- (v) The cross section of exclusive vector meson electroproduction should have a much weaker Q^2 dependence and be calculable in a model-independent way, see the discussion in Sec. 8.6.

8.13 BDR vs. parton saturation hypothesis

Properties of the BDR have certain similarities, as well as a number of qualitative and quantitative differences, from the predictions based on the parton saturation hypothesis (the Color Glass Condensate framework—CGC). On the one hand, various models using the features of the CGC explore the approximation of large gluon density evaluated within the framework of the LO BFKL approach together with the elastic eikonal approximation to stop the increase of structure functions with an increasing energy and, hence, some effects due to blackening of the interaction should be present within such models. At the same time, it has been found that corrections to the LO BFKL approximation are huge and comparable with the leading term. Thus, it should be significantly improved by a more accurate account of double logarithmic terms making it more close to the NLO DGLAP approximation (resummation models) [259–262]. So far the resummation models have not been implemented within CGC approaches.

On the other hand, in contrast to the LO BFKL approximation, the DGLAP approximation used in the evaluation of an onset of the BDR conserves longitudinal energy and momentum. Moreover, in contrast to the CGC models, the color fluctuations approach

(Sec. 3) together with the DGLAP approximation accounts for the energy-momentum conservation for multiple scattering processes and, therefore, leads to a different physical picture and predicts different phenomena.

- (i) The BDR predicts that structure functions of a hadron (nucleus) at a fixed impact parameter should increase with energy as, e.g., $F_T(x, b, Q^2) \propto \ln(x_0/x)$ as a consequence of the ultraviolet divergency of hadron renormalization of the electric charge [270]. Moreover, within the BDR structure functions of a hadron integrated over impact parameters should increase with energy as $F_T \propto \ln^3(x_0/x)$. On the contrary, the CGC models assume that “saturated” parton distributions and the composition of partons within a projectile photon should be energy independent, see e.g., [294].
- (ii) The BDR predicts that the structure functions of a heavy nucleus should depend on energy more slowly at achievable energies than the nucleon structure function since the nucleon impact parameter distribution within a heavy nucleus is flat in a wide range of impact parameters. Note that in practice, this prediction of the BDR competes with the nuclear shadowing phenomenon. On the contrary, the CGC models assume the “saturated” parton distribution of a hadron (nucleus) and, therefore, the ratio of the nucleus to nucleon structure functions should be energy independent.
- (iii) CGC models and, in particular the Balitsky-Kovchegov approximation [295,296], assume that branching of the parton showers in multi-Regge kinematics plays the dominant role practically at any energies. It follows from the account of the energy-momentum conservation that an onset of multi-Regge showers requires significantly larger energies than those required for an onset of the BDR. In particular, at the energies achievable at accelerators, the dominant diffractive processes correspond to production of masses $M^2 \approx Q^2$ and slowly increasing with energy. This theoretical observation is in accordance with the HERA data on diffractive processes, see the discussion in Sec. 5.1.3 and in particular Fig. 30.
- (iv) CGC models often employ the elastic eikonal approximation for the evaluation of hard processes, which violates the energy-momentum conservation, see Sec. 3.1.4. An analysis of the implications of the energy-momentum conservation finds that the application of the elastic eikonal approximation to high energy processes in the kinematics where inelastic processes dominate leads to serious inconsistencies.
- (v) To evaluate nuclear shadowing and an onset of the BDR, in this review we use the semiclassical approximation in the form appropriate for a quantum field theory, which we called the “color fluctuations approach”. Because of the proper account of the diffractive processes, this approximation allowed us to implement the energy-momentum conservation in the multiple collisions in the regime where amplitudes are predominantly absorptive. This is achieved by summing over the contributions of degenerate trajectories in the allowed phase space instead of taking into account just one trajectory within the elastic eikonal approximation familiar from one-dimensional quantum mechanics and often used within the CGC. (Recall that the semiclassical approximation to a many-body quantum mechanical system, where variables in the Hamiltonian cannot be separated, includes the sum over degenerate trajectories in the allowed phase space.)

- (vi) An account of the energy-momentum conservation leads to the effects mimicking energy losses. Such effects do not exist within the eikonal approximation but are characteristic for an onset of the BDR.
- (vii) Recent CGC studies also began to include the dependence of the interaction scale on the impact parameter in ep and eA scattering. (It has not been extended to the case of pp , pA , and AA collisions yet.) However, as we discussed in Sec. 8.11, at high energies and at large impact parameters, the non-perturbative QCD phase, where the chiral symmetry is spontaneously broken, should dominate and the pQCD phase would populate a moderate b region. At central impact parameters (which can be as large as R_A for nuclear targets), the BDR phase with the broken two-dimensional conformal symmetry should dominate at sufficiently high energies.
- (viii) Transverse momenta of partons within the projectile dipole, i.e., in the region of current fragmentation, are increasing with energy as a consequence of the increase of pQCD interactions with an increase of energy. Numerical calculations give for σ_L for $Q^2 = 10 \text{ GeV}^2$: $k_t^2/k_0^2 = (s/s_0)^n$ with $n \approx 0.04$ and slowly growing with Q^2 within LO DGLAP [225]. An increase with energy of parton transverse momenta in DIS in the current fragmentation region demonstrates the ambiguity of leading log approximations in the small x regime since at the fixed-order in the coupling constant, there is no such an effect. At the same time, both the BDR and CGC predict an increase of parton momenta in the center of rapidity with an increase of energy.
- (ix) In this review, we discuss properties of the BDR inspired by hard QCD phenomena only. Soft QCD phenomena are suppressed by the choice of kinematics or accounted for within the framework of QCD factorization theorems, see the discussion of the weak parton density limit. On the contrary, models of CGC explore eikonization of the LO BFKL approach to describe both soft and hard QCD phenomena.

Thus, the BDR and CGC models account for different phenomena and, therefore, make different predictions for the domain covered by HERA, RHIC, and the LHC.

9 Conclusions

In this review, we considered two distinctive regimes of nuclear shadowing: (i) the regime of moderately small x and not very large parton densities where the leading twist approximation (the QCD factorization theorem) is applicable, and (ii) the regime of very small x and large nuclei (central impact parameters) where the leading twist (LT) approximation dramatically breaks down and is replaced by the black disk regime (BDR) of the strong interaction.

In the leading twist regime, combining the Gribov technique developed earlier for hadron-deuteron scattering, the QCD factorization theorems for DIS, and QCD analyses of the HERA data on diffraction in lepton-proton DIS, we developed the theory of the nu-

clear shadowing dynamics in the leading twist approximation. In the review, the model-dependent contribution of the interactions with $N \geq 3$ nucleons of the nuclear target is treated using the semiclassical approximation in the form suited for a quantum field theory. We call this approximation to high energy processes in QCD *the color fluctuation approximation*; it takes into account the phenomenological observation that diffraction in ep DIS is dominated by large-size fluctuations of the virtual photon wave function. (The color fluctuation approach allows one to overcome the principal difficulty of the treatment of multiple inelastic interactions within the elastic eikonal approximation, i.e., in the form derived within the framework of one-dimensional non-relativistic quantum mechanics which neglects the constraints of the energy-momentum conservation.) Theoretical analyses of diffraction DIS ep HERA data demonstrate the dominance of large $\beta = Q^2/(Q^2 + M_X^2)$, where M_X is the diffractively produced mass, which unambiguously supports the dominance of the regime resembling Gribov-Glauber multiple rescatterings for $x \geq 10^{-4}$ and forms the basis for the quantitative calculations of nuclear shadowing.

Using the framework of the leading twist theory of nuclear shadowing, we make predictions for a number of quantities that can be accessed in DIS and hard photoproduction with nuclei. These include, but not limited to: (i) sea quark and gluon parton distributions and structure functions for a wide range of nuclei (from deuterium to Lead) for $10^{-5} \leq x < 1$ and $4 \leq Q^2 \leq 10^4$ GeV², (ii) nuclear impact parameter dependent PDFs and generalized parton distributions (GPDs) in nuclei and cross sections of hard exclusive processes (deeply virtual Compton scattering, exclusive production of J/ψ) with nuclei, (iii) nuclear diffractive PDFs and coherent and incoherent nuclear structure functions. It will be possible to test a number of our predictions in the near future using ultraperipheral heavy ion collisions at the LHC, with further tests in the proton-nucleus collisions at the LHC. High precision tests will be possible at a future Electron-Ion Collider (EIC). The EIC is an ideal machine to study many predictions of the leading twist theory of nuclear shadowing discussed in this review.

As x becomes very small and for hard processes off heavy nuclei at central impact parameters, the pQCD amplitudes of hard processes that rapidly increase with energy reach their maximal values dictated by the probability conservation at a fixed impact parameter in the s -channel and one enters the black disk regime (BDR) of the strong interactions. The existence of this regime and the corresponding master formulas with the predictions for hard processes follow from the conservation of probability for the collisions at a fixed impact parameter. In particular, nuclear shadowing in the total cross section of DIS, cross sections of hard diffractive (inclusive and exclusive) processes, etc., are directly and model-independently calculable within the BDR. The characteristic features of the BDR include the forever increase of structure functions of nucleons and nuclei with an increase of energy, disappearance of the approximate scale invariance (approximate Bjorken scaling) and dynamical two-dimensional conformal symmetry characteristic for pQCD, the effective restoration of vector meson dominance for the exclusive production of vector mesons, suppression of the leading hadrons in DIS final states, the post-selection "effective

fractional energy losses”, etc.

The QCD phenomena discussed in the review have serious implications for the final states produced in hadron-nucleus and nucleus-nucleus collisions. In particular, the produced matter is characterized by the interplay of three phases of QCD matter with different continuous symmetries: the non-perturbative QCD phase with spontaneously broken chiral symmetry, the pQCD phase with two-dimensional conformal invariance, and the BDR. A variety of signals distinctive for the onset of the BDR—a new QCD phase—which are feasible for the experimental observation at the LHC is suggested. Forward production of hadrons/jets in pA collisions at RHIC and the LHC would provide first tests of these expectations. Detailed studies will be possible at the Large Hadron-Electron Collider (LHeC) currently under discussion at CERN.

Acknowledgments

We thank our collaborators who were involved in a number of studies reflected in this review: H. Abramowicz, A. Freund, W. Koepf, M. McDermott, T. Rogers, W. Vogelsang, C. Weiss, and M. Zhalov. Our special thanks are due to the Ultraperipheral study group and especially to R. Vogt for investigations of the feasibility studies of the small x physics in the ultraperipheral collisions at the LHC. Over many years we enjoyed numerous illuminating discussions on many of the topics discussed in the review with J. Bjorken, S. Brodsky, L. McLerran, A. Mueller, and R. Venugopalan. We hope to continue these discussions for years to come.

We thank J. Collins for the collaboration and discussions of the QCD factorization theorems for hard diffractive processes.

We thank the H1 collaboration and Springer for allowing us to reproduce figures from Refs. [61] and [62].

This research was partially supported by the BSF (LF and MS) and DOE (MS).

Authored by Jefferson Science Associates, LLC under U.S. DOE Contract No. DE-AC05-06OR23177. The U.S. Government retains a non-exclusive, paid-up, irrevocable, worldwide license to publish or reproduce this manuscript for U.S. Government purposes.

References

- [1] J. J. Aubert *et al.* [European Muon Collaboration], *Phys. Lett. B* **123** (1983) 275.
- [2] A. Bodek *et al.*, *Phys. Rev. Lett.* **50** (1983) 1431.

- [3] A. Bodek *et al.*, Phys. Rev. Lett. **51** (1983) 534.
- [4] R. G. Arnold *et al.*, Phys. Rev. Lett. **52** (1984) 727.
- [5] S. Dasu *et al.*, Phys. Rev. Lett. **60** (1988) 2591.
- [6] G. Bari *et al.* [BCDMS Collaboration], Phys. Lett. B **163** (1985) 282.
- [7] A. C. Benvenuti *et al.* [BCDMS Collaboration], Phys. Lett. B **189** (1987) 483.
- [8] J. Ashman *et al.* [European Muon Collaboration], Phys. Lett. B **202** (1988) 603.
- [9] M. Arneodo *et al.* [European Muon Collaboration], Nucl. Phys. B **333** (1990) 1.
- [10] P. Amaudruz *et al.* [New Muon Collaboration], Z. Phys. C **51** (1991) 387.
- [11] P. Amaudruz *et al.* [New Muon Collaboration], Z. Phys. C **53** (1992) 73.
- [12] P. Amaudruz *et al.* [New Muon Collaboration], Phys. Lett. B **294** (1992) 120.
- [13] M. R. Adams *et al.* [Fermilab E665 Collaboration], Phys. Lett. B **287** (1992) 375.
- [14] M. R. Adams *et al.* [E665 Collaboration], Phys. Rev. Lett. **68** (1992) 3266.
- [15] M. R. Adams *et al.* [E665 Collaboration], Z. Phys. C **67** (1995) 403.
- [16] J. Gomez *et al.*, Phys. Rev. D **49** (1994) 4348.
- [17] P. Amaudruz *et al.* [New Muon Collaboration], Nucl. Phys. B **441** (1995) 3.
- [18] M. Arneodo *et al.* [New Muon Collaboration], Nucl. Phys. B **441** (1995) 12.
- [19] M. Arneodo *et al.* [New Muon Collaboration], Phys. Lett. B **364** (1995) 107.
- [20] M. Arneodo *et al.* [New Muon Collaboration], Nucl. Phys. B **481** (1996) 3.
- [21] M. Arneodo *et al.* [New Muon Collaboration], Nucl. Phys. B **481** (1996) 23.
- [22] K. Ackerstaff *et al.* [HERMES Collaboration], Phys. Lett. B **475** (2000) 386 [Erratum-ibid. B **567** (2003) 339].
- [23] P. Amaudruz *et al.* [New Muon Collaboration], Nucl. Phys. B **371** (1992) 553.
- [24] D. M. Alde *et al.*, Phys. Rev. Lett. **64** (1990) 2479.
- [25] M. A. Vasilev *et al.* [FNAL E866 Collaboration], Phys. Rev. Lett. **83** (1999) 2304.
- [26] L. Frankfurt, V. Guzey and M. Strikman, Phys. Lett. B **586** (2004) 41.
- [27] H. Kowalski, T. Lappi, C. Marquet and R. Venugopalan, Phys. Rev. C **78** (2008) 045201.
- [28] F. Ellinghaus, R. Shanidze and J. Volmer [HERMES Collaboration], AIP Conf. Proc. **675** (2003) 303 [arXiv:hep-ex/0212019].
- [29] A. Freund and M. Strikman, Phys. Rev. C **69** (2004) 015203.

- [30] A. Freund and M. Strikman, Eur. Phys. J. C **33** (2004) 53.
- [31] K. Goeke, V. Guzey and M. Siddikov, Eur. Phys. J. A **36** (2008) 49.
- [32] K. Goeke, V. Guzey and M. Siddikov, Eur. Phys. J. C **56** (2008) 203.
- [33] L. Frankfurt, V. Guzey, M. Strikman and M. Zhalov, JHEP **0308** (2003) 043.
- [34] L. Frankfurt, M. Strikman and M. Zhalov, Acta Phys. Polon. B **34** (2003) 3215.
- [35] K. Hencken *et al.*, Phys. Rept. **458** (2008) 1.
- [36] A. Deshpande, R. Milner, R. Venugopalan and W. Vogelsang, Ann. Rev. Nucl. Part. Sci. **55** (2005) 165.
- [37] <http://www.eic.bnl.gov/>, C. Aidala *et al.*, "Physics Opportunities with e+A Collisions at an Electron Ion Collider", White Paper Prepared for the NSAC LRP 2007, April 4, 2007.
- [38] M. Arneodo, Phys. Rept. **240** (1994) 301.
- [39] K. J. Eskola, V. J. Kolhinen and P. V. Ruuskanen, Nucl. Phys. B **535** (1998) 351.
- [40] K. J. Eskola, V. J. Kolhinen and C. A. Salgado, Eur. Phys. J. C **9** (1999) 61.
- [41] K. J. Eskola, H. Honkanen, V. J. Kolhinen and C. A. Salgado, Phys. Lett. B **532** (2002) 222.
- [42] H. Paukkunen, C. A. Salgado and K. J. Eskola, arXiv:1009.3142 [hep-ph].
- [43] M. Hirai, S. Kumano and M. Miyama, Phys. Rev. D **64** (2001) 034003.
- [44] M. Hirai, S. Kumano and T. H. Nagai, Phys. Rev. C **70** (2004) 044905.
- [45] M. Hirai, S. Kumano and T. H. Nagai, Phys. Rev. C **76** (2007) 065207.
- [46] D. de Florian and R. Sassot, Phys. Rev. D **69** (2004) 074028.
- [47] S. y. Li and X. N. Wang, Phys. Lett. B **527** (2002) 85.
- [48] K. J. Eskola, H. Honkanen, V. J. Kolhinen and C. A. Salgado, arXiv:hep-ph/0302170.
- [49] K. J. Eskola, V. J. Kolhinen, H. Paukkunen and C. A. Salgado, JHEP **0705** (2007) 002.
- [50] K. J. Eskola, H. Paukkunen and C. A. Salgado, JHEP **0807** (2008) 102.
- [51] K. J. Eskola, H. Paukkunen and C. A. Salgado, JHEP **0904** (2009) 065.
- [52] I. Schienbein, J. Y. Yu, K. Kovarik, C. Keppel, J. G. Morfin, F. Olness and J. F. Owens, Phys. Rev. D **80** (2009) 094004.
- [53] F. Arleo and T. Gousset, Phys. Lett. B **660** (2008) 181.
- [54] F. Arleo, Phys. Lett. B **666** (2008) 31.
- [55] P. Quiroga-Arias, J. G. Milhano and U. A. Wiedemann, arXiv:1002.2537 [hep-ph].

- [56] V. N. Gribov, Sov. Phys. JETP **29** (1969) 483 [Zh. Eksp. Teor. Fiz. **56** (1969) 892]; also in V.N. Gribov, *Gauge theories and quark confinement*, Phasis, Moskow, 2002, p. 53.
- [57] L. Frankfurt and M. Strikman, Eur. Phys. J. A **5** (1999) 293.
- [58] R. Brock *et al.* [CTEQ Collaboration], Rev. Mod. Phys. **67** (1995) 157.
- [59] J. C. Collins, Phys. Rev. D **57** (1998) 3051 [Erratum-ibid. D **61** (2000) 019902].
- [60] C. Adloff *et al.* [H1 Collaboration], Z. Phys. C **76** (1997) 613.
- [61] A. Aktas *et al.* [H1 Collaboration], Eur. Phys. J. C **48** (2006) 715.
- [62] A. Aktas *et al.* [H1 Collaboration], Eur. Phys. J. C **48** (2006) 749.
- [63] A. Aktas *et al.* [H1 Collaboration], JHEP **0710** (2007) 042.
- [64] A. Aktas *et al.* [H1 Collaboration], Eur. Phys. J. C **51** (2007) 549.
- [65] A. Aktas *et al.* [H1 Collaboration], Eur. Phys. J. C **50** (2007) 1.
- [66] J. Breitweg *et al.* [ZEUS Collaboration], Eur. Phys. J. C **1** (1998) 81.
- [67] J. Breitweg *et al.* [ZEUS Collaboration], Eur. Phys. J. C **6** (1999) 43.
- [68] S. Chekanov *et al.* [ZEUS Collaboration], Nucl. Phys. B **672** (2003) 3.
- [69] S. Chekanov *et al.* [ZEUS Collaboration], Eur. Phys. J. C **38** (2004) 43.
- [70] S. Chekanov *et al.* [ZEUS Collaboration], Eur. Phys. J. C **52** (2007) 813.
- [71] S. Chekanov [ZEUS Collaboration], Nucl. Phys. B **800** (2008) 1.
- [72] S. Chekanov *et al.* [ZEUS Collaboration], Nucl. Phys. B **816** (2009) 1.
- [73] S. Chekanov *et al.* [ZEUS Collaboration], Nucl. Phys. B **831** (2010) 1.
- [74] L. Frankfurt, V. Guzey and M. Strikman, J. Phys. G **27** (2001) R23.
- [75] L. Frankfurt, V. Guzey, M. McDermott and M. Strikman, JHEP **0202** (2002) 027.
- [76] L. Frankfurt, V. Guzey and M. Strikman, Phys. Rev. D **71** (2005) 054001.
- [77] V. N. Gribov and L. N. Lipatov, Sov. J. Nucl. Phys. **15** (1972) 438 [Yad. Fiz. **15** (1972) 781];
 Y. L. Dokshitzer, Sov. Phys. JETP **46** (1977) 641 [Zh. Eksp. Teor. Fiz. **73** (1977) 1216];
 G. Altarelli and G. Parisi, Nucl. Phys. B **126** (1977) 298.
- [78] D. Schildknecht, Nucl. Phys. B **66** (1973) 398.
- [79] P. Ditsas and G. Shaw, Nucl. Phys. B **113** (1976) 246.
- [80] T. H. Bauer, R. D. Spital, D. R. Yennie and F. M. Pipkin, Rev. Mod. Phys. **50** (1978) 261 [Erratum-ibid. **51** (1979) 407].

- [81] L. L. Frankfurt and M. I. Strikman, Phys. Rept. **160** (1988) 235.
- [82] L. L. Frankfurt and M. I. Strikman, Nucl. Phys. B **316** (1989) 340.
- [83] N. N. Nikolaev and B. G. Zakharov, Phys. Lett. B **260** (1991) 414.
- [84] N. N. Nikolaev and B. G. Zakharov, Z. Phys. C **49** (1991) 607.
- [85] J. Kwiecinski and B. Badelek, Phys. Lett. B **208** (1988) 508.
- [86] B. Badelek and J. Kwiecinski, Nucl. Phys. B **370** (1992) 278.
- [87] B. Badelek and J. Kwiecinski, Phys. Rev. D **50** (1994) 4.
- [88] G. Piller, W. Ratzka and W. Weise, Z. Phys. A **352** (1995) 427.
- [89] W. Melnitchouk and A. W. Thomas, Phys. Rev. D **47** (1993) 3783.
- [90] W. Melnitchouk and A. W. Thomas, Phys. Lett. B **317** (1993) 437.
- [91] W. Melnitchouk and A. W. Thomas, Phys. Rev. C **52** (1995) 3373.
- [92] W. Melnitchouk and A. W. Thomas, Phys. Rev. C **67** (2003) 038201.
- [93] B. Kopeliovich and B. Povh, Z. Phys. A **356** (1997) 467.
- [94] C. L. Bilchak, D. Schildknecht and J. D. Stroughair, Phys. Lett. B **214** (1988) 441.
- [95] G. Shaw, Phys. Rev. D **47** (1993) 3676.
- [96] S. J. Brodsky and H. J. Lu, Phys. Rev. Lett. **64** (1990) 1342.
- [97] A. Capella, A. Kaidalov, C. Merino, D. Pertermann and J. Tran Thanh Van, Eur. Phys. J. C **5** (1998) 111.
- [98] N. Armesto, A. Capella, A. B. Kaidalov, J. Lopez-Albacete and C. A. Salgado, Eur. Phys. J. C **29** (2003) 531.
- [99] N. Armesto, A. B. Kaidalov, C. A. Salgado and K. Tywoniuk, Eur. Phys. J. C **68** (2010) 447.
- [100] G. Piller, G. Niesler and W. Weise, Z. Phys. A **358** (1997) 407.
- [101] G. Piller and W. Weise, Phys. Rept. **330** (2000) 1.
- [102] A. Adeluyi and G. Fai, Phys. Rev. C **74** (2006) 054904.
- [103] N. Armesto, J. Phys. G **32** (2006) R367.
- [104] E.L. Feinberg and I. Y. Pomeranchuk, Nuovo Cimento Suppl. **III** (1956) 652.
- [105] V. N. Gribov, B. L. Ioffe and I. Y. Pomeranchuk, Sov. J. Nucl. Phys. **2** (1966) 549 [Yad. Fiz. **2** (1965) 768].
- [106] B. L. Ioffe, Phys. Lett. B **30** (1969) 123.

- [107] V.N. Gribov, *Gauge theories and quark confinement*, Phasis, Moscow, 2002, p. 3.
- [108] V. N. Gribov, arXiv:hep-ph/0006158.
- [109] R.P. Feynman, *Photon-hadron interactions*, W.A. Benjamin, Inc., Reading, 1972.
- [110] A.I. Akhiezer and I.Ya. Pomeranchuk, *Some Problems in Nuclear Theory*, Gostekhizdat, Moscow, 1952.
- [111] L. Bertocchi, *Nuovo Cim. A* **11** (1972) 45.
- [112] S. Mandelstam, *Nuovo Cim.* **30** (1963) 1113, 1127 and 1148.
- [113] R. J. Glauber, *Phys. Rev.* **100** (1955) 242.
- [114] V. N. Gribov, *Sov. Phys. JETP* **26** (1968) 414 [*Zh. Eksp. Teor. Fiz.* **53** (1967) 654].
(Reprinted in *Caneschi, L. (ed.): *Regge theory of low-p(T) hadronic interactions** 63-71) "The theory of complex angular momenta: Gribov lectures on theoretical physics." Cambridge, UK, Univ. Pr. (2003).
- [115] M. L. Good and W. D. Walker, *Phys. Rev.* **120** (1960) 1857.
- [116] H. I. Miettinen and J. Pumplin, *Phys. Rev. D* **18** (1978) 1696.
- [117] B. Z. Kopeliovich and L. I. Lapidus, *Pisma Zh. Eksp. Teor. Fiz.* **28** (1978) 664.
- [118] M. Alvioli, C. Ciofi degli Atti, B. Z. Kopeliovich, I. K. Potashnikova and I. Schmidt, *Phys. Rev. C* **81** (2010) 025204.
- [119] V. A. Abramovsky, V. N. Gribov and O. V. Kancheli, *Yad. Fiz.* **18** (1973) 595 [*Sov. J. Nucl. Phys.* **18** (1974) 308]; also in V.N. Gribov, *Gauge theories and quark confinement*, Phasis, Moscow, 2002, p. 67.
- [120] L. Bertocchi and D. Treleani, *J. Phys. G* **3** (1977) 147.
- [121] L. Frankfurt, W. Koepf, M. Strikman, *Phys. Lett. B* **405** (1997) 367.
- [122] J.D. Bjorken, *Proc. Cornell Intern. Conf. on Electron and Photon Interactions*, Cornell University Press (1972).
- [123] L. L. Frankfurt and M. I. Strikman, *Phys. Rept.* **76** (1981) 215.
- [124] L. Alvero, L. L. Frankfurt and M. I. Strikman, *Eur. Phys. J. A* **5** (1999) 97.
- [125] D. R. Yennie, *In *Cargese 1972, Proceedings, Cargese Lectures In Physics, Vol. 7*, 331-405*
- [126] M. Alvioli, C. Ciofi degli Atti, I. Marchino, V. Palli and H. Morita, *Phys. Rev. C* **78** (2008) 031601.
- [127] V. N. Gribov and A. A. Migdal, *Sov. J. Nucl. Phys.* **8** (1969) 583 [*Yad. Fiz.* **8** (1968) 1002].
- [128] B. Blaettel, G. Baym, L. L. Frankfurt, H. Heiselberg and M. Strikman, *Phys. Rev. D* **47** (1993) 2761.

- [129] L. Frankfurt, V. Guzey and M. Strikman, J. Phys. G **27** (2001) R23.
- [130] L. L. Frankfurt, G. A. Miller, M. Strikman, Ann. Rev. Nucl. Part. Sci. **44** (1994) 501-560.
- [131] A. Donnachie and P. V. Landshoff, Phys. Lett. B **296** (1992) 227.
- [132] J. Breitweg *et al.* [ZEUS Collaboration], Eur. Phys. J. C **2** (1998) 247.
- [133] L. Frankfurt, G. A. Miller and M. Strikman, Phys. Rev. Lett. **71** (1993) 2859.
- [134] V. Guzey and M. Strikman, Phys. Lett. B **633** (2006) 245.
- [135] V. Guzey and M. Strikman, arXiv:0908.1149 [hep-ph].
- [136] L. Frankfurt, A. Radyushkin and M. Strikman, Phys. Rev. D **55** (1997) 98.
- [137] L. Frankfurt, V. Guzey and M. Strikman, Phys. Rev. D **58** (1998) 094039.
- [138] H. Abramowicz, L. Frankfurt and M. Strikman, eConf **C940808** (1994) 033 [Surveys High Energ. Phys. **11** (1997) 51] [arXiv:hep-ph/9503437].
- [139] L. L. Frankfurt and M. I. Strikman, Nucl. Phys. B **148** (1979) 107.
- [140] A. Aktas *et al.* [H1 Collaboration], Eur. Phys. J. C **44** (2005) 1.
- [141] F. D. Aaron *et al.* [H1 Collaboration], Phys. Lett. B **659** (2008) 796.
- [142] M. I. Strikman and L. L. Frankfurt, Yad. Fiz. **41** (1985) 485.
- [143] S. Chekanov *et al.* [ZEUS Collaboration], Nucl. Phys. B **776** (2007) 1.
- [144] S. L. Adler, Phys. Rev. **135** (1964) B963.
- [145] M. Alvioli, H. J. Drescher and M. Strikman, Phys. Lett. B **680** (2009) 225.
- [146] L. Frankfurt, C. E. Hyde, M. Strikman and C. Weiss, Phys. Rev. D **75** (2007) 054009.
- [147] S. Chekanov *et al.* [ZEUS Collaboration], Eur. Phys. J. C **24** (2002) 345.
- [148] L. Trentadue, G. Veneziano, Phys. Lett. B **323** (1994) 201.
- [149] G. Ingelman, P. E. Schlein, Phys. Lett. B **152** (1985) 256.
- [150] J. F. Owens, Phys. Rev. D **30** (1984) 943.
- [151] F. D. Aaron *et al.* [H1 Collaboration], arXiv:1006.0946 [hep-ex].
- [152] S. Chekanov *et al.* [The ZEUS Collaboration], Eur. Phys. J. C **55** (2008) 177.
- [153] S. Chekanov *et al.* [ZEUS Collaboration], Phys. Lett. B **545** (2002) 244.
- [154] S. Chekanov *et al.* [ZEUS Collaboration], Eur. Phys. J. C **51** (2007) 301.
- [155] A. A. Affolder *et al.* [CDF Collaboration], Phys. Rev. Lett. **84** (2000) 5043.
- [156] M. Klasen and G. Kramer, arXiv:1006.4964 [hep-ph].

- [157] L. Frankfurt, V. Guzey and M. Strikman, Phys. Rev. Lett. **91** (2003) 202001.
- [158] L. Frankfurt, V. Guzey and M. Strikman, Mod. Phys. Lett. A **21** (2006) 23.
- [159] M. Lacombe, B. Loiseau, J. M. Richard, R. Vinh Mau, J. Cote, P. Pires and R. De Tourreil, Phys. Rev. C **21** (1980) 861.
- [160] H. L. Lai *et al.* [CTEQ Collaboration], Eur. Phys. J. C **12** (2000) 375.
- [161] All the relevant information about the QCDNUM evolution program can be found at <http://www.nikhef.nl/h24/qcdnum>.
- [162] J. Edelmann, G. Piller and W. Weise, Phys. Rev. C **57** (1998) 3392.
- [163] V. A. Guzey, K. Saito, M. Strikman, A. W. Thomas and K. Tsushima, Phys. Rev. D **64** (2001) 054503.
- [164] L. Frankfurt, V. Guzey and M. Strikman, Phys. Lett. B **381** (1996) 379.
- [165] V. Guzey and M. Strikman, Phys. Rev. C **61** (2000) 014002.
- [166] F. R. P. Bissey, V. A. Guzey, M. Strikman and A. W. Thomas, Phys. Rev. C **65** (2002) 064317.
- [167] V. Guzey, Phys. Rev. C **64** (2001) 045201.
- [168] W. Melnitchouk, M. Sargsian and M. I. Strikman, Z. Phys. A **359** (1997) 99.
- [169] C. W. De Jager, H. De Vries and C. De Vries, Atom. Data Nucl. Data Tabl. **36** (1987) 495.
- [170] B. Blaettel, G. Baym, L. L. Frankfurt and M. Strikman, Phys. Rev. Lett. **70** (1993) 896.
- [171] L. McLerran, arXiv:hep-ph/0311028.
- [172] L. L. Frankfurt, M. I. Strikman and S. Liuti, Phys. Rev. Lett. **65** (1990) 1725.
- [173] N. Armesto, H. Paukkunen, C. A. Salgado and K. Tywoniuk, Phys. Lett. B **694** (2010) 38.
- [174] S. Chekanov *et al.* [ZEUS Collaboration], Phys. Lett. B **682** (2009) 8.
- [175] H1 Collaboration, arXiv:1012.4355 [hep-ex].
- [176] H. L. Lai, M. Guzzi, J. Huston, Z. Li, P. M. Nadolsky, J. Pumplin and C. P. Yuan, Phys. Rev. D **82** (2010) 074024.
- [177] R. Vogt, Phys. Rev. C **70** (2004) 064902.
- [178] R. Vogt, Phys. Rev. C **71** (2005) 054902.
- [179] R. Vogt, Acta Phys. Hung. A **25** (2006) 97.
- [180] N. Armesto *et al.*, J. Phys. G **35** (2008) 054001.
- [181] L. Frankfurt, A. Freund, V. Guzey and M. Strikman, Phys. Lett. B **418** (1998) 345 [Erratum-ibid. B **429** (1998) 414].

- [182] K. Goeke, V. Guzey and M. Siddikov, Phys. Rev. C **79** (2009) 035210.
- [183] P. M. Nadolsky *et al.*, Phys. Rev. D **78** (2008) 013004.
- [184] F. D. Aaron *et al.* [H1 and ZEUS Collaboration], JHEP **1001** (2010) 109.
- [185] A. D. Martin, W. J. Stirling, R. S. Thorne and G. Watt, Eur. Phys. J. C **70** (2010) 51.
- [186] P. Newman, private communication.
- [187] I. Schienbein, J. Y. Yu, C. Keppel, J. G. Morfin, F. Olness and J. F. Owens, Phys. Rev. D **77** (2008) 054013
- [188] K. Kovarik *et al.*, arXiv:1012.0286 [hep-ph].
- [189] K. Kovarik, arXiv:1006.4988 [hep-ph].
- [190] M. Hirai, S. Kumano and K. Saito, AIP Conf. Proc. **1189** (2009) 269.
- [191] H. Paukkunen and C. A. Salgado, JHEP **1007** (2010) 032 [arXiv:1004.3140 [hep-ph]].
- [192] H. Paukkunen and C. A. Salgado, arXiv:1009.3143 [hep-ph].
- [193] A. Schwimmer, Nucl. Phys. B **94** (1975) 445.
- [194] L. Frankfurt, W. Koepf and M. Strikman, Phys. Rev. D **54** (1996) 3194.
- [195] B. Kopeliovich and B. Povh, Phys. Lett. B **367** (1996) 329.
- [196] B. Z. Kopeliovich, J. Raufeisen and A. V. Tarasov, Phys. Rev. C **62** (2000) 035204.
- [197] E. Gotsman, E. Levin, M. Lublinsky, U. Maor and K. Tuchin, Phys. Lett. B **492** (2000) 47.
- [198] E. Gotsman, E. Levin, U. Maor, L. D. McLerran and K. Tuchin, Nucl. Phys. A **683** (2001) 383.
- [199] M. McDermott, L. Frankfurt, V. Guzey and M. Strikman, Eur. Phys. J. C **16** (2000) 641.
- [200] F. E. Low, Phys. Rev. D **12** (1975) 163.
- [201] L. Frankfurt, M. McDermott and M. Strikman, JHEP **0103** (2001) 045.
- [202] A. D. Martin, W. J. Stirling, R. S. Thorne and G. Watt, arXiv:0901.0002 [hep-ph].
- [203] M. Gluck, P. Jimenez-Delgado and E. Reya, Eur. Phys. J. C **53** (2008) 355.
- [204] T. J. Chapin *et al.*, Phys. Rev. D **31** (1985) 17.
- [205] H. Abramowicz and A. Levy, arXiv:hep-ph/9712415.
- [206] H. Abramowicz, E. M. Levin, A. Levy and U. Maor, Phys. Lett. B **269** (1991) 465.
- [207] J. w. Qiu and I. Vitev, Phys. Rev. Lett. **93** (2004) 262301.
- [208] L. Frankfurt and M. Strikman, Phys. Rev. C **82** (2010) 065203.

- [209] E. Fermi, Z. Phys. **29** (1924) 315;
C.F. von Weizsacker, Z. Phys. **88** (1934) 612;
E.J. Williams, Phys. Rev. **45** (1934) 729.
- [210] J. Seely *et al.*, Phys. Rev. Lett. **103** (2009) 202301.
- [211] V. Guzey and M. Strikman, Phys. Rev. C **75** (2007) 045208.
- [212] L. L. Frankfurt and M. I. Strikman, Phys. Lett. B **382** (1996) 6.
- [213] A. B. Kaidalov, V. A. Khoze, A. D. Martin and M. G. Ryskin, Acta Phys. Polon. B **34** (2003) 3163.
- [214] M. Arneodo, A. Bialas, M. W. Krasny, T. Sloan and M. Strikman, in Proceedings of Workshop on Future Physics at HERA, Eds. G. Ingelman, A. De Roeck and R. Klanner, arXiv:hep-ph/9610423.
- [215] M. Strikman, M. Tverskoy and M. Zhalov, Phys. Lett. B **626** (2005) 72.
- [216] S. J. Brodsky, L. Frankfurt, J. F. Gunion, A. H. Mueller and M. Strikman, Phys. Rev. D **50** (1994) 3134.
- [217] J. C. Collins, L. Frankfurt and M. Strikman, Phys. Rev. D **56** (1997) 2982.
- [218] J. C. Collins and A. Freund, Phys. Rev. D **59** (1999) 074009.
- [219] A. P. Bukhvostov, G. V. Frolov, L. N. Lipatov and E. A. Kuraev, Nucl. Phys. B **258** (1985) 601.
- [220] D. Mueller, D. Robaschik, B. Geyer, F. M. Dittes and J. Horejsi, Fortsch. Phys. **42** (1994) 101 [arXiv:hep-ph/9812448].
- [221] X. D. Ji, J. Phys. G **24** (1998) 1181.
- [222] K. Goeke, M. V. Polyakov and M. Vanderhaeghen, Prog. Part. Nucl. Phys. **47** (2001) 401.
- [223] M. Diehl, Phys. Rept. **388** (2003) 41.
- [224] A. V. Belitsky and A. V. Radyushkin, Phys. Rept. **418** (2005) 1.
- [225] B. Blok, L. Frankfurt and M. Strikman, Phys. Rev. D **80** (2009) 114009.
- [226] M. Burkardt, Int. J. Mod. Phys. A **18** (2003) 173.
- [227] P. V. Pobylitsa, Phys. Rev. D **66** (2002) 094002.
- [228] K. Kumericki, D. Mueller and K. Passek-Kumericki, Nucl. Phys. B **794** (2008) 244.
- [229] L. Schoeffel, Phys. Lett. B **658** (2007) 33 [arXiv:0706.3488 [hep-ph]].
- [230] L. L. Frankfurt, A. Freund and M. Strikman, Phys. Rev. D **58** (1998) 114001 [Erratum-ibid. D **59** (1999) 119901].
- [231] A. Freund, M. McDermott and M. Strikman, Phys. Rev. D **67** (2003) 036001.

- [232] A. V. Belitsky, D. Mueller and A. Kirchner, Nucl. Phys. B **629** (2002) 323.
- [233] A. V. Belitsky, D. Mueller, A. Kirchner and A. Schafer, Phys. Rev. D **64** (2001) 116002.
- [234] L. Frankfurt, W. Koepf and M. Strikman, Phys. Rev. D **57** (1998) 512.
- [235] A. Caldwell and H. Kowalski, Phys. Rev. C **81** (2010) 025203.
- [236] S. White and M. Strikman, arXiv:1003.2196 [nucl-ex].
- [237] L. Frankfurt and M. Strikman, Phys. Lett. B **645** (2007) 412.
- [238] S. Aid *et al.* [H1 Collaboration], Z. Phys. C **72** (1996) 573.
- [239] R. Baier, D. Schiff and B. G. Zakharov, Ann. Rev. Nucl. Part. Sci. **50** (2000) 37.
- [240] K. Goulianos, arXiv:hep-ph/0407035.
- [241] K. Goulianos, Phys. Lett. B **358** (1995) 379.
- [242] L. Frankfurt, M. Strikman, C. Weiss and M. Zhalov, Czech. J. Phys. **55** (2005) B675.
- [243] A. B. Kaidalov, V. A. Khoze, A. D. Martin and M. G. Ryskin, Eur. Phys. J. C **21** (2001) 521.
- [244] M. Strikman and V. Guzey, Phys. Rev. C **52** (1995) 1189.
- [245] R. J. Glauber and G. Matthiae, Nucl. Phys. B **21** (1970) 135.
- [246] R.K. Ellis, W.J. Stirling and B.R. Webber, *QCD and Collider Physics*, Cambridge Univ. Press, 1996, p. 248.
- [247] M. Klasen and G. Kramer, Phys. Rev. D **80** (2009) 074006.
- [248] A. Morsch, in *Hard probes in heavy-ion collisions at the LHC*, Eds. M. Mangano, H. Satz and U. Wiedemann, report CERN-2004-009, CERN, 2004.
- [249] G. Baur, K. Hencken, D. Trautmann, S. Sadozsky and Y. Kharlov, Phys. Rept. **364** (2002) 359.
- [250] C. A. Bertulani, S. R. Klein and J. Nystrand, Ann. Rev. Nucl. Part. Sci. **55** (2005) 271.
- [251] M. Strikman, R. Vogt and S. White, Phys. Rev. Lett. **96** (2006) 082001.
- [252] M. Klasen and G. Kramer, Phys. Rev. Lett. **93** (2004) 232002.
- [253] S. Chekanov *et al.* [ZEUS Collaboration], Eur. Phys. J. C **23** (2002) 615.
- [254] C. A. Bertulani and G. Baur, Phys. Rept. **163** (1988) 299.
- [255] M. Gluck, E. Reya and A. Vogt, Phys. Rev. D **46** (1992) 1973.
- [256] H. Abramowicz, K. Charchula and A. Levy, Phys. Lett. B **269** (1991) 458.
- [257] M. Strikman, arXiv:0711.1625 [hep-ph].

- [258] M. Strikman, Nucl. Phys. A **827** (2009) 240C [arXiv:0903.1941 [hep-ph]].
- [259] L. Lipatov and V. Fadin, Phys. Lett. B **429** (1998) 127.
- [260] M. Ciafaloni, D. Colferai and G. P. Salam, Phys. Rev. D **60** (1999) 114036.
- [261] R. D. Ball and S. Forte, Nucl. Phys. B **742** (2006) 158.
- [262] G. Altarelli, R. D. Ball and S. Forte, Nucl. Phys. B **799** (2008) 199.
- [263] F. Gelis, E. Iancu, J. Jalilian-Marian and R. Venugopalan, arXiv:1002.0333 [hep-ph].
- [264] L. Frankfurt, V. Guzey, M. McDermott and M. Strikman, Phys. Rev. Lett. **87** (2001) 192301.
- [265] M. M. Block, Phys. Rept. **436** (2006) 71.
- [266] R.J. Eden et al., *The Analytic S-matrix*, Cambridge Univ. Press (1966), p. 287.
- [267] L. Frankfurt, M. Strikman and C. Weiss, Annu. Rev. Nucl. Part. Sci. **55** (2005) 403.
- [268] T. Rogers, V. Guzey, M. Strikman and X. Zu, Phys. Rev. D **69** (2004) 074011.
- [269] E. A. Kuraev, L. N. Lipatov and V. S. Fadin, Sov. Phys. JETP **45** (1977) 199 [Zh. Eksp. Teor. Fiz. **72** (1977) 377];
I. I. Balitsky and L. N. Lipatov, Sov. J. Nucl. Phys. **28** (1978) 822 [Yad. Fiz. **28** (1978) 1597].
- [270] V. N. Gribov, Sov. Phys. JETP **30** (1970) 709 [Zh. Eksp. Teor. Fiz. **57** (1969) 1306].
- [271] L. Frankfurt and M. Strikman, Phys. Rev. D **66** (2002) 031502.
- [272] H. Kowalski, T. Lappi and R. Venugopalan, Phys. Rev. Lett. **100** (2008) 022303.
- [273] S. Gieseke and C. F. Qiao, Phys. Rev. D **61** (2000) 074028;
S. Gieseke, “Virtual photon interactions in high energy QCD”, DESY-THESIS-2001-031.
- [274] R.K. Ellis, W.J. Stirling and B.R. Webber, *QCD and Collider Physics*, Cambridge Univ. Press, 1996.
- [275] J.J. Sakurai, Phys. Rev. Lett. **22**, 981 (1969).
- [276] H. Fraas, B.J. Read and D. Schildknecht, Nucl. Phys. **B86** (1975) 346;
G. Cvetic, D. Schildknecht and A. Shoshi, Acta Phys. Polon. **B30** (1999) 3265;
A. Donnachie and G. Shaw, in: *Electromagnetic interactions of hadrons, Vol.2*, 169, eds. A. Donnachie and G. Shaw (Plenum, New York (1978));
G. Shaw, Phys. Rev. **D47** (1993) R3676;
G. Shaw, Phys. Lett. **B228** (1989) 125;
P. Ditsas and G. Shaw, Nucl. Phys. **113** (1976) 246.
- [277] L. Bourhis, M. Fontannaz, J. P. Guillet and M. Werlen, Eur. Phys. J. C **19** (2001) 89.
- [278] L. D. McLerran and R. Venugopalan, Phys. Rev. D **49** (1994) 2233.

- [279] E. Iancu and R. Venugopalan, arXiv:hep-ph/0303204.
- [280] J. Ashman *et al.* [European Muon Collaboration], Z. Phys. C **52** (1991) 1.
- [281] F. Aversa, P. Chiappetta, M. Greco and J. P. Guillet, Nucl. Phys. B **327**, 105 (1989);
B. Jager, A. Schafer, M. Stratmann and W. Vogelsang, Phys. Rev. D **67**, 054005 (2003);
D. de Florian, Phys. Rev. D **67**, 054004 (2003).
- [282] V. Guzey, M. Strikman and W. Vogelsang, Phys. Lett. B **603** (2004) 173.
- [283] J. Adams *et al.* [STAR Collaboration], Phys. Rev. Lett. **97** (2006) 152302.
- [284] B. Meredith, Nucl. Phys. **A830** (2009) 595.
- [285] G. Rakness, private communication.
- [286] D. Kharzeev, E. Levin and L. McLerran, Phys. Lett. B **561** (2003) 93;
D. Kharzeev, Y. V. Kovchegov and K. Tuchin, Phys. Rev. D **68** (2003) 094013.
- [287] A. Dumitru, A. Hayashigaki and J. Jalilian-Marian, Nucl. Phys. A **765** (2006) 464.
- [288] E. Braidot [STAR Collaboration], arXiv:1005.2378 [hep-ph].
- [289] B. Meredith, DIS 2010 Conference Proceedings, PoS(DIS 2010)081.
- [290] M. Strikman and W. Vogelsang, Phys. Rev. D **83** (2011) 034029.
- [291] J. L. Albacete and C. Marquet, Phys. Rev. Lett. **105** (2010) 162301.
- [292] D. J. Gross and F. Wilczek, Phys. Rev. Lett. **30** (1973) 1343.
- [293] L. N. Lipatov, Phys. Lett. B **309** (1993) 394.
- [294] K. J. Golec-Biernat and M. Wusthoff, Phys. Rev. D **59** (1998) 014017.
- [295] I. Balitsky, Nucl. Phys. B **463** (1996) 99; Phys. Rev. Lett. **81** (1998) 2024; Phys. Rev. D **60** (1999) 014020; I. Balitsky, Phys. Lett. B **518** (2001) 235.
- [296] Y. V. Kovchegov, Phys. Rev. D **60** (1999) 034008.

